Dust and Cool Gas Content and Distribution in Early-Type Galaxies

by

David Henry William Glass

A thesis submitted in partial fulfilment
of the requirements for the degree of
Doctor of Philosophy
at the University of Central Lancashire

February 2024

Declaration

Type of Award: Doctor of Philosophy

School: Engineering and Computing

The work presented in this thesis was carried out at the Jeremiah Horrocks Institute for Mathematics, Physics and Astronomy, University of Central Lancashire.

I declare that while registered as a candidate for the research degree, I have not been a registered candidate or enrolled student for another award of the University or other academic or professional institution.

I declare that no material contained in the thesis has been used in any other submission for an academic award and is solely my own work.

No proof-reading service was used in the compilation of this thesis.

SIGNATURE 

NAME David Henry William Glass

Abstract

This thesis considers the content and distribution of cool Interstellar Medium (ISM) in Early-Type Galaxies (ETGs), and how it can be used to infer the evolutionary mechanisms responsible for forming ETGs in the local Universe. High-resolution observations of molecular gas via carbon monoxide (CO) emission with the Atacama Large Millimetre/submillimetre Array (ALMA) interferometric telescope in five Dusty ETGs were analysed by fitting of kinematic models, to reveal any asymmetries or additional features. A new, clean and complete sample of galaxies was created within the Galaxy and Mass Assembly (GAMA) project equatorial regions to a redshift of 0.06, with visual morphological classifications assigned where possible. Masses and properties of cool dust for galaxies with suitable photometry in the sample were obtained by fitting a single modified blackbody (SMBB) model to sub-mm photometry from the Herschel-ATLAS project. New observations of molecular gas via CO emission for 32 Dusty ETGs from the clean and complete sample were also obtained using the IRAM 30m telescope.

The results of the work indicate that for dusty ETGs in the local Universe, in low-density environments such as those in the GAMA equatorial regions, interactions and minor mergers play a significant role in their formation. These events are apparent for four of the five ALMA-observed Dusty ETGs, with the fifth affected by contamination with a background object. Molecular gas-to-dust mass ratios derived from IRAM 30m Telescope observations are less scattered at stellar masses $<3 \times 10^{10}$ $M_{\odot}$, indicating less introduction of ISM as a result of disturbance to form the ETGs. At higher stellar masses,

gas-to-dust mass ratios are lower and more scattered, with minor mergers appearing to be more significant. The observed Dusty ETGs are mostly star-forming, and appear to have been observed at a stage where ISM has settled, allowing star formation to recommence.

The estimation of dust masses using Herschel-ATLAS photometry for lower stellar-mass galaxies ($\leq 10^{9.5}$ $M_{\odot}$) appears to have been affected by lack of quantification of sub-mm excess emission, which may have led to under-estimation of dust mass. This is unavoidable without photometry at wavelengths greater than 500 μm, to constrain the longer-wavelength region of the dust emission spectrum. Nonetheless, dust masses were shown to be reduced in Dusty ETGs compared to Late-Type Galaxies (LTGs) above a stellar mass of $\sim 10^{9.5}$ $M_{\odot}$, while temperature and emissivity coefficient were found to be indistinguishable between Dusty ETGs and LTGs. Power-law relations from this work are shown for information between dust mass and star formation rate, and molecular gas mass and either dust mass or star formation rate, as expected if these properties in star-forming galaxies are linked.

Opportunities for further work have been identified. Possible projects include further observations with ALMA and the IRAM 30m telescope, to extend the results presented. Radiative transfer modelling for Dusty ETGs is also a possibility, to investigate non-equilibrium dust temperatures as an indicator of recent acquisition of dust.

Contents

Declaration ii

Abstract iii

List of Tables xii

List of Figures xv

Acknowledgements xxv

1 Introduction 1

1.1 Overview 1

1.2 Background 3

1.2.1 Galaxies and Interstellar Medium 3

1.2.2 Galaxy Morphology and Evolution in the Local Universe 6

1.2.3 Galaxy Evolution and Interstellar Medium 11

1.3 Research Topics 14

1.4 Structure of Thesis 15

2 Telescopes, Instruments, Methods and Data Sources 18

2.1 Principles of Radio Interferometry 18

2.2 Atacama Large Millimetre/submillimetre Array (ALMA) 24

2.3 IRAM 30m Telescope 29

2.4 Herschel Space Observatory 33

2.5 James Clerk Maxwell Telescope (JCMT) 36

2.6 Other Telescopes 38

2.6.1 GALEX 38

2.6.2 SDSS Telescope 38

2.6.3 Anglo-Australian Telescope (AAT) 40

2.6.4 VLT Survey Telescope (VST) 41

2.6.5 VISTA 42

2.6.6 WISE 42

2.6.7 Karl G. Jansky Very Large Array (VLA) 43

2.7 Techniques 44

2.7.1 KinMSpy and GASTimator 44

2.7.2 Stackarator 47

2.7.3 MAGPHYS 48

2.7.4 Colour and Flux Bias Corrections for H-ATLAS Data 51

2.8 Data Sources 58

2.8.1 Galaxy and Mass Assembly (GAMA) 58

2.8.2 GAMA-KiDS-GalaxyZoo 59

2.8.3 Herschel ATLAS (H-ATLAS) 60

2.8.4 SAMI Galaxy Survey 61

2.8.5 JINGLE 61

2.8.6 xCOLD GASS 62

2.8.7 Other Data Sources 62

3 Molecular Gas Distribution and Kinematics in ALMA-Observed Dusty Local Early-Type Galaxies 64

3.1 Introduction 64

3.2 Data and Methods 65

3.2.1 Observational Data 65

3.2.2 Kinematic Modelling 71

3.3 Results 74

3.3.1 Kinematic Modelling 74

3.3.2 Molecular Gas Stability Analysis 87

3.3.3 Kinematic Alignments of Molecular Gas, Ionised Gas and Stars . 91

3.3.4 ALMA Detections for GAMA177186 94

3.3.5 ALMA Detections for GAMA622305 99

3.4 Discussion of Findings 102

3.5 Conclusions for Chapter 106

4 Construction of a New, Clean and Complete Galaxy Sample 108

4.1 Introduction 108

4.2 Initial Galaxy Selection 109

4.3 Identification and Removal of Strong Active Galactic Nuclei (AGN) . . . 111

4.3.1 BPT Diagram 112

4.3.2 WHAN Diagram 114

4.3.3 Fibre Aperture Effects and AGN Detection 116

4.3.4 Manual Examination of Spectra 118

4.3.5 WISE Colour-Colour Diagram 119

4.3.6 20cm Emission 121

4.3.7 Removal of all galaxies with detected AGN 123

4.4 Removal of Galaxies With Gravitationally-Lensed Sub-mm Emission . . 123

4.5 Clean and Complete (Parent) Sample 125

4.6 Morphological Classification 125

4.6.1 Morphologies from GAMA II 126

4.6.2 Morphologies from GAMA-KiDS-GalaxyZoo 132

4.6.3 Morphological Classification at High Ellipticity 138

4.6.4 Final Morphological Classifications 140

4.6.5 Redshift Bias in Morphological Classification 143

4.6.6 Visual Inspection of ETG Sample 147

5 Galaxy Morphology and its Relationship to Galaxy Properties 148

5.1 Colour vs Stellar Mass 149

5.2 Specific Star Formation Rate versus Stellar Mass 152

5.3 r^* - J^* Colour versus u^* - r^* Colour 155

5.4 r-Band Single-Component Sérsic Index versus Stellar Mass 160

5.5 Bulge-Disc Decomposition from KiDS Images 162

5.6 Impact of removing Galaxies with AGN from the Parent Sample 168

5.7 Relative Behaviour of Numeric Morphology Indicators 169

5.8 Low-Mass ETGs with LTG Properties ("ETG Misfits") 171

5.9 Discussion of Chapter 178

6 Properties of Cool Interstellar Dust in Local Galaxies 183

6.1 Introduction 183

6.2 Spectra of Cool Dust Thermal Emission 184

6.3 Fitting of Dust Emission Models to Data 186
6.3.1 Non-Hierarchical Model Fitting 187
6.3.2 Hierarchical Model Fitting 189
6.3.3 Noise Modelling 193
6.3.4 Implementation of Fitting 194
6.4 Results 196
6.4.1 Application of Colour and Flux Bias Corrections 196
6.4.2 Results of Fitting and Comparison of Fitting Methods 197
6.4.3 Comparison of Results with JINGLE 201
6.4.4 Comparison with Results from GAMA II (MAGPHYS) 205
6.4.5 Relationship between Galaxy Dust Properties and Morphology . . 209
6.4.6 Variation of Galaxy Properties with Dust Mass 213
6.5 Discussion of Chapter 217

7 IRAM 30m Telescope Observations of Dusty Early-Type Galaxies 221

7.1 Cool Molecular Gas and CO Emission 222
7.2 Sample Selection and Observation Planning 222
7.3 Observations 235
7.4 Data Reduction 237
7.4.1 Line Detecton and Initial Flux Density Estimation 237

7.4.2 ETG Optical Inclination and ^{12}CO[1-0] Spectral Shape 245

7.4.3 Aperture Correction 246

7.4.4 Estimation of Molecular Gas Masses from ^{12}CO[1-0] Emission . 255

7.5 Relationships Between Galaxy Properties and Molecular Gas Mass 262

7.5.1 Molecular Gas Mass versus Stellar Mass 264

7.5.2 Dust Mass versus Molecular Gas Mass 268

7.5.3 Star Formation and Molecular Gas Content 270

7.5.4 Gas-to-Dust Ratio versus Stellar Mass 271

7.6 Discussion of Chapter 275

8 Discussion and Conclusions **277**

8.1 Overall Findings 277

8.2 Future Work 280

8.2.1 Short-Term Projects 280

8.2.2 Longer-Term Projects 282

Bibliography **285**

Appendix A Calculating Coordinates for Equally Spaced Points on an Ellipse 300

List of Tables

2.1 Constants for use with Equation 2.19 57

3.1 Properties of the ALMA-observed ETGs. 68

3.2 Optimal ellipse mask sizes and ALMA-observed ^{12}CO[2-1] emission fluxes for GAMA64646, 272990 and 622429. 72

3.3 Parameters for fitted molecular gas disc models with a Sérsic surface brightness profile for GAMA64646 and GAMA272990. 79

3.4 Parameters for a molecular gas central ring, bar and spiral arm structure plus an underlying disc with a Sérsic surface brightness profile for GAMA622429. 86

3.5 Total star formation rates from GAMA DR3 MAGPHYS results (0-100 Myr) and SAMI DR3 (total for maps) for GAMA64646, 272990 and 622429. 89

3.6 Kinematic position angles for molecular gas (from model fitting to ALMA data), stars and ionised gas (from SAMI DR3) for GAMA64646, 272990 and 622429. 93

4.1 Results of GAMA morphological classification for the Parent Sample based on GAMA II VisualMorphologyv03 (Moffett et al. 2016). 129

4.2 Results of morphological classification using GAMA-KiDS-GalaxyZoo (based on KiDS images) for the Parent Sample. 136

4.3 Additional Spiral galaxies (identified by GAMA-KiDS-GalaxyZoo) present in the GAMA II morphological classifications with ellipticity ≤0.7. 142

4.4 Final morphological classifications (used in the remainder of this work) for galaxies in the Parent Sample. 145

6.1 Flat priors used for SMBB model fitting. 189

6.2 Hyperparameter values (defining the overall distributions for the whole sample) from hierarchical fitting of SMBB models to 445 dusty galaxies from the Parent Sample. 199

6.3 Median parameter values and uncertainties (16th and 84th percentiles) for SMBB model parameters from hierarchical fitting of SMBB models to H-ATLAS data, for Ellipticals, Lenticulars and Spirals. 211

6.4 Significance levels for k-sample midrank Anderson-Darling tests comparing properties of dust within morphology classifications. 212

7.1 Dusty ETGs selected for observation with the IRAM 30m telescope in Summer 2019. 229

7.2 Dusty ETGs selected for observation with the IRAM 30m telescope in January 2020. 230

7.3 Measured CO line fluxes ($K(T_A^*)$ km s^{-1}) and velocity widths (km s^{-1}) for the Dusty ETGs observed with the IRAM 30m telescope. 240

7.4 u-band aperture correction factors and corrected flux densities (Jy) for ^{12}CO[1-0] and ^{12}CO[2-1] emission for the observed Dusty ETGs with detected ^{12}CO[1-0] emission. 254

7.5 O3N2 and N2 values (where they exist), selected method used for gas-phase metallicity calculation and estimated values of 12 + $\log_{10}$[O/H]. . . 259

7.6 Estimated values of α_{CO} based on gas-phase metallicity, and molecular gas mass estimates from aperture-corrected ^{12}CO[1-0] line fluxes in Table 7.4. 261

7.7 Coefficients for the trend lines in Figure 7.13. 265

7.8 Coefficients for the trend lines in Figure 7.14. 268

7.9 GDR properties for Dusty ETGs observed for this work, binned above and below a stellar mass of 3×10^{10} M$_\odot$. 273

List of Figures

1.1 SDSS DR9 gri images of spiral, elliptical and lenticular galaxies in the local Universe. 7

1.2 Star formation rate (SFR) versus stellar mass for the xCOLD GASS galaxy sample. 8

1.3 Specific star formation rate (sSFR) versus stellar mass for galaxies in the Herschel Reference Survey. 10

1.4 Dust mass versus stellar mass for galaxies in the Herschel Reference Survey, from Smith et al. (2012), their Figure 8, and references therein. . . . 13

2.1 Antennae 1 and 2 with baseline vector $\vec{b}$ receiving plane waves from a distant target with unit direction $\hat{s}$. 20

2.2 ALMA antennae forming the 12m, 7m and TP arrays. 25

2.3 Band 6 SIS mixers. 27

2.4 ALMA Baseline Correlator system (Cortes et al. 2023). 28

2.5 IRAM 30m telescope, showing the 30m dish, secondary reflector, mount and control room. 30

2.6 Atmospheric absorption at the IRAM 30m telescope, for precipitable water vapour (PWV) levels of 2mm and 4mm. 32

2.7 Herschel Space Observatory (Herschel). 34

2.8 Components of JCMT and SCUBA-2. 37

2.9 MAGPHYS model fit (wavelength-dependent luminosity versus wavelength) to 21-band photometry for GAMA64646. 52

2.10 Comparison of calculated KColP and KColE with published values in the PACS and SPIRE explanatory supplements. 56

2.11 Comparison of models for flux bias divisors for the SPIRE pasbands with published data. 57

2.12 Mollweide diagram showing the locations of GAMA, KiDS and Herschel-ATLAS survey regions. 58

3.1 ALMA-observed dusty ETGs from Sansom et al. (2019). 67

3.2 Diagnostic (WHAN) plot for AGN activity, star formation and galaxy retirement. 69

3.3 Zeroth order moment maps for GAMA64646, 272990 and 622429 ^{12}CO[2-1] emission. 76

3.4 First order moment maps for GAMA64646, 272990 and 622429. 77

3.5 Diagnostic plots for GAMA64646, 272990 and 622429. 78

3.6 Plan view of point-source model for nuclear ring, bar and spiral arms using elliptical pathways. 83

3.7 PV diagrams (data as contours, model in colour) and spectra for GAMA622429. 85

3.8 Comparison of molecular gas distribution, star formation distribution (from SAMI, adaptive binning) and Q for GAMA64646, GAMA272990 and GAMA622429. 90

3.9 Kinematics of molecular gas, stars and ionised gas (*right*), overlain on KiDS r-band log-normalised images for GAMA64646, 272990 and 622429. 92

3.10 ^{12}CO[2-1] spectrum for GAMA177186 offset object, with binning to 70.7 km/s. 95

3.11 SED fitting of photometry from H-ATLAS and ALMA for GAMA177186 (assumed to be from the offset object). 97

3.12 Effect of assumed offset object redshift on fitted dust mass and temperature. 97

3.13 VISTA J, H and Ks-band co-added image (log-normalised) of GAMA177186. 98

3.14 Spectrum for ^{12}CO[2-1] detected in GAMA622305, with GAMA622305 velocity shown in relation to the emission line. 100

3.15 Star formation rate (SAMI, adaptive binning) and ^{12}CO[2-1] emission (ALMA, shown and ringed in green) overlaid on KiDS r-band log-normalised image of GAMA622305. 100

3.16 Analysis of GAMA622305 molecular gas distribution using STACKARATOR. 103

4.1 BPT diagram showing galaxies from the Initial Complete Sample identified as AGN hosts or starburst. 115

4.2 Use of WHAN diagram to identify AGN. 117

4.3 Histograms of galaxy numbers with increasing redshift. 118

4.4 Hubble Space Telescope (HST) colourised image of the accretion disc around the central supermassive black hole of NGC4261. 120

4.5 WISE colour-colour diagram derived for the initial complete sample. . . . 121

4.6 Absolute r-band magnitude versus redshift for the Initial Sample and Parent Sample. 126

4.7 Flowchart used for GAMA II morphology classification. 128

4.8 Plots of Galactic extinction corrected g^* - r^* colour versus absolute r^*-band magnitude for the nominal morphological types identified within GAMA II. 131

4.9 Extract of flowchart used by GAMA-KiDS-GalaxyZoo volunteers to classify the morphologies of galaxies (Porter-Temple et al. 2022). 133

4.10 Probabilities for each GAMA-KiDS-GalaxyZoo morphological classification for GAMA64646 (weak spiral) and GAMA298980 (elliptical). . . 135

4.11 Plots of Galactic extincion corrected g^* - r^* colour versus absolute r^*-band magnitude for the morphological types identified within GAMA-KiDS-GalaxyZoo. 137

4.12 Distribution of ellipticities within the clean and complete Parent Sample. . 139

4.13 Ellipticity distributions within GAMA II morphology classifications for the clean and complete Parent Sample. 140

4.14 Ellipticity distributions within GAMA-KiDS-GalaxyZoo morphology classifications for the clean and complete Parent Sample. 141

4.15 Plots of Galactic extinction corrected g^* - r^* colour versus absolute r^*-band magnitude for the final sets of morphological types. 144

4.16 Fraction of detected galaxies with spiral-like features in the Parent Sample as a function of redshift from GAMA (left) and GAMA-KiDS-GalaxyZoo (right) classifications. 146

5.1 Relationship between MAGPHYS-derived stellar mass estimates and r-band absolute magnitude for LTGs and ETGs with $>3\sigma$ detection in r-band flux density. 150

5.2 Galactic extinction corrected g^* - r^* colour versus stellar mass for all galaxies in the Parent Sample. 151

5.3 Galactic extinction corrected g^* - r^* colour versus stellar mass for morphological classifications. 152

5.4 Specific star formation rate (0 - 100 Myr) versus stellar mass for all galaxies in the Parent Sample. 155

5.5 Specific star formation rate (0 - 100 Myr) versus stellar mass for morphological classifications. 156

5.6 Galactic extinction corrected u^* - r^* colour versus r^* - J^* colour for (upper) the Parent Sample. 158

5.7 Galactic extinction corrected u^* - r^* colour versus r^* - J^* colour for morphological classifications. 159

5.8 r-band Sérsic index (single component) versus stellar mass for (upper) the Parent Sample, (lower) LTGs and ETGs separately. 161

5.9 r-band Sérsic index (single component) versus stellar mass for morphological classifications. 163

5.10 r-band bulge/total light ratio versus stellar mass for the Parent Sample and for ETGs/LTGs. 166

5.11 r-band bulge/total light ratio versus stellar mass for morphological classifications. 167

5.12 SDSS g - r (corrected for Galactic extinction) versus stellar mass from MAGPHYS, for the Parent Sample and "radio-quiet" galaxies with AGN. 169

5.13 Plots of parameter spaces discussed in Sections 5.1 - 5.5, with radio-quiet, strong AGN removed *(left)* and retained *(right)* within each pair of plotted samples. 170

5.14 r-band Sérsic index versus sSFR for the Parent Sample, from single-model fits to SDSS images for the Parent Sample. 172

5.15 r-band Sérsic index versus sSFR for morphological classifications, from single-model fits to SDSS images. 173

5.16 B/T versus sSFR for the Parent Sample. Median uncertainties are shown for the plotted galaxies. 174

5.17 ETG Misfit distributions in various parameter spaces, compared with distributions of Ellipticals and LBS from the Parent Sample. 175

5.18 ETG Misfit distributions of redshift and ellpticity compared to the overall LTG sample. 176

5.19 Example KiDS r-band images (20 arcsec $\times$ 20 arcsec, log-normalised) of ETG misfits. 177

5.20 Effective r-band radius versus stellar mass for morphological classifications within the Parent Sample. 179

5.21 Effective r-band radius versus stellar mass for morphological classifications, shown as contours to 20% of peak density for each classification. . 180

6.1 Comparison of Gaussian and Student-t (3 degrees of freedom) distributions (y) for input values of x. $\mu = 0$, $\sigma = 1$. 191

6.2 Convergence measures (ζ) for hierarchical fitting of SMBB models to ETGs and LTGs. 197

6.3 Convergence measures (ζ) for non-hierarchical fitting of SMBB models to ETGs and LTGs. 198

6.4 Example fitted spectra for GAMA7839. 199

6.5 Comparison of results from hierarchical fitting methods using Gaussian and Student-t distributions. 200

6.6 Comparison of non-hierarchical fitting results with hierarchical fitting. . . 202

6.7 Dust β versus temperature arising from non hierarchical and hierarchical fitting. 203

6.8 Dust mass versus stellar mass for Parent Sample galaxies with valid H-ATLAS data for fitting to SMBB models, and for galaxies from the JINGLE survey. 204

6.9 Dust temperature and β versus stellar mass, SFR and dust mass for H-ATLAS hierarchical model fits and JINGLE results. 206

6.10 Comparison of fitted dust masses from (*upper*) non-hierarchical fitting, (*lower*) hierarchical fitting (Student-t distribution), with dust masses from GAMA II. 208

6.11 Comparison of spectra produced by SMBB ($10^7 M_\odot$, T=22K) with a two component model with cold dust ($10^{7.25} M_\odot$, T=18K) and warm dust ($10^{5.25} M_\odot$, T=50K). 209

6.12 Histograms of $\log_{10}$(dust mass ($M_\odot$)), dust temperature (K) and dust β for morphological classifications from hierarchical fitting with Gaussian and Student-t distributions. 210

6.13 Dust mass versus stellar mass for Parent Sample galaxies, and LTGs/ETGs separately. 215

6.14 Star formation rate (0 - 100 Myr) versus dust mass corrected to align with results from hierarchical SMBB fitting to H-ATLAS data. 216

6.15 Star formation rate (0 - 100 Myr) versus GAMA II dust mass corrected to align with results from hierarchical SMBB fitting to H-ATLAS data, as a function of stellar mass. 217

6.16 GAMA II dust mass corrected to align with results from hierarchical SMBB fitting to H-ATLAS data versus r-band single-model Sérsic index, for the Parent Sample. 218

7.1 Comparison of MAGPHYS-derived dust mass estimates from GAMA II and calculation from H-ATLAS 250μm emission. 224

7.2 r-band log-normalised tiles (2 arcmin $\times$ 2 arcmin) of the 32 ETGs selected for observation with the IRAM 30m telescope. 232

7.3 Herschel SPIRE 250μm tiles (2 arcmin $\times$ 2 arcmin) of the 32 ETGs selected for observation with the IRAM 30m telescope. 233

7.4 Star formation rate versus stellar mass for the Parent Sample and the IRAM 30m observed Dusty ETGs. 234

7.5 GAMA II dust mass versus stellar mass for the Parent Sample, and the Dusty ETGs selected for observation with the IRAM 30m telescope. . . . 234

7.6 Emission spectra (~110 GHz) for 32 Dusty ETGs observed with the IRAM 30m telescope. 242

7.7 Emission spectra (~220 GHz) for 32 Dusty ETGs observed with the IRAM 30m telescope. 243

7.8 Comparison of integrated fluxes from integration of manually selected bins and Gaussian profiles fitted to spectral lines. 244

7.9 Comparison of spectra from the IRAM 30m telescope and ALMA for GAMA272990. 248

7.10 u-band luminosity density versus MAGPHYS-estimated SFR (<100 Myr) for the Spirals and Ellipticals/Lenticulars samples derived in Chapter 3. . 251

7.11 KiDS u-band aperture correction estimation for GAMA272990. 253

7.12 Molecular gas mass versus stellar mass for the Dusty ETGs. 264

7.13 Molecular gas mass versus stellar mass for galaxies from this work and other surveys for comparison. 266

7.14 Dust mass versus molecular gas mass for galaxies from this work and Davis et al. (2015). 269

7.15 SFR versus molecular gas mass for the Dusty ETGs. 270

7.16 SFR versus molecular gas mass for galaxies from xCOLD GASS, Dusty ETGs observed for this work, Dust-Lane ETGs and Void Galaxies. 272

7.17 Molecular gas to dust mass ratio (GDR) versus stellar mass for Dusty ETGs and Dust-Lane ETGs. 274

A.1 Equally-spaced points on an ellipse and the diffferences between the angles subtended by these and an equivalent number of equally-spaced angles. 301

A.2 Comparison of actual values of $\delta\alpha$ for an ellipse with a fitted model. . . . 302

A.3 Equally-spaced points generated using the Python code for an ellipse. . . 304

Acknowledgements

I am extremely grateful to all staff at the Jeremiah Horrocks Insitute for Mathematics, Physics and Astronomy, University of Central Lancashire, UK, for opening the door to my research in astronomy via their BSc(Hons) Astronomy programme based on distance learning. This in itself was a highly enriching experience, and provided opportunities for learning, travel and outreach beyond the course of study. I am especially grateful to my supervisor, Dr Anne E. Sansom, for inviting me to assist with research during the Summers of 2015 and 2016 which created the opportunity for postgraduate study, and for all the ongoing guidance throughout my studies as a postgraduate student. Prof. Cristina C. Popescu, my second supervisor, also provided me with very useful guidance throughout the research.

This work made use of preliminary data from the GAMA-KiDS-GalaxyZoo project, and I am grateful to Dr Lee Kelvin for providing this. I am also grateful to Dr. George Bendo of the University of Manchester, for his guidance in the reduction of data from the ALMA telescope, and to Dr. Timothy A. Davis of the University of Swansea for his guidance on the use of his software packages to analyse ALMA observations. Thanks also to Dr Isabella Lamperti, formerly of University College London, for providing her scripts for fitting dust emission models to sub-mm photometry.

My research in astrophysics would have been far more challenging without excellent software tools and online resources, in particular Python, the Common Astronomy Software Applications (CASA) package, LaTeX, NASA's Astrophysics Data System (ADS)

and arXiv. These allowed rapid data processing and development of ideas, and I could maintain progress even during the COVID-19 pandemic when I was confined at home. I am also grateful to the staff at the IRAM 30m Telescope, especially for the opportunity to observe Dusty ETGs discussed in this work remotely from home during the pandemic.

Huge thanks are also due to my wife Fiona, who supported and encouraged me from day one of my studies in astronomy. She has put up with my long hours of study and my trips away during my postgraduate research and before in my professional life, and saw me through the more challenging times. Hopefully I will be around more after this.

My parents, Stuart and Patricia Glass, provided the solid grounding and support which first got me through school, then university in the 1980s, and throughout my life since. They have been on my side the whole time, and I cannot thank them enough. Sadly my father passed away late in December 2022, and he is fondly remembered. This work is dedicated to my Mum and Dad.

Chapter 1

Introduction

1.1 Overview

This thesis examines the content and distribution of cool interstellar medium (ISM, dust and molecular gas at ~20 - 30K), to investigate how these properties can reveal the mechanisms responsible for causing Late-Type Galaxies (LTGs) to evolve into Early-Type Galaxies (ETGs). Cool dust (e.g. 20 - 30K) emits thermal radiation as a continuum at sub-millimetre wavelengths (e.g. Hildebrand 1983), which allows the dust mass, properties and (with suitable angular resolution) its distribution in a galaxy to be studied. Cool molecular gas contains molecules such as carbon monoxide and other radicals or molecules which, unlike molecular hydrogen at this temperature, produce line emission at sub-millimetre or millimetre wavelengths that can be observed (Wilson et al. 2009). This emission allows molecular gas distribution and masses to be studied.

In general, galaxies appear to evolve over time from star-forming LTGs, with spiral morphologies for more massive examples, into more quiescent ETGs with less star formation and smooth morphology (e.g. Martin et al. 2007; Salim et al. 2007; Schiminovich et al. 2007). The generic name for the processes that cause this evolution and reduction

in star formation is quenching (Peng et al. 2010). The reverse of this process, rejuvenation, can also occur by adding fresh ISM to a quiescent ETG (e.g. Thomas et al. 2010; Mancini et al. 2019). Early work examining the evolution of visually classified ETGs, some within a cluster environment, concluded that they contained little or no ISM (e.g. Gallagher 1972; Bregman et al. 1992), and the term "red and dead" became synonymous with ETGs. However, the presence of ISM in some ETGs is now established, in particular in the form of cool molecular gas (e.g. Wiklind et al. 1995; Young et al. 2011; Davis et al. 2011) and ionised gas (e.g. Macchetto et al. 1996; Sarzi et al. 2007; Bryant et al. 2019; Deeley et al. 2020) relevant to this work. The content and distribution of this ISM within ETGs can indicate the mechanisms causing their evolution from LTGs as explained in Section 1.2.3. More recent work on this topic was based on ETG samples which specifically target features such as dust lanes (Davis et al. 2015), or drawn from nearby ETGs only (Davis et al. 2011; Young et al. 2011; Smith et al. 2012). In this work, ETGs and other galaxies for study are drawn from larger, volume-limited, clean and complete samples out to a redshift of 0.06 (see Section 4.1). Galaxies selected from clean and complete samples are unbiased rather than based on features of interest, so results based on them can be analysed statistically and should apply to the wider galaxy population.

The research presented in this thesis includes the analysis of high-resolution (~0.7 arcsec FWHM) images (from interferometry) of cool ISM in five local Dusty ETGs (Sansom et al. 2019), alongside results from existing optical Integral Field Unit (IFU) observations of stellar and ionised gas kinematics. The work presented in Chapter 3 on this topic has been published in a peer-reviewed journal (Glass et al. 2022). Using data from the Galaxy and Mass Assembly (GAMA) survey (Driver et al. 2009), a parent galaxy sample was constructed, to allow optically-selected ETGs for observational studies to be selected in an unbiased way and to examine how galaxy properties change from LTG to ETG. Cool dust masses were estimated for galaxies within the clean and complete sample using observations from the Herschel-ATLAS survey (H-ATLAS, Eales et al. 2010; Valiante et al. 2016), and dust properties explored in relation to other galaxy properties with changes from LTG to ETG. The results of new observations of cool molecular gas

content and kinematics (via carbon monoxide (CO) emission) obtained with the IRAM 30m telescope are also presented, along with an analysis of the behaviour of molecular gas content with changing galaxy properties for these ETGs.

1.2 Background

In this section, relevant aspects of galaxy morphology and interstellar medium (ISM), and their relationship to galaxy evolution, are outlined to provide context for the research described within this thesis. Much of the text in Sections 1.2.2 and 1.2.3 has been adapted from Glass et al. (2022).

1.2.1 Galaxies and Interstellar Medium

A galaxy can be defined as a gravitationally-bound stellar system which has sufficient gravitational mass to retain ISM within its structure (Cimatti et al. 2019). A range of different components form ISM, which can be gaseous or solid. Particulate dust, made from sub-μm diameter grains and built from elements such as carbon, silicon and iron (Whittet 2003), could be present with a mass of ~0.1 - 1% of stellar mass in a star-forming galaxy (e.g. Smith et al. 2012). Cool (~20 - 30K) molecular gas, which is mostly molecular hydrogen (H_2) and atomic helium at an approximately primordial mass ratio, could be present at ~10% of the stellar mass in star-forming galaxies (e.g. Saintonge et al. 2017). Hydrogen (with helium and metals) also exists at higher temperatures which progress from atomic (e.g. >100 - 8000K) to ionised (e.g. 8000 - 10^6K) gas as temperature increases (Sparke & Gallagher 2007).

The ISM phases can co-exist in a galaxy due to pressure equilibrium and are inter-related, with dust acting as a solid catalyst for the conversion of cooled atomic gas to molecular forms e.g. $2H \rightarrow H_2$, as reviewed by Herbst et al. (2005). Given that molecular

hydrogen is the main ingredient for the formation of new stars in a galaxy, this process allows an influx of atomic gas from outside a galaxy, from cosmic filaments via the galaxy halo, to sustain star formation over Gyr timescales (e.g. Feldmann 2020). However, quenching mechanisms can disrupt ongoing star formation. Smethurst et al. (2017) separate quenching mechanisms into secular (internal) and environmental (external), although the classification of mechanisms as such is not always clear as shown below. Man & Belli (2018) also provide a review of quenching mechanisms, based on the different stages of gas accretion followed by new star formation and how these can be disrupted.

Mass quenching covers any mechanism that is a function of galaxy mass, and is independent of galaxy environment (Peng et al. 2010). Smethurst et al. (2017) define it as any process which slows the supply and consumption of gas in a galaxy as it increases its mass. One mechanism which may cause this is known as "halo quenching", where at higher galaxy halo masses ($>10^{12}$ $M_{\odot}$) the supply of external gas is disrupted or the gas is prevented from cooling (Gabor & Davé 2015), referred to as cosmological starvation (Feldmann & Mayer 2015). Peng et al. (2015) discuss strangulation as a mechanism in similar terms, with their research indicating that it can occur in galaxies with stellar mass $< 10^{11}$ $M_{\odot}$ and over timescales of ~4 Gyr. Another is stellar feedback e.g. from supernovae (Darvish et al. 2016). Mass quenching is thought to be common amongst galaxies in less dense environments (Kormendy & Kennicutt 2004), and it has also been attributed to the evolution of galaxies falling into more dense galaxy groups or clusters (Peng et al. 2012). It appears to be more relevant at high redshift (e.g. $z > 1$) than in the local Universe, with environmental mechanisms being more important locally (e.g. Darvish et al. 2016).

Morphological quenching arises through galaxy morphology changes, and either stabilises molecular gas against star formation or accelerates star formation leading to rapid consumption of molecular gas. Galactic bulge growth stabilises molecular gas within it against star formation, by increasing molecular gas turbulence (Martig et al. 2009). This mechanism can operate at galaxy halo masses below 10^{12} $M_{\odot}$, and can be either secular, or

environmentally driven by minor mergers or misaligned gas infall. The action of a galactic bar can drive molecular gas towards the centre of a galaxy, accelerating star formation and gas consumption (Athanassoula 1992a). Formation of bars can be internally-driven but also can be driven tidally by galaxy interactions or my merger activity (Cavanagh & Bekki 2020). In both cases, these mechanisms could therefore be either secular or environmental.

Feedback from AGN has the potential to either render molecular gas incapable of forming stars, e.g. by increasing its turbulence, or remove it from a galaxy into its halo, and is needed in simulations to prevent galaxies from growing to unfeasible stellar masses (Smethurst et al. 2017, and references therein). This feedback could be positive, increasing star formation, or negative, and is supported by the increased fraction of galaxies containing AGN with properties between those of star-forming LTGs and passive ETGs (the "Green Valley", see Section 1.2.2) where galaxies appear to be transitioning to passive status (Smethurst et al. 2017, and references therein). AGN could be triggered as a result of external activity, such as mergers or tidal interactions, or as a result of secular bar growth, both driving gas to the galaxy centre (see above).

Mergers of all scales have the capability of quenching galaxies where they can occur. Major mergers can lead to giant passive ellipticals when the merging galaxies are of similar mass (Xilouris et al. 2004). Mergers with increasingly different galaxy masses will tend to leave disc structure intact within the more massive galaxy, but can destroy spiral structure, create kinematic misalignments and fuel AGN (Davis et al. 2011; Glass et al. 2022). They can occur in less dense environments, with likelihood increasing with density to levels at the outskirts of clusters, until cluster densities are reached and relative galaxy velocities become too great for collisions to be likely (Smethurst et al. 2017, and references therein).

Non-merger events such as fly-bys can also lead to quenching, by tidal interaction known as harassment which can induce asymmetry (e.g. Glass et al. 2022) and tidal features (Hood et al. 2018) in optical images, re-arrange gas into bars and rings (Glass

et al. 2022, and references therein), or pull the gas from a galaxy (e.g. Bialas et al. 2015). As with mergers, they can occur in environments of any density, including voids (Domínguez-Gómez et al. 2022, see also Chapter 7) and dense regions in clusters (e.g. Zabel et al. 2019).

1.2.2 Galaxy Morphology and Evolution in the Local Universe

Galaxies in the local Universe (redshift $z \leq 0.06$ in this work) have been shown in many studies to exhibit bimodality in properties within certain parameter planes. However, as discussed later in this Section, limits on certain galaxy properties can impose bimodality onto continuum behaviour. The earliest example of bimodality found for galaxy properties in the local Universe is the classification of elliptical and lenticular ETGs with smooth morphologies, and LTGs with spiral arms or irregular features (Hubble 1926), examples of which are shown in Figure 1.1.

Bimodality is also apparent in optical colour versus absolute magnitude diagrams (CMDs), with LTGs forming a "blue cloud" and ETGs forming a "red sequence" (Baldry et al. 2004; Bell et al. 2004; Faber et al. 2007; Martin et al. 2007). Plots of derived star formation rate (SFR) versus stellar mass show star-forming galaxies lying along or near to a star-forming main sequence (SFMS), starburst galaxies lying above the SFMS and other galaxies with reduced star formation rates lying below (e.g. Daddi et al. 2007; Elbaz et al. 2007; Noeske et al. 2007; Saintonge et al. 2017). An example is shown in Figure 1.2, with further examples in Chapter 5.

Galaxies also exist in the relatively sparse "Green Valley" (GV) (Wyder et al. 2007) between blue/red and star-forming/passive regions (apparent in Figure 1.2), with intermediate properties between ETGs and LTGs. However, some doubt has been cast recently on the existence and nature of the GV, with galaxies in the local Universe exhibiting a continuum of properties (Eales et al. 2017, 2018, see Figure 1.3). The GV may be due partly to the effects of colours bunching together in optical surveys, by reaching limits on

M81 (Spiral) M49 (Elliptical) M102 (Lenticular)

20×20 arcmin 12×12 arcmin 8×8 arcmin

Figure 1.1: SDSS DR9 gri images of spiral, elliptical and lenticular galaxies in the local Universe (http://www.sdss3.org/dr9/).

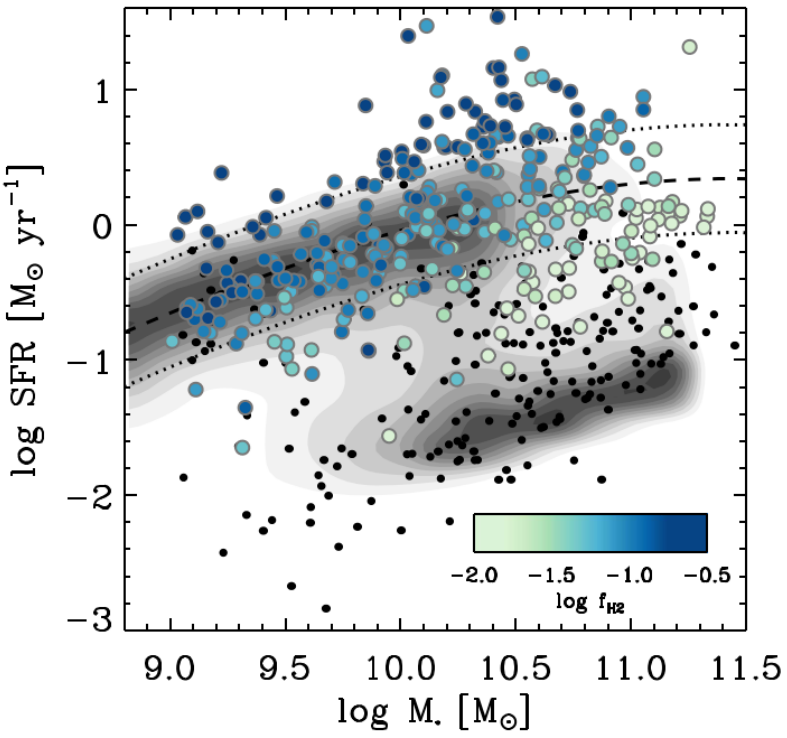

Figure 1.2: Star formation rate (SFR) versus stellar mass for the xCOLD GASS galaxy sample, colour-coded according to molecular gas mass fraction f_{H2} (Saintonge et al. 2017, their Figure 8). Black dots are xCOLD GASS observed galaxies with no detectable CO emission for conversion to molecular gas mass. Grayscale shading is the general galaxy distribution from the Sloan Digital Sky Survey (SDSS, Section 2.8.7). Dotted lines indicate the Star Formation Main Sequence (SFMS) and a ±0.4 dex spread.

red and blue colours in galaxies. Conversely, galaxies featuring in sub-mm surveys by the Herschel Space Observatory (Section 2.4) show a "green mountain" in similar plots due to Malmquist bias, because galaxies in the GV have increased ratios of sub-millimetre to optical luminosity and are more readily detected. The exclusion of GV galaxies with Active Galactic Nuclei (AGN) from galaxy samples may also deepen the apparent GV, by excluding galaxies where AGN happen to be active as part of their duty cycles (Hickox et al. 2014). AGN in GV galaxies are likely to be fuelled by gas driven inwards by the same processes that cause galaxies to transition into the GV (Lanz et al. 2022).

Overall, there is a strong possibility that limits and biases in current galaxy property measurements tend to mask underlying continuum behaviour galaxy properties in the local Universe. In spite of the uncertain significance of the GV, it is acknowledged that galaxies within this parameter space are evolving, and many are in transition between LTG and ETG, with passive ETGs as the endpoints of evolution (e.g. Martin et al. 2007; Salim et al. 2007; Schiminovich et al. 2007; Martin et al. 2018). The quenching mechanisms responsible for this transition, discussed in Section 1.2.1, can have shorter or longer timescales. Some lead to relatively rapid change (e.g. minor mergers) with timescales of $\sim$1 Gyr, while some lead to slower (secular) change with timescales of several Gyr (e.g. Smethurst et al. 2017, 2018; Phillipps et al. 2019). The low density of galaxies in the GV in plots such as Figure 1.2 has been attributed to a possible short timescale of evolution ($<$1 Gyr) from LTG to ETG (e.g. Salim 2014). Given that longer evolutionary timescales are possible, the GV then requires an alternative explanation as discussed above.

However, the question of which mechanisms are dominant in forming the ETG population in the local Universe remains open, with various studies indicating different mechanisms as more significant. Depending on the galaxy samples and methods used, studies indicate dominance by merger activity leading to relatively rapid evolution (Baldry et al. 2004; Kaviraj et al. 2012) or slower processes such as starvation (Peng et al. 2015; Eales et al. 2017; Phillipps et al. 2019, Section 1.2.1). A mixture of fast-acting mergers and

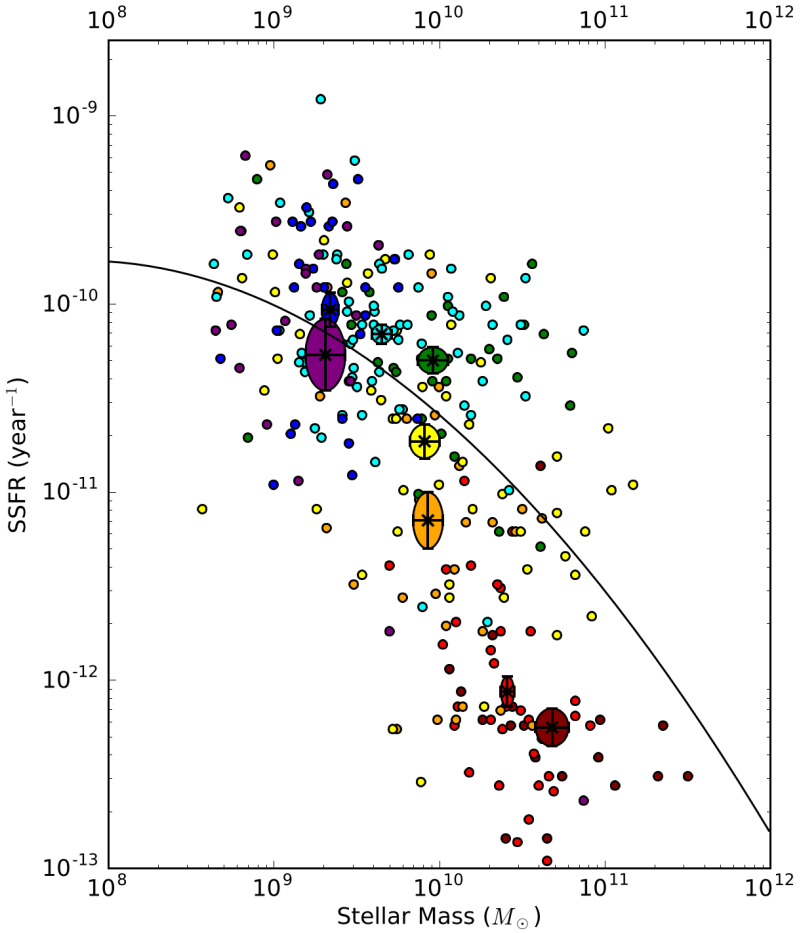

Figure 1.3: Specific star formation rate (sSFR) versus stellar mass for galaxies in the Herschel Reference Survey (Eales et al. 2017, their Figure 2, see also references therein.). Colours represent visual morphological classifications - Ellipticals/Lenticulars (maroon), Lenticulars (red), Spirals (orange, yellow, green, cyan), Irregulars/Dwarf (purple). Ellipses coloured by galaxy morphology represent 1σ uncertainties. The solid line is a second-order polynomial fitted to the data.

slower internal mechanisms could be in operation in parallel, with mergers more significant in less dense environments (Schawinski et al. 2014; Smethurst et al. 2017; Deeley et al. 2020). Rejuvenation is also possible, with an injection of fresh ISM into an ETG triggering new star formation and re-entry into the GV for a time (e.g. Thomas et al. 2010; Mancini et al. 2019). Different mechanisms can also occur in different regions within the same galaxy. M33 has star formation levels consistent with starbursts around its central region, the SFMS in its main disc and GV in its outer disc, implying that different regions within a galaxy can evolve according to different spatial and temporal scales (Thirlwall et al. 2020).

The likelihood and type of evolutionary mechanism also drives a relationship between the fractional presence of morphology types and the number density of galaxies in a region, with smooth ETGs more likely to be present in dense cluster environments (Dressler 1980). Mechanisms such as ram pressure stripping and harassment in dense galaxy clusters are capable of removing ISM from cluster galaxies, rendering them quiescent (Zabel et al. 2019, and references therein). On the other hand, minor mergers and interactions tend to be more significant in less dense environments such as field (e.g. Davis et al. 2011; Kaviraj et al. 2012; Davis et al. 2015; Glass et al. 2022). The proportions of different quenching mechanisms at work in different environments remain unclear.

1.2.3 Galaxy Evolution and Interstellar Medium

ETGs were once thought to have little or no cool ISM (e.g. Gallagher 1972; Bregman et al. 1992). However, it is now known that some visually-classified ETGs across all environments have significant ISM content, with levels similar to those for LTGs in some cases (e.g. Young et al. 2011; Smith et al. 2012; Agius et al. 2013; Davis & Young 2019). Agius et al. (2015) examined dust masses and star formation in galaxy samples in the dense Virgo cluster environment and in the less dense GAMA survey regions, and concluded that galaxies in less dense environments have proportionally more ISM mass and

star formation than those in the Virgo cluster. Zabel et al. (2019) found that half of the observed galaxies in the Fornax cluster had detectable levels of molecular gas, but the molecular gas was disturbed in about half of the galaxies where detections were achieved. As described in Section 1.2.1, the evolution of galaxies in dense cluster environments is different to that of galaxies in less dense environments, where ISM is influenced by different mechanisms. This work concentrates on less dense environments within the GAMA regions, where relative velocities of galaxies are generally reduced and changes to content and distribution of ISM have been used previously to indicate evolutionary mechanisms at work (e.g. Davis et al. 2011, 2015).

The content and distribution of ISM in ETGs can be used as evidence of evolutionary mechanisms responsible for their ongoing evolution. e.g. to identify ETGs which have undergone merger activity during their evolution. This could be major mergers of galaxies with similar mass, which are highly disruptive and can form giant elliptical galaxies (e.g. Xilouris et al. 2004), or recent minor mergers involving a substantially smaller ISM-rich galaxy which can leave disc structure intact (e.g. Davis et al. 2011; Kaviraj et al. 2012). A lack of trend in dust mass with stellar mass in local ETGs (Figure 1.4) within the ATLAS-3D survey (Cappellari et al. 2011) indicates external addition of dust, rather than addition via internal processes, which would form a trend (Smith et al. 2012). Kinematic misalignment between cool molecular gas (traced by carbon monoxide (CO) line emission) and stellar mass within galaxies can be evidence of merger activity (Davis et al. 2011), although further analysis is needed to identify misalignment associated with other effects such as relatively slow accumulation of gas within a disc over long periods following a merger (van de Voort et al. 2015).

Conversely, trends in ISM content with other properties, symmetrical distribution or good kinematic alignment between ISM and stellar mass can be evidence for evolution either via slower internal (secular) processes which do not disturb alignments significantly, or via merger activity further back in time after which ISM has settled into alignment. A rapid addition of fresh ISM to a galaxy, which could be tilted, counter-rotating or even

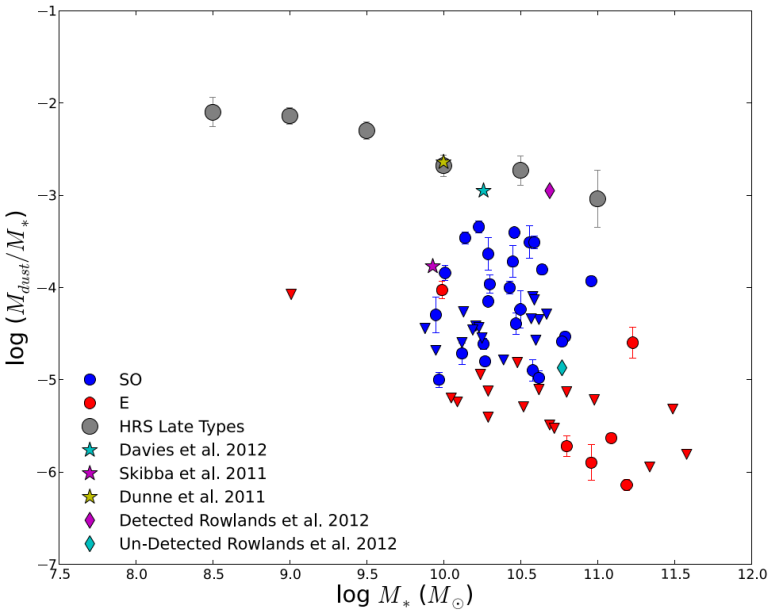

Figure 1.4: Dust mass versus stellar mass for galaxies in the Herschel Reference Survey, from Smith et al. (2012), their Figure 8, and references therein.

polar in orientation compared to stellar mass (e.g. Shapiro et al. 2010; Davis et al. 2011; Buta 2017; Martinsson et al. 2018), might settle into alignment with stars within a few dynamical timescales e.g. ~100 Myr for the inner parts of ETGs (Tohline et al. 1982), although asymmetries have been found observationally to persist beyond this timescale (van de Voort et al. 2018).

Also of interest in this work is the mass ratio of molecular gas to dust in galaxies. There are competing mechanisms which can create or deplete both molecular gas and dust, which are linked to the evolution of galaxies. Dust is created by core-collapse supernovae or by stellar winds from Asymptotic Giant Branch (AGB) stars, and can increase in mass and grain size by accretion of metals from the gas phase. Dust is also destroyed by shocks from supernovae, sputtering by cosmic rays and destruction by high-energy photons if the dust environment is poorly shielded (Clark et al. 2023, and references therein). Alongside other diagnostics, the gas-to-dust mass ratio (GDR) can be used to infer evolutionary mechanisms at work. For example, a high GDR indicates significant

accretion of low-metallicity molecular gas from external sources, or significant dust destruction. Conversely, low GDR indicates high rates of consumption or loss of molecular gas, or significant accretion of dust from external sources. Clark et al. (2023) also describe the current view of the relationship between GDR and gas-phase metallicity, with grain growth causing metals to be transferred from gas to dust. Changes in trends of GDR with metallicity can be used to identify when grain growth is occurring or is absent.

1.3 Research Topics

The overall theme of this thesis is the study of the cool ISM in ETGs, and what it can reveal about the evolutionary mechanisms that form ETGs from LTGs. Based on the discussion presented above, four relevant research topics emerge that are addressed within this thesis.

1. The use of resolved observations of the ISM distribution to explore the evolutionary history of ETGs, in particular evidence of interactions or mergers causing asymmetry in distribution.

2. Development of a large, clean and complete sample of galaxies within a defined volume for study, classified according to visual morphology from optical images. A clean sample should contain only galaxies that meet selection criteria, and contaminant galaxies are removed as far as practicable. A complete (volume-limited) sample contains all galaxies meeting selection criteria within a given volume of space. With minimal selection criteria based on e.g. absolute luminosity (as a proxy for stellar mass) and resolvable size to avoid the selection of stars, the clean and complete sample should be free of anecdotal selections e.g. based on colour, star formation or morphology. Statistical analysis of trends from the sample should be applicable to the wider galaxy population.

3. Exploration of a range of galaxy properties using the clean and complete sample,

to investigate whether continuum behaviour exists, whether property limits impose bimodality and how visual morphology affects galaxy properties.

4. Evaluation of dust masses and properties for Herschel-detected galaxies within the Herschel-ATLAS survey (Section 2.4), exploration of how they vary with stellar mass, morphology and other galaxy properties, and comparison of their properties with those from similar surveys.

5. Estimation of molecular gas mass for Dusty ETGs from new observations with the IRAM 30m telescope (Section 2.3). Comparison of molecular gas masses with other galaxy properties, and results from other surveys of molecular gas mass, to investigate any evolutionary differences between the observed galaxies and others.

1.4 Structure of Thesis

To address the research topics described above, the thesis is divided into a further eight Chapters, as described below.

Chapter 2 provides background on the telescopes used for all aspects of this work, with more detail provided for those telescopes whose observations are studied in detail. The principal methods for data analysis are also discussed, along with the sources of data from observational surveys.

Chapter 3 describes the analysis of observations of five Dusty ETGs using the Atacama Large Millimetre/submillimetre Array (ALMA) in 2016 (Sansom et al. 2019). Three of the selected ETGs were unexpectedly found to contain massive ($>10^9$ $M_\odot$) molecular gas reservoirs with significant spatial extent (~few kpc). The reservoir structures are fitted with kinematic models to reveal any irregularities, and compared with stellar and ionised gas kinematics from optical Integral Field Unit (IFU) observations. Detections for the remaining two ETGs are also analysed to investigate their origins and properties.

In Chapter 4, a new, clean and complete sample of galaxies is created from catalogue data, with visual morphological classifications assigned where appropriate. The purpose of the sample and sub-samples is twofold. They can be used to investigate how galaxy properties change with visual morphology, to investigate whether the early bimodal view of galaxy evolution remains true or whether there is a continuum of properties from LTG to ETG, as discussed by Eales et al. (2018). They can also be used to create unbiased samples of galaxies within ranges of properties of interest for observational studies. An analysis of whether continuum behaviour for galaxy properties exists within the clean and complete sample for a range of galaxy properties and morphologies is presented in Chapter 5.

The galaxy samples created in Chapter 4 are also used to examine the properties and content of cool interstellar dust in galaxies, as described in Chapter 6. Dust masses are available for many of the sample galaxies from GAMA (Section 2.8.1), from fitting of model spectra to photometry from far UV to sub-mm using MAGPHYS (Section 2.7.3). These are compared where possible using fitting of a dust emission model to H-ATLAS observations (Eales et al. 2010; Valiante et al. 2016) of sub-mm emission from galaxies, which also yields estimates of mean dust temperature and emission properties. The behaviour of dust masses and properties is then examined in relation to other galaxy properties, including visual morphology, to investigate trends which may indicate evolutionary mechanisms at work and the possible origins of the dust.

Chapter 7 describes the planning, implementation and analysis of new observations of cool molecular gas in 32 of the dustiest ETGs from the Parent Sample using the IRAM 30m Telescope. The aim was to obtain cool molecular gas masses for these galaxies, to explore how molecular gas mass and GDR behave with changes in other galaxy properties, again to explore evolutionary mechanisms taking place. The results are also compared with those from other surveys which examined mostly LTGs, to explore any similarities or differences between Dusty ETGs and LTGs. They are also compared with observations from other galaxy samples chosen on the basis of specific evolutionary pathways. Chapter

8 provides an overall discussion and conclusions for the work.

Throughout this thesis, flat ΛCDM cosmology is assumed with $\Omega_m = 0.7$, $\Omega_\lambda = 0.3$ and $H_0 = 70$ km s^{-1} kpc^{-1}.

Chapter 2

Telescopes, Instruments, Methods and Data Sources

This thesis uses results of observations from a diverse range of telescopes and instruments, from far ultraviolet to radio frequencies. New observations were made for this work, and many catalogues of previous observational results and derived products are used. This Chapter describes the telescopes and instruments, key data processing methods and data sources relevant to this thesis.

2.1 Principles of Radio Interferometry

In Chapter 3, high-resolution (e.g. <1 arcsec FWHM) observations of mm-wavelength emission from dust and molecular gas within dusty local ETGs (Sansom et al. 2019) are analysed. These observations were obtained using interferometry, via the Atacama Large Millimetre/submillimetre Array (ALMA) (Section 2.2). In this Section, the principles of interferometry are outlined. The description below is based on Condon & Ransom (2015) and Cortes et al. (2023).

CHAPTER 2

Interferometry at mm and radio wavelengths makes use of the electromagnetic wave (sinusoidal) emission at a given frequency from a target, received by pairs of antennae known as elements separated by a distance vectors known as baselines. For an array of N antennae, there are N(N - 1) / 2 baselines. The time delay in arrival between the emission at two antennae forming an element affects the relative phases of the emission at each antenna. The two electronic signals from each antenna are multiplied in a specialist computer known as a correlator, generating amplitude and phase information for the resultant interference patterns in the form of complex numbers referred to as visibilities. The visibilities for each element are assigned to coordinates in the (u,v) plane, which is a coordinate system in units of wavelength reflecting the North and East components of the distances between antennae of each element as observed by the target. The baseline pair coordinates in the (u,v) plane change as the Earth rotates during a course of an observation. The van Cittert-Zernicke theorem (van Cittert 1934; Zernike 1938) allows the visibilities in the (u,v) plane to be converted to source intensities on the sky, by exploiting the fact that the visibilities in the (u,v) plane are a 2-dimensional Fourier transform of the on-sky image. However, the information within the (u,v) plane from an interferometer is incomplete because of the finite number of baselines available. It is therefore necessary to employ image cleaning techniques to extract scientific data from "dirty" synthesised images which contain unwanted artefacts arising from the incomplete (u,v) plane coverage. A more detailed explanation of these principles is provided below.

Figure 2.1 shows a 1-dimensional interferometer consisting of two antennae, 1 and 2, with dishes to maximise the received emission. The antennae are separated by a distance vector $\vec{b}$, and receive plane waves from a distant, extended source with a central on-sky direction represented by a unit vector $\hat{s}$. The time delay in arrival of signals along $\hat{s}$ at antenna 1 compared to antenna 2, known as the geometric delay τ_g, is the distance travelled L divided by the local speed of light c, i.e. $\vec{b} \cdot \hat{s}/c$. If τ_g between the antennae is adjusted out by modifying the time axis of the signal from Antenna 1 from time t to $t - \tau_g$, the phase difference between the signals is zero along the direction $\hat{s}$ which is referred to as the phase centre of the element.

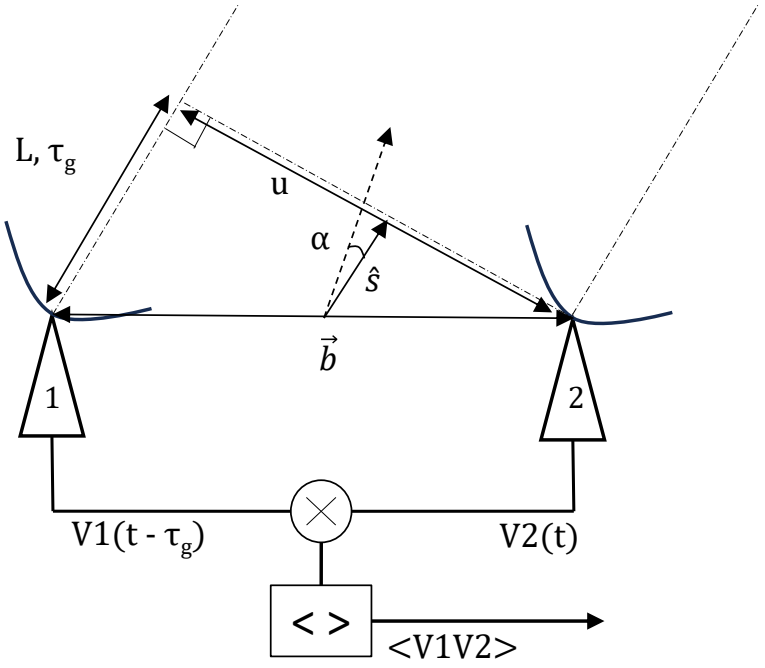

Figure 2.1: Antennae 1 and 2 with baseline vector $\vec{b}$ receiving plane waves from a distant target with unit direction $\hat{s}$ (the phase centre). On-sky emission away from the phase centre is at an angle α from $\hat{s}$. Additional emission travel distance L and arrival time delay along $\hat{s}$, τ_g, are shown. Signal voltages V_1 (phase adjusted for τ_g) and V_2 from the antennae are multiplied in a correlator and time averaged (adapted from from Cortes et al. (2023), their Figure 3.4).

At some small angle α from $\hat{s}$ (Figure 2.1), signal time delays beyond those compensated for are introduced and increase with α. The on-sky position of emission away from the phase centre is given by $l = \sin(\alpha)$. Based on the perpendicular separation distance of the signals u (Figure 2.1) as a multiple of observed wavelength, the increased path length travelled by the offset emission due to shift from the phase centre is $u.\sin(\alpha)$, or ul. The voltage at Antenna 2 compared to Antenna 1 is phase-shifted because of the additional time delay introduced by the angle α, and can be expressed in terms of the phase angle introduced as follows (see also Cortes et al. (2023), their Equation 3.12):

$$V_2 = V_1 \left(\cos\left(ul\right) - i.\sin\left(ul\right)\right) = V_1 \exp\left(-2\pi i \left(ul\right)\right) \tag{2.1}$$

Note that at the phase centre, the phase angle is zero and the signals are said to be auto-correlated. Away from the phase centre, signals have a finite phase angle and are cross-correlated. The principle can be extended to two dimensions, using an orthogonal distance v perpendicular to u, also as a multiple of observed wavelength, and an on-sky position m orthogonal to l, giving:

$$V_2 = V_1 \exp\left(-2\pi i \left(ul + vm\right)\right) \tag{2.2}$$

The u and v distances, in units of observed wavelength, are effectively a view from the target of the baseline lengths during the course of the observation, and by convention are aligned North - South and East-West. These distances form coordinates in the (u,v) plane. The voltages V_1 and V_2 are fed to the correlator, which returns the following time-averaged product:

$$\langle V_1 V_2 \rangle = \int \int_{\alpha} \left\langle V_1 \left(l, m\right)^2 \right\rangle \exp\left(-2\pi i \left(ul + vm\right)\right) dldm \tag{2.3}$$

With appropriate calibration, the time-averaged voltage squared can be converted to emission intensity I_ν (flux per unit frequency and on-sky solid angle at observed frequency

v). Equation 2.3 then gives the complex visibility for the element, $\mathcal{V}_\nu$ (see also Cortes et al. (2023), their Equation 3.18):

$$\mathcal{V}_\nu(u,v) = \int\int_\alpha I_\nu(l,m)\exp\left(-2\pi i\left(ul+vm\right)\right)dldm \tag{2.4}$$

Equation 2.4 shows that the visibilities within the (u,v) plane form a 2-dimensional Fourier transform of the on-sky image. Therefore, an on-sky image of the target at the observed wavelength could be recovered, by performing an inverse Fourier transform of of the visibilities within the (u,v) plane according to the van Cittert-Zernicke theorem:

$$I_\nu(l,m) = \int\int_\alpha \mathcal{V}_\nu(u,v)\exp\left(2\pi i\left(ul+vm\right)\right)dudv \tag{2.5}$$

If the (u,v) plane were completely populated by visibilities, a full image could be reconstructed by inverse Fourier transform shown in Equation 2.5. However, the finite number of baselines for a typical interferometer means that there are gaps in the (u,v) plane. The resultant "dirty" image, constructed from an inverse Fourier transform of the available visibilities within the (u,v) plane, will have artefacts arising from these gaps (referred to as sidelobes) as well as the required science information. It is possible to recover useful science information from a dirty image using cleaning techniques, an early example of which was created by Högbom (1974). A "dirty beam" is constructed by replacing the visibilities at their (u,v) coordinates with delta functions and performing the inverse Fourier transform shown as Equation 2.5. The highest flux density is then identified in the dirty image, and is recorded at the relevant sky coordinates in an empty array of the same size as the dirty image. The product of flux density and dirty beam is subtracted from the dirty image at the relevant coordinates. The next highest flux density is then identified, transferred and subtracted, and the process is repeated until a defined endpoint is reached. The cleaning process is made more effective if the emission removed from the dirty image by cleaning is constrained to regions where emission is known to exist, which can be user-defined in advance. The clean image, containing all the emission

transferred from the dirty image, is then convolved with the "clean beam" which is a 2-dimensional Gaussian profile fitted to the central portion of the dirty beam (Condon & Ransom 2015). Finally, the residual noise in the dirty image after removal of flux is added to clean image.

Further refinements are possible to improve the cleaned image, depending on the requirements of the observation. It is possible to multiply visibilities by weightings, to emphasise shorter or longer baselines. A natural weighting scheme weights according to baseline signal RMS noise, and therefore favours shorter baselines with less noise. The resultant clean image therefore improves surface brightness sensitivity at the expense of resolution. Conversely, uniform weighting adjusts visibilities according to the inverse of number density at points within the (u,v) plane. The greater emphasis on longer baselines then results in better spatial resolution, but reduced surface brightness sensitivity. A hybrid (Briggs) weighting scheme can also be used which combines both these methods as a compromise. A further option is uv tapering which down-weights visibilities according to a radial position from the (u,v) plane centre, reducing he contribution from the longest baselines and increasing surface brightness sensitivity at the expense of resolution. Primary beam correction can also be applied to the clean image by dividing it by a 2-dimensional inverse representation of the beam for a single dish (e.g. an Airy disc). This ensures that emission further away from the phase centre is correctly scaled.

The achievable resolution from a multi-antenna interferometric telescope is set by the longest baseline used, and is approximately λ/b_{max}. There is also a limit on the maximum on-sky angular scale of emission, governed by the ability for phase differences in emission across its distribution to be identified. The maximum recoverable scale (MRS) for an interferometric telescope is governed by the shortest baseline distance used b_{min}, and can be estimated from Cortes et al. (2023), their Equation 3.28:

$$MRS \simeq 0.6\lambda/b_{min} \tag{2.6}$$

More compact antenna arrays are therefore more suited to larger-scale emission and lower resolutions, while more dispersed arrays favour smaller scales of emission at higher resolution. MRS is typically limited by the minimum spacing of dishes, set to avoid mechanical clashing and excessive shielding of one dish by another at greater angles from zenith.

The above analysis considers extended emission but at a relatively small angular displacement from the phase centre which can be managed with a single pointing. To observe extended emission across larger on-sky regions, it is necessary to make several observations and mosaic them together. The observations presented in Chapter 3 (Sansom et al. 2019) were performed with a single pointing.

2.2 Atacama Large Millimetre/submillimetre Array (ALMA)

The ALMA telescope was used for high-resolution observations of ^{12}CO[2-1] line emission from dusty ETGs (Sansom et al. 2019), explored further in Chapter 3. The technology used by ALMA to obtain interferometric observations using the principles discussed in Section 2.1 is discussed below (Cortes et al. 2023).

ALMA is located at high altitude (5000m) on the Chajnantor Plateau, Atacama Desert, Chile (23° 01′ 09″ S, 67° 45′ 12″ W), where the ambient air is normally exceptionally dry and atmospheric opacity at mm wavelengths is therefore minimised. Currently it makes use of up to 66 antennae with primary parabolic dishes and secondary reflectors to Cassegrain foci (Figure 2.2). The 12 m array uses up to 50 antennae with 12 m diameter primary dishes, and was used for the observations discussed in Chapter 3. Baselines are adjustable by moving the antennae using specialist vehicles to locations prepared with level foundations, and range from 15m to 16km. Also available is the 7 m array, or Atacama Compact Array (ACA), based on 12 antennae with 7m dishes and with baselines

Figure 2.2: ALMA antennae forming the 12 m, 7 m and TP arrays. The four antennae forming the TP array are ringed in blue. The 7m array is ringed in orange, and the 12m array is to the left. A telescopic boom lift (red) is visible by a 12 m antenna to the right, for scale (Cortes et al. 2023).

ranging from 9 - 30 m. Four further antennae with 12 m diameter dishes are associated with the 7 m array, forming the Total Power (TP) array for single-antenna observations of targets to observe total emission.

During an annual observation cycle, antennae forming the 12 m array are arranged initially with the most compact baselines, for observations of larger-scale emission (largest MRS) with lower resolution. As the cycle proceeds, the antennae are relocated outwards to form further planned arrays, with decreasing MRS and increasing resolution. The observations discussed in Chapter 3 were made with the 12 m array, but each with slightly different arrays using ~40 of the 12 m antennae with baselines from ~15m to to ~640m (Sansom et al. 2019). MRS values for the observations were therefore 10 - 11 arcsec at 230 GHz (1.3mm) for ^{12}CO[2-1] line emission (Equation 2.6), and angular resolution was ~0.65 arcsec FWHM (Sansom et al. 2019). ALMA is capable of observing within specified frequency bands numbered 1 - 10 increasing in frequency, to make use of frequencies where atmospheric opacity is minimised. The observations

discussed in Chapter 3 used Band 6, which spans from 211 - 275 GHz (1.1 - 1.4 mm). The discussion below provides information on hardware related to Band 6 observations in particular.

Each antenna has a frontend assembly at the Cassegrain focus, to receive incoming photons and produce a corresponding electrical signal, and a backend system to produce digital signals for transmission to the correlator via fibre-optic cables. Also included at this location is a Water Vapour Radiometer (WVR), which tracks atmospheric precipitable water vapour (PWV) content along the antenna line-of sight, and an amplitude calibration device which imposes ambient temperature and hot (80°C) loads on the receiver inputs for calibration. The frontend assembly contains receivers for each of the observed frequency bands, operating at a temperature of 4K to minimise thermal noise. For Band 6 observations, non-linear SIS (semiconductor/insulator/semiconductor) mixers (Figure 2.3) are used to combine the incoming signal with that from precisely-tuned local oscillators (LOs). The non-linear mixing produces sidebands (heterodynes), which are signals containing the spectral information from the incoming signal but are shifted in frequency to defined values either side of the LO frequency (Wilson et al. 2009). This principle is used to align the incoming signal frequency with the required backend input, irrespective of the incoming frequency, and allows a single backend to cover a wide range of incoming frequencies. The backend provides four digitised basebands with defined frequency ranges with frequency widths of up to 2 GHz, covering the upper and lower sidebands (LSB, USB) and two orthogonal polarisations per sideband for the correlator. Each baseband can then be sub-divided into up to four spectral windows (spws) with widths of up to 1.875 GHz. As an example, the observations discussed in Chapter 3 (Sansom et al. 2019) generated four spws of 1.875 GHz each. Three spws had 128 frequency channels of 31.25 MHz width, with the fourth having 3840 channels but smoothed to a frequency width of 976.6 KHz. The aim was to observe continuum emission in three lower-resolution spws

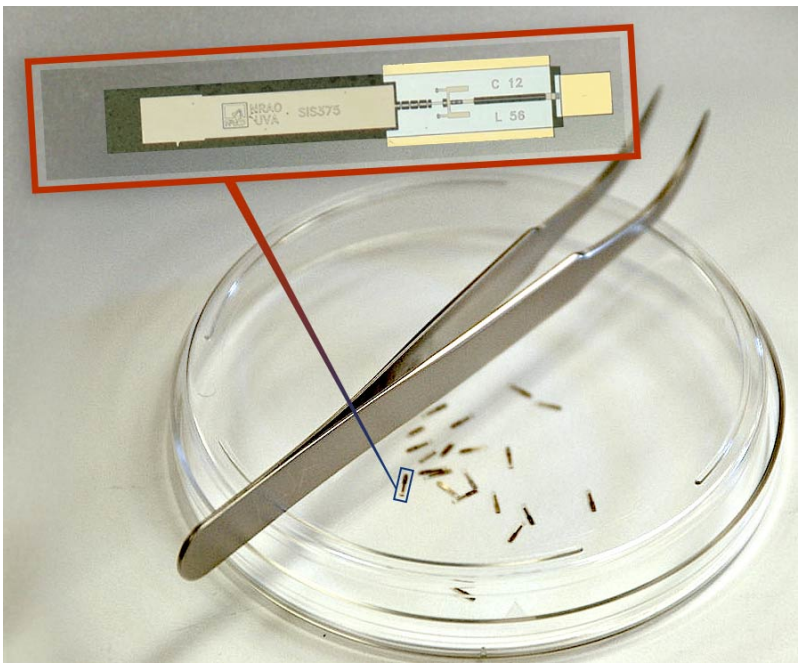

Figure 2.3: Band 6 SIS mixers. Petri dish and tweezers provide scale. (https://public.nrao.edu/gallery/band-6-sis-mixer/, accessed 26/10/23).

and ^{12}CO[2-1] line emission in the fourth.

The digitised signals from the backend of each antenna are sent to the correlator (Escoffier et al. 2007) via fibre-optic cables. The baseline correlator (BLC, Figure 2.4) is used for observations using the 12m array, and is located in a building near to the antennae. It consists of a bank of bespoke computers which carry out the operations discussed in Section 2.1 on all incoming signals, including the tracking of time delays needed to establish the phase centres for each element of antennae. The auto-correlated signals (Section 2.1) are used for for normalising the cross-correlated signals, for pointing and focussing and for estimations of system noise temperatures. The cross-correlated signals are used for interferometry. The output from the correlator is an ALMA Science Data Model (ASDM) which contains all observational information necessary for users to create science products in a standardised format for compatibility with processing software (e.g. CASA[1], the

Figure 2.4: ALMA Baseline Correlator system (Cortes et al. 2023).

Common Astronomy Software Applications package).

Observations with ALMA require initial (and possibly repeated) calibrations against celestial objects with known properties The following types of calibration are relevant to the observations discussed in Chapter 3:

- *Flux calibration*: this provides an observation-specific conversion from signal strength (expressed as temperature, K) to flux density in Janskys (Jy). Objects with well-defined flux densities such as quasars or planets can be used.

- *Phase calibration*: this provides a live measurement of atmospheric effects on signal phase, to allow phase centres to be correctly established. Any suitably bright object with non-polarised emission and close to the observational target can be used.

- *Bandpass calibration*: this allows the bandwidths of the observations to be established correctly. Suitably bright celestial objects with flat spectra in the range of interest are suitable for this, e.g. quasars.

- *Delay calibration*: this allows time-dependent delays in signals from the antennae

[1]https://casa.nrao.edu/

to the correlator to be adjusted, ensuring that the relative phases of the signals from the antennae are correct.

- *Gain calibration*: this ensures that frequency-dependent variations in gain and phase across the measured range of frequencies are correct.

Gain and delay calibrations are also performed using on-sky measurements, to compensate for frequency-dependent gain changes and shifts in element time delays as observations proceed. The calibrator observations are applied by the user in CASA, along with other calibration activities such as manual inspection and flagging of bad data for removal e.g. because of high RMS noise levels, excessive shadowing of a dish, sudden phase changes, and significant changes in atmospheric PWV and opacity. The user typically receives an initial CASA script generated by an ALMA support specialist containing these steps, to produce an initial clean and calibrated dataset for creation of science products. Image production, using either the method by Högbom (1974) (Section 2.1) or more advanced methods, is implemented via functions within CASA, e.g. TCLEAN. An additional initial script from an ALMA support specialist for image production is normally provided for use in CASA.

2.3 IRAM 30m Telescope

Observations of ^{12}CO[1-0] and ^{12}CO[2-1] emission from ETGs presented in Chapter 7 were performed by this author using the IRAM 30m telescope. Observations from the xCOLD GASS survey (Saintonge et al. 2017), the CO-CAVITY pilot survey of void galaxies (Domínguez-Gómez et al. 2022) and observations of ETGs with kinematic misalignments of dust and stars (Davis et al. 2015), also undertaken with the IRAM 30m telescope, are used for comparison with the new observations. This Section describes the telescope and instrumentation used for all these observations.

The IRAM 30m telescope is located near the summit of Pico Veleta, Andalucia,

Figure 2.5: IRAM 30m telescope, showing the 30m dish, secondary reflector, mount and control room (credit: D. H. W. Glass).

Spain (03:23:33.7 W, 37:03:58.3 N) at an altitude of 2,850m (Figure 2.5). it is intended for mm-wavelength observations, and consists of a 30m diameter dish on an ALT-AZ mount with a surface roughness of ~50μm for good reflective properties when observing at mm wavelengths. The curvature of the dish with changing elevation is maintained by its homologous design, which preserves good focus but allows the focus to be displaced on the sky with elevation (Baars et al. 1994). Pointing checks prior to observation are therefore very important. Pointing accuracy is ±3 arcsec or better, and is improved by pointing checks immediately prior to observation (Greve et al. 1996). Telescope beam sizes are ~22 arcsec for ^{12}CO[1-0] emission (rest frequency 115.27 GHz) and ~11 arcsec for ^{12}CO[2-1] emission (rest frequency 230.54 GHz). The GAMA equatorial regions (Chapter 3) were straightforward to observe with the telescope at this latitude, with targets describing an arc from the horizon to a peak of ~50° elevation.

Light is fed to a Nasmyth focus (f/D = 9.7) from the 30m dish via a 2m diameter secondary reflector, where various frontend instruments are available. These convert the

incoming photon stream into electrical signals which can be digitised and processed numerically in back-end equipment. For this work, the EMIR 8-mixer receiver (Carter et al. 2012) was used as the frontend for observations, together with the Fast Fourier Transform Spectrograph (FTS) and the Wideband Line Multiple Autocorrelator (WILMA) back-ends[2] for spectral analysis of the incoming signals.

The Eight Mixer Receiver (EMIR) has four operating frequency bands, chosen to operate within frequency ranges where atmospheric absorption of incoming emission is minimised (Figure 2.6). Bands E090 (83 - 117 GHz) and E230 (200 - 267 GHz) were selected to measure ^{12}CO[1-0] and ^{12}CO[2-1] emission simultaneously. Two orthogonal polarisations are measured for each band simultaneously, hence there are four bands, two receivers per band and eight receivers in total. For this work, E090 covered ^{12}CO[1-0] emission, while E230 covered ^{12}CO[2-1] emission. All observed line frequencies are redshifted ($0.025 \leq z \leq 0.06$) but remain within the ranges of the bands. Within each receiver, the incoming photons are sent via a horn and guide channels to a mixer chip similar to that shown in Figure 2.3, where they are mixed non-linearly with a accurately tuned signal from an external Local Oscillator (LO) and converted to electrical signals . One of the resultant sidebands (Wilson et al. 2009) is then compatible with the frequencies required by backends (see also Section 2.2).

Calibration of the instrumentation is achieved using hot (ambient) and cold (cryostat with liquid nitrogen) sources as references to produce signals of known strengths. Atmospheric conditions are also measured and taken into account during calibration. The results of calibration allows incoming electronic signal amplitudes to be converted to corrected antenna temperatures (T_A^*). The corrected antenna temperature T_A^* is the measure of signal strength within spectra from the back-end spectrographs reported to observers, and is a blackbody temperature equivalent to the signal power reaching the antenna via the dish (Equation 7.3) corrected for losses along the pathway to the source and input from rearward-facing sidelobes (e.g. Wilson et al. 2009, their Section 8.2.5). Factors are

[2]https://publicwiki.iram.es/Backends

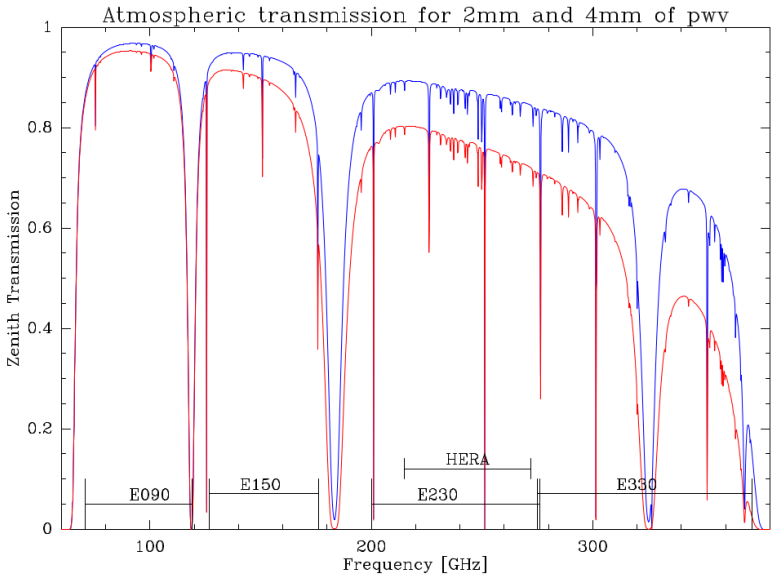

Figure 2.6: Atmospheric absorption at the IRAM 30m telescope, for precipitable water vapour (pwv) levels of 2mm and 4mm (from https://www.iram.fr/GENERAL/calls/s21/30mCapabilities.pdf). The four EMIR bands are also shown.

available to convert T_A^* into flux density in Jy (Chapter 7).

All observations for this work were performed using Wobbler Switching (WSW) mode. The wobbler tilts the secondary mirror and deflects the telescope beam off the target by a specified small angle in a specified plane (horizontal in this work), in one direction and then the other, allowing sky backgrounds to be sampled and subtracted from on-target spectra.

The telescope and instrumentation are controlled via a terminal using the PAKO[3] command-line interface, via an IRAM server which can be accessed within the telescope local control room or remotely. Typically an observer prepares scripts with PAKO commands in advance of observation, and the commands are copied and pasted into the interface sequentially. This is an essential step when using pool observing, where a visiting observer may be making observations for a project apart from their own. Scripts for PAKO

[3]https://www.iram.es/IRAMES/ncs30m/

need to be written as clearly and simply as possible, to minimise opportunity for human error when operating the telescope. A typical script would include commands to perform initial pointing, focus and re-pointing checks using bright mm-wavelength emission from planets or quasars, selection and setup of frontend and backend for observation, target acquisition and short, repeated calibrations and observations of the target to accumulate sufficient signal for later analysis.

2.4 Herschel Space Observatory

The Herschel Space Observatory (Pilbratt et al. 2010), referred to as Herschel in this work) was a spacecraft designed to provide observations at sub-mm wavelengths which would be challenging or impossible to achieve from the ground. Two of the three instruments aboard Herschel provided observations for the Herschel ATLAS survey (Eales et al. 2010), results from which are used extensively in Chapter 6. Once launched, Herschel was located at 2nd Lagrangian point (L2) of the Sun/Earth/Moon system. It was in operation from August 2009 to April 2013, when its helium coolant reservoir was depleted.

The main components of Herschel (Figure 2.7) are described below.

- *Optics*: The primary mirror for Herschel was 3.5m diameter, made from silicon carbide. A undersized secondary mirror, also silicon carbide, created an effective aperture for the telescope of 3.28m and reflected incoming light to the Cassegrain focus (f/8.7 Griffin et al. 2010). The assembly was fixed, with no moving parts requiring deployment after launch of the spacecraft and no focussing requirements in service.

- *Payload module*: The payload module featured the insulated cryostat vacuum vessel, containing the superfluid helium tank (2367 litres), cooling systems and instruments. The cryostat was designed to maintain the instrument sensors at temperatures of ~0.3K, and other instrument components at 1.7 K and 4.5 K (Duband

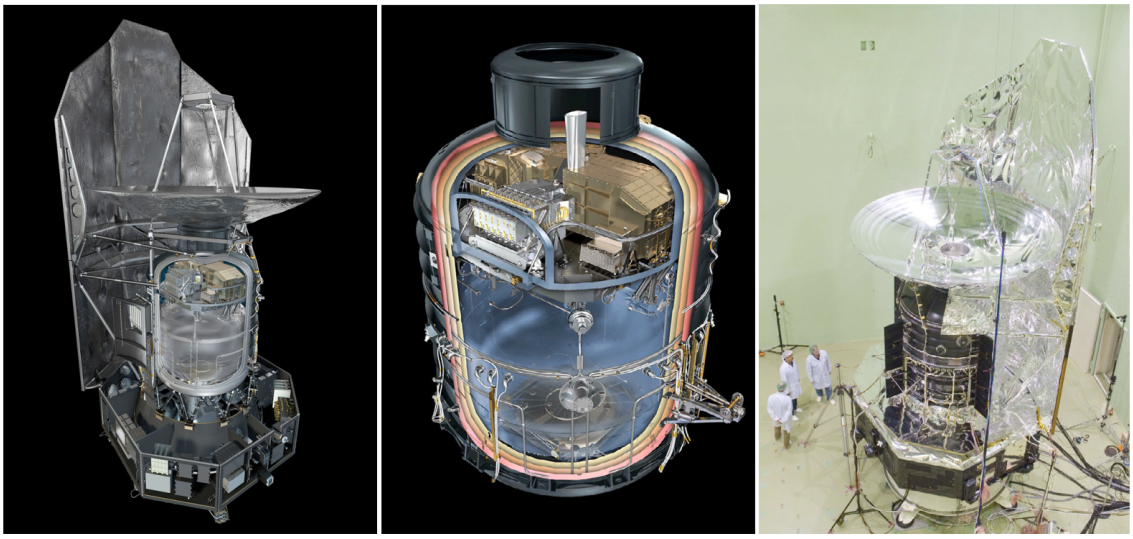

Figure 2.7: Herschel Space Observatory (Herschel). *Left*: spacecraft assembly, showing the primary/secondary mirrors, payload module, sunshield and service module below the payload module. *Centre*: payload module, showing the cryostat vessel and insulation system (coloured) with instruments at the top. *Right*: spacecraft undergoing acoustic testing, with personnel for scale. (Pilbratt et al. 2010).

et al. 2008). Cooling was achieved using superfluid helium (^{3}He) coolant, using a sorption pump to drive the coolant through the system. The pump system uses adsorption onto activated carbon (charcoal) followed by desorption of helium with successive temperature swings to move helium through the cooling systems in zero gravity, while avoiding the need for moving parts (Duband et al. 2008).

- *Service module*: The service module provides all other control and communication functions required by the spacecraft.

The two instruments relevant to this work are the Photodetector Array Camera and Spectrometer (PACS, Poglitsch et al. 2010), and the Spectral and Photometric Imaging REceiver (SPIRE, Griffin et al. 2010). Both instruments included photometers and spectrometers, but only the photometers are of relevance to this work. PACS provided photometry at passbands centred on 160μm (red) and either 70μm (blue) or 100/mum (green) selected by a filter wheel, while SPIRE provided passbands of 250μm (PLW), 350μm (PMW) and 500μm (PLW). The third instrument, the Heterodyne Instrument for the Far Infrared (HIFI), failed early within the mission but was successfully reactivated shortly afterwards (Pilbratt et al. 2010).

Detailed descriptions of PACS and SPIRE are provided by Poglitsch et al. (2010) and Griffin et al. (2010), summarised as follows. PACS used 2 closely-spaced bolometer arrays of 16 $\times$ 16 pixels for the red filter, and 4 $\times$ 2 arrays of 16 pixels for green/blue filters, giving a field of view of $\sim$1.75 x 3.5 arcmin. SPIRE differed from PACS in having hexagonally-packed bolometers fed by individual feedhorns, to optimise sensitivity and stray light rejection. Bolometer numbers were 43 for 500μm, 88 for 350μm and 139 for 250μm, giving a field of view for the photometer of 4 arcmin x 8 arcmin. Of the observational strategies provided for photometry, scan mapping was the optimal selection in many cases. This involved slewing the spacecraft along a defined path at a set angular rate, then reversing the track to run perpendicular to the previous one. Optimal slewing rates are different for PACS and SPIRE, but slewing rates of 20 and 60 arcsec sec^{-1} allowed photometry with PACS and SPIRE in parallel. This allowed multi-passband surveys of

larger areas of sky to be performed efficiently. The strategy was used for the Herschel ATLAS survey (Eales et al. 2010) used within this work (Section 2.8.3).

2.5 James Clerk Maxwell Telescope (JCMT)

Observations with the James Clerk Maxwell Telescope (JCMT)[4] were used by the JINGLE project, along with data from Herschel, to characterise the masses and properties of interstellar dust (Saintonge et al. 2018; Lamperti et al. 2019, see Chapter 5). The telescope and SCUBA-2 instrument (Figure 2.8) used for these observations are described below.

JCMT is located on Mauna Kea, Hawai'i (19° 49' 22.2' N, 155° 28' 37.0" W) at an altitude of 4092m. It is designed for observations at sub-mm wavelengths, and consists of a 15m parabolic dish on an Alt-Az mount with a secondary reflector feeding instruments at Nasmyth foci. The dish is made of separate panels, maintained in alignment using stepper motors to ensure good focus at all orientations. The dish surface roughness is approximately 24 μm, to ensure good reflective properties at sub-mm wavelengths. Pointing accuracy is ±2 arcsec or better (e.g. Buckle et al. 2009). Beam sizes at 450 μm and 850 μm are 7.9 arcsec and 13.0 arcsec FWHM respectively.

Instruments are available for continuum observations via bolometric cameras and line emission via heterodyne receivers. The instrument relevant to this work is the Submillimetre Common-User Bolometer Array 2 (SCUBA-2), a bolometric multi-pixel camera for observing continuum emission at 450μm and 850 μm (Holland et al. 2013). The field of view is 45 arcmin x 45 arcmin. It provides ~10,000 pixels in total, ~5000 for each wavelength, via four 40×32 arrays per wavelength. The bolometers are Transition-Edge Sensors (TES), which transition from superconducting to non-superconducting resistance at a precise temperature (180 mK at 450 μm, 140 mK at 850 μm). A photon arriving

[4]https://www.eaobservatory.org/

Figure 2.8: Components of JCMT and SCUBA-2. *Left*: Front of main dish and secondary reflector (credit: D.H.W. Glass). *Centre*: Rear of dish, showing linkages to stepper motors for dish panel alignment (credit: D.H.W. Glass). *Right*: SCUBA-2 detector housing (credit: EAO).

at a sensor causes a sensor to increase in temperature, which increases the sensor resistance. The sensor reverts to superconducting on re-cooling, in preparation for the next photon arrival. The sensors are maintained at the correct temperatures by a closed-cycle refrigeration system based on ^{3}He/^{4}He refrigerant.

Observing with JCMT normally involves mapping a region of sky. Mapping is achieved by moving the dish in a set pattern around the target, and recording the position (pointing coordinates) of the dish and the received emission with time as the dish moves. This information is then used to bin the received emission into defined pixels to create the required map with an appropriate resolution. Common patterns for dish movement are CV (Constant Velocity) DAISY, which describes a precessing off-centre elliptical pattern around the target but maintains the target on the sensor array, and PONG which describes patterns similar to bouncing off walls defining the observation boundaries. CV DAISY is recommended for small and compact sources with scales of 3 arcmin or less, and was the main method employed for galaxy observations discussed in this work (Section 2.8.5). Observation planning is usually performed using an online tool[5], and data reduction is performed using the STARLINK package available from EAO[6].

[5]https://proposals.eaobservatory.org/jcmt/calculator/scuba2/time

[6]https://starlink.eao.hawaii.edu/starlink

2.6 Other Telescopes

Several other telescopes were used by others to create catalogues of observational data and derived products, in particular the Galaxy and Mass Assembly (GAMA) project (Driver et al. 2009) discussed in Section 2.8.1. These telescopes are described below in outline.

2.6.1 GALEX

The GALEX satellite (Martin et al. 2005) was designed to observe at far ultraviolet (FUV, 1350–1750 Å) and near-ultraviolet (NUV, 1750–2750 Å) wavelengths, to study aspects of star formation in galaxies. It was launched in 2003, and operated from an inclined Earth orbit. The telescope and instrument combination was a 50cm diameter modified Ritchey-Chrétien design with a focal length of 3m and a circular field of view of 1.2°, feeding four channels. Two channels, relevant to this work, were for FUV and NUV photometry, while the remaining two were for spectroscopic observations. Angular resolution was typically 4.5 arcsec (FUV) and 6 arcsec (NUV).

GALEX was used for a number of surveys, in particular the Medium Imaging Survey (MIS) which was to survey an area of 1000 square degrees with a sensitivity of m_{AB} (AB apparent magnitudes, see Section 4.6.1) of ~23. Photometry from this survey was used by the GAMA project (Section 2.8.1) as part of its panchromatic data survey (Driver et al. 2016), allowing the use of MAGPHYS (Section 2.7.3) to estimate galaxy properties which are used extensively in subsequent Chapters.

2.6.2 SDSS Telescope

The Sloan Digital Sky Survey (SDSS) Telescope (Gunn et al. 2006) is located at Apache Point Observatory, USA (32° 46’ 50” N, 105° 49’ 14” W) at an altitude of 2788m. It is based on a Ritchey-Chrétien design, with a 2.5m diameter primary mirror (f/2.25) feeding

aspheric correctors via a secondary mirror achieving an overall focal ratio of f/5. One corrector is for photometry, the other is for spectroscopy. The SDSS camera (Gunn et al. 1998) uses 30 2048 × 2048 CCDs for imaging, yielding a pixel angular scale of ∼0.4 arcsec which is approximately 2.5 pixels per beam FWHM with typical seeing. The field scale is 13.51 × 8.98 arcmin. The camera acquires images in five SDSS passbands with defined peak wavelengths (Fukugita et al. 1996), referred to in this work as u (350nm), g (480 nm), r (625 nm), i (770 nm) and z (910 nm). The original SDSS spectrograph could record up to 640 spectra simultaneously, acquired via fibre-optic cables from a plate with holes corresponding to the required targets in a given field. It had a spectral resolution (R) of 1800, and covered a wavelength range of ∼3900 to 9100Å via two 2048 × 2048 pixel CCD detectors. The fibres have a 3 arcsec diameter field of view (e.g. Kewley et al. 2006)

The telescope was the source of the observations for SDSS (York et al. 2000), which obtained photometry and optical spectra for ∼1 million galaxies in defined areas of the sky, including those in the GAMA regions (Section 2.8.1). This photometry was used in GAMA catalogues for target selection, and for the determination of optical aperture-corrected flux densities for the five SDSS passbands. SDSS images were used by GAMA for morphological classification of galaxies in the GAMA equatorial regions (Section 4.6.1), and are used for illustration of galaxy features within this work. Spectra from SDSS are used in GAMA catalogues of derived products such as emission line strengths, and were used for identification of AGN within galaxies via optical line emission diagnostics where they were identified as the best available spectrum for a particular galaxy (Sections 4.3.1 and 4.3.2).

2.6.3 Anglo-Australian Telescope (AAT)

The Anglo-Australian Telescope[7] is at the Siding Springs Observatory, Australia (31° 16' 31" S, 149° 04' 01" E) at an altitude of 1100m. It has an equatorial mount and a 3.9m primary mirror with a focal length of 12.7m. Its primary instrument of interest for this work is the the Two Degree Field facility (2DF, Lewis et al. 2002), a robotic optical fibre positioner for obtaining spectroscopy of up to 400 objects over a 2° field of view simultaneously. Objects are targeted via drilled plates that are placed robotically within the telescope's field of view, with holes corresponding to the targets of interest. Up to 400 fibre-optic cables are attached to the holes in each plate, each with a ∼2.1 arcsec diameter field of view. Light from each cable is then routed to the AAOmega spectrograph (Saunders et al. 2004), which covers a wavelength range of 370-950 nm with spectral resolutions (R) from 1400-10000. This spectrograph was used to obtain spectra for galaxies within the GAMA equatorial regions (Section 2.8.1), primarily for redshift determinations. The spectra are also used in GAMA catalogues of derived products such as emission line strengths alongside SDSS spectra (Section 2.6.2).

The AAOmega spectrograph was also used to receive light from the Sydney-AAO Multi-object Integral field spectrograph (SAMI, Croom et al. 2012), used for SAMI Survey (Croom et al. 2021a) which observed 3068 galaxies to obtain spatially-resolved spectra. SAMI is based on 13 "hexabundles" of 61 fibre-optic cables each. The individual fibre positions at the entrance end of the hexabundles are known. Hexabundles are plugged into to a drilled plate at a set orientation such that the fibre positions can be assigned to on-sky locations, with each hexabundle corresponding to a desired galaxy target. The plate is mounted on a lens system at the telescope prime focus, which optimises the field of view (1° diameter) with respect to the plate. Each hexabundle then had a field of view of 14.5 arcsec. Observations of galaxies employed a dithering technique (Sharp et al. 2015) which allowed optical spectra to be constructed for a field of view of ∼16 arcsec per hexabundle with a spaxel resolution of 0.5 arcsec. Spectra within SAMI data cubes cover two

[7] https://aat.anu.edu.au/

wavelength ranges, 3700 – 5700 Å at a spectral resolution of R ∼1730, and 6250 – 7350 Å at R ∼4500. Observations and derived data from the SAMI Galaxy Survey (Croom et al. 2021a) are used in Chapter 3, for comparison of stellar and ionised gas kinematics with the kinematics of molecular gas in ALMA-observed ETGs.

2.6.4 VLT Survey Telescope (VST)

The VLT Survey Telescope (VST, Capaccioli et al. 2005) is at the Paranal Observatory, Chile (24° 37' 41" S, 70° 24' 18" W), at an altitude of 2635 m. Its purpose is to provide seeing-limited, wide-field surveys from near ultraviolet to near infrared, in support of the Very Large Telescope (VLT) and for other projects. It consists of a 2.61 m diameter, f/5.5 modified Ritchey-Chrétien telescope on an Alt-Az fork mount. To achieve seeing-limited observations (∼0.5 arcsec), the primary mirror is fitted with 84 actuators to provide adaptive optics, and the secondary mirror is moveable for optimal observation. The system provides a field of view of 1° width. The VST is fitted with OmegaCAM (Cappellarao 2005), which is a wide-field camera with a mosaic CCD sensor containing ∼16000 x 16000 pixels. The sensor has a pixel scale of 0.21 arcsec, and it observes the VST 1° width field of view. The filters provided for the camera are based on the SDSS ugriz system (Section 2.6.2).

The main role of VST observations in this work is the provision of images from the Kilo-Degree Survey survey (KiDS, de Jong et al. 2015) for morphology classification of galaxies in the GAMA equatorial regions by the GAMA-KiDS-GalaxyZoo project (Section 2.8.2). VST images from KiDS are also used for illustration of specific galaxies, because of their superior resolution and depth compared to SDSS images.

2.6.5 VISTA

The Visible and Infrared Survey Telescope for Astronomy (VISTA, Emerson et al. 2004; Sutherland et al. 2015) is located at the Paranal Observatory, Chile (24° 36' 57" S, 70° 23' 51" W) at an altitude of 2518 m. It has a 4.1m primary mirror and a 1.24m secondary mirror on an Alt-Az mount, with a modified Ritchey-Chrétien design matched to the optics of the VIRCAM camera at the Cassegrain focus. The optical arrangement achieves a focal ratio is f/3.26 with a field of view of 1.65° diameter. Active optics maintain collimation of the telescope, by tipping the primary mirror and moving the secondary (Sutherland et al. 2015). The VIRCAM camera (Sutherland et al. 2015) has a 0.34-arcsec pixel scale, and sixteen 2048 × 2048 detector chips giving a total pixel count of ~67 million. The camera operates with infrared filters labelled Z, Y, J, H and K in order of increasing central wavelength from 0.8 - 2.3 μm.

Observations in ZYJHK passbands were obtained from the VISTA Kilo-degree Infrared Galaxy (VIKING) survey (Edge et al. 2013) which used the VISTA telescope (Emerson et al. 2004; Sutherland et al. 2015) to observe galaxies including those in the GAMA and H-ATLAS regions. GAMA made use of images and aperture corrected photometry from this survey in their panchromatic data release (Driver et al. 2016), used as an input to MAGPHYS (Section 2.7.3).

2.6.6 WISE

The Wide-field Infrared Survey Explorer (WISE) satellite (Wright et al. 2010) provided photometry from two whole-sky surveys for four mid-infrared passbands, W1 (3.4μm), W2 (4.6μm), W3 (12μm) and W4 (22μm). The aim was to provide imaging and photometry for galaxies, stars, star-forming regions, planetary debris discs and asteroids, with greater sensitivity than previous satellite missions operating at similar wavelengths. The satellite includes a 40cm diameter telescope (f/3.375), with four detectors each having

1024 × 1024 pixels yielding a pixel scale of 4.75 arcsec and a field of view width of ∼47 arcmin. Binning (2 × 2) was applied to the W4 band (Mainzer et al. 2005). The satellite was placed in a low-Earth, sun-synchronous orbit, observing when the Earth provided shielding from the Sun. The detectors operated at 17K, cooled by a solid hydrogen-based cryostat (Mainzer et al. 2005). The system achieved 5σ point source sensitivities less than 0.08, 0.11, 1, and 6 mJy for the four bands in the absence of source confusion, and achieved PSFs were 6.1, 6.4, 6.5 and 12.0 arcsec for W1 - W4 respectively (Wright et al. 2010).

Observations from the WISE all-sky survey (Wright et al. 2010) were used by the GAMA project, to provide photomery for their panchromatic data release (Driver et al. 2016), used as an input to MAGPHYS (Section 2.7.3) for estimating galaxy properties used extensively in this work. WISE photometry was also used to identify galaxies containing AGN (Section 4.3.5).

2.6.7 Karl G. Jansky Very Large Array (VLA)

The Karl G. Jansky Very Large Array (VLA) (Heeschen 1975) is an interferometric radio telescope (Section 2.1) on the the Plains of San Agustin, New Mexico, USA (34°04' 43" N, 107° 37' 04" W), at an altitude of 2124 m[8]. it uses 28 antennae with 25 m dishes, of which 27 are in use at one time. The antennae are distributed in a Y-shaped pattern on rails, and can be moved to specific positions to form one of four configurations A - D. Of relevance to this work is configuration B, with has a maximum baseline length of 7.08 miles (11.4 km). This configuration was used for the VLA-FIRST (Faint Images of the Radio Sky at Twenty-cm) survey (Becker et al. 1994), which provided continuum flux densities at 20cm wavelength (1.5 GHz) for individual galaxies. The survey achieved a resolution of 5.4 arcsec FWHM, and a 1σ sensitivity in co-added images of ∼0.14 mJy (White et al. 1997). Flux densities for detections at 20cm from this survey were assigned

[8]https://public.nrao.edu/telescopes/VLA/

to galaxies in GAMA catalogues, and this information was used in this work to identify galaxies with strong AGN (Section 4.3.6).

2.7 Techniques

Several methods are used to provide numerical estimates of galaxy properties within this thesis. Detailed descriptions of these methods are provided below.

2.7.1 KinMSpy and GASTimator

KinMSpy was first presented by Davis et al. (2013), and is intended to build model ALMA data cubes for galaxies (with two spatial axes and a velocity axis). The aim is to create models which show realistic surface brightnesses and kinematics (i.e. Doppler shift) of emission that can be matched to actual ALMA observations.

The Python code[9] for KinMSpy creates models of rotating disc galaxies by distributing line emission over numerous point sources (”cloudlets”) in the galaxy plane with equal emission, such that the point sources are more concentrated where emission is stronger. The point source distribution can be axisymmetric from the galaxy centre with a defined radial profile, or be placed according to defined coordinates. Velocities are then assigned to each spatial coordinate e.g. using an appropriate radial velocity distribution, which can be axisymmetric circular, bisymmetric e.g to represent a galactic bar (Spekkens & Sellwood 2007), or other user-specified distribution. A Gaussian velocity dispersion can also be superimposed on the model velocities. The point-sources are then oriented to a given position angle and ellipticity, and emission and line-of-sight velocities are calculated per user-defined pixel to represent an observation. The resultant model matches the spatial and velocity dimensions and pixel/velocity bin sizes specified by the user, with flux

[9]https://github.com/TimothyADavis/KinMSpy

densities at specific spatial and velocity locations imposed by the model. An additional step is to convolve the 2-dimensional spatial maps per velocity bin with a 2-dimensional Gaussian profile representing the clean beam from the ALMA observation to be simulated (Section 2.1).

Models generated using KinMSPy can be fitted to ALMA observations using GAStimator[10], which provides a straightforward means of setting up Python code to fit models from KinMSpy to data. GAStimator makes use of Bayesian inference to fit a model with defined parameters to data, based on repeated sampling of parameters according to an appropriate algorithm. In this case, Markov-chain Monte Carlo (MCMC) Gibbs sampling (e.g. Casella & George 1992) is used to control parameter sampling and generate chains of sampled parameters from which posterior distributions can be obtained. Median parameter values from fitting and 1σ uncertainties can be derived from these distributions.

MCMC-based sampling of parameters to produce likelihood estimates makes use of Bayes' theorem, which is expressed as follows:

$$P(A|B) = P(B|A)\,\frac{P(A)}{P(B)} \tag{2.7}$$

where A represents a set of parameters within a model, and B represents a set of data to be fitted. $P(A)$ is the prior probability that the initial parameter estimates are correct, and $P(B|A)$ is the probability that the data fits the model (i.e. a goodness of fit). $P(A|B)$ is then the posterior probability that the parameters are correct given the data. $P(B)$ is a normalisation factor which can be neglected if simply maximising values of $P(A|B)$ (replaced by likelihood L):

$$L \propto P(B|A)\,P(A) \tag{2.8}$$

The theorem shows how initial (prior') knowledge of the model parameters can be

[10]https://github.com/TimothyADavis/GAStimator

improved to form posterior probabilities if the probability that data fits the model $P(B|A)$ can be calculated. In this case, prior probabilities $P(A)$ are set to 1 for each input parameter is within specified bounds and 0 otherwise (known as "flat" priors), and $P(B|A)$ is replaced by a log-likelihood expression for goodness of fit, an example of which is provided as Equation 6.5 in Section 6. The likelihood ($\log(L)$) is then built by repeatedly sampling parameter values A using an appropriate algorithm to explore the parameter space efficiently.

When performing model fitting using this type of technique, it is important to establish whether the sampling has led to convergence of the parameters, i.e. successive samples are drawn at random around a solution and are not correlated with previous sample results. Also, it is important to establish that sufficient samples have been drawn to create valid posterior distributions. Convergence of models fitted with GAStimator was assured by inspection of trace plots (fitted value versus step number) for each parameter, to ensure that the parameter space was frequently sampled over the prior range. If serial correlation was detected, with meandering trace plots and only a few major peaks and troughs, fitting was repeated with an increased number of steps. This was an issue for parameter pairs with degeneracy. Plots of autocorrelation parameter calculated using tools within EMCEE (Foreman-Mackey et al. 2013, 2019) versus number of steps were also used, to ensure that the number of model steps used was sufficient to achieve small autocorrelation parameters ($\sim$0) for all fitted parameters and to select a suitable "burn-in" interval after which the sampled chains are not correlated and are exploring optimum parameter values.

If two competing models for data are being compared, the ratios of $P(B)$ for each model can be compared, and their ratio gives an indication of whether one model is preferred over another. However, estimation of $P(B)$ for multiparameter models via MCMC is complex and computationally expensive (Wall & Jenkins 2003). A simpler estimate can be be obtained using the Bayesian Information Criterion (BIC, Schwartz 1978; Liddle 2007):

$$BIC = k \ln(n) - 2ln\left(\hat{L}\right) \tag{2.9}$$

where k the number of fitted parameters, n the number of data points fitted and $\hat{L}$ the maximised Bayesian likelihood from Equation 2.8. The ratio of BICs for each model can also indicate whether one model is favoured over another. It is generally possible to achieve a better fit using a model with more fitted parameters, but the BIC addresses this by disfavouring models with more fitted parameters unless the fit is significantly better.

2.7.2 Stackarator

The STACKARATOR[11] package (Davis et al., in prep.) is designed to concentrate weak emission within an ALMA data cube into a single spectral peak, based on prior information on the location of emission in spatial and velocity coordinates from another observation (or other appropriate source e.g. a model). For example, a resolved map of ionised gas velocities may be available from an IFU observation, e.g. SAMI (Section 2.6.3), and may be at a lower spatial resolution than the ALMA data cube of interest.

STACKARATOR estimates the velocity of emission at each spaxel from the supplied prior information, using interpolation where the spatial resolution of the ALMA observation is greater than that of the prior map. It then re-samples the emission along each spaxel into relative velocity bins, with reference to the velocity assigned to each spaxel from the prior map. If the prior map genuinely aligns with the emission in the ALMA data cube, the resultant spectral peak will be centred on zero velocity. Each bin in the spectrum will be assigned a different number of points because of variations in the locations of emission along spaxels, hence the signal to noise ratio per bin will vary. STACKARATOR provides this information as an output. The main output of interest from STACKARATOR is a plot of flux density per velocity bin with reference to the velocities in the prior map. With this approach, any kinematic information (e.g. the double-horned spectrum from a rotating

[11] https://github.com/TimothyADavis/stackarator

disc, see Section 3.3.1) is lost. However, the spectral line is much narrower and the peak is increased, allowing weaker distributed emission to be detected above the prevailing noise level. Flux is conserved during this process, so an integral of the spectral line still represents the total emitted flux for the spectral line.

STACKARATOR can carry out the above steps either for the cube as a whole to produce a single combined spectral line, or for concentric elliptical regions to obtain radial distributions of flux. Figure 3.16 shows the results of using STACKARATOR on the whole data cube for the ALMA-observed dusty ETG GAMA622305 (Sansom et al. 2019).

2.7.3 MAGPHYS

Multi-wavelength Analysis of Galaxy Physical Properties (MAGPHYS) is a software tool for estimating galaxy properties relating to stars and interstellar medium from multi-wavelength photometry in the range 912Å to 1mm (da Cunha et al. 2008). The galaxy properties of interest are parameters for model spectral energy distributions (SEDs) for stellar emission and absorption by dust at ultra-violet to near infra-red wavelengths, and for re-radiation of absorbed energy by dust at infra-red and sub-mm wavelengths. The total spectrum for a galaxy is built by combining these spectra, pre-built in libraries with known input parameters, to achieve an energy balance between radiation emitted by stars and radiation absorbed and re-emitted by ISM. For each combination of SEDs fitted, a marginalised likelihood term is calculated and is used to assign best fit values and uncertainties for each galaxy parameter. Of particular interest in this work are fitted values of stellar mass, total dust mass and star formation rate (SFR), and the means by which these can be determined are described below. MAGPHYS was used by the GAMA project (Section 2.8.1) to estimate properties for >197000 their selected galaxies, using 21-band photometry gathered from surveys using the telescopes discussed in Section 2.6 and Herschel (Section 2.4). The results are presented in their panchromatic data release catalogue (Driver et al. 2016).

The SEDs for stellar emission are based on models by Bruzual & Charlot (2003), and cover a wavelength range of 91 Å - 160 μm. The SEDs for stellar emission provided with MAGPHYS cover stellar ages from 10^5 - 2×10^{10} yr, and a range of metallicities and star formation histories. A Chabrier (2003) initial mass function (IMF) is assumed, and the evolution of low- and intermediate-mass stars into thermally-pulsing asymptotic giant branch (AGB) stars is addressed using methods by Marigo & Girardi (2007). Attenuation due to absorption of stellar emission by ISM (dust and gas) uses a simple model from Charlot & Fall (2000) which accounts for the increased density of stellar birth clouds which absorb and attenuate emission from newly-formed stars in addition to ISM. This extra absorption decreases over a timescale of $\sim 10^7$ yr, leaving ISM as the sole source of absorption and re-emission of stellar radiation.

A key parameter from MAGPHYS used in this work is star formation rate (SFR, $M_\odot$ yr^{-1}). SFR is used to build the library SEDs as an input parameter to the following relation using the emission and attenuation properties outlined above, which gives the stellar luminosity density after attenuation as a function of time:

$$L_\lambda = \int_0^\infty \psi\left(t - t'\right) S'_\lambda\left(t'\right) \exp\left(-\hat{\tau}_\lambda\left(t'\right)\right) d\lambda \tag{2.10}$$

where L_λ is luminosity density at wavelength λ, $\psi\left(t - t'\right)$ is the star formation rate at time $t - t'$, $S'_\lambda\left(t'\right)$ is luminosity per unit wavelength per unit mass emitted by a stellar population of age t' (starting with a known IMF), and $\hat{\tau}_\lambda\left(t'\right)$ is the effective optical depth of dust seen by stars of age t'. This relation is per unit stellar mass, so the resultant SED can be scaled by stellar mass as another parameter of interest in this work. Star formation rates are set using an exponentially declining model, starting at uniformly-sampled past times from 0.1 - 13.5 Gyr and with a time constant that increases with time, to cover starburst, normal star formation and quiescence. Random bursts of star formation with equal probability of occurrence over time are superimposed on the continuous model, with starburst amplitude and duration drawn from defined ranges.

The emission of absorbed energy by dust considers four emitting components, namely polycyclic aromatic hydrocarbons (PAHs) and dust which is either hot, warm or cold. Library spectra are built per unit dust mass, so that dust mass as a parameter of interest can be fitted by scaling. The SED for the emission of cool dust takes the following form (Hildebrand 1983):

$$L'_\lambda = \kappa_\lambda B_\lambda (T_d) \tag{2.11}$$

$$\kappa_\lambda = \kappa_{\lambda,0} \left(\frac{\lambda}{\lambda_0} \right)^{-\beta} \tag{2.12}$$

where L'_λ is the luminosity density per unit mass, κ_λ is the mass absorption coefficient at wavelength λ, B_λ is the wavelength-based Planck function at dust temperature T_d, and β is the emissivity coefficient. The reference values κ_0 and λ_0 are 0.077 m^2 kg^{-1} at 850 μm, as used by Dunne et al. (2011) and in Chapter 6.

Dust associated with PAH emission (3 - 5 μm) has a fixed temperature of 850K in the model, with β = 1. Hot dust, heated by stochastic processes, has equal emission contributions from dust at two temperatures (130K and 250K), and β = 1. Warm dust, in equilibrium with the surrounding radiation field, has a range of temperatures and β = 1.5. Cold dust, also in equilibrium with the prevailing radiation field, has a range of temperatures and β = 2. Strong PAH spectral features in the range 3 - 5 μm are added via specific model spectra. The output from MAGPHYS contains the total dust mass, and does not present the masses of dust at various temperatures.

It should be noted that MAGPHYS treats the dust as if it is separate from, and in front of, the stellar emission. The absorption and re-radiation of stellar emission is therefore only an approximation of true galaxy behaviour, where stars and ISM are mixed. Also, no attempt was made to address additional emission from AGN within galaxies, which could add further emission to multi-waveband photometry. Emission from lower-luminosity

AGN should have little effect on the method (da Cunha et al. 2008), but fitted results from galaxies containing AGN should be treated with caution.

MAGPHYS includes a set of 25,000 model spectra covering stellar emission and ISM absorption and a set of 50,000 spectra covering re-radiation by dust, built using the methods described above to cover a suitably large range for all parameters to be fitted. All spectra are normalised to Solar luminosity, and can be scaled during fitting to input photometry while maintaining the balance of emitted, absorbed and re-radiated energy.

An example of a model fit to photometry is shown in Figure 2.9, for the ETG GAMA64646 studied in Chapter 3. The fitted stellar emission (flux) at shorter wavelengths is shown, alongside the best model fit to the supplied photometry. Absorption at shorter wavelengths and re-radiation at longer wavelengths of stellar emission by the ISM is apparent from the model fit when compared to stellar emission. The spectral peaks associated with PAH emission are visible, along with the sub-mm emission from cool dust.

2.7.4 Colour and Flux Bias Corrections for H-ATLAS Data

Flux density measurements within H-ATLAS (Section 2.8.3) were made using filters on board Herschel (Section 2.4), each with its own spectral response. In practice, the flux density measured through a passband is the spectrum of the emission being observed multiplied by the filter spectral response. The photometry presented for H-ATLAS DR1 (Valiante et al. 2016) assumes spectral energy that is independent of frequency, such that νS_ν is a constant. The flux densities presented therefore should to be corrected for more accurate work to reflect the actual emitted spectrum of interest, using a process referred to as colour correction. The detailed implementation of colour correction for this work is discussed below.

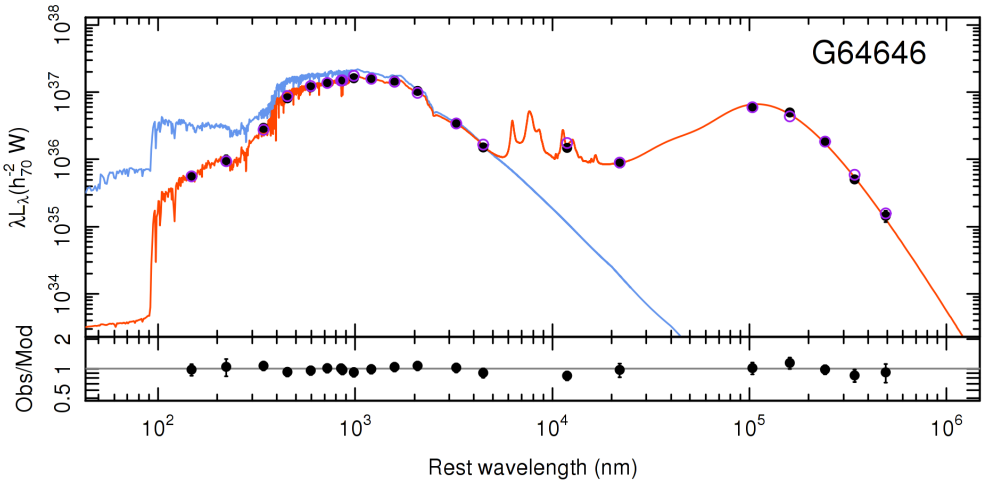

Figure 2.9: MAGPHYS model fit (wavelength-dependent luminosity versus wavelength) to 21-band photometry for GAMA64646. Stellar emission is shown in blue, best model fit is shown in red. Solid points are integrated fluxes from photometry at rest wavelengths, circles are integrated fluxes for each passband filter derived from the model (http://www.gama-survey.org/dr3/tools/sov.php).

Given an observed continuum emission with flux density S(ν) as a function of frequency ν, a telescope detector records a flux F based on the filter response curve R(ν) as follows (for unresolved sources, where the change in beam shape with frequency does not affect the total flux density measured):

$$F = \int_{-\infty}^{\infty} S(\nu)R(\nu)\eta(\nu)d\nu \tag{2.13}$$

This equation includes the frequency-dependent aperture efficiency of the telescope $\eta(\nu)$, which is the fraction of photons arriving at the telescope that reach the detector. Dividing this flux by the flux density S(ν_0) at the central passband frequency ν_0 gives a measure of the effective frequency width of the passband, $\Delta\nu$:

$$\Delta\nu = \frac{\int_{-\infty}^{\infty} S(\nu)R(\nu)\eta(\nu)d\nu}{S(\nu_0)R(\nu_0)\eta(\nu_0)} \tag{2.14}$$

For a spectrum with flat spectral energy discussed above, Equation 2.14 becomes:

$$\Delta\nu_{flat} = \frac{\int_{-\infty}^{\infty} \nu^{-1}R(\nu)\eta(\nu)d\nu}{\nu_0^{-1}R(\nu_0)\eta(\nu_0)} \tag{2.15}$$

Similarly, the frequency width for a Single Modified Blackbody (SMBB) spectrum (Equation 2.11) is:

$$\Delta\nu_{SMBB} = \frac{\int_{-\infty}^{\infty} B(\nu)(\frac{\nu}{\nu_0})^{\beta}R(\nu)\eta(\nu)d\nu}{B(\nu_0)R(\nu_0)\eta(\nu_0)} \tag{2.16}$$

Bearing in mind that the published catalogue flux density is proportional to the measured flux divided by the frequency width of the passband, a multiplier that can be applied to the catalogue flux densities to correct them for a modified blackbody spectrum is $\Delta\nu_{flat}/\Delta\nu_{SMBB}$. Using Equations 2.15 and 2.16, this multiplier (applicable to unresolved sources only) is:

$$KcolP = \nu_0^{\beta+1} B(\nu_0) \frac{\int_{-\infty}^{\infty} \nu^{-1} R(\nu)\eta(\nu)d\nu}{\int_{-\infty}^{\infty} B(\nu)\nu^{\beta} R(\nu)\eta(\nu)d\nu} \tag{2.17}$$

This is identical to Equation 5.25 in Valtchanov (2018) for the SPIRE instrument aboard Herschel, with their term for spectral power for the flat spectrum α_{pip} set to -1. Note that KcolP is a multiplier for the flux densities in the Herschel-ATLAS catalogues. Guidance for other instruments such as the Herschel PACS instrument (PACS Team 2019) and the AKARI-FIS instrument (Yam 2010) present colour corrections based on the actual emission filter width / flat emission filter width, and the catalogue flux densities must be divided by the resultant correction factors. In this work, all colour correction factors for flux densities from both PACS and SPIRE are derived as multipliers to avoid any confusion.

The analysis above applies to unresolved (point) sources. For extended sources, Valtchanov (2018) introduce the variation of beam size with observed frequency Ω_ν into Equation 2.17 to create a new multiplier:

$$KcolE = \nu_0^{\beta+1} B(\nu_0) \frac{\int_{-\infty}^{\infty} \nu^{-1} R(\nu)\eta(\nu)\Omega_\nu d\nu}{\int_{-\infty}^{\infty} B(\nu)\nu^{\beta} R(\nu)\eta(\nu)\Omega_\nu d\nu} \tag{2.18}$$

Rather than relying on numerical integration to solve Equations 2.17 and 2.18 for flux densities from SPIRE, actual values of KColP and KColE for a grid of temperature and β values were extracted from the Herschel Interactive Programming Environment v15.0.1 (HIPE, Balm 2012). These were used to create lookup tables for use with the Python-based function Scipy.interp2d, which return interpolated values of KColP or KColE when supplied with a value of temperature and β. The decision on whether to apply KColP (unresolved) or KColE (resolved) to a flux density was based on the type of photometry used to obtain flux densities within the H-ATLAS catalogue. Aperture photometry was used for all resolved sources, so if the H-ATLAS catalogue showed the aperture size associated with a flux density, KColE is the correct factor to apply. However, an aperture of

-99. indicated that the MADX approach (Maddox & Dunne 2020) was used for photometry where sources are unresolved, in which a Gaussian profile was fitted to the image to obtain photometry (see also Section 2.8.3). KColP was then applied.

A similar approach was not possible for flux densities from PACS, because colour corrections are not directly available within HIPE. Numerical integration was used to solve Equation 2.18 for all PACS-derived flux densities, since these were obtained using aperture photometry and are treated as extended sources. The method described in the PACS explanatory supplement (PACS Team 2019) states that the terms $\eta(\nu)$ and Ω_ν are set to 1. The filter profiles for the relevant PACS filters (green (100μm) and red (160μm)) are available from the SVO Filter Profile Service (Rodrigo & Solano 2020). However, these profiles need to be multiplied by a frequency-dependent bolometer absorption factor which accounts for light loss along the optical path of the telescope (PACS Team 2019). Tabular data are available for this via HIPE, and lookup tables similar to those obtained for the SPIRE passbands were derived for use in this work. Figure 2.10 shows the excellent agreement between the implementation of these methods and the example tabular data provided in the explanatory supplements for PACS and SPIRE (Valtchanov 2018; PACS Team 2019).

A further correction for SPIRE data is recommended to account for "flux bias", where a portion of the measured flux density is from background source confusion even after background subtraction. Best estimates for values of flux bias correction factors (divisors) are published in Valiante et al. (2016), their Table 6. The data were fitted with exponential functions of the following form, for use in Python code:

$$F_{bias} = 1 + Y.e^{-\left(\frac{S_\nu}{S_{\nu 0}}\right)} \tag{2.19}$$

where Y is a constant and $S_{\nu 0}$ is a reference flux density. The correction factors are greater for lower flux densities, because a greater proportion of the measured flux density is from background source confusion. The proportion diminishes as the measured flux

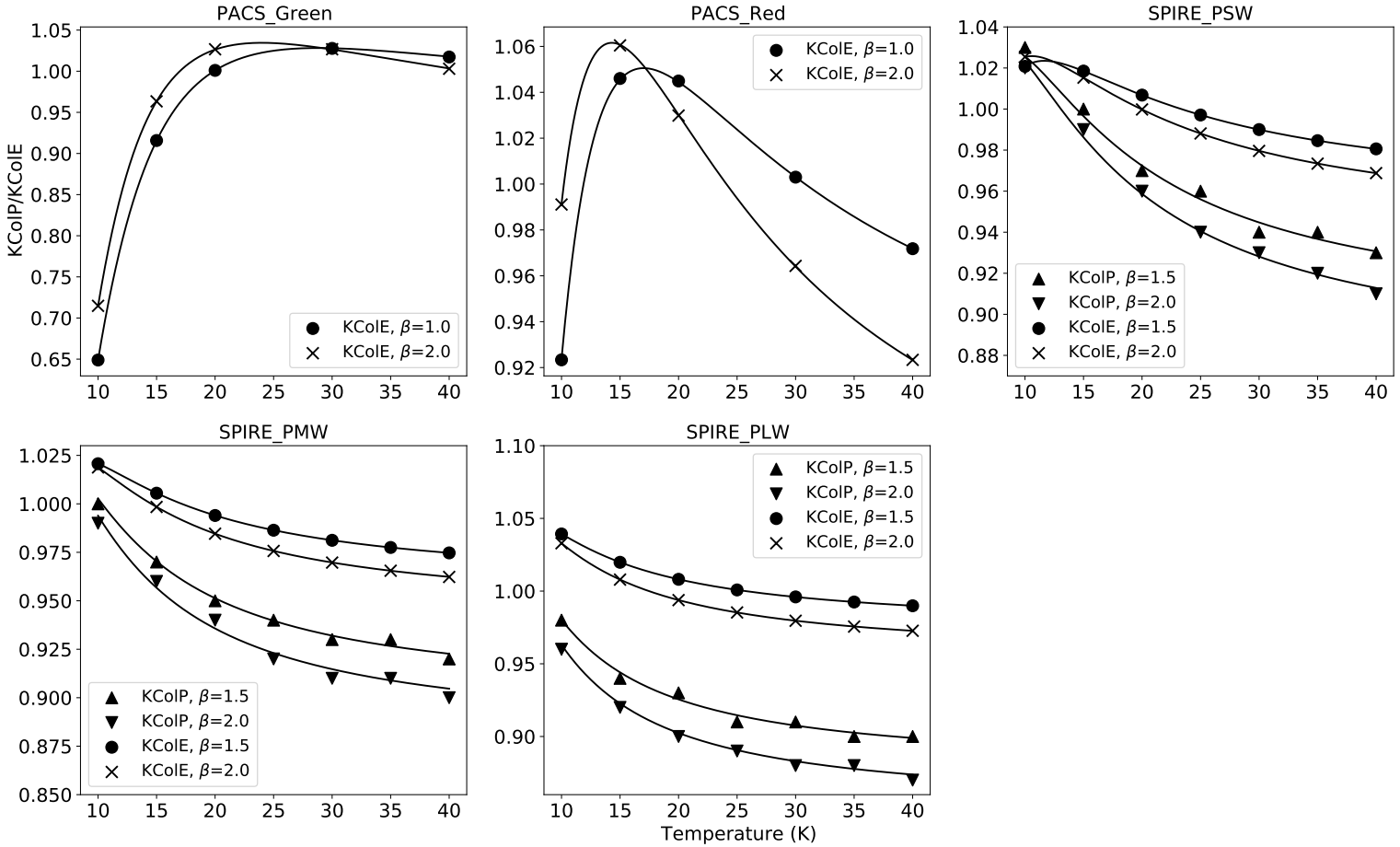

Figure 2.10: Comparison of calculated KColP and KColE (black curves) with published values (points) in the PACS and SPIRE explanatory supplements. The scatter in published KColP values for SPIRE passbands in Valtchanov (2018) is due to limited precision in the data tables.

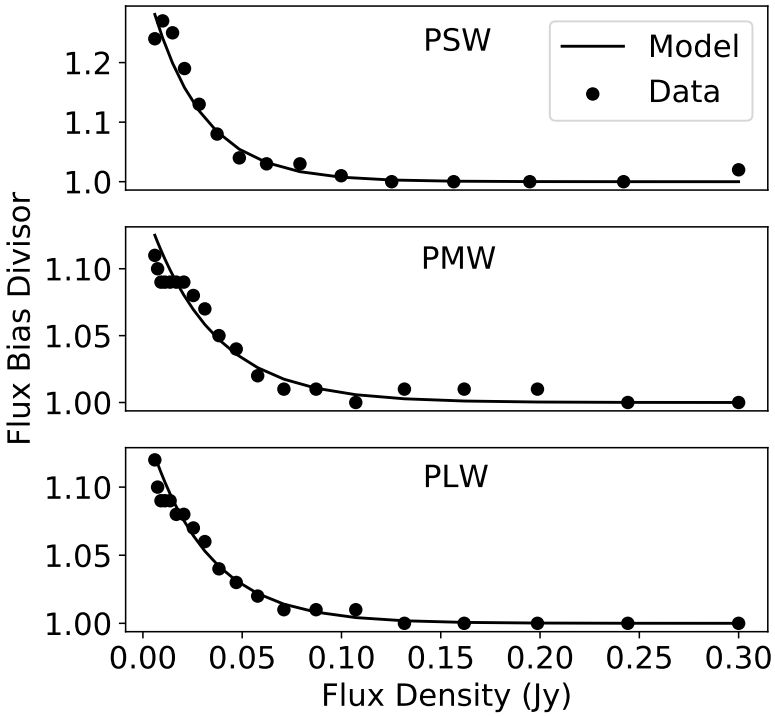

Figure 2.11: Comparison of models for flux bias divisors for the SPIRE passbands with published data.

density increases. Figure 2.11 shows the empirical fits of the model to the published values, and Table 2.1 shows the values of the constants used for each passband.

Table 2.1: Constants for use with Equation 2.19

SPIRE Filter	Y	$S_{\nu 0}$ (Jy)
PSW (250 μm)	0.55	0.025
PMW (350 μm)	0.15	0.033
PLW (500 μm)	0.15	0.03

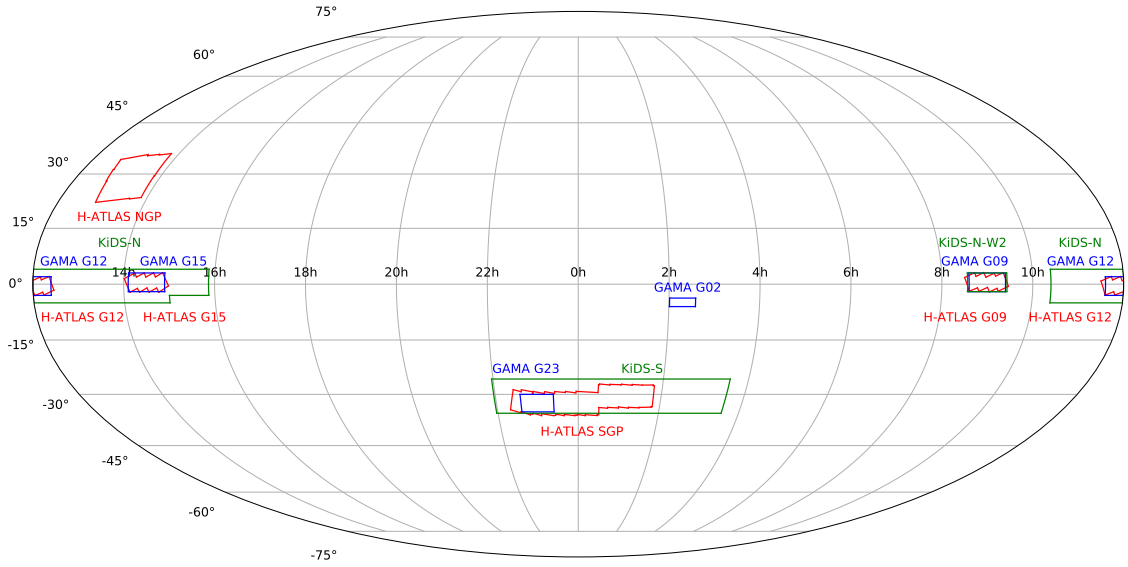

Figure 2.12: Mollweide diagram showing the locations of GAMA, KiDS and Herschel-ATLAS survey regions (http://www.gama-survey.org/, https://kids.strw.leidenuniv.nl/, https://www.h-atlas.org/).

2.8 Data Sources

This work makes extensive use of public data releases from previous observational surveys. The main surveys of interest in this work are described below. Figure 2.12 shows the regions of sky covered by the principal surveys used, based on survey descriptions within the relevant project documentation.

2.8.1 Galaxy and Mass Assembly (GAMA)

The Galaxy and Mass Assembly (GAMA) project (Driver et al. 2009) has delivered catalogues of data for over 200,000 galaxies. The aim of the project was to provide complete datasets for galaxies in five regions of the sky, to study aspects of galaxy evolution at low to medium redshift. Three regions of interest in this study, known as the GAMA

equatorial regions (G09, G12 and G15), are centred on 9h, 12h and 14.5h RA and 0° DEC (Figure 2.12). The GAMA project provided complete spectroscopic data for targets within the regions of interest to an r-band absolute Petrosian magnitude from Sloan Digital Sky Survey (SDSS) observations (York et al. 2000) of 19.8. The spectra were of particular interest for obtaining spectroscopic redshifts and line intensities for calculating parameters such as diagnostics indicating the presence of strong Active Galactic Nuclei (AGN). GAMA also has partnership arrangements with other current and planned observational programmes described in this Chapter, and provides catalogues of photometric data over 21 passbands from far UV to sub-mm wavelengths. Other catalogues of data products cover visual morphology and properties of galaxies derived from observations.

The relevant GAMA data releases[12] for this work are GAMA II, which was partially made public with the remainder kept within the project team pending completion (Liske et al. 2015), and GAMA DR3 (Baldry et al. 2018) from which some data are used in Chapter 2 because of its public availability at the time. The complete set of GAMA II catalogues was made public in 2022 (Driver et al. 2022), along with GAMA DR4 which contains other information not used in this work. All GAMA II catalogues used in this work are confirmed as being current at the time of publication of this thesis. Details of individual GAMA II catalogues are provided at the point of use.

2.8.2 GAMA-KiDS-GalaxyZoo

The GAMA-KiDS-GalaxyZoo[13] project (Kelvin et al., in prep., see also Holwerda et al. 2019; Porter-Temple et al. 2022)) provides visual morphology classifications for over 49,000 galaxies in the GAMA equatorial regions, based on classifications by volunteer classifiers using a project-specific flowchart (Section 4.6.2). Total numbers and fractions of classifier votes for each node of the flowchart are provided. The morphological classification work presented in Section 4.6.2 is based on pre-release classification data (January

[12]http://www.gama-survey.org/

[13]https://blog.galaxyzoo.org/author/thebamf/

2018), which has been corrected for classifier reliability. Seeing-limited (0.5 - 0.7 arcsec FWHM) colour images from the Kilo-Degree Survey (KiDS) (de Jong et al. 2015) were used for morphological classification, which allow better analysis of fine detail within galaxies e.g. faint spiral structure not apparent in SDSS images used with GalaxyZoo previously (Lintott et al. 2008, 2011). The images were obtained using from VST and OMEGACam (Section 2.6.4). Images from KiDS are used in this work to illustrate galaxies and their features.

2.8.3 Herschel ATLAS (H-ATLAS)

The H-ATLAS project (Eales et al. 2010) used Herschel (Section 2.4) to map the three GAMA equatorial regions in five sub-mm wavelengths. The PACS 100μm and 160μm filters were used for H-ATLAS, along with all three SPIRE filters at 250μm, 350μm and 500μm. This range of wavelengths is suitable for capturing the peak continuum thermal emission from cool material, specifically interstellar dust at temperatures of ~20 - 30K, and defining a portion of the spectrum of the emission either side of the peak. The H-ATLAS DR1 data release[14] (Valiante et al. 2016) provides a catalogue of aperture-corrected flux densities for source detections with >2.5σ detection in one of the PACS instrument passbands and >4σ detection in one of the SPIRE instrument passbands. Achieved noise levels (1σ) for SPIRE were 7.4 (250μm), 9.4 (350μm) and 10.2 (500μm) mJy, and for PACS typical values of 44 (green) and 49 (red) mJy were achieved. Conventional aperture photometry was used to estimate flux densities for galaxies that are resolved in images from PACS and SPIRE. For unresolved objects in SPIRE images with their larger beam diameters, the MADX (Maddox & Dunne 2020) approach was used which uses matched filtering of SPIRE images using filters based on the PSFs of each SPIRE passband. Beam-shaped (Gaussian) profiles are then fitted at the peak locations to obtain flux densities.

[14]https://www.h-atlas.org/public-data/download

2.8.4 SAMI Galaxy Survey

The SAMI galaxy survey (Croom et al. 2021a) provides over 3,000 galaxy observations AAT and SAMI with the AAOmega spectrograph (Section 2.6.3), which together provide optical spectra for individual spaxels across an image field. Median seeing for the survey was ~1.5 arcsec FWHM. Using an observation strategy based on dithering (Sharp et al. 2015), individual spectra were obtained for 0.5 x 0.5 arcsec spaxels for a galaxy over a 16.5 arcsec image diameter. Data products for DR3 of the survey (Croom et al. 2021a) include data cubes for galaxies containing the spectra for each spaxel, and maps determined from spectra of derived parameters such as star formation rate, stellar velocity and ionised gas velocity. The maps are of particular interest for comparison with results from observations of ISM distribution and kinematics (Chapter 3).

2.8.5 JINGLE

The JINGLE survey (Saintonge et al. 2018) provided observations at 850μm from JCMT (Section 2.5) for 193 galaxies to supplement Herschel observations in fitting cool dust emission models to spectra. The galaxies lie within the GAMA North Galactic Pole (NGP) and the equatorial regions, with redshifts in the range $0.01 \leq z \leq 0.05$ and stellar masses $>10^9 M_\odot$. The JINGLE sample galaxies are predominantly late-type and star-forming with a low number of early-types, because of selection criteria based on 3σ detection at 250μm and 350μm in H-ATLAS to increase the likelihood of detection at 850μm. JINGLE will also provide mm-wavelength CO line emission data for target galaxies obtained using JCMT, but at the time of submission of this work these results were not yet available.

2.8.6 xCOLD GASS

The xCOLD GASS survey (Saintonge et al. 2017) provides observations of molecular gas emission for 532 galaxies in the range $0.01 \leq z \leq 0.05$ from the IRAM 30m Telescope (Section 2.3), from which molecular gas masses were obtained for comparison with other galaxy properties. The survey was conducted in stages. The initial COLD GASS survey targeted 366 galaxies, randomly selected from SDSS with stellar mass $>10^{10}$ $M_{\odot}$ and redshift z between 0.025 and 0.05. All target galaxies are within the footprint of the ALFALFA atomic gas (HI) radio emission survey using the Arecibo radio telescope (Giovanelli et al. 2005), to allow atomic and molecular gas behaviour to be compared across the sample. Later, the lower mass limit was reduced to 10^9 $M_{\odot}$ by observing an additional 166 galaxies at redshifts between 0.01 and 0.02. Sample selection took no account of star formation rate or morphology. Figure 1.2 shows that galaxies with detected CO emission either lie on the SFMS and within the Green Valley (GV) discussed in Chapter 1, and the results are therefore of use in this work to show the behaviour of galaxies containing molecular gas within various parameter spaces.

2.8.7 Other Data Sources

Two additional surveys for molecular gas in galaxies are used for comparison with results from this work. The CO-CAVITY pilot survey (Domínguez-Gómez et al. 2022) obtained estimates of molecular gas mass for 20 void galaxies, which are in exceptionally sparse environments and should be evolving with little or no external influence. The sample galaxies have stellar masses in the range $\sim 10^9$ - 10^{10} $M_{\odot}$, and visual examination of SDSS gri images of the 13 galaxies with detected molecular gas masses (i.e. not upper limits) revealed flocculent or faint spiral features within them. However, two of the Void galaxies, VGS31 and VGS31a (a companion to VGS31), are close by and appear to have interacted gravitationally. In contrast, Davis et al. (2015) studied the molecular gas content of bulge-dominated ETGs with substantial dust lanes as evidence of recent minor

merger activity. The 15 ETGs with detected CO emission from this study are used as a contrast to those from the CO-CAVITY survey, which should have avoided such activity. Both of these surveys were conducted recently with the IRAM 30m Telescope and the same instrumentation (Section 2.3) as the new observations in presented in Chapter 7, which means that all reported or observed line emission fluxes can be converted to molecular gas masses using the same techniques.

Two significant surveys which provide observations of dust and molecular gas are not used in this work at present, but can be considered at a later stage. The Herschel Reference Survey (HRS, Boselli et al. 2010) used Herschel to map cool dust emission from nearby galaxies between 15 and 25 Mpc distant, and observations of molecular gas emission are also available from various sources (Boselli et al. 2014, and references within). The ATLAS3D survey (Cappellari et al. 2011) used Herschel to survey cool dust emission from a complete sample of 260 ETGs to a distance of 42 Mpc, with cool dust and molecular gas masses available (Young et al. 2011; Smith et al. 2012). Future work should concentrate on ensuring that dust and molecular gas masses from these surveys and the ones currently discussed are all derived using consistent approaches before making comparisons. Also, the DustPedia[15] project provides catalogue data for many galaxies observed with Herschel, and may prove useful for future comparative work.

[15]http://www.dustpedia.astro.noa.gr/

Chapter 3

Molecular Gas Distribution and Kinematics in ALMA-Observed Dusty Local Early-Type Galaxies

3.1 Introduction

As explained in Chapter 1, the distribution of cool ISM in Early-Type Galaxies (ETGs) can provide clues on the evolutionary mechanisms responsible for their formation from Late-Type Galaxies (LTGs). To investigate this, five dusty ETGs in the local Universe were selected for observation at mm wavelengths by ALMA (Section 2.2), with the observational results published in an initial paper (Sansom et al. 2019) for which this author was a co-author. The observations provided resolved (~0.7 arcsec FWHM) images across a range of frequencies of the cool dust emission and ^{12}CO[2-1] emission (rest frequency 230.5 GHz). The work presented in this Chapter is an analysis of the observational results, to investigate how they can be used to indicate evolutionary mechanisms at work. The investigations concentrated on fitting simplified kinematic models to the observations for three of the ETGs, to obtain structural and velocity information and to subtract from the

observations to reveal any additional features. The analysis also included comparisons with spatial and kinematic information from IFU observations using the SAMI instrument (Section 2.8.4), which provided information on the distribution and kinematics of stars and ionised gas. An analysis of the observations for the remaining two ETGs, which were unsuitable for such modelling, is also provided.

This work was published in December 2022 in the Monthly Notices of the Royal Astronomical Society (Glass et al. 2022). The text below is taken from Section 2 onwards of the paper. Throughout this Chapter, continuum millimetre-wavelength emission detected by ALMA is assumed to be from the Rayleigh-Jeans spectrum of cool dust unless stated otherwise.

3.2 Data and Methods

3.2.1 Observational Data

Selections of dusty ETGs for ALMA observation are described in (Sansom et al. 2019). The ALMA-observed ETGs (GAMA64646, 177186, 272990, 622305, 622429) are from a complete sample within the GAMA equatorial regions (Agius et al. 2013). All are in low-density environments, with surface densities to the fifth nearest neighbour in the range 0.06 - 0.4 Mpc^{-2} from the GAMA DR3 (Section 2.8.1) catalogue EnvironmentMeasuresv05. They were selected as being amongst the dustiest within the ETG sample, with estimated Herschel-detected dust masses in the range $2 – 8 \times 10^7$ $M_\odot$ (Sansom et al. 2019, see their figure 2). They were therefore expected to contain significant masses of cool molecular hydrogen, based on previously determined gas-to-dust mass ratios for ETGs (e.g. Smith et al. 2012). The ETGs were also selected to have ellipticity > 0.2 to ensure that line-of-sight velocity profiles can be recovered throughout the ETGs, and effective optical radii of 4" < Re < 10" to maximise the likelihood of observing ISM distribution with ALMA with a single pointing. An emission line width of 150 km s^{-1}

was assumed for observation planning to estimate emission line strengths, along with an assumed ISM spatial extent of half the optical effective radius (Davis et al. 2013).

Selection of the observed ETGs from their original parent sample was partly on the basis of smooth morphology and the absence of strong active galactic nucleus (AGN) activity (Agius et al. 2013). Table 3.1 shows key properties of the ETGs from GAMA DR3 catalogues. Since these ALMA observations, deeper and sharper optical images have become available from the Kilo-Degree Survey (Section 2.6.4). Figure 1 shows r-band, log-projection, optical images from KiDS, for the five ALMA-observed ETGs, and the ALMA-detected molecular gas and dust (Sansom et al. 2019). Two of the ETGs (GAMA64646, 622305) have faint spiral structure, which is apparent in the deeper KiDS images but not in SDSS (Section 2.6.2) images used originally for morphological classification. In addition, optical line emission diagnostics (Section 4.3.2) derived from more recent GAMA DR3 catalogues show that GAMA622429 is associated with strong AGN activity (Figure 3.2). Nonetheless, these galaxies are of interest in this study to examine evolutionary mechanisms at work to form ETGs. GAMA64646 and 272990 are shown in Figure 3.2 as having weak AGN activity, but this has not affected the detection of widely-distributed massive molecular gas reservoirs. None of the five targets are in the star-forming region of Figure 3.2.

Figure 3.1 also shows that GAMA64646 has a faint tidal tail to the left, which is not associated with galaxy GAMA64647 (redshift ~0.12) at the apparent end of the tail. GAMA272990, although classified as an elliptical using SDSS images, appears to have faint disc-like structure, slightly asymmetric, with faint ring features within it. GAMA622305 appears to be elongated towards the lower left of the image, and GAMA622429 has signs of disturbance within lower portion of the disc.

The ALMA-detected massive molecular gas reservoirs within three of the ETGs (GAMA64646, 272990, 622429) have greater detected spatial extents (11 – 18") than predicted at the observation planning stage. A less massive region of molecular gas was detected in GAMA622305, located off-centre by ~4 arcsec but coincident with the galaxy

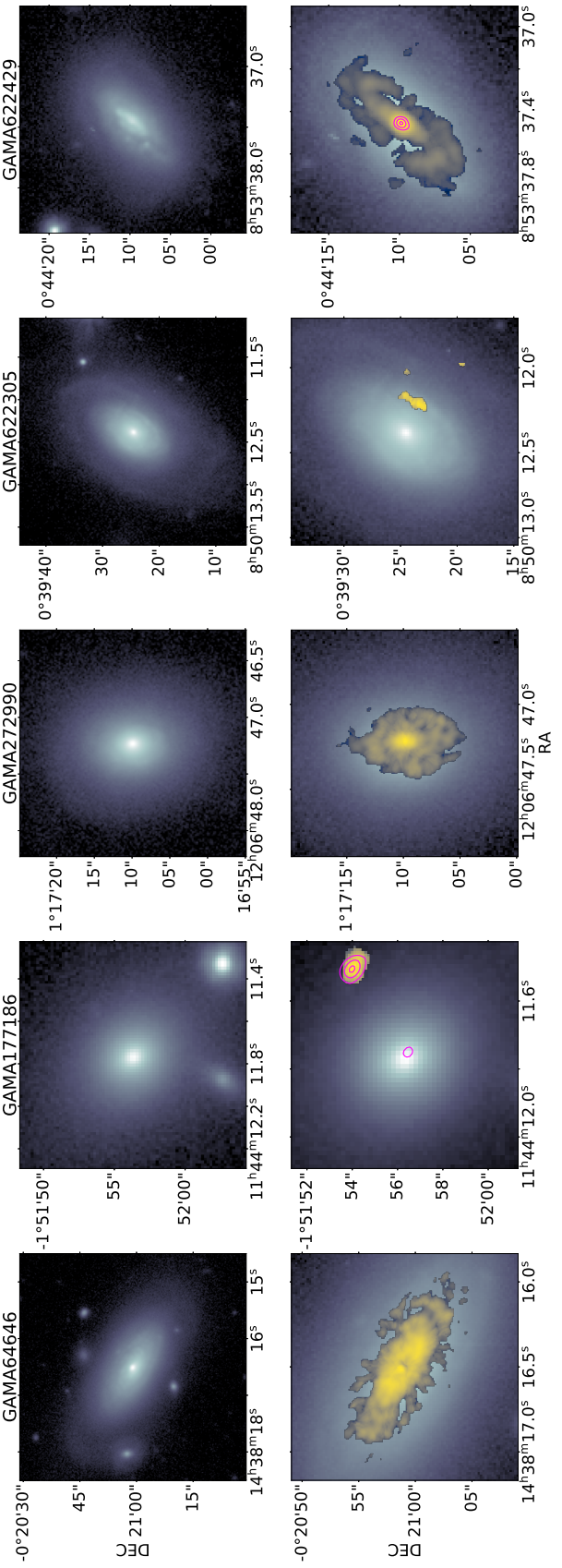

Figure 3.1: ALMA-observed dusty ETGs from Sansom et al. (2019). *Upper:* log-normalised KiDS r-band images of the ALMA-observed ETGs. *Lower:* zoomed in, ALMA-detected dust emission (magenta contours) and log-normalised ^{12}CO[2-1] emission (yellows) overlain.

Table 3.1: Properties of the ALMA-observed ETGs. Optical effective radii from GAMA DR3 were obtained from fitting a single Sérsic surface brightness profile (Equation 3.1) to optical images. Dust mass estimates from GAMA DR3 were estimated using MAGPHYS (Section 2.7.3). Detected molecular gas masses are from Sansom et al. (2019). The molecular gas mass for GAMA177186 is for the offset object, assuming ^{12}CO[2-1] emission at the redshift of GAMA177186.

ETG	Morphology	Redshift (Heliocentric)	$\log_{10}$(Stellar Mass ($M_\odot$))	$\log_{10}$(Molecular Gas Mass ($M_\odot$))	$\log_{10}$(Dust Mass ($M_\odot$))	Optical (r-band) Effective Radius (arcsec)
GAMA64646	S0-Sa	0.0369	$10.89^{+0.00}_{-0.08}$	9.51±0.03	7.54±0.05	9.92±0.06
GAMA177186	E	0.0476	$10.30^{+0.08}_{-0.15}$	8.54±0.06	$7.23^{+0.08}_{-0.13}$	3.19±0.10
GAMA272990	E	0.0411	$10.53^{+0.08}_{-0.05}$	9.38±0.03	$7.38^{+0.07}_{-0.04}$	3.80±0.03
GAMA622305	S0-Sa	0.0426	$10.62^{+0.01}_{-0.04}$	$7.81^{+0.08}_{-0.10}$	$7.63^{+0.06}_{-0.08}$	4.66±0.02
GAMA622429	S0-Sa	0.0409	$10.51^{+0.13}_{-0.04}$	9.85±0.03	$7.63^{+0.01}_{-0.00}$	4.31±0.03

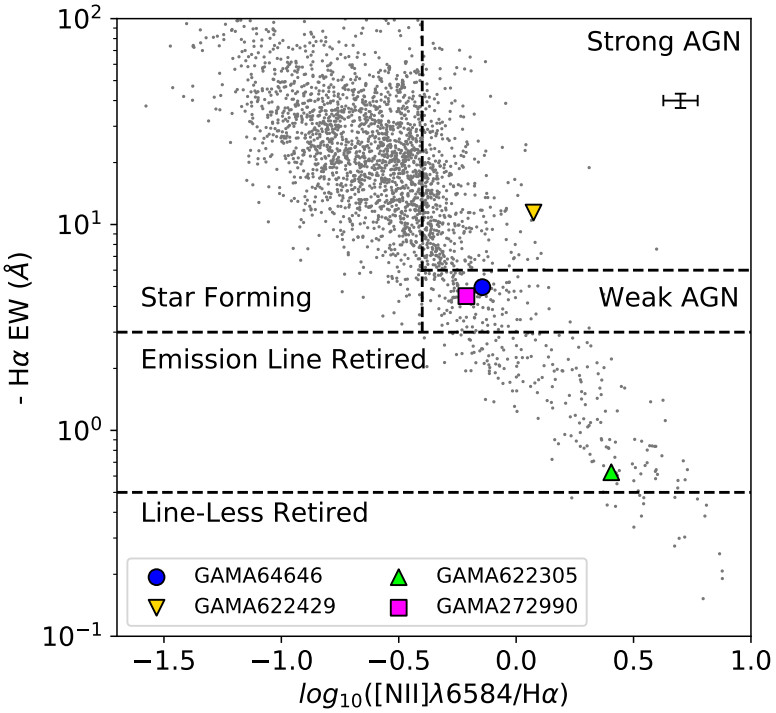

Figure 3.2: Diagnostic (WHAN) plot for AGN activity, star formation and galaxy retirement using Hα equivalent width versus [NII]λ6584/Hα (Section 4.3.2), showing the characteristics of the ALMA-observed ETGs. GAMA177186 is not shown because its spectrum does not include suitable emission lines (i.e. it is a line-less retired galaxy). Grey points show a new complete galaxy sample from the GAMA equatorial regions (redshift z $\leq$ 0.06, see Chapter 4). Demarcations and terminology for regions on the diagram are from Herpich et al. (2016).

disc along the line of sight. Emission line widths (400 – 500 km s^{-1}) are wider than than predicted but not unexpected (e.g. van de Voort et al. 2018). Line emission was detected in the observation for GAMA177186, but in a compact region ~4 arcsec from the centre.

Dust detection was challenging with all these observations, because of the maximum recoverable angular scale (MRS, Equation 2.6) of ~10 arcsec achieved by the array configuration used. Any dust distribution with greater angular scales than this would not be detected. The surface brightness of the total dust emission is reduced if the dust is more widely distributed than assumed during observation planning, needing longer observation times to achieve detections. Centrally-concentrated continuum emission (presumably dust) was detected for GAMA177186 and GAMA622429, and a compact region of continuum emission was detected in the same location as line emission in the observation of GAMA177186 (Sansom et al. 2019).

Observations and data from SAMI (Section 2.6.3) are also used in this work. Kinematic maps derived from optical spectra for stars and ionised gas are available for all ALMA-observed ETGs except GAMA177186, which allow the alignment of molecular gas and these components to be assessed. Maps of derived star formation rate (SFR) are also available, for comparison with molecular gas location and predicted star formation potential from molecular gas properties (Sections 3.3.2 and 3.3.3). These SFR maps are acknowledged as being clean but not complete, such that confirmed regions of star formation are highlighted but others may have been missed. This is because methods to separate star formation effects in optical spectra from other excitation mechanisms are not robust. Star formation rate is estimated from Hα emission, which is also associated with AGN activity and supernova shockwaves, and the effects could not be separated at the time (Medling et al. 2018).

3.2.2 Kinematic Modelling

Idealised axisymmetric kinematic models were constructed for the three detected massive molecular gas reservoirs using KinMSPy (Section 2.7.1) to highlight deviations from symmetrical distributions within the data and to provide information on rotational velocity and velocity dispersion. Initial modelling with KinMSPy used point sources distributed according to axisymmetric Sérsic surface brightness profiles, i.e. surface brightness (brightness per unit observed surface area) as a function of radius from the galaxy centre (Equation 3.1, Sérsic 1963).

$$\ln(S) = \ln(S_0) - \left(\frac{R}{r_0}\right)^n \tag{3.1}$$

where S is surface brightness at radius R, S_0 is surface brightness at the centre, r_0 is a radial scaling factor and n is the Sérsic index. Surface brightness profiles of this form are derived from actual galaxy profiles. For example, a Sérsic index of ∼1 is typical of disc galaxies, while an index of ∼4 is associated with elliptical galaxies or bulges.

All kinematic position angles are oriented such that rotation velocities run from negative to positive. Equation 3.2 shows the empirical arctangent-based model for radial velocity used, which gives a rapid rise in rotation velocity from the galactic centre followed by a relatively constant velocity (e.g. van de Voort et al. 2018).

$$v_c = \left(\frac{2v_{\rm flat}}{\pi}\right)\arctan\left(\frac{R}{R_0}\right) \tag{3.2}$$

where v_c is the circular velocity (km s^{-1}) at radius R (arcsec), $v_{\rm flat}$ is the far-field circular velocity (km s^{-1}) and R_0 is a radial scaling factor (arcsec).

In some cases the fitted far-field circular velocity may be greater than the maximum observed velocities e.g. derived from spectra, because the velocity profile in Equation 3.2 continues to increase weakly beyond the extent of the galaxy. Velocity dispersion

Table 3.2: Optimal ellipse mask sizes and ALMA-observed ^{12}CO[2-1] emission fluxes for GAMA64646, 272990 and 622429.

Galaxy	Major Diameter (arcsec)	Minor Diameter (arcsec)	Position Angle (°)	^{12}CO[2-1] Flux (Jy km s^{-1})
GAMA64646	19.2	12.0	62	35.0 ± 3.5
GAMA272990	17.3	9.4	3	21.0 ± 1.4
GAMA622429	13.0	10.3	135	61.9 ± 3.9

was also applied to the model, in this case as a spatially constant value everywhere in the molecular gas disc. Finally the models were convolved with a synthesised beam derived from the ALMA observation, to allow comparison of model and data.

To avoid the fitting of models to observational data away from the ETGs, where primary beam correction during ALMA data reduction (Section 2.1) may amplify noise towards the edge, a unique elliptical mask per ETG capturing the ^{12}CO[2-1] emission was applied to each velocity frame for data and model before calculating χ^2 or log likelihood. A curve-of-growth approach was used to optimise the spatial dimensions of elliptical masks. Initial elliptical masks were created based on the dimensions and position angles of molecular gas in zeroth-order moment maps, and a multiple of the dimensions was found which led to a maximum total flux while minimising the mask area. Table 3.2 shows the resultant dimensions and position angles of the masks, along with the flux values determined. Uncertainties in the flux values include 6% calibration uncertainty for the ALMA flux calibrators[1] added in quadrature. The total fluxes are in agreement with the fluxes derived in Sansom et al. (2019) within errors, so the molecular gas masses in Table 3.1 are unchanged.

The parameters for a model data cube can be adjusted to fit an ALMA observation. Initial fits were achieved using SCIPY.OPTIMIZE.MINIMIZE to find a minimal χ^2. The

[1] https://almascience.eso.org/sc/

Nelder-Mead algorithm (Nelder & Mead 1965) was used for fitting, which is a direct search method for the minimum result within a multidimensional parameter space which avoids the need to compute derivatives. A minimal rectangular volume for fitting was selected around the emission region, to contain the optimal elliptical masks determined by curve-of-growth (Table 3.2). A representative RMS noise per pixel (in Jy beam^{-1}) was determined from velocity frames outside of the emission region but within the optimal elliptical mask. The number of point sources for axisymmetric disc components was set to a default value of 100,000 within KinMSpy, which was found to give similar results to simulations with greater numbers of points while retaining smoothness in zeroth order moment maps. The centroids for the spatial and velocity axes were also fitted, to ensure that uncertainties in these parameters are correctly reflected in uncertainties for others. These were found to have uncertainties less than half the size of the pixels or velocity bins.

The Python implementation of GAStimator (Section 2.7.1), designed for use with KinMSpy, was then used to refine the fit obtained using scipy.optimize.minimize and to determine posterior distributions for the model parameters. Flat priors were used, with wide but physically realistic upper and lower limits. Initial estimates for parameters were based on fitted parameters from scipy.optimize.minimize.

When fitting models to data with many points (in this case, up to ~600,000), the variance in χ^2 becomes large if the noise within the data is used for fitting (van den Bosch & van de Ven 2009), resulting in extremely narrow posterior distributions. The approach taken to avoid this was to scale the noise to achieve uncertainties that take the variation in χ^2 into account. A 2-stage approach was used, which first scales down the RMS noise within the data to achieve a reduced χ^2 of ~1 for the model fit (using the result from scipy.optimize.minimize) and then multiplies it by an additional factor of $(2N)^{1/4}$, where N is the number of data points being fitted (Mitzkus et al. 2017; Smith et al. 2019). The use of the number of fitted pixels for N ensures that the factor is conservatively large, because the pixels oversample the spatial plane in the data compared to a beam area of ~36 pixels.

Estimates of parameter uncertainties from model fitting are then conservatively large. It is also possible to apply a covariance matrix within the calculation of log likelihood, which accounts for the correlated uncertainty between pixels A detailed discussion of this approach is provided by Tsukui et al. (2022), and Smith et al. (2019) apply this to their model fitting as well as the inflation of RMS noise described above. However the number of elements within this covariance matrix is N^4, and the computer memory needed to invert it becomes rapidly excessive with increasing number of pixels[2]. In practice the contribution to errors from variance in χ^2 dominates over correlated pixel-to-pixel variation (Davis et al. 2020), so the covariance matrix is not used.

3.3 Results

3.3.1 Kinematic Modelling

Figure 3.3 shows zeroth order moment maps for GAMA64646, 272990 and 622429, including ALMA data, fitted models and residuals (data - model) for ALMA-observed ^{12}CO[2-1] emission. Maps for data and residuals have been masked to highlight faint emission, by creating masks for each spatial frame in the data cube to capture emission above a certain level (e.g. >1.5 times the RMS noise), and using the masked cube for analysis (Dame 2011; Davis et al. 2013). This process avoids dilution of faint emission where present in spatial frames per velocity bin by noise in others. Figure 3.4 shows first-order moment maps for masked data and models, with velocity differences between data and models also shown. Figure 3.5 shows azimuthally-averaged surface brightness plots, position-velocity (PV) diagrams for a 1-beam (5-pixel) strip along major axes and spectra for each galaxy. Findings for each galaxy are discussed in turn below. It is assumed that the emission is from optically thin CO, which is consistent with molecular gas being broken up into many smaller clouds (the "mist model", Bolatto et al. 2013). Each cloud

[2]https://web.ipac.caltech.edu/staff/fmasci/home/astro_refs/PixelNoiseCorrelation.pdf

behaves as if it is optically thin. Larger clouds are likely to suffer from self-absorption of the CO emission and become optically thick, such that the observed emission may only arise from the surface of the cloud (Wilson et al. 2009). Although optically-thick emission can be used as a tracer of the presence of CO, quantifying the total ^{12}CO[2-1] emisson from the cloud will be underestimated.

The ALMA data for GAMA64646 and GAMA272990 were fitted with a model based on a single axisymmetric disc with a Sérsic surface brightness profile and a single parameter for velocity dispersion. Total fluxes were fixed at the value in Table 3.2. Table 3.3 shows the parameter values and 1σ uncertainties using MCMC fitting of models to data.

Attempts were also made to model additional features (central unresolved source and outer ring) using KinMSpy, introducing six additional parameters. Small reductions ($\sim$1% and $\sim$3%) in χ^2 were achieved, with χ^2 approximately equating to Bayesian Information Criterion (Section 2.7.1). The very small reduction in BIC indicates a slight preference for the more complex model. However, attempts to extract posterior distributions for the additional parameters using the increased RMS noise discussed above were not successful, with uncertainties at least as large as the fitted parameters. The same effect was found when attempting to fit an unresolved central source only along with a disc. The single-disc model is therefore discussed below.

GAMA64646

Comparison of model and data indicate that the molecular gas disc in GAMA64646 is relatively axisymmetric. Symmetry is apparent in the zeroth and first order moment residual maps, the PV diagram and the spectrum (Figures 3.3, 3.4 and 3.5). The arctangent-based rotation velocity profile model accounts well for the profile in the data, apparent in the first-order moment maps and the PV diagram. The residual map and the elliptical azimuthal average plot both indicate that there are weak additional features present. A

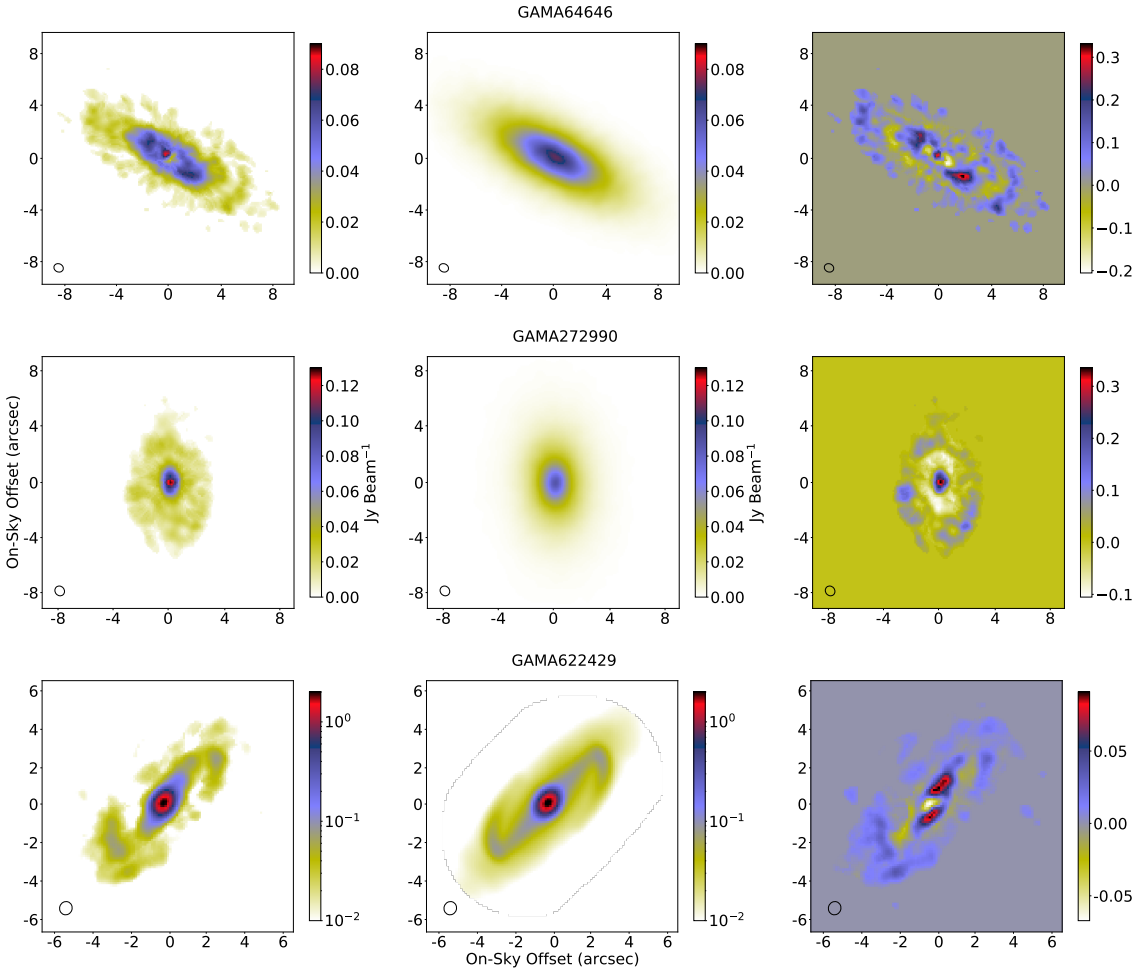

Figure 3.3: Zeroth order moment maps for (*left*) masked data, (*centre*) model and (*right*) masked fractional residual ((data - model)/maximum value of data) for (*top*) GAMA64646, (*middle*) GAMA272990, (*bottom*) GAMA622429 ^{12}CO[2-1] emission. Images for GAMA622429 are log-normalised and truncated at 0.01 Jy Beam^{-1}. Synthesised beam FWHM is shown in black. Colours indicate emitted flux in Jy beam^{-1} or residual.

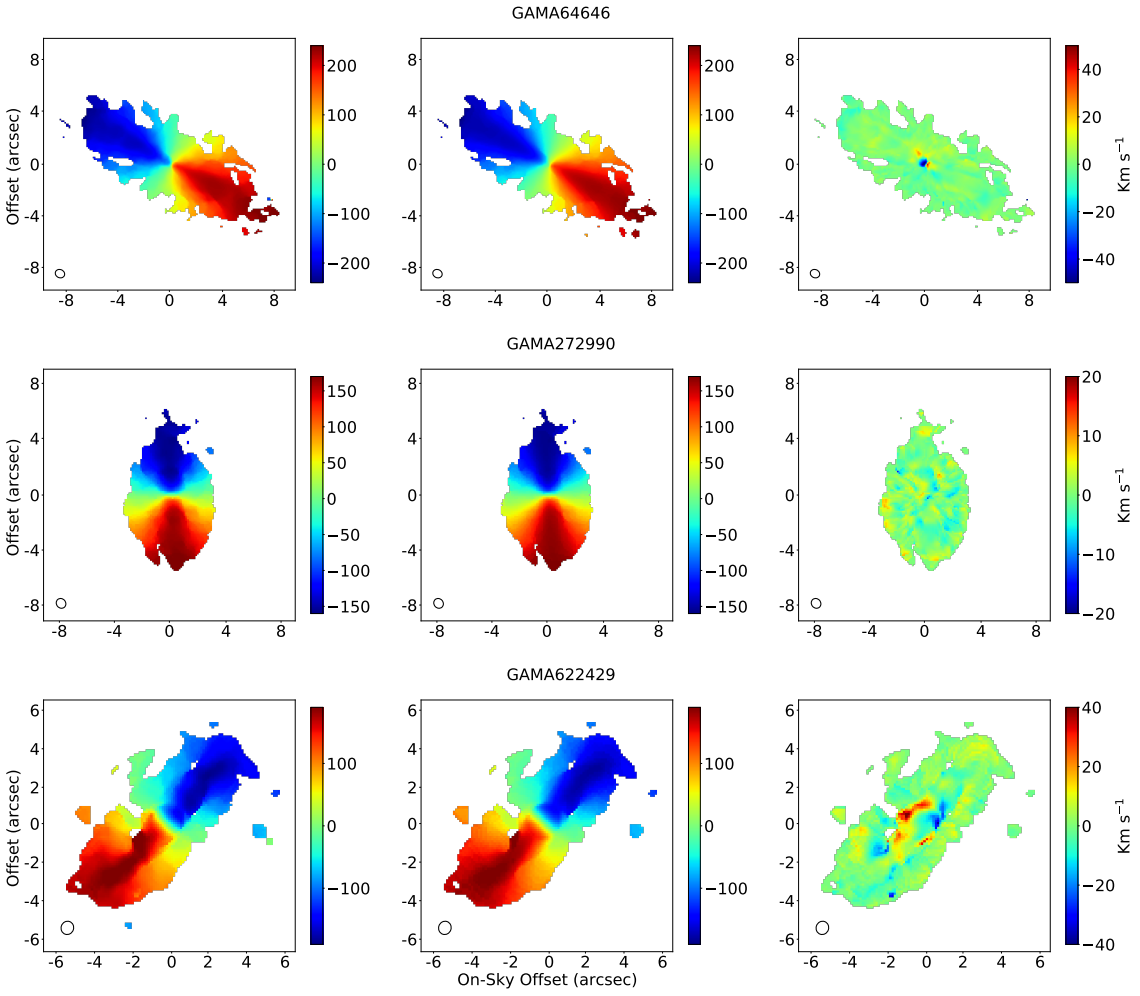

Figure 3.4: First order moment maps for (*left*) masked data, (*centre*) masked model and (*right*) masked velocity difference (data - model) for (*top*) GAMA64646, (*middle*) GAMA272990, (*bottom*) GAMA622429 ^{12}CO[2-1] emission. Synthesised beam FWHM is shown in black.

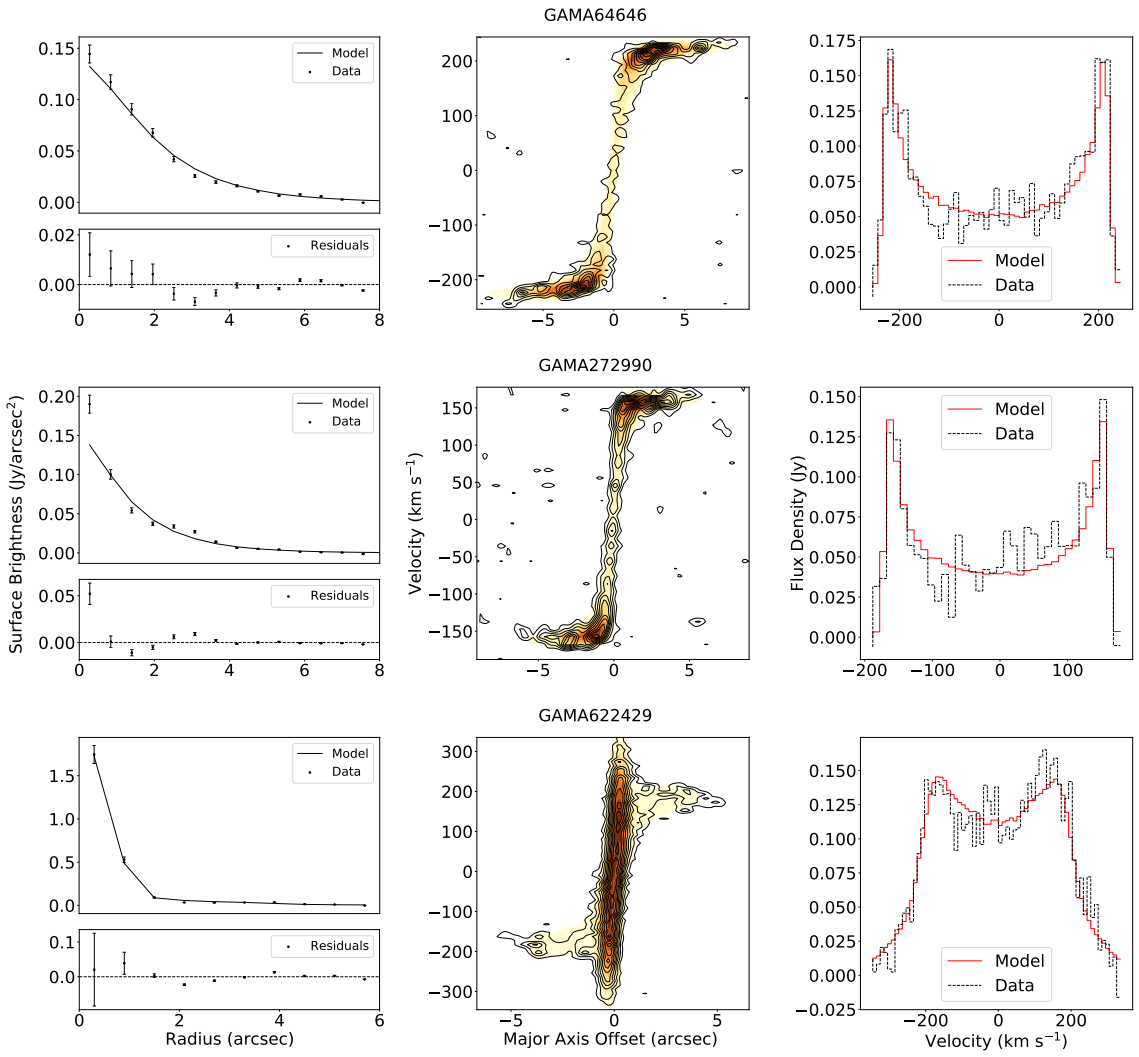

Figure 3.5: Diagnostic plots for (*top*) GAMA64646, (*middle*) GAMA272990, (*bottom*) GAMA622429. *Left*: Azimuthal average surface brightness profiles. *Centre*: Position-Velocity (PV) Diagrams, data shown as contours, model shown as colour. *Right*: spectra, derived from the total flux per velocity frame within the elliptical masks.

Table 3.3: Parameters for fitted molecular gas disc models with a Sérsic surface brightness profile for GAMA64646 and GAMA272990. Spatial and velocity centroids were also fitted but are not shown.

Parameter	GAMA64646		GAMA272990	
	Prior Range Lower/Upper	Value	Prior Range Lower/Upper	Value
Kinematic position angle (°)	40/90	62.0 ± 0.5	-7/13	3.49 ± 0.81
Inclination (°)	45 /85	66.6 ± 0.9	35/75	50.9 ± 1.9
Max. circular velocity (km s^{-1})	150/350	250.9 ± 3.0	100/300	211.1 ± 5.4
Velocity scaling factor (arcsec)	10^{-6}/0.5	0.18 ± 0.05	10^{-6}/1.5	0.047 ± 0.02
SB profile scale factor (arcsec)	0.01/6	3.9 ± 0.5	0.01/7	1.59 ± 0.60
Sérsic index	0.05/3	$0.70\ ^{+0.11}_{-0.09}$	0.05/4	$1.02\ ^{+0.25}_{-0.20}$
Velocity dispersion (km s^{-1})	1/30	$7.1\ ^{+1.3}_{-1.1}$	1/30	$6.0\ ^{-1.2}_{-1.0}$

bright, unresolved central feature creates additional surface brightness at the centre, and bright features away from the centre are suggestive of an inner ring-like structure ~4 arcsec from the centre. An outer ring also appears to be present in the residual map, and is apparent as a slight bump in the azimuthal average surface brightness profile at ~6 arcsec. Perturbations by interaction with another galaxy can generate ring-like features, such as collisional rings or pseudo-rings. However, rings formed by resonance effects (4:1 Lindblad resonance for inner rings) dominate observed rings in galaxies (Buta & Combes 1996).

The first order moment map set for GAMA64646 (Figure 3.4) shows a central feature in the residual velocity map, with relative line-of-sight velocities reduced at the actual centre and increased just outside of this region. The features could be explained by the presence of a weak AGN within this ETG (Figure 4.2), creating its own orbital or jet-like flows within the surrounding molecular gas at relatively close range.

The PV diagram for GAMA64646 shows minor regions of flux at low offset from the centre but high velocity which are not fitted by the single-component model. The central feature appears to be unresolved, which places an upper limit on its diameter (1 beam, ~5 pixels) of ~450 pc. It might be a small concentration of molecular gas around a supermassive black hole (SMBH), consistent with the presence of a weak AGN (Figure 4.2). The profiles in Figure 3.5 show that the emission from the central feature does not dominate the overall molecular gas emission.

The inner ring includes two diametrically opposed bright patches, apparent in the residual zeroth-order map. These could be an effect of observing the inclined ring, where an apparent overlap of the front and rear portions of the ring is viewed along the line of sight. They could also be an effect associated with a bar, where the bar ends interact with the inner ring (see Buta & Combes (1996) for examples in optical images). The zeroth order moment map for GAMA64646 (Figure 3.3) shows no indication of a bar. Instead, an annular region partially depleted in molecular gas completely encircling the bright central feature is apparent. A former bar could have been disrupted (e.g. Comerón et al. 2014)

possibly by an interaction, or molecular gas could have been funnelled by a bar towards the centre creating the bright central feature. Overall, GAMA64646 may have undergone a past perturbation (e.g. >100 Myr ago, van de Voort et al. (2018)), and has settled into its observed configuration.

GAMA272990

GAMA272990 is classified visually as an elliptical galaxy within GAMA II. The ALMA observation studied here shows an embedded molecular gas disc with an effective morphological classification of S0 at this wavelength, but but this does not affect the visual morphology. The molecular gas disc has an asymmetric distribution between North and South is apparent in the zeroth order moment map (Figure 3.3), with more emission in the lower part of the image than the upper. The spectrum (Figure 3.5) shows a noticeable tilt, with flux density increasing from negative to positive velocity, consisent with the spatially asymmetric emission. There is also an irregular emission region at the North of the molecular gas disc, apparent in the zeroth order moment map. The first order moment maps (Figure 3.4) shows very good agreement between the observed and model velocities, with only minor irregularities. The PV diagram (Figure 3.5) shows that the model with the arctangent-based circular velocity profile (Equation 3.2) fits the data well. The azimuthally-averaged surface brightness plot (Figure 3.5) shows that the single Sérsic profile disc model underestimates the emission at the centre of the ETG and at a region ~ 3 arcsec from the centre. The residual zeroth order moment map (Figure 3.3) shows that there is a brighter central feature and a ring-like structure at ~3 arcsec. However, the central feature appears to be unresolved, and as with GAMA64646 this could be a concentration of molecular gas with an upper limit on radius of 1 beam (~500pc). GAMA272990 has a weak AGN (Figure 4.2), consistent with this finding. The profiles in Figure 3.5 show that the emission from the central feature does not dominate the overall molecular gas emission.

The KiDS r-band image (Figure 3.1) shows that GAMA272990 has the optical characteristics of an elliptical galaxy beyond the embedded CO disc (Figure 3.1). This elliptical structure could indicate a past energetic disturbance, randomising previously circular stellar orbits and forming a stellar halo. One possibility for the recent evolution of GAMA272990 is the merger of two gas-rich disc galaxies, forming an elliptical with an embedded gas disc with the combined rotational energy of the gas from both progenitors (Ueda et al. 2014). It is also possible that the disc is the result of a merger between an existing elliptical galaxy and a gas-rich object. It is likely that GAMA272990 was disturbed relatively recently, causing molecular gas to settle into the observed disc/ring structure and creating a lop-sided distribution of molecular gas. Molecular gas has accumulated around the centre of the ETG, forming the bright unresolved central region which could be associated with a central SMBH.

GAMA622429

The zeroth order moment map for GAMA622429 (Figure 3.3) shows a bright central feature resembling a nuclear ring, a bar and faint spiral arm structure (Figure 3.1). However, its visual morphology is consistent with an S0 ETG and is unchanged. The apparent features were modelled by positioning point sources to create these structures, using the inClouds functionality in KinMSpy. Point sources were distributed along loci defined by ellipses, with a whole ellipse perpendicular to the bar used for a nuclear ring and opposite quadrants of ellipses used for a bar and spiral arms. Davis et al. (2013) show examples of models of bar and spiral structures (based on logarithmic spiral loci) in their Figure 10. Sellwood & Wilkinson (1993, their sections 4, 5 and 6) provide further information on galactic bars, their associated stellar orbits and their relationship to observed molecular gas distributions modelled by Athanassoula (1992b) which form the basis of the point source model in Figure 3.6. The bar major radius a and minor radius b define all these features, with b also used for the nuclear ring major axis and a for the spiral arm major axis. Separate factors n_1 and n_2 were applied to a and b to define the minor axis

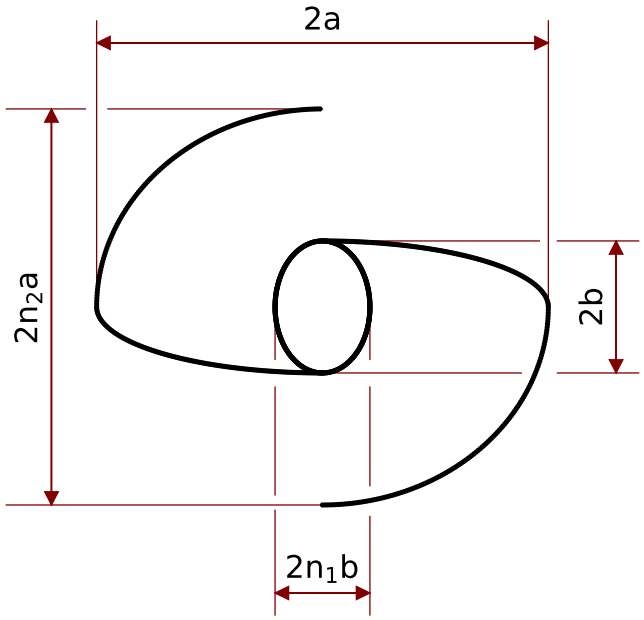

Figure 3.6: Plan view of point-source model for nuclear ring, bar and spiral arms using elliptical pathways. All dimensions are defined by the bar major and minor radii, a and b, with scaling parameters n_1 and n_2.

for the elliptical loci of the nuclear ring and the spiral arm. The value for n_2 was fixed at 1.72 as indicated by initial model fitting using SCIPY.OPTIMIZE.MINIMIZE, because initial MCMC-based model fitting shows this parameter to be highly uncertain. Point sources were distributed uniformly along their loci, using an empirical model to position sources equally around ellipses or elliptical segments (Appendix A). These additional components were modelled with 100,000 point sources in total, distributed amongst the three features in proportion to their emitted flux. Bisymmetric flow was applied to the cloudlets within the bar region using the description of Spekkens & Sellwood (2007) as implemented in KINMSPY, defined by radial and tangential velocities in relation to the galaxy centre and the a and b parameters for scaling. This was superimposed on an axisymmetric radial velocity profile as described in Section 3.2.2. A fixed position angle of 6° was also applied to the nuclear ring component, as indicated by initial fitting but with high uncertainty.

The resultant fitted model on its own (using SCIPY.OPTIMIZE.MINIMIZE) was only partially successful, leaving an unfitted double-horned feature in the spectrum suggestive of an underlying rotating disc (Figure 3.7, *upper*). Attempts to fit an axisymmetric disc

surface brightness profile based on Equation 3.1 were equally unsuccessful. The model attempted to fit the central bright region with a near edge-on disc, possibly emulating a bar-like structure, and also failed to fit the double-horned feature (Figure 3.7, *lower*). The kinematic position angle (PA) of the fitted structures were found to be ∼315°, consistent with the PA of the overall molecular gas distribution for this ETG. Figure 3.3 confirms that the molecular gas bar and the major axis of the overall molecular gas distribution are fortuitously aligned. A rotating molecular gas disc with a Sérsic surface brightness profile and a common PA for all features was therefore added to the cloud model, using the approach described in Section 3.2.2. Attempts to fit a separate PA for the bar compared to the disc will lead to high uncertainty in the result because of the high inclination of the ETG.

Table 3.4 shows the parameter values and 1σ uncertainties using MCMC fitting of this refined model to the data. The PV diagram for data and model (Figure 3.5) shows that this model fits the data well. The zeroth order moment map for residuals (Figure 3.3) shows a slight decline in bar surface brightness with radius compared to the flat profile of the model, similar to profiles in optical images for bars in SB0 galaxies (Sellwood & Wilkinson 1993, and references therein). This is also reflected in the model for the nuclear ring, which is elongated along the length of the bar (n_1 = 2.2). This effect has probably led to an over-estimate of the flux allocated to the nuclear ring model, by including flux from the inner regions of the bar. The total flux of the model is $64.0^{+5.9}_{-5.7}$ Jy km s^{-1}, which agrees with the value from curve of growth analysis within the uncertainties (Table 3.2). Almost half of this emission arises from the nuclear region of the ETG.

The first order moment maps for GAMA622429 (Figure 3.4) show general agreement between velocities from observation and the model, but significant features (approximately beam size) are present in the residual map forming arc-like structures around the centre. Only the feature above the centre in the zeroth order moment residual map is consistent with the equivalent feature in the first order moment residual map. The features could be orbiting around or falling into the centre of the ETG, where there is a strong

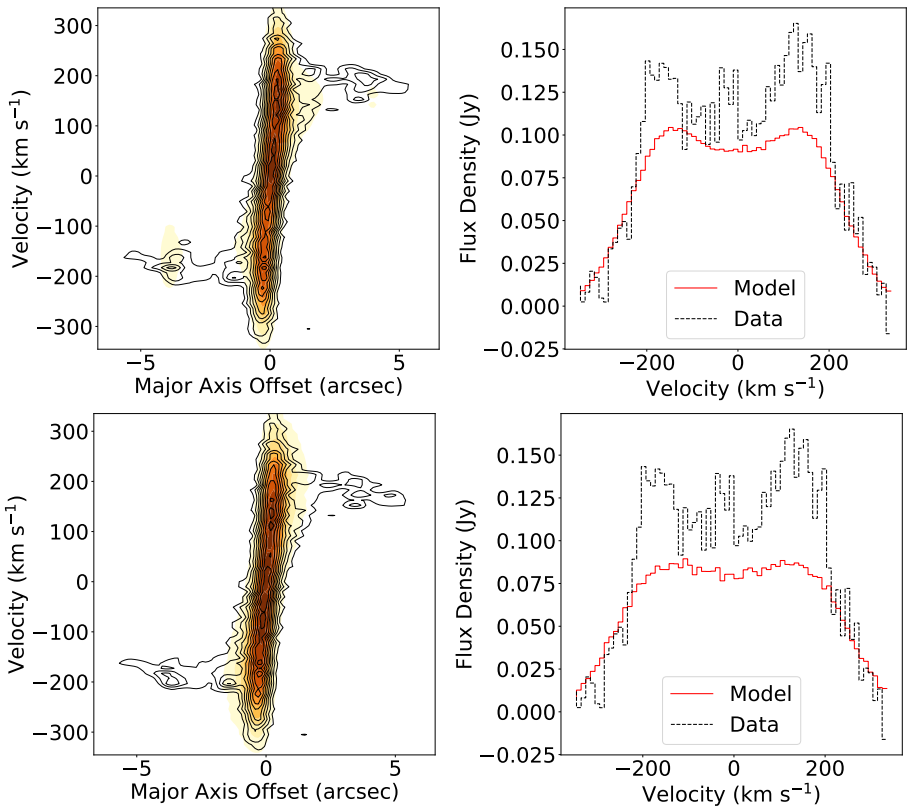

Figure 3.7: PV diagrams (data as contours, model in colour) and spectra for GAMA622429 fitted with a ring + bar + spiral arms model (*upper*), axisymmetric disc with a Sérsic surface brightness profile (*lower*), see Equation 3.1.

Table 3.4: Parameters for a molecular gas central ring, bar and spiral arm structure plus an underlying disc with a Sérsic surface brightness profile for GAMA622429.

Common Parameters	Prior Range Lower/Upper	Value
Kinematic position angle (°)	290/350	316.8 ± 1.5
Inclination (°)	50/85	$72.3\ ^{+2.3}_{-2.9}$
Far-field circular velocity (km s^{-1})	160/260	$207.8\ ^{+9.1}_{-8.2}$
Vel. profie scale factor (arcsec)	0.01/1	$0.12\ ^{+0.15}_{-0.08}$
Parameter (Nuclear ring, bar, spiral arms)	**Prior Range**	**Value**
Line flux (nuclear ring) (Jy km s^{-1})	1/40	$28.5\ ^{+1.6}_{-1.8}$
Line flux (bar) (Jy km s^{-1})	0.01/50	$3.5\ ^{+2.8}_{-2.3}$
Line flux (spiral arms) (Jy km s^{-1})	1/16	$3.4^{+1.8}_{-1.5}$
Velocity dispersion (km s^{-1})	30/170	$99.1\ ^{+11.8}_{-16.8}$
Bar radius (a) (arcsec)	2/6	$3.8\ ^{+0.4}_{-0.3}$
Nuclear ring major radius (b) (arcsec)	0.001/1	0.23 ± 0.07
Nuclear ring minor radius scale factor (n_1)	0.001/6	$2.2\ ^{+0.7}_{-0.9}$
Bar radial velocity (km/s)	0.1/350	$79.2\ ^{+55.0}_{-34.3}$
Bar tangential velocity (km/s)	0.001/150	$48.8\ ^{+43.4}_{-29.8}$
Parameter (Disc)	**Prior Range**	**Value**
Flux (Jy km/s)	1/50	28.7 ± 4.6
SB profile scale factor (arcsec)	0.001/15	$1.7\ ^{+1.5}_{-1.1}$
Sérsic index	0.1/4	$1.38\ ^{+0.60}_{-0.49}$
Velocity dispersion (km s^{-1})	1/50	$25.9\ ^{+7.3}_{-6.1}$

AGN (Figure 3.2).

The fitted spectrum for GAMA622429 (Figure 3.5) shows some excess flux, mainly at positive velocity but also as a spike at relative velocities just below zero. The latter does not correlate to any features and may be a noise effect. The residual zeroth order moment map (Figure 3.3) also shows excess flux, as a diffuse extended structure coinciding with the spiral arm in the lower portion of the image (positive velocity). One explanation for this is recent minor merger activity, which has added molecular gas to the ETG with insufficient time to allow it to smooth out fully. The KiDS optical image (Figure 3.1) supports this, with irregularities apparent in the lower portion of the disc where the diffuse patch of excess CO emission was detected. Molecular gas could then have been funnelled towards the galaxy centre, forming the very bright central feature and fuelling its strong AGN (Figure 3.2). Alternatively, the action of the bar could be disturbing molecular gas within the spiral arms on that side of the galaxy. The bar itself could have been produced following a perturbation.

3.3.2 Molecular Gas Stability Analysis

The possibility for new star formation within the ETGs with dominant molecular gas discs (GAMA64646 and 272990) was explored using the Toomre stability criterion, Q (Toomre 1964; Boizelle et al. 2017; van de Voort et al. 2018), which estimates whether a perturbation within a rotating gas disc subject to velocity dispersion would lead to gravitational collapse and the formation of star-forming regions. Equations 3.3, 3.4 and 3.5 summarise the approach, which require deprojected values for gas surface density based on the model galaxy inclination angle. The fitted rotation velocity profiles (Equation 3.2) and constant velocity dispersion values were used for this. SI units are used throughout. The Toomre stability criterion Q is given by:

$$Q = \frac{\kappa \sigma_{gas}}{\pi G \Sigma_{gas}} \tag{3.3}$$

$$\kappa = \left(R \frac{d\Omega^2}{dR} + 4\Omega^2 \right)^{0.5} \tag{3.4}$$

where κ is the epicyclic frequency, σ_{gas} is the gas velocity dispersion, G is the gravitational constant, Σ_{gas} is the molecular gas surface density, and Ω is the angular velocity at radius R ($\Omega = v_c/R$). The derivative term in Equation 3.4 is evaluated for the arctangent-based profile in Equation 3.2 as follows:

$$\frac{d\Omega^2}{dR} = \frac{2}{R^3} \left(\frac{2 v_{flat}}{\pi} \right)^2 \arctan\left(\frac{R}{R_0} \right) \left(\frac{R R_0}{R^2 + {R_0}^2} - \arctan\left(\frac{R}{R_0} \right) \right) \tag{3.5}$$

Values of Q less than 1 normally show that the molecular gas is unstable against collapse, and so should form stars efficiently. However, the uncertainties in molecular gas mass estimates from ^{12}CO[2-1] emission are such that this is not an appropriate threshold for this work. The uncertainty of CO to H_2 mass-to-light ratio (±30%) and ^{12}CO[2-1] to ^{12}CO(1-0) line strength ratio (±50%) (Sansom et al. 2019, and references therein) suggest that values of Q >2 are indicative of stability against star formation and Q <0.5 are indicative of instability leading to star formation. Values of Q between these limits indicate increasing likelihood of star formation as Q decreases.

Maps of star formation rate (SFR) per spaxel are available from SAMI DR3, calculated from maps of Hα emission from SAMI observations (Medling et al. 2018). These were used to indicate where star formation is actually occurring compared to expectations from values of Q. Overall star formation rates are also available for each galaxy from GAMA DR3 in the catalogue MagPhysv06, derived using spectral energy distribution (SED) fitting with MAGPHYS (Section 2.7.3). Table 3.5 shows the total estimated star formation rates from the SAMI DR3 maps compared to estimates from GAMA DR3. Uncertainties for the SFR estimates from SAMI are derived from the uncertainty in the

Table 3.5: Total star formation rates from GAMA DR3 MAGPHYS results (0-100 Myr) and SAMI DR3 (total for maps) for GAMA64646, 272990 and 622429.

Galaxy	Visual Morphology	Star Formation Rate (GAMA DR3) ($M_\odot$ yr^{-1})	Star Formation Rate (SAMI DR3) ($M_\odot$ yr^{-1})
GAMA64646	S0	$1.06^{+0.14}_{-0.00}$	1.36 ± 0.09
GAMA272990	E	$0.78^{+0.11}_{-0.17}$	0.75 ± 0.05
GAMA622429	S0	$4.39^{+0.59}_{-0.20}$	0.25 ± 0.02

empirical relation used to estimate them from Hα line luminosities (Dopita et al. 2005; Medling et al. 2018).

Table 3.5 shows that total SFRs from GAMA DR3 and SAMI DR3 are in reasonable agreement for GAMA64646 and 272990. However, there is a significant discrepancy between values for GAMA622429. This is attributed to the approach taken by the SAMI survey to mask regions where Hα emission could be contaminated by emission sources other than star formation (Medling et al. 2018), as discussed in Section 3.2.1. The presence of a strong AGN within GAMA622429 may be causing significant masking of spaxels with star formation. As an indication of which of the two SFR estimates may be correct, the molecular gas depletion times for an approximate molecular gas mass of 7×10^9 $M_\odot$ (Sansom et al. 2019) are predicted to be ~2 Gyr for the GAMA estimate and ~30 Gyr for the estimate from SAMI. The true estimate of SFR is likely to be between these values, probably closer to the GAMA estimates. Molecular gas depletion times for GAMA64646 and 272990, each containing ~few $\times 10^9$ $M_\odot$ (Sansom et al. 2019) are ~1 Gyr and ~3 Gyr.

Figure 3.8 compares the location of molecular gas in GAMA64646, 272990 and 622429 and the location of star forming regions detected by SAMI. These are affected by atmospheric seeing (FWHM ~2 arcsec, Croom et al. 2021a), compared to the

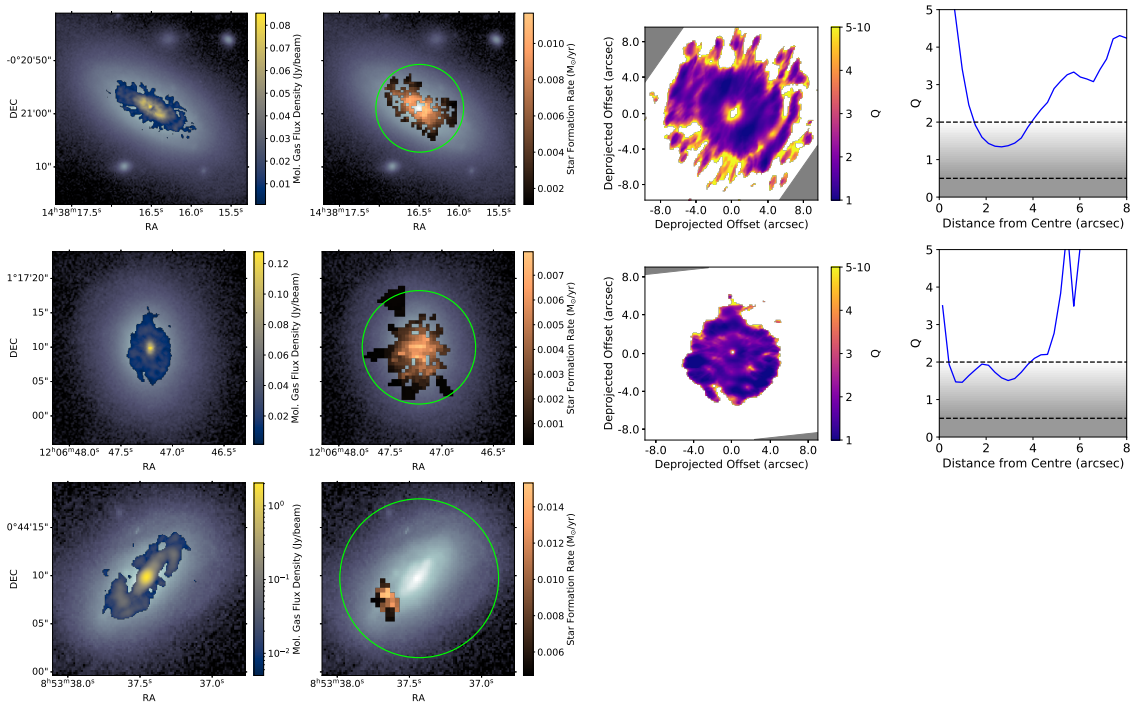

Figure 3.8: Comparison of molecular gas distribution, star formation distribution (from SAMI, adaptive binning) and Q for *top:* GAMA64646, *middle:* GAMA272990, *bottom:* GAMA622429. *Left:* masked zeroth order moment maps of molecular gas overlain on KiDS r-band log-normalised images. Molecular gas distribution for GAMA622429 is log-normalised. Images are fully contained within the ALMA field of view (~45 arcsec). *Centre left:* SAMI star formation maps overlain on log-normalised KiDS r-band images. Field of view (16.5 arcsec, Sharp et al. (2015)) shown in green. *Centre right:* Maps of Q (deprojected) calculated using constant velocity dispersion and masked flux density. *Right:* azimuthal average plots of Q, with potential for star formation shaded from white (highly unlikely, Q > 2) to dark grey (highly likely, Q < 0.5).

ALMA image beam size FWHM of ~0.7 arcsec. The comparison is generally good for GAMA64646 and 272990, but poor for GAMA622429 because of the spaxel masking issues discussed previously. Fine details such as the absence of star formation at the centre of GAMA64646 are apparent in both the molecular gas map and the star formation map. The SAMI field of view (~16.5 arcsec) is also shown in the diagram, to highlight that alignment of molecular gas and star formation is not affected by image truncation. This field was derived from Sharp et al. (2015), their Figure 9 which shows how dithered images are stacked to create the field of view. The ALMA field of view (~45 arcsec) is greater than the size of the images shown.

Figure 3.8 also shows maps of the Toomre stability criterion (Q), and azimuthal average values of Q determined from the maps. Star formation for GAMA64646 is likely in the range 1 - 4 arcsec from the centre, which is in reasonable agreement with the star formation map in Figure 3.8. The absence of star formation towards the centre is predicted, although the masking of star formation by AGN activity in the SAMI SFR map could be contributing to this. Star formation for GAMA272990 is likely from close to the centre to ~4 arcsec from the centre, which again is in reasonable agreement with actual star formation shown in Figure 3.8. The equivalent plots for GAMA622429 were not developed because of the presence of the bar, for which the assumption of circular motion of the molecular gas used to calculate Q presented previously is not applicable. Overall, these calculations of Q from the ALMA observations and kinematic modelling successfully predict the observed star formation distribution in these detected massive molecular gas discs.

3.3.3 Kinematic Alignments of Molecular Gas, Ionised Gas and Stars

The relative kinematic PAs of ETGs can be used to indicate whether recent merger activity has occurred. If kinematic PAs of stars and molecular gas are well aligned, a significant merger is unlikely to have deposited additional ISM into the ETG recently e.g. within

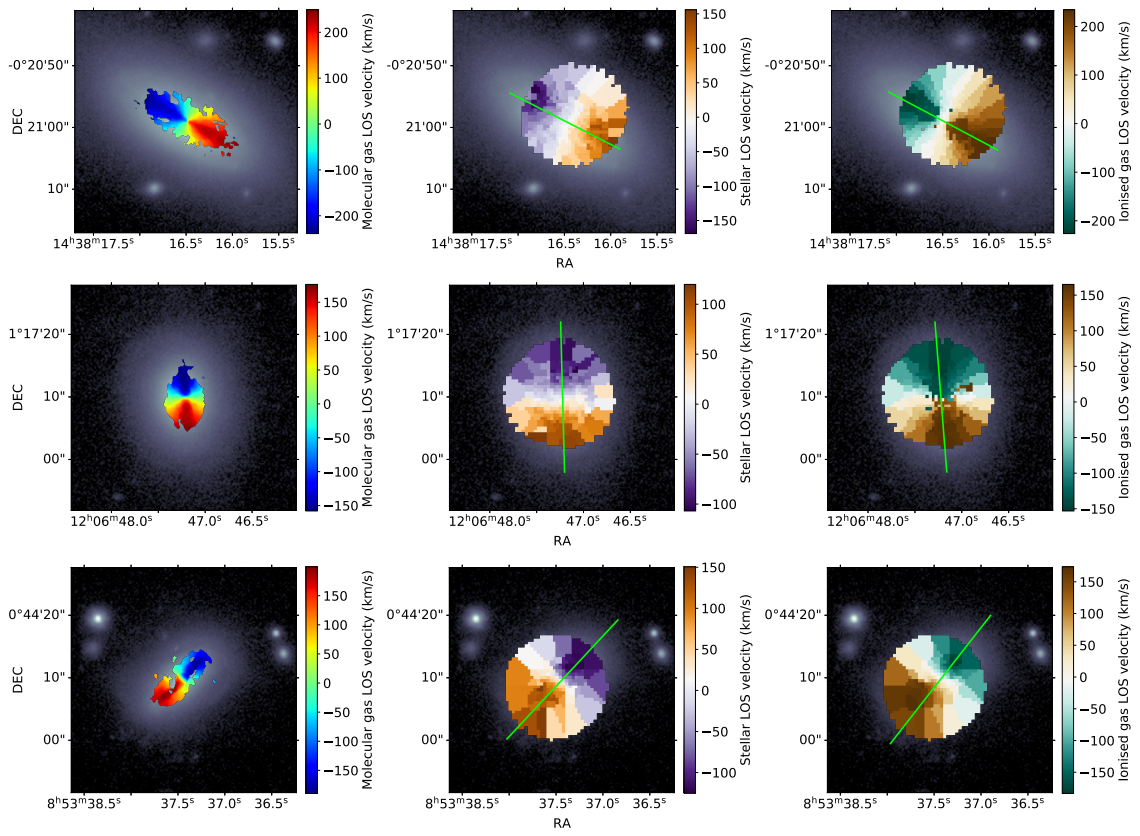

Figure 3.9: Kinematics of molecular gas (*left*), stars (*centre*) and ionised gas (*right*), overlain on KiDS r-band log-normalised images. *Top:* GAMA64646, *middle:* GAMA272990, *bottom:* GAMA622429.

a few dynamical timescales (∼100 Myr). Conversely, poor alignment (or even counter-rotation) can indicate relatively recent deposition of ISM via an external source (Davis et al. 2011).

Maps of molecular gas kinematics and fitted kinematic position angles were compared with kinematic maps of stars and ionised gas from SAMI DR3. Figure 3.9 shows the first order moment maps for molecular gas from ALMA data and velocity maps for stars and ionised gas for the three ETGs subject to kinematic modelling, overlain on log-normalised r-band images of the ETGs. Table 3.6 shows the tabulated kinematic PAs from SAMI compared to the derived PAs for molecular gas from kinematic modelling (Section 3.2.2).

Table 3.6: Kinematic position angles for molecular gas (from model fitting to ALMA data), stars and ionised gas (from SAMI DR3) for GAMA64646, 272990 and 622429.

Galaxy	Molecular Gas PA (°)	Ionised Gas PA (°)	Stars PA (°)
GAMA64646	62.0 ± 0.5	62.0 ± 0.2	63.0 ± 1.0
GAMA272990	3.5 ± 0.8	4.5 ± 0.2	1.5 ± 1.5
GAMA622429	315.8 ± 1.6	322.5 ± 0.2	317.0 ± 1.6

The first-order moment maps for molecular gas show generally smooth distributions, and do not themselves indicate interaction or disturbance. However, some evidence for interactions derived from molecular gas velocities is apparent in some diagnostic plots shown in Figure 3.5, as discussed in Section 3.3.1 . The kinematics of molecular gas, stellar and ionised gas (presumably from star formation) are well-aligned (within a few degrees) in all cases. There is a reduction in peak line-of-sight rotation velocity for stars compared to molecular and ionised gas for GAMA64646 and GAMA272990, likely due to asymmetric drift where stars lag behind the local standard of rest and are significantly more pressure supported than molecular gas (Strömberg 1946). The stellar kinematic map for GAMA64646 (Figure 3.9) may show a faint bifurcation in rotation velocity profile at both ends of the stellar disc major axis, visible as localised decreases in velocity at the extreme ends of the disc close to the green major axis line. This could arise from disturbance such as a tidal interaction such as those shown in optical images in van de Voort et al. (2018), leading to alterations in stellar orbital velocities at the outer edge of the galaxy, or it could simply be a noise effect. The alignments for GAMA272990 are possibly because molecular gas, star formation and ionised gas all lie within the embedded disc discussed previously.

3.3.4 ALMA Detections for GAMA177186

GAMA177186 is classified as an elliptical galaxy within GAMA DR3, with very little ongoing star formation (SFR $0.05^{+0.02}_{-0.01}$ $M_\odot$ yr^{-1} from MagPhysv06). With ALMA, only a small detection of millimetre continuum (dust) emission was found at the centre of the ETG itself, with no molecular gas detected (S19). No SAMI DR3 SFR or kinematic maps are available for this ETG. Because of its elliptical morphology, it is possible that GAMA177186 formed from the merger of two similar-sized galaxies (Xilouris et al. 2004). Any cool molecular gas present is likely to have been consumed by star formation as a result of the merger, leaving a ”red and dead” elliptical galaxy.

However, detection of millimetre line and continuum emission is apparent in maps from the ALMA observation, ∼4 arcsec from the ETG centre. GALFIT (Peng et al. 2010) was used to confirm that the ALMA-detected offset source is unresolved, with shape parameters consistent with that of the ALMA synthesised beam. This type of source confusion is a known issue when using Herschel observations to select targets for ALMA observations, because of the beam sizes of the Herschel observations (∼7 - 35 arcsec for a 3.5m aperture). Multiple objects detected within a single Herschel beam can lead to offset or multiple ALMA detections not associated with the intended target (Karim et al. 2013).

Figure 3.10 shows the ALMA-observed emission line spectrum for the offset object. The spectrum is binned by a factor of 7 to 70.7 km/s, and the emission line (shown in grey) is detected with flux/uncertainty of 7.6. The boundaries of the emission line were selected manually, on the basis of forming a coherent line with bin emission generally above the prevailing noise level. Integrating the spectrum yields a flux of 2.3 ± 0.3 Jy km/s, which is similar to the value reported in Sansom et al. (2019). However, the spectrum has a flat top, which is associated with optically thick emission. As explained in Section 3.3.1, optically thick emission arises from the surface of a molecular gas structure only, and calculated molecular gas masses from observed fluxes are therefore underestimates.

The measured line width for the spectrum in Figure 3.10 is approximately 840 ± 70

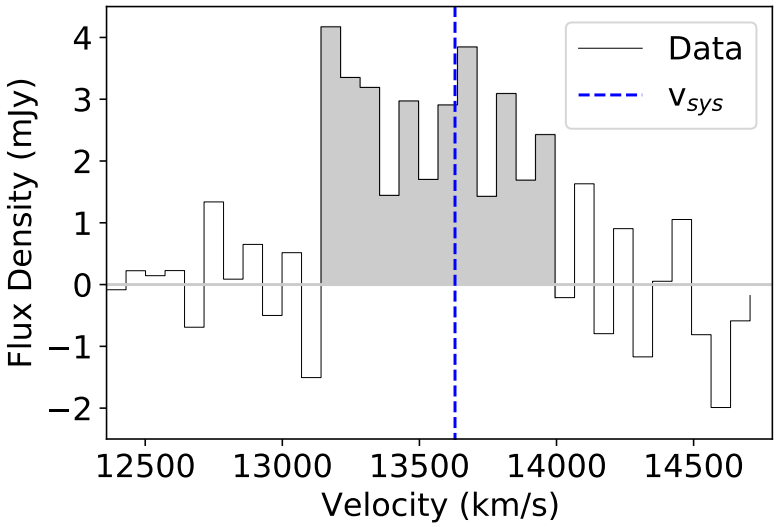

Figure 3.10: ^{12}CO[2-1] spectrum for GAMA177186 offset object, with binning to 70.7 km/s. vsys is the recession velocity of GAMA177186 calculated from heliocentric optical redshift. v_{sys} is the radio velocity of the ETG.

km/s (allowing an uncertainty of ±1 bin), centred within 1 bin of the radio velocity of GAMA177186. The first order moment map for the object (S19) shows that the object is rotating, and the maximum circular velocity would then be approximately 420 ± 35 km/s. This is consistent with values for massive galaxies (e.g. stellar mass $>10^{11}$ $M_{\odot}$) (e.g. Kassin et al. 2007). An alternative explanation is that the wide emission line is from two aligned dusty satellite galaxies orbiting GAMA177186. The large line width alone is therefore not conclusive evidence of high redshift for the object, but this remains a possibility.

Data from H-ATLAS DR1 (Valiante et al. 2016) shows sub-mm emission assigned to GAMA177186 detected in SPIRE passbands but not PACS passbands. When combined with photometry from the ALMA continuum map for GAMA177186 (Sansom et al. 2019), a consistent spectrum is obtained (Figure 3.11). However, the derived flux density from the ALMA continuum map could be dominated by synchrotron emission from GAMA 177186 (Condon 1992), and the SPIRE measurements could be from dust within the galaxy that is undetected by ALMA due to MRS issues. The alignment of data points

within the SED could therefore be coincidental. The analysis below is therefore for illustration only, and assumes that the Herschel-detected flux densities are from the offset object only.

The spectrum in Figure 3.11 was fitted with a single modified blackbody (SMBB) model representing a uniform dust population (Equations 6.1, 6.2 and 6.3), with an emissivity coefficient (β) of 2, a mass absorption coefficient of 0.077 m^2 kg^{-1} at 850 μm (Dunne et al. 2011, and references therein) and the ETG heliocentric redshift of 0.0476 from GAMA DR3. Colour corrections to measured flux densities at the fitted temperature were close to unity and therefore were not applied. This gave a dust mass of $10^{8.1\pm0.5}$ $M_\odot$ and a temperature of 10.5 ± 0.6 K. Fitting the three SPIRE data points alone gave a dust temperature of 10.9 ± 1.8 K, so the ALMA-based flux density measurement is reasonably well aligned with those from SPIRE. Fitting was found to be equally successful for any positive redshift supplied to the model, with dust temperature increasing linearly with redshift and dust masses varying within an order of magnitude over the redshift range considered (Figure 3.12). The predicted dust temperature with the object at the redshift of GAMA177186 is consistent with dust temperatures found in the outskirts of M33 (Thirlwall et al. 2020) and other spiral galaxies where energy density of radiation fields is low (see also Popescu & Tuffs (2003)). However, this dust temperature is lower than the average generally found in ETGs (~25K, Smith et al. 2012) and spiral galaxies (~20K) (Davies et al. 2012). It is therefore possible that the ALMA-detected dust emission is from warmer dust at a higher redshift. It should also be noted that the SMBB model is only an approximation for galaxies, which can be expected to have dust populations at higher temperatures alongside the cool dust (see Section 6.5.4). The measured spectrum is the combined emission from all dust populations.

If the line emission shown in Figure 3.10 is from a source at high redshift, the emission is not from ^{12}CO[2-1] but some other line whose emission is redshifted to produce the spectrum in Figure 3.10. Possible candidates are shown in Figure 3.12, along with the required redshift to produce the detected emission line. [CII] emission (158μm) is

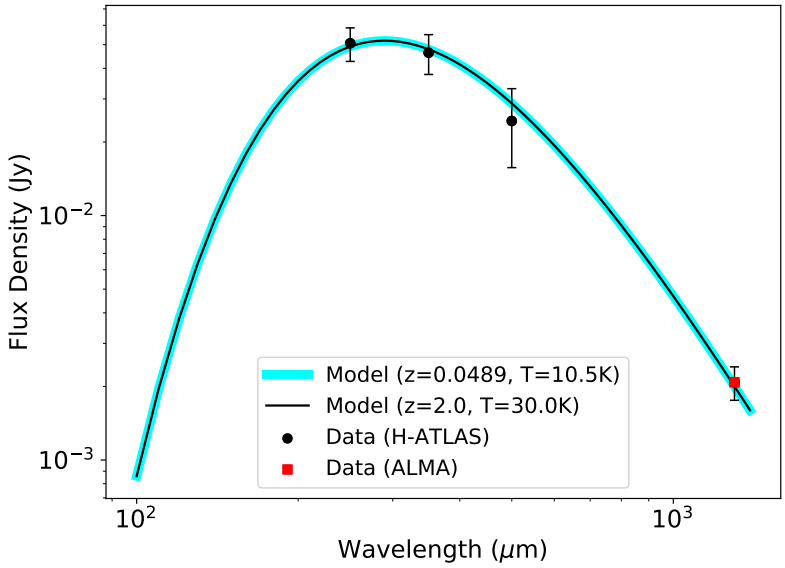

Figure 3.11: SED fitting of photometry from H-ATLAS and ALMA for GAMA177186 (assumed to be from the offset object).

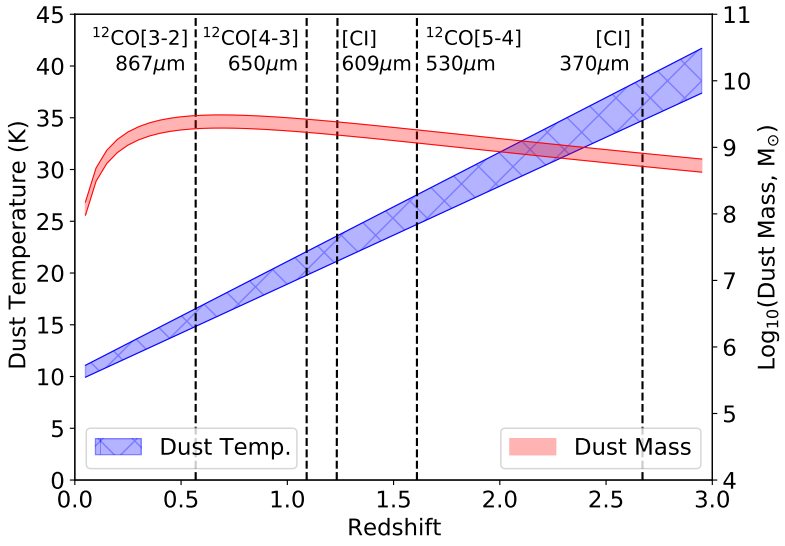

Figure 3.12: Effect of assumed offset object redshift on fitted dust mass and temperature. Colour bands show 1σ uncertainty range. Other emission lines possibly responsible for the detected line emission are also shown, along with their rest wavelengths and associated redshift to produce the detected emission line.

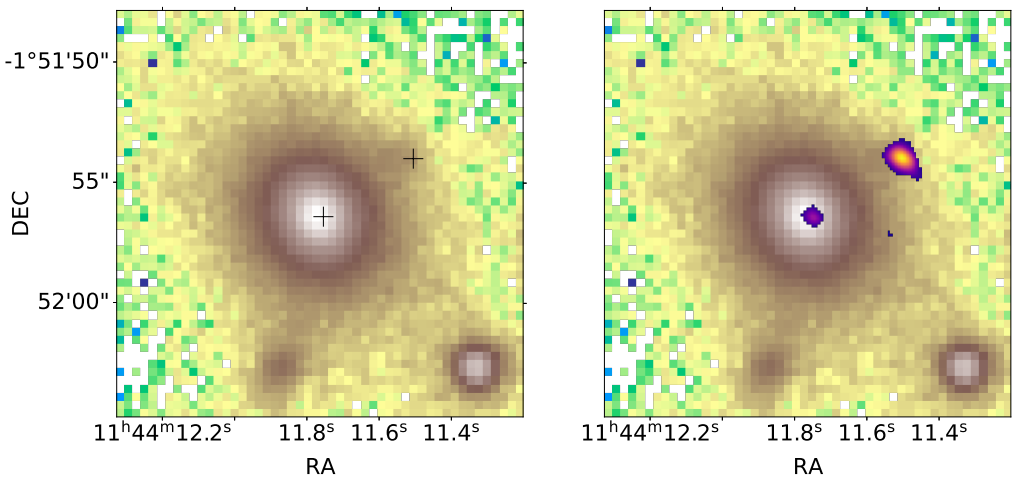

Figure 3.13: VISTA J, H and Ks-band co-added image (log-normalised) of GAMA177186 shown in yellow/brown/white. *Left*: centres of ALMA detections are shown as plus signs. *Right*: Map of continuum detections are shown in blue/pink/yellow, overlain on the VISTA image.

also a candidate, requiring a redshift of 7.6 to produce the detected line. Although minimum gas temperatures for significant excitation to produce some of the lines discussed exceed the predicted dust temperatures at their associated redshifts, molecular gas and dust temperatures could be different so these lines could still be relevant.

On balance, the evidence for a high redshift for the offset object is not conclusive. One way of resolving this is to examine a very faint source apparent in VISTA (Emerson et al. 2004) J, H and Ks-band images from the VIKING survey (Edge et al. 2013) close to the ALMA-detected source. This source is not visible in VISTA Z or Y bands. When the pointing uncertainty of VISTA (~1 arcsec, Sutherland et al. (2015)) is taken into account, the H/J/Ks-band emission and the ALMA detection are probably aligned (Figure 3.13). Deeper infra-red images with multiple passbands would confirm the presence of the feature photometrically and possibly allow a photometric redshift to be estimated.

3.3.5 ALMA Detections for GAMA622305

Figure 4.2 shows GAMA622305 as a retired galaxy with some emission lines present in its spectrum, at least some of which are attributed to ionising radiation from old stellar populations. Its SFR from GAMA DR3 MAGPHYSv06 is $0.49^{+0.02}_{-0.04}$ $M_\odot$ yr^{-1}.

The ALMA observation of GAMA622305 (Sansom et al. 2019) also did not detect the dust content expected from Herschel observations, probably due to MRS issues discussed earlier (Section 3.2.1). However, a compact, elongated region of molecular gas was detected, with a central frequency close to that expected for ^{12}CO[2-1] emission within the galaxy (Figure 3.1). This source is offset from the galaxy centre, with a length of approximately 2 kpc. The first order moment map for this object (Sansom et al. 2019) shows a velocity distribution from low positive to low negative velocity along its length, with a velocity difference across the object of $\sim$100 km s^{-1}. The velocity profile is consistent with velocities of ionised gas shown in maps from SAMI, suggesting that the object is following the general rotation profile of the ETG.

The ALMA-observed spectrum for the object shown in Figure 3.14 is binned by a factor of 3 (30.3 km s^{-1} bins) compared to the spectrum shown in Sansom et al. (2019). Integrating the emission line (shaded grey) gives a flux density of 0.66 ± 0.14 Jy km s^{-1}, which is 0.1 Jy km s^{-1} greater than that reported in Sansom et al. (2019) due to better definition of the emission line after binning. The emission line is detected with flux/uncertainty of 4.7.

Figure 3.15 shows the location of the detected molecular gas in relation to a ring of SAMI DR3-detected star-forming regions within the galaxy. The spatial and velocity alignment of the molecular gas and ETG suggests that the molecular gas is associated with the star forming ring. The total SFR from this map is 0.28 $M_\odot$ yr^{-1}, which is less than the value from GAMA quoted earlier and suggests that either some star formation was not detected by SAMI or the MAGPHYS value is an over-estimate. The molecular gas mass of the object is estimated to be $\sim 8 \times 10^7$ $M_\odot$ by adjustment of the result in Sansom et al.

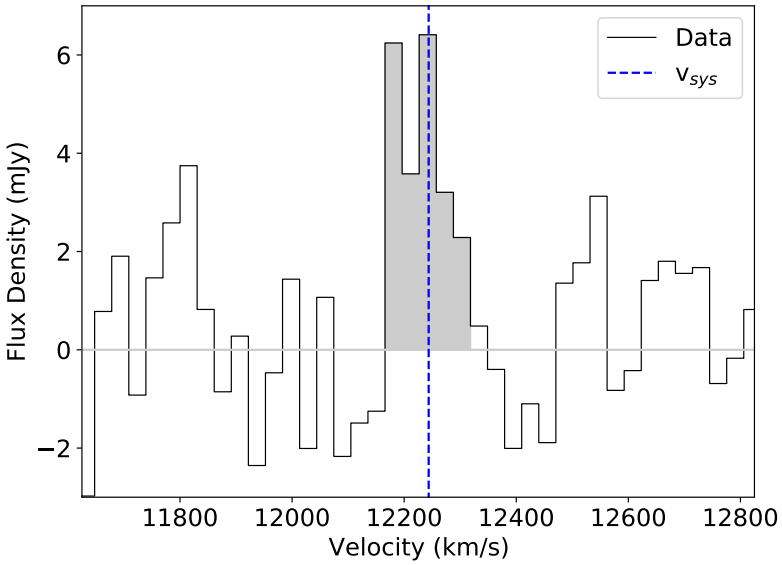

Figure 3.14: Spectrum for ^{12}CO[2-1] detected in GAMA622305, with GAMA622305 velocity shown in relation to the emission line. v_{sys} is the radio velocity of the ETG.

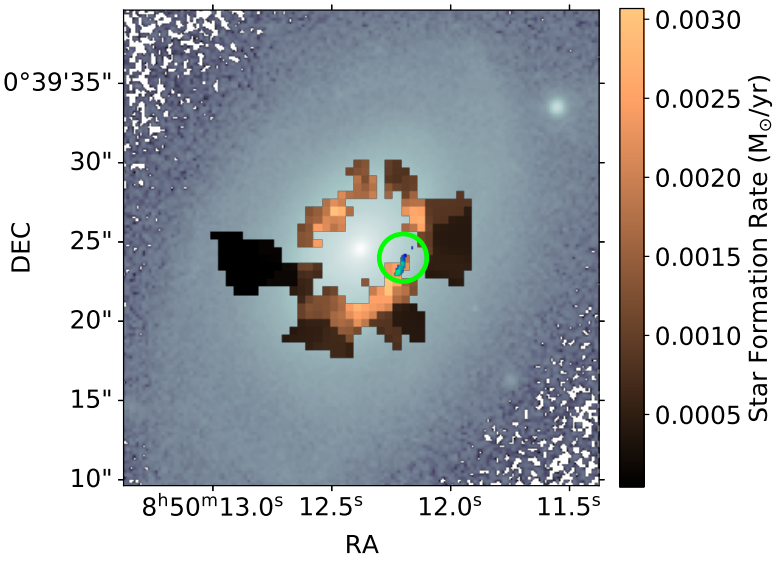

Figure 3.15: Star formation rate (SAMI, adaptive binning) and ^{12}CO[2-1] emission (ALMA, shown and ringed in green) overlaid on KiDS r-band log-normalised image of GAMA622305.

(2019) to account for the increase in flux. This and the major axis dimension are both at least an order of magnitude greater than the most massive giant molecular clouds in other galaxies (e.g. Bolatto et al. 2008). The object could be a GMC complex (e.g. Kirk et al. 2015) within the star forming ring, suggestive of clumpy star formation.

The presence of star formation in a ring within GAMA622305 suggests the presence of additional molecular gas to the feature discussed above, but this is not apparent during visual inspection of the data cube. However, emission in the data cube can be stacked using *a priori* information on likely molecular gas velocity at defined spatial locations from an independent source, e.g. an ionised gas velocity map from SAMI. The STACKARATOR package (Section 2.7.2) was used to create a single spectral peak for ^{12}CO[1-0] emission relative to the expected velocities and locations from a SAMI ionised gas map. The stacked spectral line (Figure 3.16, upper right) has an integrated flux of 4.98 ± 0.34 Jy km s^{-1}, which is a factor of ∼7.5 greater than the flux of the molecular gas region shown in Figure 3.15. By extrapolation of the molecular gas mass quoted above for the highlighted region, the molecular gas mass in this ETG is then at least $\sim 6 \times 10^8$ M$_\odot$.

To test whether this detection of additional flux using STACKARATOR is genuine, STACKARATOR was used to sample regions of the ALMA data cube coinciding spatially with ionised gas emission but at different velocities. This was achieved by scaling the SAMI velocity map by factors of 0.5, 0.8, 1.2 and 1.5. Figure 3.16 (lower left) shows that the strength of the detected spectral line increases as the factor is increased towards 1, and then declines as the factor is increased further. Use of the unmodified SAMI velocity map for ionised gas with STACKARATOR therefore maximises the recovery of molecular gas emission, and the location of the recovered molecular gas emission coincides with ionised gas along the spatial and velocity axes.

Use of STACKARATOR to stack emission in elliptical annuli with a width of ∼2 ALMA beams (10 pixels, 1.2 arcsec) shows a sharp upturn in flux at ∼4 arcsec radius followed by a decline (Figure 3.16, lower right). The star forming ring has dimensions broadly consistent with this upturn (Figure 3.16, upper left), as expected if molecular gas and star

formation are spatially coincident.

The optical image of GAMA622305 (Figure 3.1) shows asymmetry, with the stellar distribution extended towards the lower left of the image. This ETG is therefore likely to have experienced a recent interaction that distorted it. New molecular gas could have been acquired during this event or existing molecular gas could have been disturbed, leading to the formation of a molecular gas ring with star formation as discussed previously. Formation of the ring by purely secular means (Buta & Combes 1996) cannot be ruled out, but this ETG has been disturbed. Any pre-existing ring would have to be preserved through the disturbance.

3.4 Discussion of Findings

Of the five ETGs observed with ALMA, three (GAMA64646, 272990 and 622429) were found to contain massive ($>10^9$ $M_\odot$) molecular gas reservoirs. A fourth (GAMA622305) was found to contain a molecular gas feature consistent with a GMC complex and additional molecular gas probably in a ring structure, likely associated with a star-forming inner ring within the ETG. The main ALMA detection for the remaining ETG, GAMA177186, was from an object likely to be at a higher redshift than the target. This ETG is therefore not discussed further in terms of its evolution inferred from molecular gas content and distribution. However, the information presented for the remaining four of the observed ETGs with detected molecular gas can be used to infer the mechanisms responsible for their recent evolution.

The information presented shows that all four ETGs have undergone disturbance of some kind. GAMA64646 appears to have undergone a tidal disturbance, probably leading to a star-forming ring in the SAMI observation and a tidal tail in optical images. GAMA272990 has an elliptical appearance in optical images which can be a product of a

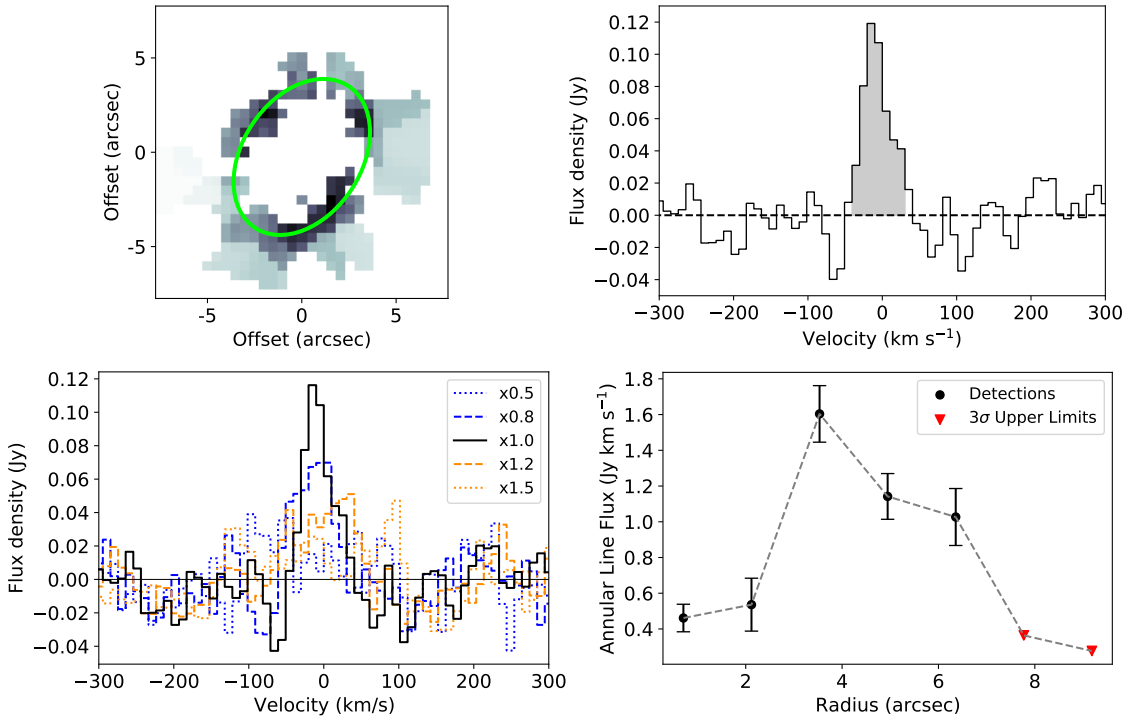

Figure 3.16: Analysis of GAMA622305 molecular gas distribution using STACKARATOR. *Upper left*: star formation map (adaptive binning) from SAMI. Overlaid ellipse has a major radius of 4.5 arcsec, PA 146.5°, inclination 46.5° from GAMA II r-band data. *Upper right*: Emission line spectrum from stacking of whole data cube by Stackrator, using ionised gas velocity map from SAMI. Detected line is shown in grey. *Lower left*: Spectra recovered when applying a multiple to the SAMI ionised gas velocity map. *Lower right*: Fluxes in consecutive annular ellipses from STACKARATOR.

merger (e.g. Davis & Young 2019), with an asymmetric, star-forming embedded molecular gas disc. GAMA622429 has asymmetric molecular gas distribution and evidence of asymmetric disturbance in optical images, both coinciding with star formation detected in the SAMI observation. GAMA622305 appears to have undergone a tidal disturbance, which probably created a star-forming ring detected with SAMI that is coincident with the molecular gas feature detected by ALMA. It is possible that the molecular gas in these ETGs in low-density environments was acquired through merger activity at some point (Davis et al. 2011; Kaviraj et al. 2012; Alatalo et al. 2013), but other interactions may have contributed to their observed appearance and behaviour.

The three massive molecular gas reservoirs detected by these ALMA observations all have a greater spatial extent than assumed for observation planning. A median spatial extent for cool ISM of 1 - 2 kpc or half the optical (r-band) effective radius was assumed, based on previous evidence of molecular gas extents in ETGs (e.g. Davis et al. 2013). Converting the radial scale factors and Sérsic indices into effective radii containing 50% of the ^{12}CO[2-1] emission (MacArthur et al. 2003), the effective radii of cool ISM for these three ETGs are in the range 2.8 - 5.2 arcsec (2.3 - 4.3 kpc), which is generally larger than the spatial extents originally assumed for molecular gas in ETGs. Future observation planning for cool ISM in Dusty ETGs should be based on larger spatial extents, to ensure that all emission is accounted for.

The five observed ETGs were selected mainly on the basis of having relatively large Herschel-observed dust masses and being free of strong AGN activity. Source confusion within the Herschel observation led to the selection of GAMA177186. GAMA622429 was selected in spite of having a strong AGN, probably due to incomplete line emission information to detect AGN activity. However, the ALMA observation of GAMA622429 has proved to be useful. In spite of this, the study of galaxies with strong AGN is not recommended for future studies of this type because estimates of SFR and other properties from optical data may not be reliable. ETGs with weak AGN activity (Figure 4.2) can be observed and studied successfully, because this study has shown that useful information

can be gained from observing their widely-distributed ISM.

The gas depletion times and star formation rates for the two ETGs with massive molecular gas rotating discs (GAMA64646, 272990) can be compared with the Milky Way Galaxy (MWG), which is also acknowledged as being a GV galaxy. The MWG has less molecular gas (6.5×10^8 $M_\odot$, Roman-Duval et al. 2016), similar star formation rates (1.25 ± 0.2 $M_\odot$ yr^{-1}, Natale et al. 2022), and hence a shorter molecular gas depletion time (H_2 mass / SFR) of ~0.5 Gyr. The MWG appears as a GV galaxy within colour-magnitude diagrams (e.g. Boardman et al. (2020), their Figure 1) along with many other Dusty ETGs (e.g. Agius et al. 2013). These two ALMA-observed Dusty ETGs with CO emission dominated by disc-like molecular gas reservoirs therefore differ from the MWG in terms of their future evolution. Their molecular gas reservoirs are not forming stars as fast as the MWG, which itself only has a modest SFR for its stellar mass. Reasons for this low star formation efficiency can be investigated in future studies.

The nature of the possible progenitors of GAMA272990 and GAMA622429 which may have undergone mergers cannot be studied with the data used here. Studies of the distributions of stellar populations and gas-phase metallicity using spectroscopy or IFU observations may assist in identifying the circumstances behind the mergers in more detail. For example, the stellar population ages for the embedded star-forming disc in GAMA272990 might be relatively young if the feature formed as a result of a recent merger, and gas-phase metallicities may be significantly different from stellar metallicities.

This work demonstrates that optical IFU observations can complement high-resolution interferometric observations (along spatial and frequency axes) of cool ISM in galaxies, but high-resolution observations provide unique information on the cool ISM itself and star formation arising from cool molecular gas. Star formation regions in rotating molecular gas discs from SAMI IFU observations align well with those determined from ALMA observations in this work. The Toomre stability criterion does seem to predict the places where molecular gas is observed to collapse to form stars, at

least in this small sample of ETGs. However, because the SAMI star formation maps are designed to be clean but not complete as described above they can fail to identify star formation. Observations with high spatial and spectral resolution (e.g. interferometric) are also essential when investigating kinematic alignment of cool molecular gas, stars and ionised gas.

The evidence presented above indicates that the object offset from GAMA177186 could be a massive, dust- and gas-rich rotating object at relatively high redshift, but its redshift cannot be identified uniquely at present. It can be studied further if additional observations of sufficient depth become available at infra-red and other wavelengths.

3.5 Conclusions for Chapter

This study has examined ALMA observations of ^{12}CO[2-1] emission and continuum emission from five dusty (ISM-rich) visually-classified ETGs in low-density environments. These were selected from a complete sample within the GAMA equatorial fields with $z \leq 0.06$. Axisymmetric or bisymmetric kinematic modelling was used to quantify structures and velocity profiles within the molecular gas, and differences between models and data were used to highlight possible deviations from equilibrium indicative of the evolution of these ETGs. IFU maps and data from SAMI DR3 and data from GAMA DR3 provide further information.

Four of the ETGs have massive (~few $\times$ 10^8 - few $\times$ 10^9 $M_\odot$), extended molecular gas reservoirs with radii effictive radii ~ 3 - 5 kpc, apparent in the ALMA observations of molecular gas. All four of these ETGs appear to be undergoing evolution driven by disturbances. GAMA64646 and GAMA622305 appear to be evolving as a result of relatively mild external disturbances leading to environmental secular evolution. This is highlighted by faint distortions and tidal tails in optical images, and star-forming inner rings revealed by ALMA and IFU observations. GAMA272990 appears to be evolving due to a recent

and more energetic interaction, leaving an elliptical appearance with an embedded star-forming molecular gas disc. GAMA622429 may have undergone a minor merger, based on asymmetry in its molecular gas distribution and asymmetric disturbance apparent in optical images. The remaining ETG (GAMA177186) was affected by source confusion, from an object which could be a massive gas- and dust-rich object at high redshift. Further observations are needed to establish the nature of this object conclusively.

Overall, the observations and analysis indicate that a high proportion of Dusty ETGs in low-density environments have undergone some kind of interaction as part of their recent evolution, although more observations of such targets are needed to verify and better quantify this result. Secular evolution over several gigayears can then complete the transformation of the ETGs from star-forming to passive. High-resolution interferometric observations are also shown to complement IFU observations, allowing a more complete picture of the evolution of these ETGs to be examined. Molecular gas distribution in the visually-classified Elliptical GAMA272990 has a disc-like morphology, and in the Lenticular GAMA622429 molecular gas has a spiral configuration, but their classifications as E and S0 are unchanged because Hubble classifications relate to visual morphology only.

Chapter 4

Construction of a New, Clean and Complete Galaxy Sample

4.1 Introduction

This Chapter describes the construction of a volume-limited, clean and complete sample of galaxies covering all morphological types within the GAMA equatorial regions (Section 2.8.1), and subsets of LTGs and ETGs. Definitions of volume-limited, clean and complete are as follows. The GAMA equatorial regions cover defined regions of the sky, and selection of galaxy redshift limits within these regions allows all galaxies within defined volumes of the Universe to be studied. The clean nature of the sample means that it is free of contaminants, i.e. free of galaxies that do not meet selection criteria (or at least, as free as possible). Sample completeness and volume-limited means that the sample contains all galaxies within the selected volume of the Universe that meet selection criteria. Unlike incomplete, anecdotal samples based on specific galaxy features (e.g. dust lanes, Davis et al. 2015), volume-limited, clean and complete samples allow statistical evaluation of galaxy properties, and random selections from these samples are likely to have statistics that apply to the wider sample.

The galaxy samples created in this Chapter are used for the remainder of this work, as follows. They are used initially to investigate the possibility that evolving galaxies in the local Universe have a smoothly-changing continuum of properties from LTG to ETG, as proposed by Eales et al. (2017), rather than a bimodal LTG/ETG split (Chapter 5). The behaviour of interstellar dust content and properties in relation to other galaxy properties is considered in Chapter 6. The ETG sample created here is also useful to select ETGs for observational studies that meet further selection criteria, e.g. limitations on flux density or angular size to match the capabilities of a telescope, as shown in Chapter 7.

4.2 Initial Galaxy Selection

A complete Initial Sample of galaxies was built first, with valid spectroscopic redshift data and with criteria that allow the assignment of morphologies from available GAMA II catalogues (Section 2.8.1). Details of the specific GAMA catalogues, filtering methods and the filtering to build the Initial Sample are provided below.

GAMA II catalogues with the required data are available in Flexible Image Transport System (FITS) format (Wells et al. 1981), and are analysed in this work using Python scripts developed by this author. The catalogues are first converted to Astropy.Table format, which allows straightforward access to data based on column name. Filtering of galaxies using Astropy.Table format, e.g. within specified redshift limits, was performed using masks created from bitwise Boolean expressions in Python. For example, all galaxies in a Table with redshifts between 0.02 and 0.6 and absolute magnitudes greater than -17.4 can be isolated to form a new Table with a single line of Python script. This is a recognised method for filtering Astropy.Table data, and is effective where multiple criteria are to be met[1]. Other commands in Astropy.Table allow tables to be joined, e.g. via an inner join (Boolean *AND*) or an outer join (Boolean *OR*) based on properties in a common property column. Inner joins are particularly useful in identifying galaxies that

[1]https://docs.astropy.org/en/stable/table/access_table.html

are common to multiple TABLE arrays, via their unique GAMA *CATAID* identification number for each galaxy.

The Initial Sample was constructed as follows. The GAMA II catalogue TILINGCATV46 (221,373 galaxies), containing all possible GAMA targets, was used to identify genuine galaxies (i.e. not stars or artifacts) within the GAMA survey based on a survey class variable (SURVEY_CLASS $\geq$ 1), indicating that 219,957 targets within the catalogue are genuine galaxies. A second catalogue, GAMA II DISTANCESFRAMESV14 (339,693 galaxies) was used to identify galaxies with GAMA or SDSS spectroscopy suitable for redshift determination based on a spectroscopy quality variable (NQ >2), yielding 330,542 galaxies. GAMA II SERSICCATSDSSV09 (221,373 galaxies) was then used to identify galaxies with SDSS r-band effective radius from a fitted surface brightness profile model greater than 1.2 arcsec (see Section 3.2.2), to ensure that the selected galaxies are resolved in SDSS images compared to local seeing conditions, yielding 131,821 galaxies. The results from these three selections were then subject to an inner join based on galaxy identifier CATAID, creating the Initial Sample of 120,843 galaxies.

An Initial Complete Sample of galaxies was then constructed by imposing limits on flow-corrected spectroscopic redshift (Tonry et al. 2000) from GAMA II DISTANCESFRAMESV14, and SDSS r-band absolute Petrosian magnitude M_r corrected for Galactic extinction, derived from data in GAMA II TILINGCATV46. Flow-corrected redshifts have been corrected for radial motion not associated with cosmological expansion, and allow more reliable distance estimates based on redshift. In practice, these corrections are small for the galaxies in the derived samples. Redshift limits of $0.002 \leq z \leq 0.06$ were also chosen for compatibility with the completeness limits for certain GAMA II catalogues, especially VISUALMORPHOLOGYV03 (Section 4.6.1) containing visual morphology information (Moffett et al. 2016). An M_r limit of $\leq$ -17.4 was selected, which corresponds to the GAMA II apparent Petrosian magnitude limit for spectroscopic completeness ($r \leq 19.8$) at the maximum sample redshift of 0.06. Absolute magnitudes were calculated from catalogue apparent Petrosian r-band magnitudes in the GAMA catalogue TILINGCATV46

(used for GAMA target selection) using distance moduli published within the GAMA catalogue DistancesFramesv14 (column DM_70_30_70). The resultant Initial Complete Sample contains 4,936 galaxies.

The limit on absolute r-band magnitude (-17.4) in this work represents galaxies of approximately the magnitude of the Small Magellanic Cloud (SMC). The NASA Extragalactic Database (NED)[2] provides a V-band apparent magnitude for the SMC of 2.25 ± 0.1 and a distance modulus of 18.9. (de Vaucouleurs 1960) estimate the (B-V) colour of the SMC as +0.4, and using an approximate relation between r-band magnitude, V and (B-V)[3] an approximate apparent r-band magnitude of 2.2 is obtained. The absolute r-band magnitude of the SMC is then -16.7.

4.3 Identification and Removal of Strong Active Galactic Nuclei (AGN)

For the purposes of this study, it is important to remove galaxies with strong Active Galactic Nuclei (AGN). The synchrotron emission from strong AGN will interfere with the longer-wavelength thermal emission from galactic dust (e.g. Condon 1992) used in this work to estimate dust properties, as shown in Chapter 4. The resultant sub-mm spectrum used for estimation of dust masses and properties would not be representative of the dust alone. AGN are also associated with dust tori (Jaffe et al. 1993, see Section 4.3.5), and cool ISM is generally more centrally concentrated if a strong AGN is present. Therefore it is more challenging (but not impossible) to use cool ISM distribution as an evolutionary indicator in these instances. The ALMA observation of GAMA622429 (Chapter 3) illustrates this point, although in this instance it was possible to recover information about the evolution of the galaxy.

[2]http://ned.ipac.caltech.edu/

[3]http://www.sdss3.org/dr8/algorithms/sdssUBVRITransform.php

To ensure that as many strong AGN are identified and removed as possible, multiple techniques are used as described below. None of the methods used are perfect individually, but the use of multiple methods aims to increase the overall reliability of strong AGN removal. While even the use of multiple methods cannot guaranteed to be completely reliable, it should ensure that the effect of strongly active galaxies on results discussed later is reduced as far as practicable.

4.3.1 BPT Diagram

Baldwin et al. (1981) proposed the use of the emission from de-excitation within specific atoms in ionised gas (HII regions) to identify the presence of different excitation mechanisms, including those associated with AGN. Ionising radiation from OB stars within star forming regions was found to create a clear trend when the emission line strength (flux) ratio [OIII]λ5007/Hβ from HII regions was plotted against [NII]λ6583/Hα, initially flat then trending downwards with increasing [NII]λ6583/Hα (see Figure 4.1 for an example). The plot is referred to as a BPT diagram, after its developers. The emission lines in brackets are "forbidden" lines, which can occur but only under specific conditions. In relatively high-density gases collisional excitation of ionised atoms to the necessary levels for forbidden line emission does occur, but collisional de-excitation occurs preferentially because of the relatively long duration of the excited state. However, in the very low particle density environments associated with ISM in HII regions ($\sim$1000 m^{-3}), collision probabilities for excitation and de-excitation are much reduced and atoms can remain excited long enough for the forbidden de-excitations to occur (Condon & Ransom 2015).

The BPT diagram in Figure 4.1 shows distinct trends to the left and right. On the upper right, an increasing trend is shown between the two line ratios. Starting on the left, another trend is apparent which is flat initially then decays with increasing [NII]λ6583/Hα. Garg et al. (2022) discuss the these trends within the BPT diagram, in terms of the prevailing radiation field causing the ionisation and the metallicity of the emitting HII regions,

as summarised below.

The trend on the right is due to increasing ionisation levels with increasing AGN activity. Both the forbidden [OIII] and [NII] line fluxes are sensitive to prevailing ionising radiation levels (Condon & Ransom 2015), so stronger AGN activity cause the strengths of both lines to increase relative to hydrogen emission lines. The slope of this trend is therefore positive.

On the other hand, the flat then decreasing trend apparent in the remainder of the plot is dependent on the metallicity of the stars and surrounding HII regions. [NII] flux from HII regions increases with metallicity for the same radiation level from OB stars, but [OIII] flux has a more complex relation, driven by a different relation between [OIII] emission and ionisation than for [NII]. As metallicity increases, [OIII] abundance increases but photosphere temperatures of OB stars responsible for the ionisation and subsequent line emission from neighbouring HII fall (e.g. Massey et al. 2005). Following the trend from the right, metallicity decreases from high to low in the BPT diagram. [OIII] emission increases initially relative to Hβ as photosphere temperatures of OB stars increase, until a balance is reached between increasing [OIII] emission with decreasing metallicity and decreasing [OIII] abundance. The [OIII]/Hβ ratio is then approximately constant.

The BPT diagram can be used to identify sources of ionisation leading to the observed emission line ratios within a galaxy, by imposing appropriate demarcations on the diagram separating regions where particular ionisation mechanisms are dominant. Kewley et al. (2001) developed a theoretical relation between these ratios for use with a BPT diagram, to separate galaxies whose line ratios are due to AGN only from those with combined AGN and emission from starburst activity (Figure 3.2). Later, Kauffmann et al. (2003) established a semi-empirical relationship by modifying the Kewley et al. (2001) relation to separate galaxies with stronger AGN, including composite galaxies hosting both AGN and starburst activity, from those without. An alternative relation was published by Stasińska et al. (2006) based on an different stellar emission models to those used by Kewley et al. (2001), with later claims that the stellar emission models used by Kewley

et al. (2001) over-estimated the ionising radiation fields affecting HII regions (Werle et al. 2020). The relations by Kewley et al. (2001) and Kauffmann et al. (2003) are used in this work for compatibility with recent studies of ISM in galaxies that are used as comparators e.g. in Chapter 5 (e.g. Saintonge et al. 2017).

A BPT diagram for the Initial Complete Sample (Section 4.2) was constructed as follows. The GAMA II catalogue GaussFitSimplev05 contains line intensity data derived from fits of single Gaussian functions to emission and absorption lines from GAMA II (where available) and SDSS spectra for each galaxy. Galaxies within this catalogue were first identified with line fluxes and uncertainties for the four relevant spectral lines (catalogue columns OIIIR, HA, NIIR, HB) all greater than zero, from the best spectra for use within the catalogue (flag IS_BEST = 1). Negative fluxes imply absorption rather than emission. From this cut, galaxies were identified with line flux/uncertainty ratios ≥3. The galaxies with relevant emission line data were then cross-matched with the initial complete sample. Their BPT parameters were evaluated and compared against the Kaufmann et al. (2003) criteria, to identify those galaxies that are potential hosts to stronger AGN. These include composite galaxies with ionisation due to both an AGN and star formation.

Figure 4.1 shows the BPT plot derived for the Initial Complete Sample. Of the 4,936 galaxies in the initial complete sample, 2,244 (45%) have valid spectral data with positive line fluxes and ratio of line flux to uncertainty ≥3. A total of 358 galaxies were identified as having AGN based on the Kauffmann et al. (2003) criterion.

4.3.2 WHAN Diagram

Cid Fernandes et al. (2010, 2011) developed a diagnostic plot using just two spectral lines, Hα and [NII]λ6583, to separate galaxies possessing AGN from galaxies with emission lines arising from old stellar populations (e.g. binary stars). The diagram was originally referred to as the EWHαN2 plot (Cid Fernandes et al. 2010) based on the use of Hα emission line equivalent width (EW) and the Hα and [NII] emission line strengths, but

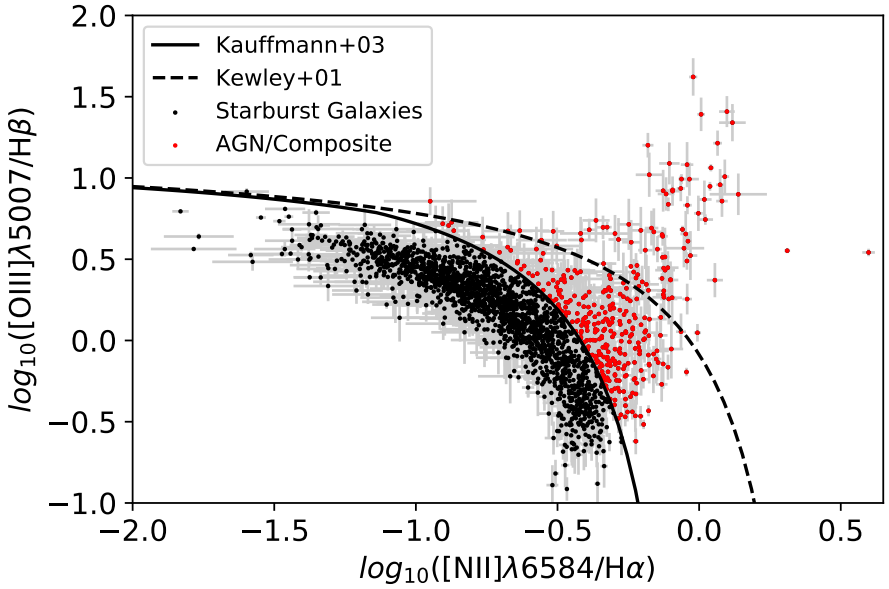

Figure 4.1: BPT diagram showing galaxies from the Initial Complete Sample identified as potential AGN hosts or starburst. Galaxies that qualify as AGN hosts are highlighted in red.

this was later simplified to WHAN (Cid Fernandes et al. 2011). Their plot uses the same horizontal axis as the BPT diagram, but uses the Hα line EW on the vertical axis (Figure 4.2, left). The method is not as reliable as the BPT diagram for detecting AGN because it relies on less information than the BPT diagram and the effect of AGN power relative to the optical continuum on Hα EW is empirical (Cid Fernandes et al. 2010). However, it can be applied to a larger population of galaxies because it does not need all four detected spectral lines needed for the BPT diagram. The plot highlights galaxies that are star-forming, possessing strong or weak AGN, or are "retired" galaxies with little new star formation but either with relevant emission lines (emission-line retired, ELR) or without emission lines (line-less retired, LLR) (Herpich et al. 2016). The impact of metallicity and ionisation from AGN on [NII]λ6583/Hα is the same as for the BPT diagram (Section 4.1), but the Hα equivalent width is related empirically to the power output due to ionising radiation relative to the optical output from stellar emission (Cid Fernandes et al. 2010). Considered together, they can separate AGN from star-forming galaxies, and star-forming

galaxies from those with ionisation due to older stellar populations.

Figure 4.2 shows the WHAN diagram for galaxies in the initial complete sample, with strong AGN highlighted. Positive emission line fluxes for emission with line flux/uncertainty ratios ≥3 were used throughout. The diagram has been modified from that originally published, to align the vertical demarcation of the star-forming/AGN regions with that from the BPT diagram (Figure 4.1). The original diagram used a boundary value for [NII]λ6583/Hα of -0.4 to separate galaxies with AGN from star forming galaxies, derived from Stasińska et al. (2006). In this work, the boundary value has been adjusted to -0.32, to define the upper edge of the star forming galaxy plot in Figure 4.2. A similar threshold of -0.3 was derived by Gavazzi et al. (2011), as a compromise between the original WHAN horizontal axis threshold of -0.4 and the horizontal axis asymptote for the AGN selection line by Kauffmann et al. (2003).

A total of 258 galaxies are identified as possessing strong AGN by this method. The galaxies with weak AGN are left in the sample because the presence of a weak AGN does not seem to impact SED fitting for dust emission or lead to very strong central concentration of ISM (see observations of GAMA64646 and 272990 in Chapter 2). Figure 4.2 (right) shows a Venn diagram comparing the galaxies with strong AGN from the BPT diagram with those from the WHAN diagram. Use of the WHAN diagram has identified a further 92 galaxies which may possess strong AGN, with a total number of 450 identified by BPT and WHAN.

4.3.3 Fibre Aperture Effects and AGN Detection

A known issue when using spectra of galaxies obtained through fibre-optic cables to classify galaxies using BPT and WHAN (Sections 4.3.1 and 4.3.2) is the effect of the small on-sky diameter of the fibre aperture. For galaxies that are relatively very close, light from the central regions only is transmitted to the spectrograph and AGN effects should dominate these spectra. For more distant galaxies, more light from regions away from the

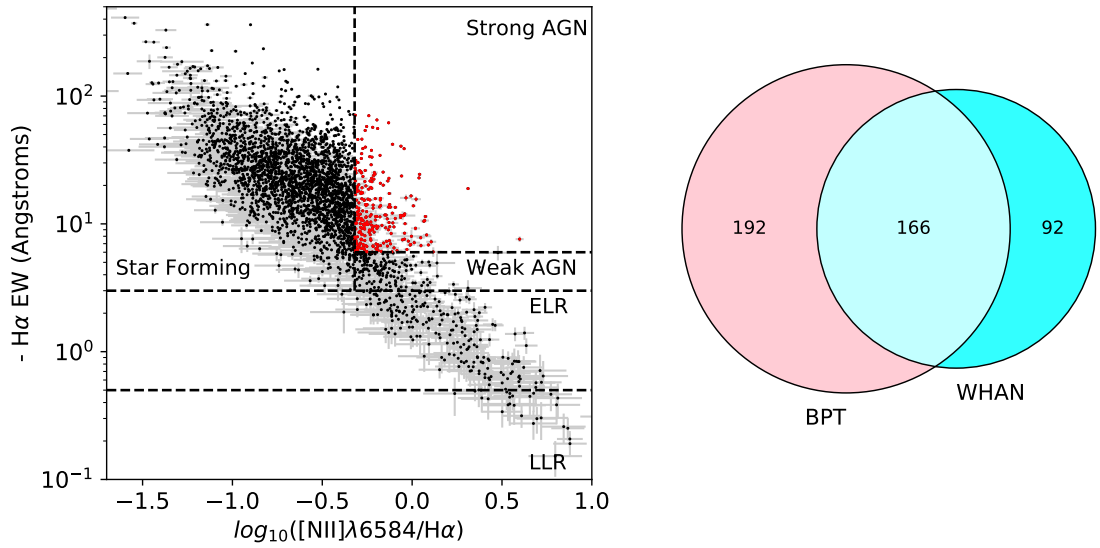

Figure 4.2: Use of WHAN diagram to identify AGN from the Initial Complete Sample. *Left*: WHAN diagram derived for the Initial Complete Sample. Galaxies qualifying as AGN hosts are highlighted in red. *Right*: Venn diagram showing the overlap between the results of using BPT and WHAN to identify AGN in the initial complete sample.

centre is received, diluting the light from the central regions. This effect may influence the absolute and relative strengths of the emission lines of interest for the BPT diagram, by weakening them and superimposing emission lines e.g. from star formation (Gómez et al. 2003). Kewley et al. (2006) imposed an upper redshift limit of 0.04 to avoid this issue. However, Agostino et al. (2023) examined this effect by obtaining spatially-resolved spectra for a selection of X-ray bright but lineless ("optically dull") galaxies. They concluded that, for spectra provided by SDSS with a 3 arcsec fibre aperture (Section 2.6.2), swamping by continuum light or dilution of spectra from AGN by those from star formation are not responsible for weak or atypical emission lines. Instead, the emission lines are genuinely weak. The 2df instrument used by GAMA (Section 2.6.3) has fibres with a 2.1 arcsec aperture, and similar arguments apply.

The impact of aperture effects on AGN detection via optical emission lines can be

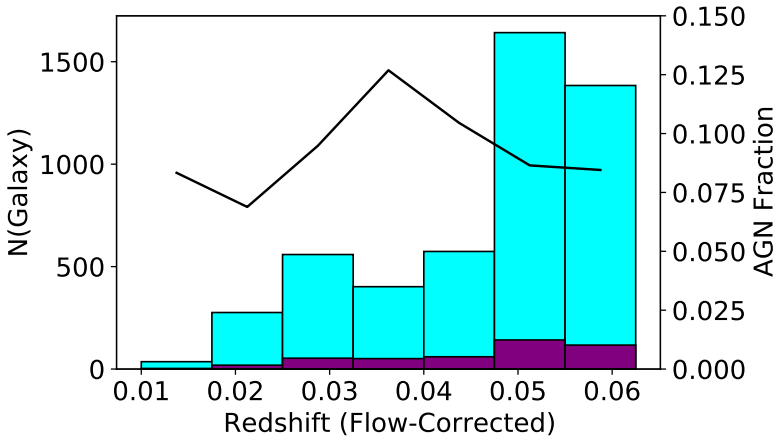

Figure 4.3: Histograms of galaxy numbers with increasing redshift. *Cyan*: The Initial Complete Sample before AGN removal, *Purple*: galaxies identified as having AGN via optical line diagnostics. The black line is the fraction of galaxies in each bin with AGN from optical diagnostics.

investigated using the samples created in this work. Figure 4.3 shows histograms of the number of galaxies in the Initial Complete Sample and galaxies with AGN identified by optical line diagnostics. The fraction of detected galaxies with increasing redshift is also shown as a trend line. There is no clear trend in the fraction of galaxies detected with increasing redshift, indicating that there is no clear issue with contamination of spectra as redshift increases. A downward trend would indicate increasing contamination of spectra by light from the outer regions of galaxies, as the fibre field of view covers greater radial distances with increasing redshift. Fibre aperture effects are therefore not considered further in this work.

4.3.4 Manual Examination of Spectra

Of the 4,936 galaxies identified in the initial complete sample, 4,925 had spectra of sufficient quality within GAMA II GaussFitSimplev05 to confirm the presence or absence of

the necessary line emission for analyses by BPT and WHAN diagrams. For the remaining 11, incomplete spectra only showing some spectral regions[4] were available for five of them, and only one of these (GAMA375530) had visible [NII] and H_α emission above the continuum noise level. The other four were kept in the sample because the available fragments of spectra covered the spectral range for use in BPT and WHAN diagrams and were free of relevant line emission. GAMA375530 was identified later as having an AGN by its 20cm continuum emission (Section 4.3.6), and was removed. The remaining six were kept in the sample, because statistically only a small portion of these might contain strong AGN and the number is low.

4.3.5 WISE Colour-Colour Diagram

Mateos et al. (2012) created a diagnostic diagram based solely on photometry from WISE infra-red observations (Section 2.8.7) to identify galaxies with AGN obscured by dust, e.g. from a dust torus surrounding the central supermassive black hole (Antonucci 1993; Jaffe et al. 1993, (Figure 4.4)) that is oriented to maximise obscuration towards the observer. The concept is based on the absorption of optical to X-ray radiation from the AGN by dust and re-emission at mid-IR wavelengths, and involves plotting colours based on the differences in magnitudes between WISE passbands.

The GAMA II catalogue WISECatv02 (Cluver et al. 2014) provides flux densities and recommended apparent AB magnitudes (see Section 4.6.1) for galaxies for the WISE passbands W1 (3.4μm), W2 (4.6μm) and W3 (12μm) which are required for this method. These were converted to Vega magnitudes using published magnitude offsets (-2.699, -3.339, -5.174, -6.620 for W1 - W4)[5] for compatibility with the Mateos et al. (2012) diagnostic diagram. No Galactic extinction correction was applied, because the effects of extinction at the wavelengths for the WISE passbands (>1μm) are minimal and similar over the wavelength range considered (Gordon et al. 2003, their Figure 10). Galaxies with

[4] http://www.gama-survey.org/dr2/tools/sov.php

[5] https://wise2.ipac.caltech.edu/docs/release/allsky/expsup/sec4_4h.html#conv2ab

Figure 4.4: Hubble Space Telescope (HST) colourised image of the accretion disc around the central supermassive black hole of NGC4261, consisting of gas and embedded dust. Toroidal morphology is apparent. Image size is 4.25 x 3.75 arcsec, with 0.44 arcsec pixels.

$>5\sigma$ detection of flux density were selected for analysis, in line with Mateos et al. (2012). However, experimentation showed that one galaxy, GAMA417403, was found to have an AGN with 4.3σ detection in one WISE passband, and was flagged as containing an AGN. Reducing the detection level from 5σ to 3σ introduced galaxies with large uncertainties in magnitudes into the analysis, and did not introduce any further AGN hosts apart from GAMA 417403.

Figure 4.5 shows the 1,836 galaxies in the Initial Complete Sample with $>5\sigma$ detection of flux density plotted on the Mateos et al. (2012) diagnostic diagram, and GAMA417403 because it has been flagged as containing an AGN. The criteria for detection of obscured AGN within this diagram (forming a wedge-shaped region) are also shown, with galaxies identified as AGN highlighted. The plot is similar to that in Mateos et al. (2012), their Figure 2, with most galaxies centred on a y-axis value of around zero and galaxies rising upwards from this towards the selection region for AGN. This method identified six galaxies with AGN overall, four of which are in addition to

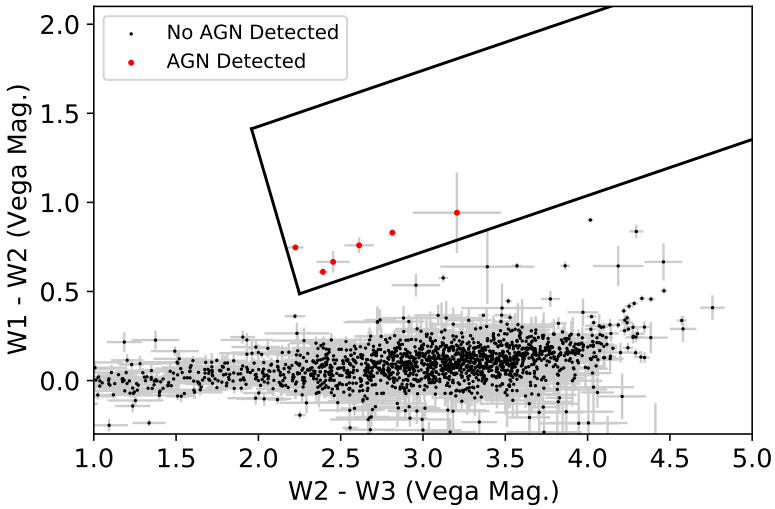

Figure 4.5: WISE colour-colour diagram derived for the initial complete sample. Galaxies lying within the wedge-shaped region are identified as containing AGN.

those identified by BPT and WHAN. This brings the total number of galaxies with AGN to 454.

4.3.6 20cm Emission

AGN are known to emit synchrotron radiation at radio wavelengths with a power-law spectral energy distribution (SED). A typical exponent for this power law in terms of wavelength is 0.5 – 0.7 (e.g. Condon 1992, their Figure 1). If a flux density measurement at one wavelength for such a spectrum is available, the power law spectrum can be used to estimate the flux density at other wavelengths. This principle can be adopted as explained below to detect AGN of interest from continuum emission from galaxies at 20cm in the Initial Complete Sample, using data from from the VLA FIRST survey (Section 2.8.7).

For this work, AGN whose synchrotron spectra might interfere with the SED for dust emission at $\leq 850\mu$m are removed using this method. The criterion used is that the flux density for a galaxy at 20cm from the VLA FIRST survey is less than 10 mJy. This

ensures that the flux density from synchrotron emission at 850 μm, where the SCUBA-2 camera (Holland et al. 2013) on the James Clerk Maxwell telescope (JCMT) operates (Section 2.8.7), is less than 0.7 mJy. This is below the sensitivity that is practical to observe with this telescope and camera for a single pointing with the DAISY scan pattern (for less-extended sources), based on tests with the observation planning tool for JCMT[6]. A sensitivity of 1.2 mJy/beam (~15 arcsec FWHM at 850μm can be achieved in around 4 hours total observing time in good weather, at a target elevation averageing 40° and using the recommended 6.5 arcsec per pixel map scale. Possible JCMT observations were used to set the criterion for AGN removal because it is possible to achieve better constraints on dust mass and properties by combining flux densities from JCMT/SCUBA-2 with data from Herschel (Saintonge et al. 2018; Lamperti et al. 2019). The analysis in Chapter 4 is based on Hershel data alone, and future research may wish to combine this with JCMT observations for more detailed investigations.

The GAMA II catalogue TilingCatv46 contains flux densities at 20cm from VLA FIRST for many galaxies, including all 4,936 galaxies in the initial complete sample. Of these, 11 had flux densities of 10 mJy or over at 20cm, five of which are in addition to those identified by BPT, WHAN and WISE photometry. These galaxies are referred to as "radio-loud" in this work, while the remaining AGN-bearing galaxies are "radio-quiet". The 11 radio-loud galaxies were identified as suspected AGN hosts, and the total number of galaxies identified with AGN is therefore 459.

Of the five galaxies which are radio-loud but are not identified as AGN by the diagnostics used in this work, four are confirmed as AGN by other means. Three of them (GAMA77967, 205082 and 238211) have radio-loud AGN identified by excess 20cm continuum emission compared to expectations from star formation (Best et al. 2005). GAMA238211 is an obscured AGN (Weston et al. 2017) within a merging group (Tempel et al. 2017). The remaining galaxy, GAMA375530, features in a star-forming galaxy group based on detection by GALEX (Section 2.6.1) ultraviolet photometry. It remains

[6]https://proposals.eaobservatory.org/jcmt/calculator/scuba2/time

classified as having an AGN because it cannot be shown that its radio continuum emission is wholly from star formation.

4.3.7 Removal of all galaxies with detected AGN

A combined set of galaxies with AGN was created using Astropy.Table Boolean outer joins, sequentially adding in further subsets after each outer join. A total of 459 galaxies were found to have AGN by the combination of methods used above that qualify for removal from the initial complete sample. Subtracting these from the Initial Complete Sample leaves 4,477 galaxies that are free of strong AGN.

4.4 Removal of Galaxies With Gravitationally-Lensed Sub-mm Emission

It is possible that the sub-mm emission from some of the galaxies in the initial complete sample is not from the galaxies themselves, but is from a much more distant source along the line of sight. This emission from the more distant object would be gravitationally lensed by the foreground galaxy of interest, and would appear stronger than if measured directly from its point of origin. Because of this, the sub-mm emission in these cases would not represent the dust content of the galaxy, and SED fitting would then give misleading results. Methods for identifying gravitationally-lensed continuum emission from distant dust sources, and their application to the galaxy sample derived earlier, are presented below.

A straightforward test of whether sub-mm emission detected by Herschel (Section 2.4) is gravitationally lensed is to examine whether it has been substantially redshifted. A simple test based on this principle was proposed by Negrello et al. (2010), who considered

sources with a Herschel measured flux density over 100 mJy at 500μm to be gravitationally lensed. However, Nayyeri et al. (2016) and Negrello et al. (2017) later found that galaxies that are bright at the longer-wavelength Herschel passbands could also be relatively close-by and bright at sub-mm wavelengths. This criterion is therefore not used.

The method adopted was that of González-Nuevo et al. (2012), which uses a combination of criteria to detect suitably strong emission sources which are likely to be at high redshift (e.g. $z \geq 1.2$), based on the changes in the observed dust emission spectrum due to redshift:

- Flux density at 250 μm $\geq$ 35 mJy;
- Flux density at 350 μm $\geq$ 85 mJy;
- Ratio of flux densities at 350 μm and 250 μm > 0.6;
- Ratio of flux densities at 500 μm and 350 μm > 0.4.

These criteria were selected to detect galaxies whose cool dust sub-mm spectra have been substantially redshifted. Cool dust emission from a local galaxy might have a peak at wavelengths around 150 μm, with falling flux densities beyond that. However, the equivalent redshifted spectrum might have a peak beyond 500 μm and either increasing flux densities or a reduced negative slope with increasing wavelength from 250, 350 and 500 μm Herschel passbands.

The sub-mm flux densities needed for detecting gravitationally lensed sub-mm emission were obtained from the H-ATLAS DR1 (v1.2) catalogue (Section 2.8). Galaxies with $\geq 3\sigma$ detection at 250, 350 and 500μm were selected, and a sample of galaxies that meet the criteria above was created. This sample was then inner-joined with the initial complete sample of 4,477 galaxies after AGN removal. 19 galaxies were found to meet the criteria for gravitational lensing, and were removed. This leaves 4,458 galaxies in the required clean and complete sample. It is possible that some of the removed galaxies have

sub-mm emission that is actually within the redshift range for the initial complete sample, and may simply have colder dust temperatures than anticipated. However, because of the low numbers selected for removal this will have a small impact on the parent sample. The number of galaxies meeting the Negrello et al. (2010) criterion (with 3σ detection at 500μm) is 105, only one of which features in the galaxies selected on the basis of the criteria by González-Nuevo et al. (2012). It is therefore likely that 104 of these galaxies compliant with the Negrello et al. (2010) criterion are actually relatively local sources and not distant gravitationally-redshifted emission.

4.5 Clean and Complete (Parent) Sample

A total of 4,458 galaxies remain from the Initial Complete Sample of 4,936 galaxies, after removal of galaxies with AGN identified with multiple techniques and removal of galaxies with suspected gravitationally lensed sub-mm emission. This sample is referred to in this work as the Parent Sample. Figure 4.6 compares the initial sample and the Parent Sample in a plot of M_r versus redshift. No major gaps appear in the distribution, which would otherwise indicate a selection bias. In summary, the Parent Sample contains galaxies of all morphological classifications within the GAMA equatorial regions within redshift limits of $0.002 \leq z \leq 0.06$, with galaxies containing strong AGN removed by multiple techniques. It has also been screened for galaxies affected by gravitationally-lensed sub-mm emission, with affected galaxies removed.

4.6 Morphological Classification

The Parent Sample contains galaxies of all morphological types, with no attempt made to select on the basis of morphology. Visual morphological classifications need to be

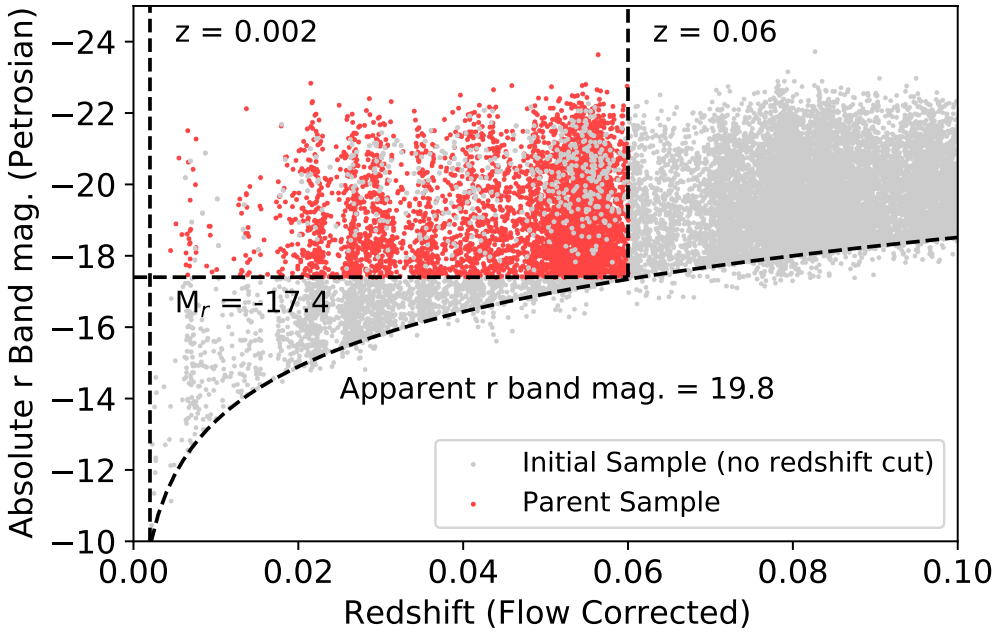

Figure 4.6: Absolute r-band magnitude versus redshift for the Initial Sample and Parent Sample. Error bars are too small to be plotted effectively.

assigned to the galaxies where possible, to allow differences and trends for galaxy properties for different morphologies (and continuous numeric measures of morphology) to be explored. Two methods are used in this work. One is the morphology classifications which feature in GAMA II catalogue VisualMorphologyv03. The other is classification by volunteers from the general public using a decision tree, as part of the GAMA-KiDS-GalaxyZoo project (Section 2.8.2). Classifications by both methods are described below, with comparisons and final classifications for all galaxies. This work treats all galaxies with smooth morphology in optical images as early-type (ETGs).

4.6.1 Morphologies from GAMA II

The GAMA II catalogue VisualMorphologyv03 contains 38,795 galaxies in the GAMA equatorial regions, classified by at least one of the following works: Moffett et al. (2016), Robotham et al. (2014), Kelvin et al. (2012), Driver et al. (2011) and Lintott et al. (2011).

Images from SDSS (Section 2.8.7) were used for visual classification by a team of specialists. The classifications by Moffett et al. (2016) are used in this work, based on a flowchart which is reproduced in Figure 4.7. Galaxies are initially selected according to whether they are spheroid dominated, disc dominated, Little Blue Spheroids (LBS) or in fact stars. Spheroid and disc dominated galaxies are then classified according to whether they are single or multicomponent, and if multicomponent whether they have galactic bars. Where a classification is possible, galaxies were assigned a code within the catalogue corresponding to a nominal Hubble type. The codes of interest in this work are:

- 1: E (spheroid dominated, single component)
- 2: LBS (Little Blue Spheroid)
- 11: S0/Sa (spheroid dominated, multicomponent, unbarred)
- 12: SB0/SBa (spheroid dominated, multicomponent, barred)
- 13, Sab - Scd (disc dominated, multicomponent, unbarred)
- 14, SBab - SBcd (disc dominated, multicomponent, barred)
- 15: Sd/Irregular (disc dominated, single component)

Codes 3 - 9 are not used in GAMA II classifications, and 10, referring to non-elliptical galaxies, is not used in this work. It must be noted that the Hubble types allocated to galaxies are not definitive, especially for spiral features. For example, interacting or merging disc galaxies could be classified as code 13 (Sab - Scd) because of disc-dominated structure and multiple features within the disc, and not because of spiral features. In addition, codes 11 and 12 do not distinguish between lenticular galaxies (S0, SB0) and bulge-dominated, weak spirals (Sa, SBa). This means that a sample of lenticulars derived from this catalogue will have some level of contamination by weak spiral galaxies without the smooth morphology used to classify ETGs in this work. The LBS

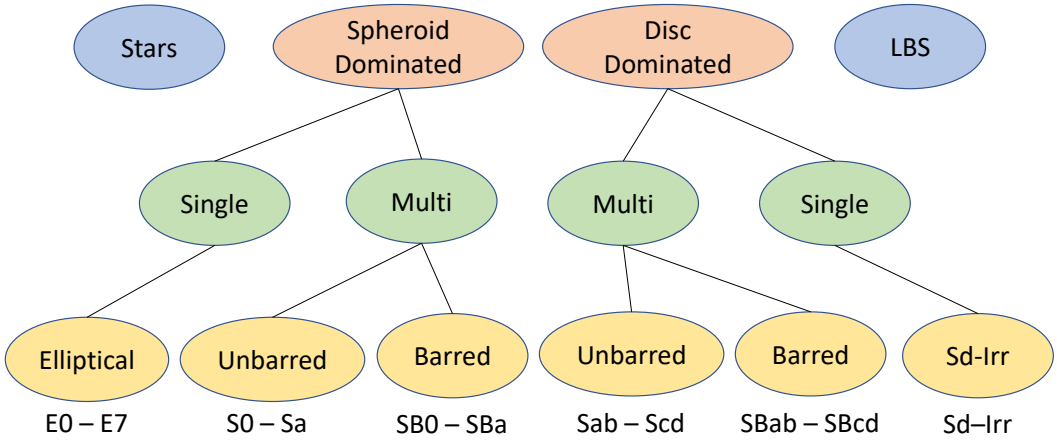

Figure 4.7: Flowchart used for the GAMA II morphology classifications presented in GAMA II VisualMorphologyv03 (Moffett et al. 2016). The endpoint Hubble types are nominal only.

classification was used to highlight compact, spheroidal galaxies that are probably undergoing intermittent, stochastic star formation (Kelvin et al. 2014). In this work, galaxies with and without bars are combined when creating morphological classifications.

Subsets of galaxies from the Parent Sample were created using Astropy.Table.Join and Python-based filtering methods to isolate relevant morphology classification code presented above. Table 4.1 summarises the numbers of galaxies corresponding to each code within GAMA II VisualMorphologyv03. Only ten out of 4,458 galaxies are unclassified. Of these, nine could not be assigned a morphology classification (code 60) and one was not in the catalogue. Examination of SDSS images of the nine unclassified galaxies using the GAMA II Single Object Viewer[7] showed that all of them were located within the footprint of larger galaxies, making visual classification impossible.

[7]http://www.gama-survey.org/dr3/tools/sov.php

Table 4.1: Results of GAMA morphological classification for the Parent Sample based on GAMA II VisualMorphologyv03 (Moffett et al. 2016).

Code & Nominal Hubble Type	No.
1: E	618
11, 12: S0/Sa, SB0/SBa	663
13, 14: Sab/Scd/SBab/SBcd	1119
15: Sd/Irr	1888
2: Little Blue Spheroid (LBS)	160
60: Not Classified	9
Not in catalogue	1
TOTAL:	**4458**

Figure 4.8 illustrates the separations of the morphological classifications on a colour-magnitude plot. Each plot shows the optical colour (difference in AB magnitude for SDSS g^* and r^* passbands[8]) against absolute r-band AB magnitude (as a proxy for stellar mass, see Section 5.1) calculated using apparent AB magnitude and distance moduli discussed in section 4.2. Better separation of the Red Sequence and Blue Cloud can be achieved by plotting u^* - r^* instead of g^* - r^* (e.g. Salim 2014). However, u-band photometry avaible from GAMA is less complete than for g-band, and the uncertainties on u-band flux densities are greater than those for g-band photometry. Apparent AB magnitudes were calculated using flux densities in the GAMA II catalogue 21BandPhotomv03 (Driver et al. 2016) derived using SExtractor (Bertin & Arnouts 1996), which locates objects within an image and performs photometry on them. The photometry for SDSS and near-infrared passbands in this catalogue is derived using the r-band Kron radius (Kron et al. 1983) and is corrected for Galactic extinction. An alternative GAMA II catalogue, Lambdarv01, is also available that provides similar photometry but derived using the purpose-built package Lambdar (Wright et al. 2016). Photometry data from both catalogues produce similar plots within this Chapter, but slightly more galaxies in the Parent Sample (~5%) have

[8] * means corrected for Galactic extinction.

data within 21BandPhotomv03 than LambdarCatv01. The former is therefore used for this work for illustrative plotting where required. AB magnitudes are chosen for relative simplicity of calculation from supplied flux densities in Jy using a constant zero-point flux density across passbands. Catalogue flux densities are converted to AB magnitudes using Pogson's relation as follows (Oke & Gunn 1983):

$$m_{AB} = -2.5log_{10}F_{\nu} - 48.60 \tag{4.1}$$

where F_{ν} is flux density in cgs units of erg s^{-1} cm^{-2} Hz^{-1}. This relation can be converted to the following form when using flux densities per passband in Jy. The constant in Equation 4.1 can be divided by 2.5 and made a divisor of the flux density. Evaluating $10^{\frac{48.6}{2.5}}$ yields a value of 3.631×10^{-20} erg s^{-1} cm^{-2} Hz^{-1}, which is equivalent to 3,631 Jy (1 Jy is 10^{-23} erg s^{-1} cm^{-2} Hz^{-1}). Equation 4.1 can then be written as:

$$m_{AB} \simeq -2.5log_{10}\left(\frac{S_{\nu}}{3631Jy}\right) \tag{4.2}$$

where S_{ν} is the flux density per passband in Jy.

The grey points in Figure 4.8 represent 4,435 galaxies from the Parent Sample that have g^*- and r^*-band flux densities in 21BandPhotomv03 with $>3\sigma$ uncertainty. The coloured points show the locations of galaxies with different GAMA II morphological classifications. Note that the left-hand edge of the galaxy distribution in the plots is not smooth. This is because the original galaxy selection (Section 4.2) is based on SDSS r-band Petrosian magnitudes as supplied in the GAMA II TilingCatv46 used for target selection. Use of calculated AB magnitudes as described above may give slightly different results.

Figure 4.8 shows that the location of E and Sab/Scd/SBab/SBcd galaxies are as expected and coincide with features previously identified within this parameter space (Baldry et al. 2004; Bell et al. 2004; Faber et al. 2007; Martin et al. 2007). E galaxies

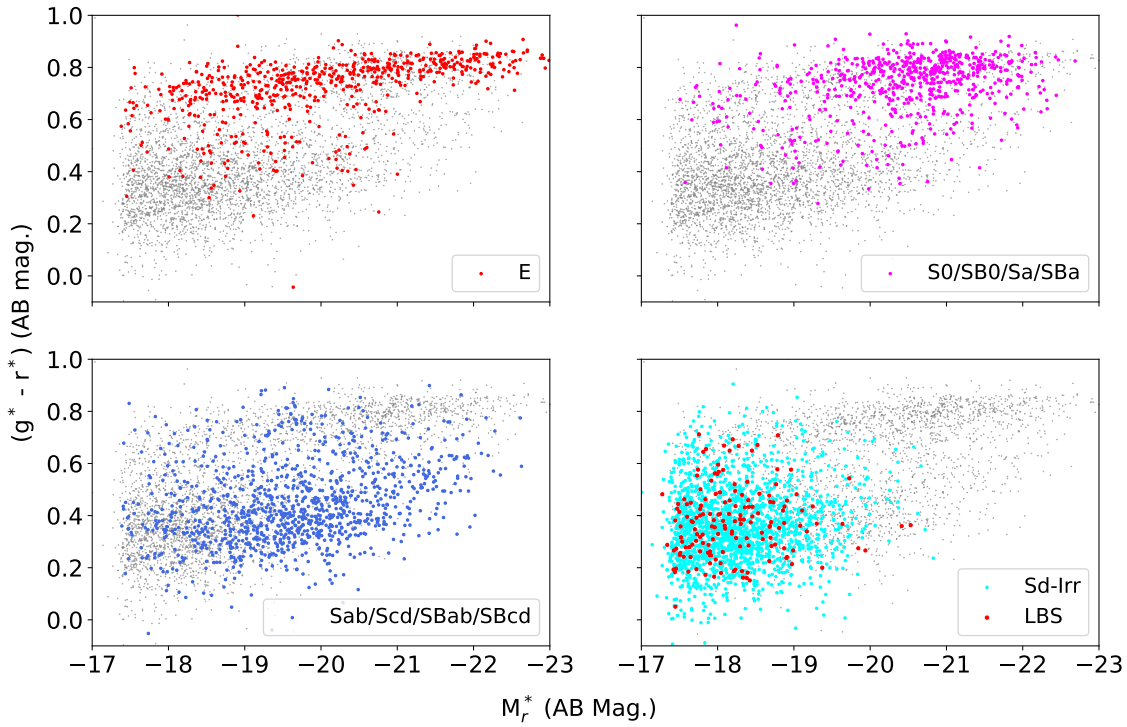

Figure 4.8: Plots of Galactic extinction corrected g* - r* colour versus absolute r*-band magnitude for the nominal morphological types identified within GAMA II. Grey points are for galaxies in the whole Parent Sample for comparison.

generally lie on the ”red sequence”, a narrow distribution of galaxies with red optical colours (higher g* - r*) becoming slightly bluer at lower stellar mass (i.e. higher absolute r-band magnitude). Sab/Scd/SBab/SBcd galaxies generally lie in the ”blue cloud”, a more expansive region at lower stellar mass with bluer optical colours. Between these is the less-populated ”Green Valley” (GV) region (Wyder et al. 2007). A degree of scatter into different regions can be expected for these populations. For example, red spirals (Masters et al. 2010) and blue ellipticals (Schawinski et al. 2009) are known galaxy types.

The location of Sd/Irr and LBS galaxies in Figure 4.8 occupy the same parameter space as each other, at at the lower-mass end of the Blue Cloud with a few galaxies lying within the GV. The location of S0/Sa galaxies (barred or unbarred) is less well-defined,

with more scatter away from the red sequence at higher stellar mass towards the blue cloud. This could be due to the presence of galaxies with weak spiral (or in general, late-type) features which are not identified by the methods used for morphological classification in GAMA II. This contamination of the S0/Sa sample has the potential to distort any comparisons with the sample of spiral galaxies, and some means of reducing this contamination is needed. The next section uses an alternative method of morphological classification to identify these weak spirals, and allow the removal of as many of them as possible from the early-type classifications within the parent sample.

Also apparent in Figure 4.8 (top left panel) is a population of bluer elliptical galaxies at lower brightness compared to the majority of the S0/Sa galaxies shown in the top right panel. These are also apparent in subsequent sections, and are discussed further in Section 5.8.

4.6.2 Morphologies from GAMA-KiDS-GalaxyZoo

The allocation of morphology classifications to individual galaxies within GAMA-KiDS-GalaxyZoo is done using a flowchart used by volunteer classifiers from the general public. The relevant section of the flowchart developed by GAMA-KiDS-GalaxyZoo and used in this work is shown in Figure 4.9. The volunteer classifiers were shown high-resolution colour optical images from the KiDS survey (Section 2.8.2), scaled to ensure that galaxies have approximately the same apparent size on screen. The first decision relevant to this work is whether a galaxy being classified is smooth or has features. If it has features, the subsequent question explores whether the galaxy is edge-on. If not, then the galaxy is classified as having a bar or no bar (not used in this work), and whether the galaxy has spiral arms or not. The latter criterion is different to those used for GAMA II to identify spiral galaxies and is used to produce cleaner ETG samples later on. Subsequent questions within the flowchart are not used in this work, and are not shown in Figure 4.9.

The preliminary data catalogue for GAMA-KiDS-GalaxyZoo (Kelvin et al., in

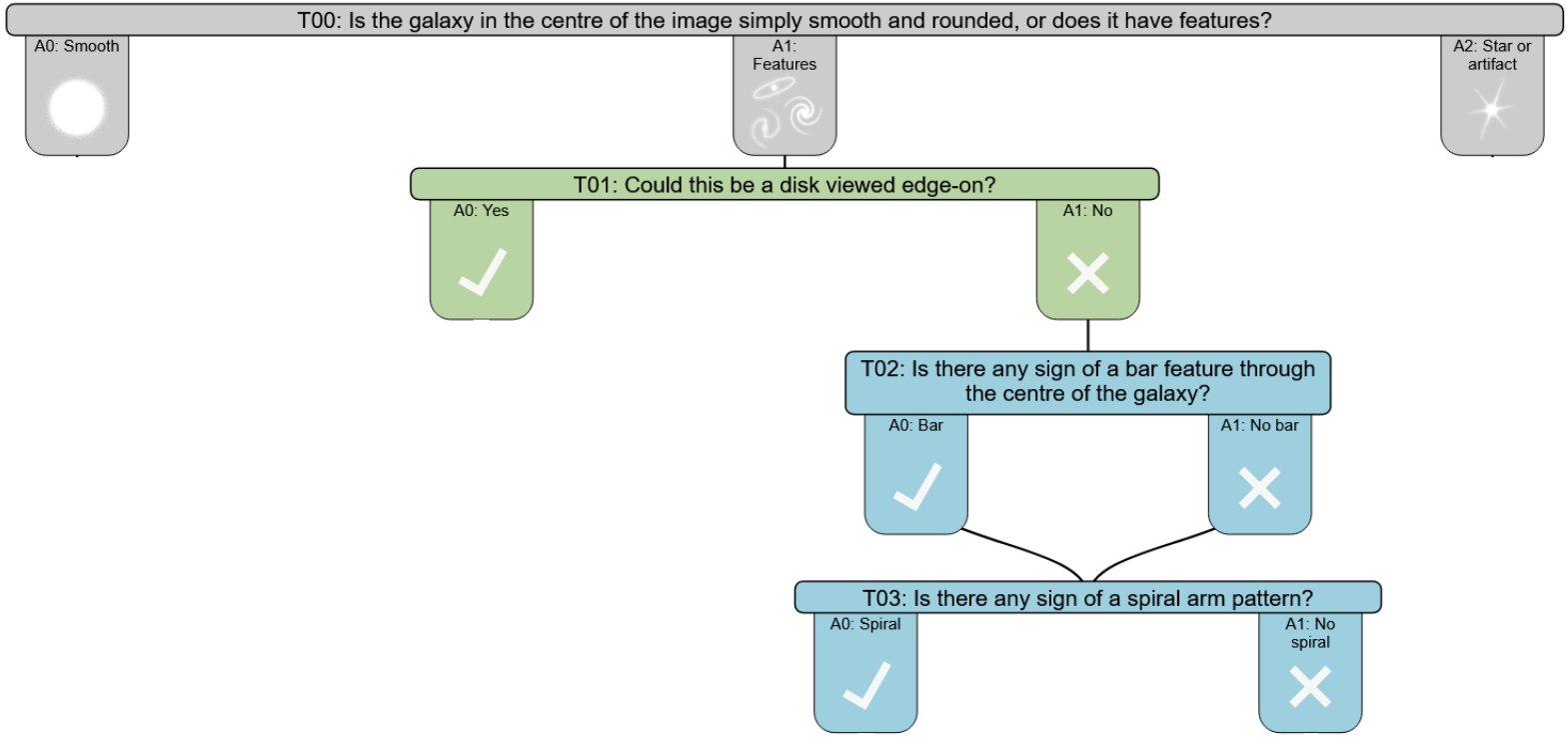

Figure 4.9: Extract of flowchart used by GAMA-KiDS-GalaxyZoo volunteers to classify the morphologies of galaxies (Porter-Temple et al. 2022).

prep.), supplied in January 2018, contains the number of votes for each question in each category for each galaxy, along with the fraction of the votes for each question in a category. The vote numbers have been corrected for the reliability of individual classifiers. The method used in this study to classify individual galaxies treats the vote fractions for each question as probabilities that the answer is true (Hart et al. 2016). Multiplying the vote fractions along a pathway through the flowchart is then the probability that the endpoint of the pathway is true. On this basis, this study classifies the galaxies in the Parent Sample according to endpoints referred to as smooth, edge-on, spiral, no-spiral and star/artefact. These endpoints represent a complete set within the flowchart in Figure 4.9 with no other parallel pathways, and the probabilities for the categories derived for any given galaxy will sum to 1. The number of votes for the endpoint also needs to be 5 or greater in this study, to avoid statistical issues with small samples (Hart et al. 2016). It was expected initially that the smooth classification would represent spheroidal galaxies (ellipticals), and edge-on and no-spiral galaxies would represent lenticular galaxies.

Endpoint classifications were assigned to galaxies in the Parent Sample by selecting the maximum probability above a threshold of 0.4. Selecting the dominant probability above this threshold ensures that only one other probability could approach the dominant one, with the remainder being significantly lower. If the threshold were as low as 0.33, it would be possible to have one dominant probability of 0.34 and two others above 0.3, making a choice of meaningful classification more challenging. Any galaxy with all probabilities less than 0.4 is regarded as unclassified. For comparison, a previous study used a threshold probability >0.5 to ensure clean samples at the expense of completeness (Hart et al. 2016). This study aims to produce samples which are as clean and complete as possible, so a reduction in threshold is appropriate to improve completeness.

As an example of this process, the detailed probabilities for GAMA64646, a weak spiral galaxy observed by ALMA in 2016 (Sansom et al. 2019), are presented. Figure 4.10 shows the vote fractions for this galaxy within the GAMA-KiDS-GalaxyZoo catalogue. The bar chart shows that the highest probability assigned to a classification is 0.47 for

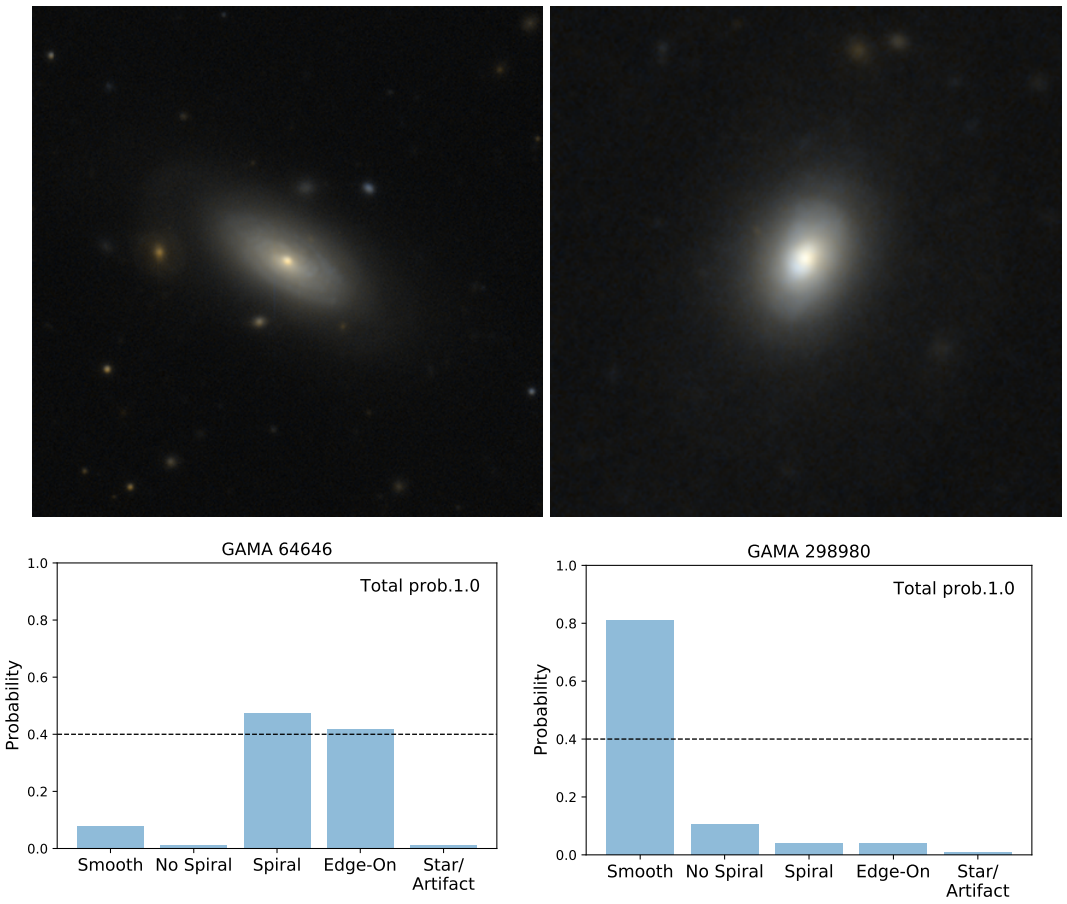

Figure 4.10: Probabilities for each GAMA-KiDS-GalaxyZoo morphological classification for GAMA64646 (weak spiral) and GAMA298980 (elliptical). Images are tiles shown to GAMA-KiDS-GalaxyZoo classifiers.

spiral, with edge-on next at 0.4. The other classifications have significantly lower probabilities, summing to 0.13. Although GAMA64646 was identified as an ETG in a previous ETG sample from GAMA by Agius et al. (2013), and was selected for observation by ALMA as discussed in Chapter 2, this new work using images from KiDS has identified weak spiral features within it and it is now classified as Spiral. Also shown in Figure 4.10 are the probabilities for GAMA298980, which show that smooth morphology is clearly preferred by the classifiers. The finding is consistent with the visual classification as Elliptical from GAMA II VisualMorphologyv03.

The method described above was applied to the Parent Sample. Of the 4,458 galaxies

Table 4.2: Results of morphological classification using GAMA-KiDS-GalaxyZoo (based on KiDS images) for the Parent Sample.

Classification	No.
Smooth	2480
No Spiral	361
Spiral	797
Edge-on	395
Star/Artifact	41
Unclassified	382
Not in catalogue	2
TOTAL:	**4458**

in the clean and complete Parent Sample, 4,456 have classification data from GAMA-KiDS-GalaxyZoo. Table 4.2 shows the numbers of galaxies assigned to each endpoint classification. Significantly more galaxies are classified as Smooth (2,480) compared to the total number of ETGs (1,441) from GAMA II classifications (Table 4.1).

Figure 4.11 shows the galaxies for each endpoint classification plotted on colour magnitude diagrams. With the exception of spiral galaxies, the classifications have galaxies split between the blue cloud and the red sequence. The smooth and no-spiral classifications includes galaxies along the red sequence as could be expected, but also include a dominant number of less luminous (lower stellar mass) galaxies in the blue cloud that also meet the smooth and no-spiral criteria. The edge-on criterion has identified a mix of galaxies based on colour, presumably split across morphologies. Only the spiral classification appears successful, because it mostly traces the Blue Cloud successfully towards higher-mass red spirals. Based on the classification for GAMA64646 as having very faint spiral features shown in Figure 4.10, these spirals identified using GAMA-KiDS-GalaxyZoo data are likely to have genuine spiral features within the images used for classification.

The number of spirals in the sample identified by this method is less than the number

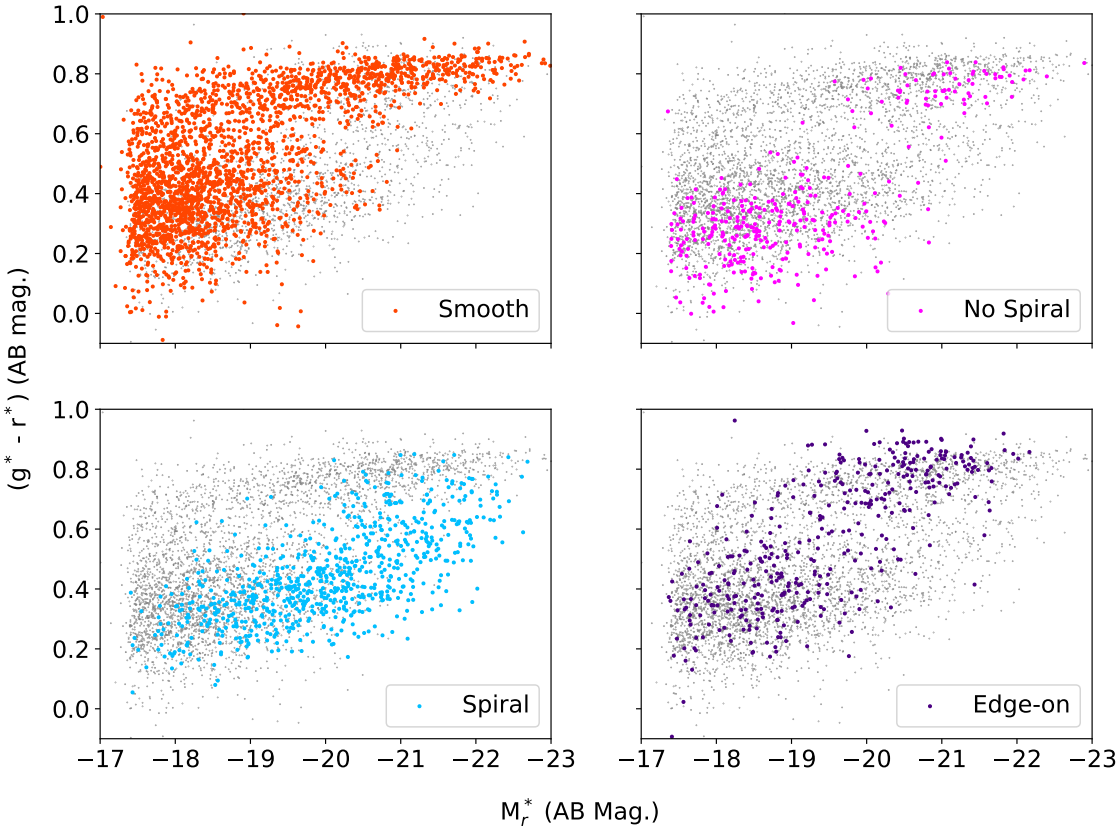

Figure 4.11: Plots of Galactic extinction corrected g* - r* colour versus absolute r*-band magnitude for the morphological types identified within GAMA-KiDS-GalaxyZoo. Grey points are for galaxies in the whole Parent Sample for comparison.

of "spirals" (classification codes 13 and 14) from GAMA II, in spite of the improved spatial resolution of the images used for classification (797 compared to 1,119). This could be because the criterion used for identifying spirals are different for each method, with only GAMA-KiDS-GalaxyZoo selecting on actual spiral features. The volunteer classifiers for GAMA-KiDS-GalaxyZoo as a whole could also have been taking a cautious approach to classification, and were more inclined to assign galaxies to the smooth, no-spiral and edge-on categories. This could explain why a significant number of galaxies (382) are unclassified using GAMA-KiDS-GalaxyZoo data because of split voting. It

could also explain the significant numbers of smooth (2,480) and edge-on (395) galaxies, because classifiers could place the more challenging cases in these categories rather than consider more complex options. This is explored further in Section 4.6.3.

Overall, this GalaxyZoo method has not been successful for isolating ETGs in the Parent Sample, because the classification options did not specifically select them. However, it is capable of distinguishing objects with features from those without, independently of galaxy colour. This is particularly the case for Smooth and Edge-on classifications. The identification of spiral galaxies, including those with weak spirals, is useful to remove some possible contaminant spiral galaxies from the ETG samples created using GAMA II data. This is implemented in in Section 4.6.4. It may be possible to use later selections within the GAMA-KiDS-GalaxyZoo flowchart to refine morphological classifications, but this is left for future research.

4.6.3 Morphological Classification at High Ellipticity

The number of edge-on galaxies identified from GAMA-KiDS-GalaxyZoo data (395), with a mixture of ETG and LTG properties, suggests that some could be edge-on lenticular or spiral galaxies that could not be identified as such. The effect of ellipticity on morphology classification is therefore investigated in this section.

Figure 4.12 shows the ellipticity distribution for all galaxies in the Parent Sample, derived using fits of single-component Sérsic surface brightness profile (Equation 3.1) from GAMA II SersicCatSDSSv09. There are very few galaxies with extremely high or low ellipticities, with most having ellipticities between 0.15 and 0.85.

Figure 4.13 shows the ellipticity distributions (derived from axis ratios) for the GAMA II morphology classifications shown in Table 4.1. The number of spheroidal galaxies (E/LBS) is very low at ellipticities greater than 0.7, which is to be expected given that the Hubble classification E7 represents the limit for Ellipticals or other

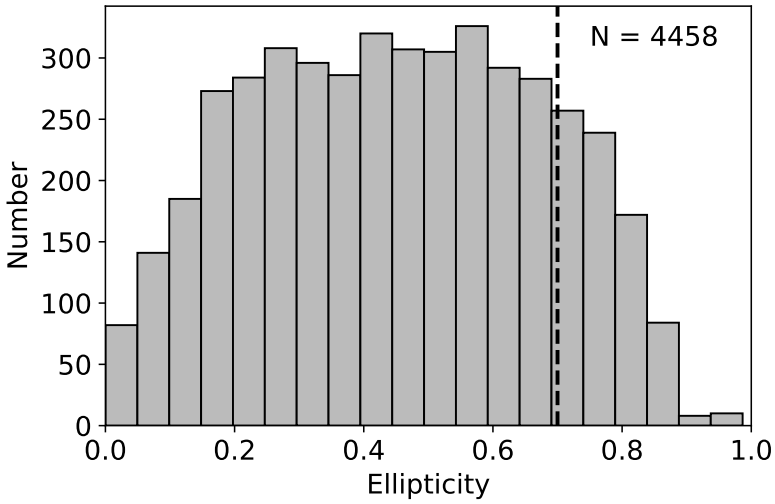

Figure 4.12: Distribution of ellipticities within the clean and complete Parent Sample.

spheroidal galaxies. Ellipticities for LBS also appear to be generally greater than those for Es, suggesting that they may be flatter. The remaining classifications, including those for Sab/Scd/SBab/SBcd and S0/SB0/Sa/SBa show ellipticity distributions extending to high values of ellipticity >0.85, in line with the general ellipticity trend for the whole sample. The classification scheme in Figure 4.9 allows the assignment of morphologies to galaxies at high ellipticity, but the relationship between these classifications and the actual galaxy morphologies at high ellipticity remain uncertain.

Figure 4.14 shows a similar plot of ellipticity distributions for the GAMA-KiDS-GalaxyZoo classifications shown in Table 4.2. The classification of galaxies as Smooth has a similar overall distribution to the whole Parent Sample shown in Figure 4.12. This suggests contamination by disc galaxies, because spheroidal galaxies should have ellipticities <0.7. However, the numbers of classifications as Spiral, No Spiral or Unclassified decrease sharply with increasing ellipticity beyond 0.7, while numbers of galaxies classified as edge-on increase sharply. It is possible that the availability of the edge-on classification has prevented a decision being made about whether galaxies with ellipticities greater

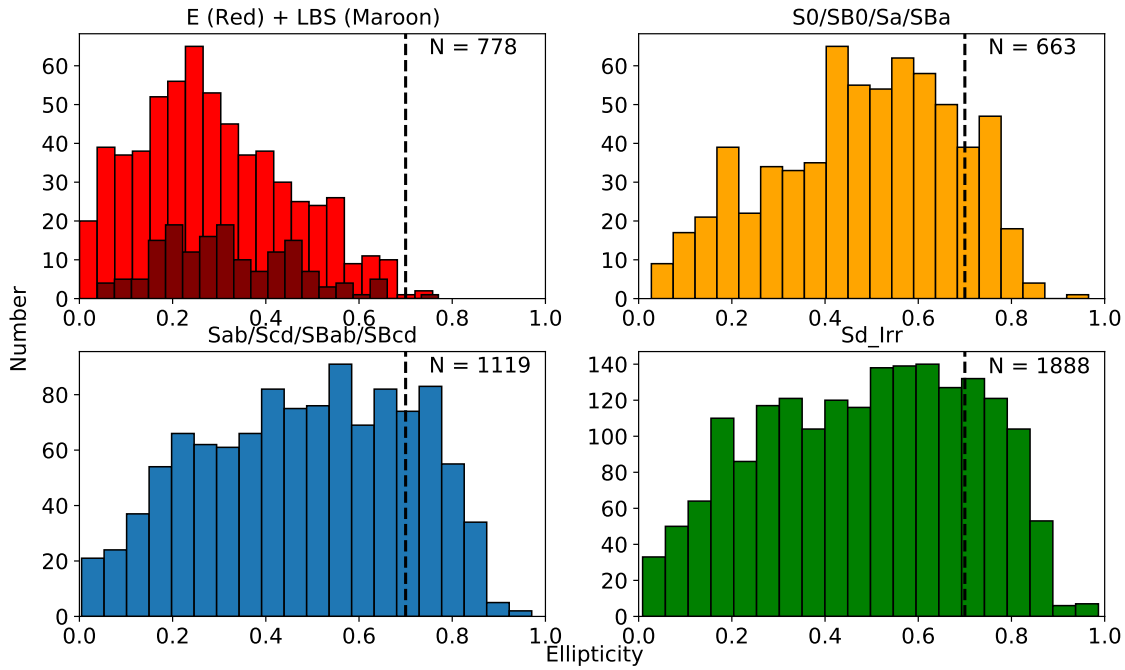

Figure 4.13: Ellipticity distributions within GAMA II morphology classifications for the clean and complete Parent Sample.

than 0.7 have spiral features or not. Given this limitation, use of morphological classification from GAMA-KiDS-GalaxyZoo data and the methods presented above needs to be restricted to those galaxies with ellipticities ≤0.7. It may be possible to develop other metrics for spiral structure using the catalogue data focussing on detailed shape information, but that is left for future research.

4.6.4 Final Morphological Classifications

Of the two morphological classification methods used above, the GAMA II method appears to provide fewer non-classifications according to Hubble type and arguably is more successful on this basis. However, the classification of early-type disc galaxies is known to be affected by the inclusion of galaxies with weak spiral features, i.e. those not detected by the methods used by Moffett et al. (2016) for the GAMA II morphology catalogue.

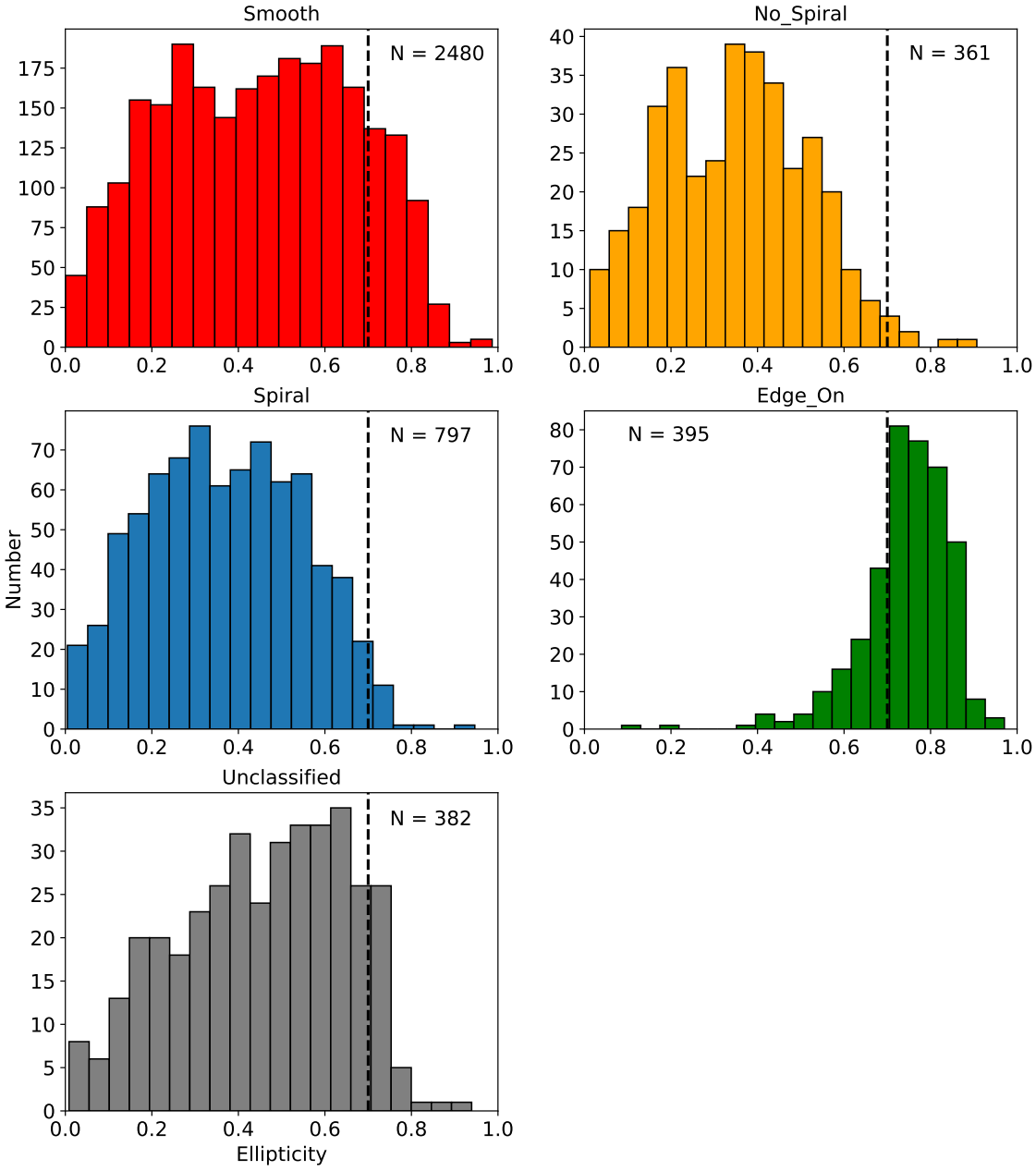

Figure 4.14: Ellipticity distributions within GAMA-KiDS-GalaxyZoo morphology classifications for the clean and complete Parent Sample.

Table 4.3: Additional Spiral galaxies (identified by GAMA-KiDS-GalaxyZoo) present in the GAMA II morphological classifications with ellipticity ≤0.7.

Classification	No.	No. of Weak Spirals	Percentage	No. After Spiral Removal
E	616	8	1.3	608
S0/Sa	569	108	18.9	461
LBS	159	3	1.9	156
TOTAL	1344	119	8.8	1225

This is shown by using the set of Spiral galaxies from GAMA-KiDS-GalaxyZoo, which can identify weak spiral features to the limits of resolution within KiDS images, to identify weak spiral galaxies in addition to those identified within GAMA II. Table 4.3 shows the number of additional weak spiral galaxies present in the GAMA II classifications for ellipticals, S0/Sa and LBS galaxies. No Spirals are removed from the Sd-Irr sample because these are already LTGs and as such may have some spiral structure present.

The overall level of contamination of the ETGs identified in GAMA II as weak spirals is ∼9%. However, the contamination is nearly all within the disc galaxies, where ∼19% of the galaxies identified as Lenticulars have weak spiral structure within KiDS images compared to SDSS. The resultant sample of 1,225 ETGs with weak spiral galaxies removed therefore has reduced contamination by Spirals. However, a future galaxy survey with even deeper and sharper images than those from KiDS could find more. This should be borne in mind when interpreting data from the galaxy samples, along with the redshift bias identified in Section 4.6.5.

Based on the findings of Section 4.6.3, final morphology classification in this work is restricted to galaxies with r-band ellipticities at or below 0.7. Beyond this, galaxies with spiral features cannot be clearly identified from data within GAMA-KiDS-GalaxyZoo and dealt with appropriately to produce clean samples of ETGs. The 726 high-ellipticity

galaxies (e >0.7) are placed in a new ”High-Ellipticity” category.

To achieve the cleanest ETG samples possible with the data available, weak spiral galaxies identified by GAMA-KiDS-GalaxyZoo were subtracted from the Lenticulars, Ellipticals and LBS classifications within GAMA II and added to a total Spirals classification to produce a final list of morphological classifications for the Parent Sample (Table 4.4). The classification names are used for the remainder of this work. Figure 4.15 shows colour-magnitude plots for the final morphological classifications. The most significant improvement compared to the original GAMA classifications (Figure 4.8) is a reduction in the number of higher luminosity (higher stellar mass), bluer S0-Sa galaxies within the GV by the removal of spirals identified by GAMA-KiDS-GalaxyZoo. The resultant Lenticulars set now forms a less-dispersed Red Sequence. The High-Ellipticity set (ellipticity > 0.7) contains galaxies in locations consistent with various morphologies, as expected because these galaxies have not been assigned classifications using the methods within this work. The population of lower-brightness Ellipticals discussed in Section 4.6.2 appear to be still present.

It must be remembered that the GAMA II morphological classifications (Table 4.1), and hence the final morphological classifications, are based on specific features (spheroid/disc, single/multicomponent) representative of galaxy morphologies and therefore may not represent formal classifications on an individual basis. However, they can be categorised as early-type or late-type. Table 4.4 also shows these lumped classifications, where ETGs include Ellipticals, Lenticulars and LBS as having smooth morphology, and LTGs include Spirals and Sd/Irr.

4.6.5 Redshift Bias in Morphological Classification

Morphology classification studies based on images with fixed angular resolution will be biased by the challenges of detecting spiral features in galaxies at higher redshifts. Fixed

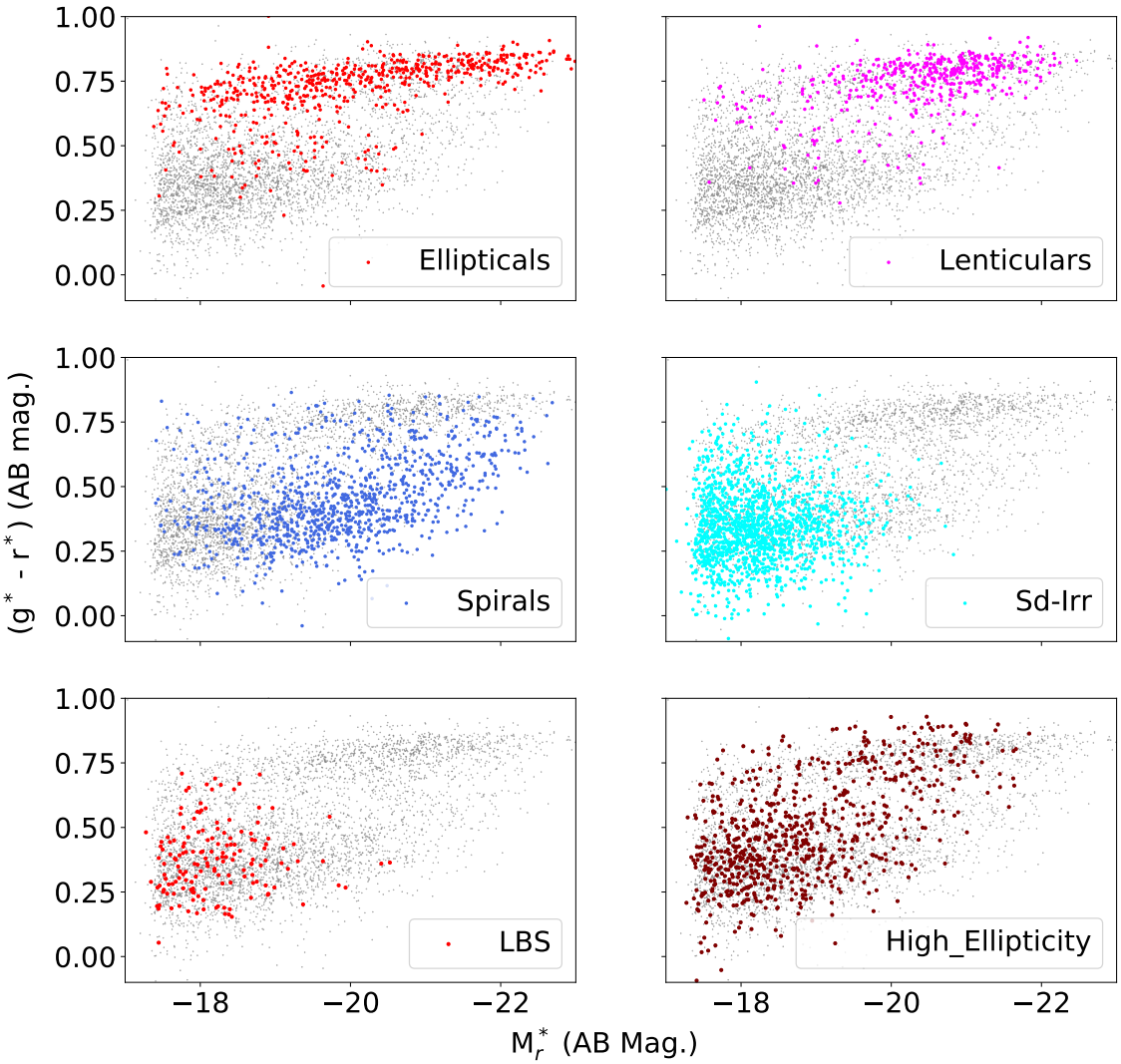

Figure 4.15: Plots of Galactic extinction corrected g* - r* colour versus absolute r*-band magnitude for the final sets of morphological classifications. Grey points are for galaxies in the whole Parent Sample for comparison.

Table 4.4: Final morphological classifications (used in the remainder of this work) for galaxies in the Parent Sample.

Classification	No.
Ellipticals	608
Lenticulars	461
Spirals	1016
Sd-Irr	1481
LBS	156
High-Ellipticity	726
Not classified	10
TOTAL	4458
All ETGs	1225
All LTGs	2497
TOTAL CLASSIFIED	3722

angular resolution means greater on-sky distances per unit transcribed angle as redshift increases. The effect of redshift bias can be investigated using the sets of galaxies classified as spirals from GAMA and GAMA-KiDS-GalaxyZoo. Galaxies in the Parent Sample and in spirals samples from GAMA II and GAMA-KiDS-GalaxyZoo were binned and plotted according to flow-corrected redshift (appropriate for distance determination). Figure 4.16 shows that the fractions of identified spirals in the Parent Sample as a function of redshift declines steadily from minimum to maximum redshift for both classification methods. This indicates that both methods become less effective at detecting galaxies with spiral-like features as redshift increases, and some weak spiral galaxies therefore may still be present in the early-type galaxy classifications defined above. This assumes that the fraction of galaxies with spiral-like features as defined for each classification study is constant with redshift over the range considered.

Figure 4.16 also shows that the GAMA II approach for morphological classification

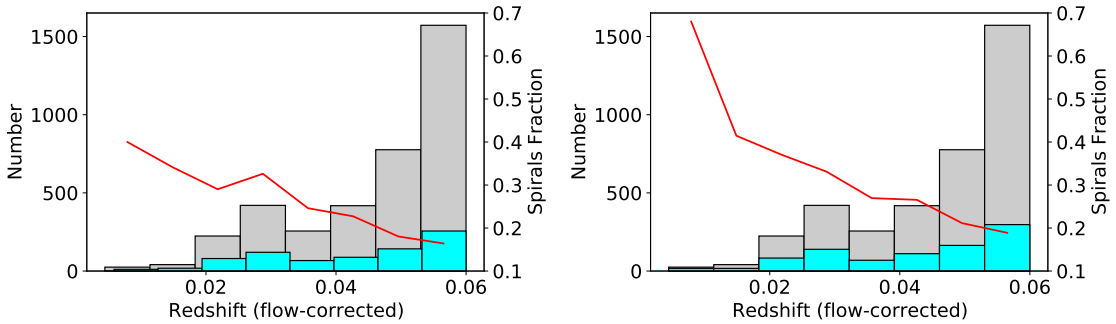

Figure 4.16: Fraction of detected spirals in the Parent Sample as a function of redshift from GAMA (left) and GAMA-KiDS-GalaxyZoo (right) classifications. Grey bars are Parent Sample galaxies with ellipticity <0.7, blue bars are spirals. The red line is the fraction of spirals detected (right-hand y axis).

consistently detects significantly more galaxies labelled as spirals than GAMA-KiDS-GalaxyZoo at all redshifts. Overall, the fraction of spirals from GAMA II data is 44% compared to 19% from GAMA-KiDS-GalaxyZoo. For the lowest redshift bins within both plots in Figure 4.16, where spiral features are most likely to be detected because of lower redshifts, 40% of galaxies are spirals according to GAMA-KiDS-GalaxyZoo while 68% are spirals according to GAMA II. For comparison, Dressler (1980) (their Figure 2) found a high proportion of spiral and irregular galaxies (e.g. 40 - 60%) in less dense environments, so the GAMA detection rate may be optimistic. The reasons for the higher detection rate of spirals within GAMA II are probably related to the methods used for classification in this study, which are based on singe or multiple structures present and are not definitively tied to morphological types as discussed in Section 4.6.1. It is possible that some of the features used to detect late-type structures could occur in some early-types, especially those that are still in transition across the Green Valley (e.g. following a disruptive merger). Nonetheless, the GAMA II classifications are maintained as the primary ones for this work to ensure that samples of early-types created above contain as few late-type galaxies as possible. In spite of the lower number of spiral galaxies found, the GAMA-KiDS-GalaxyZoo Spirals sample allowed the detection and removal of at least some additional weak spirals from the GAMA II sample (Section 4.6.4).

4.6.6 Visual Inspection of ETG Sample

As a quality check for the final ETG classifications, KiDS colour images from GAMA-KiDS-GalaxyZoo for the 1,069 Ellipticals and Lenticulars in the definitive samples (Table 4.4) were inspected by two of the project team (DG/AES) to see if they were genuinely ETGs. The KiDS images used were those used by the volunteer classifiers for GAMA-KiDS-GalaxyZoo, and were higher resolution and deeper than the SDSS images used for classification by GAMA. The consensus is that 911 ETGs (85%) are definitely classifed as such. A total of 71 ETGs (7%) were found to have faint or broken spiral structure which did not lead to Spiral classifications using GAMA-KiDS-GalaxyZoo data, and 87 ETGs (8%) were found to have irregularities. A range of other features were also found, such as prominent nuclear features with bars and inner rings for disc-like ETGs, discussed in Section 3.3.5. Kelvin et al. (2018) studied the range of galaxy morphologies from GAMA-KiDS-GalaxyZoo across the GV in more detail, and also found a range of such features in GV galaxies. It was suggested that less violent evolutionary mechanisms were at work in the GV, to preserve the more fragile features such as rings and lenses.

Overall, the classification schemes employed appear to have identified ETGs which mostly lack LTG-like spiral structure in KiDS optical images. However, loss of image detail with increasing redshift, and resolution and depth limits for the state-of-the-art KiDS survey, mean that some visually-classified LTGs may still be present. The final Ellipticals and Lenticulars samples were left unchanged, because the ∼15% of these ETGs that are not totally smooth do not have well-defined spiral features and are not definitely LTGs.

Chapter 5

Galaxy Morphology and its Relationship to Galaxy Properties

The primary aim of this thesis is to examine how studying the cool ISM within ETGs can indicate how galaxies evolve to become ETGs. In addition, the properties of the subsets of galaxies based on morphological classification can be compared, firstly to see if the classifications are distinct in various parameter spaces and secondly to see if there is evidence for continuum (i.e. smoothly changing) behaviour in properties instead of the bimodal behaviour apparent in certain parameter spaces (e.g. colour-magnitude plots shown in Figues 4.8 and 4.11). Eales et al. (2018) propose that such bimodal behaviour can be due to natural upper and lower limits on galaxy properties or observational bias rather than a relatively sudden evolution from one state to another, and a continuum of galaxy properties exists behind it. In this Chapter, various plots of galaxy properties are presented to explore whether other galaxy properties display behaviour closer to a continuum rather than exhibiting bimodality due to limits on properties. In particular, continuous numeric measures of morphology are considered as well as the discrete visual classifications presented in Table 4.4, to see if they are more successful in revealing continuum behaviour of galaxy properties.

Photometry and derived estimates of properties from GAMA II 21BandPhotomv03 are used as the primary source of information for this study. The primary source for estimates of stellar mass and star formation rate is GAMA II MagPhysv06, which uses aperture-matched photometry over 21 bands from far ultra-violet to sub-mm wavelengths within GAMA II LambdarCatv01, fitted to templates for galaxy spectra using MAGPHYS Section 2.7.3.

Throughout the remainder of this Chapter, plots of galaxy properties across various parameter spaces are shown in two ways. The first is a scatter plot, to show the extent of the data within a parameter space. The second is a density (contour) plot to show how galaxy properties are distributed. The true extent of the data can sometimes be lost when constructing contour plots, hence the use of a scatter plot in addition. The use of unshaded contours also allows overlaps of populations within a parameter space to be illustrated.

5.1 Colour vs Stellar Mass

Bimodality in colour-magnitude diagrams is expected, because star forming and passive galaxies at opposite regions of the diagram have limits on colours (Eales et al. 2018). The principle was used in Section 4.6.1, 4.6.2 and 4.6.4 to illustrate how different morphological classifications behave. SDSS r-band absolute magnitude in these plots can be used as a proxy for stellar mass when only photometry is available, because the majority of the stellar mass in any galaxy consists of stars at Solar mass or lower (e.g. Salpeter 1955). These lower-mass stars emit a significant portion of their luminosity in r-band. The principle has also been demonstrated empirically by others, e.g. Mahajan et al. (2018). Figure 5.1 shows the relationship between r-band absolute magnitude and estimated stellar mass from MAGPHYS (Section 2.7.3) for LTGs and ETGs with with $>3\sigma$ detections in r-band flux density. Separate trends are apparent for ETGs and LTGs due a lower proportion of r-band emission to total emission for LTGs, but on the whole the use of M_r can be used to approximate stellar mass (albeit within a factor of $\sim$10 at the lowest stellar masses

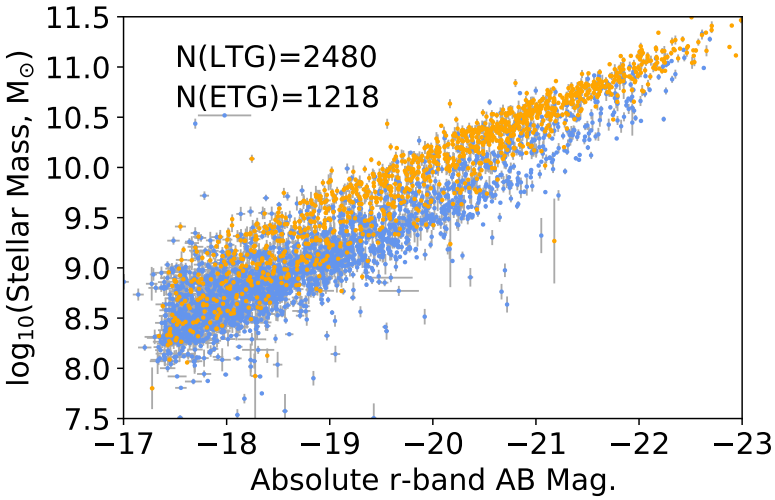

Figure 5.1: Relationship between MAGPHYS-derived stellar mass estimates and r-band absolute magnitude for LTGs (blue) and ETGs (orange) with $>3\sigma$ detection in r-band flux density.

considered).

In this section, g^*-r^* colour is plotted against stellar mass from MAGPHYS spectral energy distribution (SED) fitting (Section 2.7.3). Figure 5.2 shows the plot for all galaxies in the Parent Sample with $>3\sigma$ detections in g- and r-band flux density (including those with high ellipticity). Clustering of galaxies is evident at more extreme ”red” and ”blue” colours as discussed previously, so a continuum is not apparent. The Figure also shows the diagram for ETGs and LTGs separately (Section 4.6.4). The two samples form the expected Blue Cloud for LTGs and Red Sequence for ETGs, with a more sparsely-populated GV also apparent. An overlap between ETGs and LTGs in the GV is apparent, implying that a range of morphological features is present in this parameter space. This behaviour has been reported previously by Kelvin et al. (2018) who found a variety of morphologies present in the GV for a similar population of galaxies, and attributed this behaviour to a range of evolutionary mechanisms at work which preserve fragile features such as galactic rings.

Figure 5.3 shows the same plot but for individual morphological classifications from

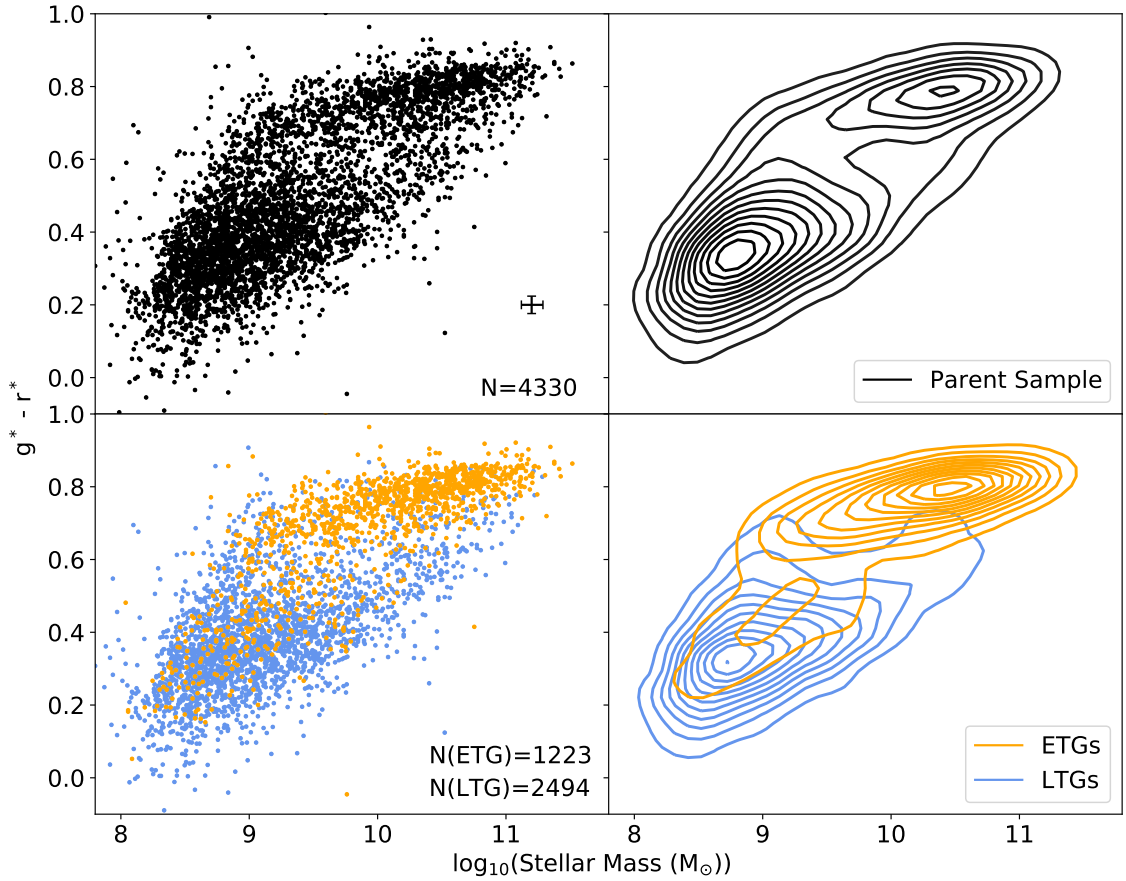

Figure 5.2: Galactic extinction corrected g^* - r^* colour versus stellar mass for all galaxies in the Parent Sample, and ETGs/LTGs plotted separately. Median uncertainties for the Parent Sample are shown for illustration.

Section 4.6.4. The number of galaxies available for plotting per classification is also shown. A low number of galaxies from the catalogues (34) are not included in these plots, because of a lack of appropriate photometry in 21BandPhotomv03. The segregation of LTGs and ETGs remains apparent, along with extension into the GV region for all morphologies. A small population of ellipticals and a few Lenticulars with relatively low stellar mass ($\sim 10^{9.5}$ $M_\odot$) can be seen to have bluer colours than most of their type, and overlap the LTGs. The bluer Ellipticals also seem to have an association with LBS. The parameter spaces explored below also highlight a similar population, which is considered

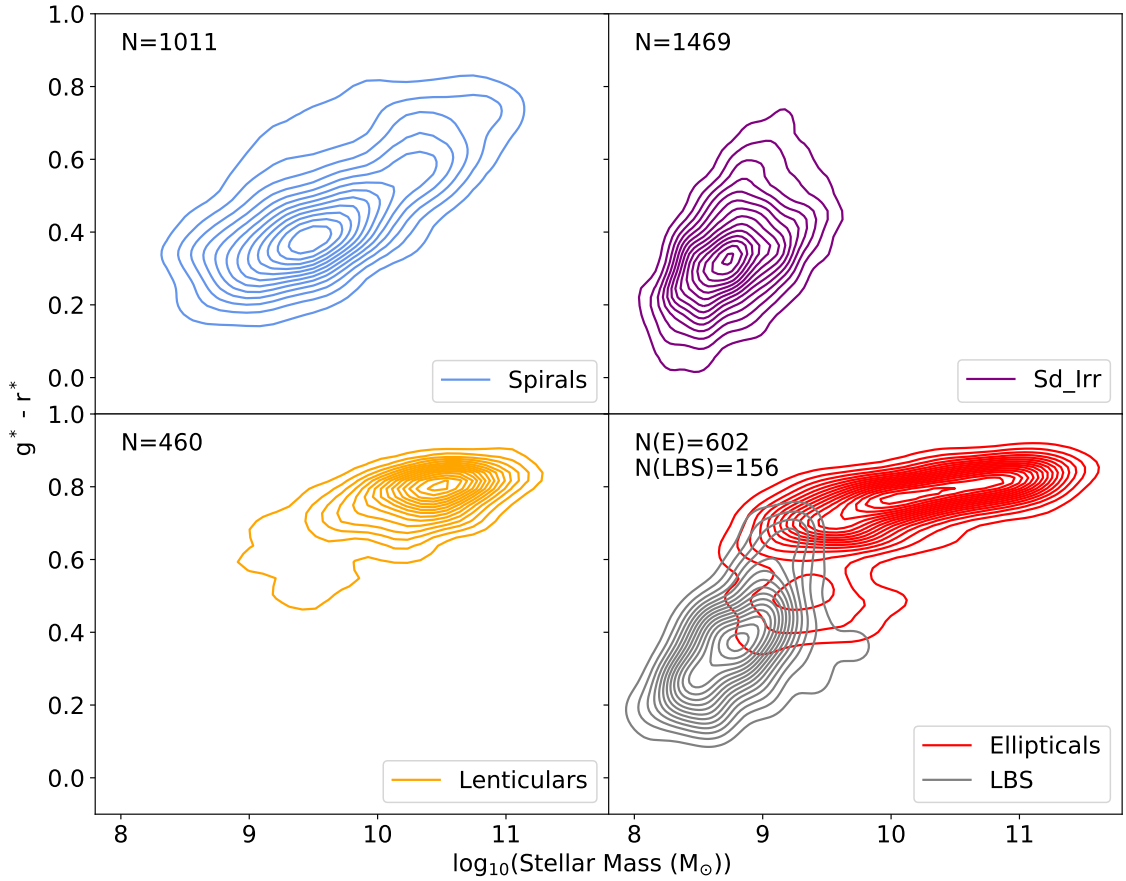

Figure 5.3: Galactic extinction corrected g^* - r^* colour versus stellar mass for morphological classifications.

further in section 5.8. With the exception of this bluer, low-mass ETG population, the ETG and LTG populations are behaving broadly as expected within this parameter space (e.g. Baldry et al. 2004).

5.2 Specific Star Formation Rate versus Stellar Mass

GAMA II MagPhysv06 contains fitted estimates from MAGPHYS (Section 2.7.3) of specific star formation rates (sSFR) (i.e. star formation rate per unit stellar mass) as well as

stellar mass. Specific star formation rate is of interest because when plotted against stellar mass it has been found to form a SFMS for LTGs in particular (e.g. Saintonge et al. 2018). sSFRs are available to different time intervals within GAMA II MagPhysv06, e.g. 0-100 Myr, 0-1 Gyr. The 0-100 Myr interval (catalogue entries SFR_0_1Gyr and sSFR_0_1Gyr) is of particular interest, because the optical light emission will be dominated by OB stars (to B4) that are associated with new star formation and whose typical lifespans match this interval (e.g. Sparke & Gallagher 2007). Longer intervals will include older stellar populations with no new star formation occurring. A very small number of galaxies in the Parent Sample (7 in total) do not have these data, either because suitable photometry was not available for fitting or fitting was not successful. For plotting, the best-fit sSFR values are used and uncertainties (1σ, upper and lower bounds) in sSFR are calculated using the 16th, 50th and 84th percentile values for sSFR (0 - 100 Myr) provided in the catalogue. The "best fit" values for SFR, sSFR and stellar mass form are consistent with each other, such that sSFR is SFR divided by stellar mass.

Figure 5.4 shows plots of sSFR versus stellar mass for all galaxies in the Parent Sample (including those with high ellipticity), to explore whether a continuum in galaxy properties exists within this parameter space. Clustering is apparent at higher sSFR, in a region corresponding to the SFMS (Section 1.2.2). Weaker clustering is also apparent at lower sSFR (around 10^{-12}yr^{-1}). The plots also show that sSFR is reduced in some galaxies with higher stellar mass, especially in the ETG sample (see also Eales et al. (2017), their Figure 1.3). This phenomenon is referred to as "downsizing", where star formation occurs in successively less massive galaxies as the Universe moves forward in time (Cowie et al. 1996). Agius et al. (2015, their Figure 12) showed that downsizing also occurs in ETGs. Overall, the plot for all galaxies (top left) does show a degree of continuum behaviour, with galaxies spreading from the SFMS to regions of lower sSFR. The clustering at low sSFR could arise due to very low sSFRs sustained over long periods (e.g. Gyr) within ETGs, due to ongoing, sporadic pockets of star formation within small residual molecular gas reservoirs, or due to acquisition of fresh molecular gas due to mergers (rejuvenation, e.g. Thomas et al. 2010; Mancini et al. 2019). UV emission from evolved stars, unrelated

to ongoing star formation could also contribute to this clustering at low sSFR by causing false assignment of UV light to star formation when fitting template spectra to photometry.

Figure 5.4 shows the same plot for LTGs and ETGs separately. The sequence is apparent for LTGs, but with more scatter in the lower-mass region where Sd-Irr galaxies are present in large numbers. Some scatter of LTGs towards lower sSFR along the whole sequence is apparent, which can be expected if star formation has been affected while LTG morphological features are preserved. The ETGs are much more dispersed across the parameter space, starting within the SFMS and spreading out to very low sSFR values. ETGs appear to form a cluster with sSFR values of around 10^{-12} yr^{-1} at a median stellar mass of around $10^{10.5}$ $M_{\odot}$, which is greater than that for the majority of LTGs seen along the SFMS in the plot.

Figure 5.5 shows plots of sSFR versus stellar mass for different morphological classifications. The LTG classifications behave as expected, and form a SFMS as discussed above and ETGs scatter away from the SFMS across the GV towards lower SFR. However, the Lenticulars and in particular the Ellipticals show clustering of galaxies at lower mass ($\sim 10^{9.5}$ $M_{\odot}$) with elevated sSFR. These galaxies comply with the morphological criteria for ETGs in the GAMA II catalogues and were not classified as spirals (weak or otherwise) using data from GAMA-KiDS-GalaxyZoo (Section 4.6.2), but have ongoing star formation. There also appears to be an association between the star-forming ETGs and LBS in this plot. These star-forming ETGs are isolated and studied further in Section 5.8.

Overall, plots of sSFR versus stellar mass show morphological classes behaving broadly as expected, except for the group of star-forming ETGs identified in the current Parent Sample. Other classifications reliant on star formation rate to identify ETGs (e.g. Croom et al. 2021b, their Figure 8) would only identify the passive ETGs where evolution is largely complete and ISM contents could be reduced. ETGs with star formation are specifically of interest within this work, because of the ISM presence needed for star formation.

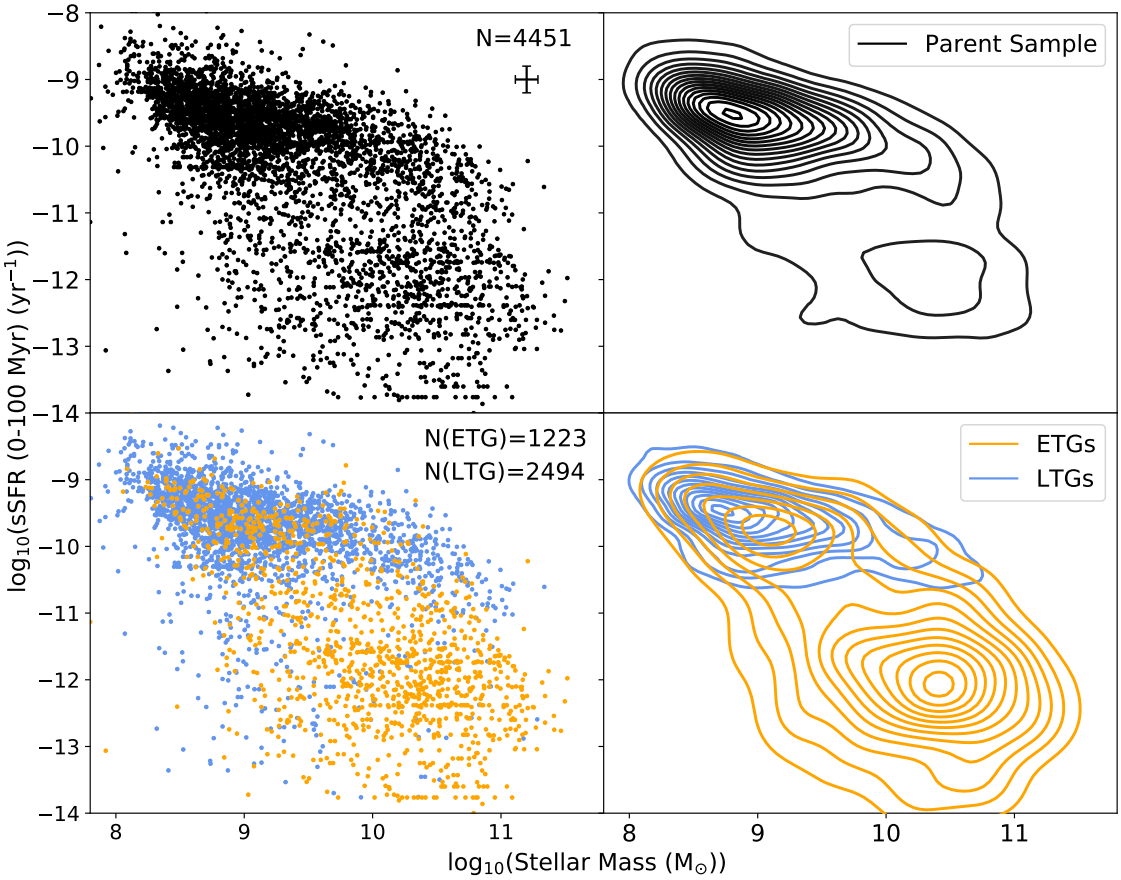

Figure 5.4: Specific star formation rate (0 - 100 Myr) versus stellar mass for all galaxies in the Parent Sample, and for ETGs and LTGs separately. Median uncertainties for the Parent Sample are shown for illustration.

5.3 r* - J* Colour versus u* - r* Colour

Labbé et al. (2005) demonstrated that a specific two-colour plot can be used to separate star-forming and passive galaxies into distinct regions, and Wuyts et al. (2007) showed that plotting Johnson-Cousins (U - V) versus (V - J) colours can achieve this for galaxies at low and high redshifts. Depending on the photometric system used and the filters available, it is possible to substitute other filters for U, V or J and achieve the same effect (Wang et al. 2017). As explained in Section 2.8.1, GAMA photometry is based on SDSS

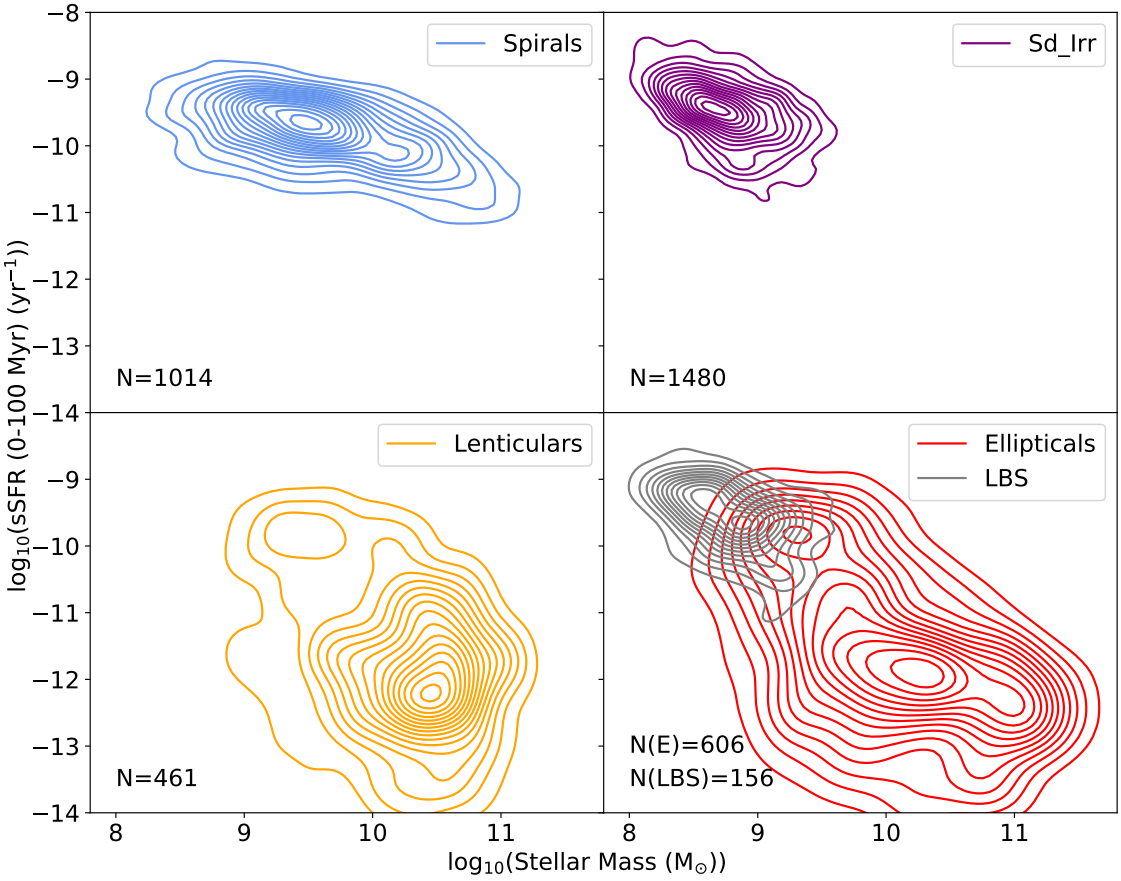

Figure 5.5: Specific star formation rate (0 - 100 Myr) versus stellar mass for morphological classifications.

passbands (ugriz) for optical and VISTA passbands (ZYJHK) for near infra-red data. Figure 5.6 uses (u^* - r^*) and (r^* - J^*) AB magnitudes to create a two-colour plot for all galaxies in the Parent Sample (including those with high ellipticity), to explore whether a continuum in galaxy properties exists within this parameter space. Only 3,881 galaxies from the Parent Sample can be plotted, because of a shortage of u-band photometry with $>3\sigma$ detection in GAMA II 21BandPhotomv03. Limits on colours of star-forming and passive galaxies cause clustering within the plot as seen with the colour-magnitude diagrams in Section 5.1, so no continuum is apparent.

Figure 5.6 also shows the same plot for LTGs and ETGs separately. The LTG and ETG samples are separated with a degree of overlap corresponding to the GV, as also seen in the previous plots. The scatter plot uses sSFR (0-100 Myr) as a third parameter, and the behaviour in terms of star formation is similar to that shown by Wang et al. (2017). ETGs feature towards the top of the diagram, with a decline in sSFR from top right (ETGs with some star formation) to top left (passive ETGs). With appropriate demarcations, this effect can be used to identify true passive ETGs or conversely highlight ETGs with ongoing star formation (and hence the ISM required for this). However, it should not be used for estimating visual morphology for unresolved galaxies, unless a galaxy's position at the extreme ends of diagram suggests a unique classification as LTG or ETG.

Similar plots for specific morphological classifications (Figure 5.7) show good separation of lenticular galaxies from LTGs (Spiral and Sd-Irr). A small population of "bluer" ETGs appears to overlap with "redder" LBS in this plot, consistent with findings from the previous two plots.

Overall, this plot does not directly show continuum behaviour for this parameter space, but sSFR does seem to form a continuum across the colour space. The trends apparent in the plot are consistent with those identified by its developers (Labbé et al. 2005; Wuyts et al. 2007). The sub-population of elliptical galaxies with properties similar to LTGs is also highlighted, illustrating that they do not conform to expected properties of ETGs from previous studies, but are more consistent with the upper end of LBS properties

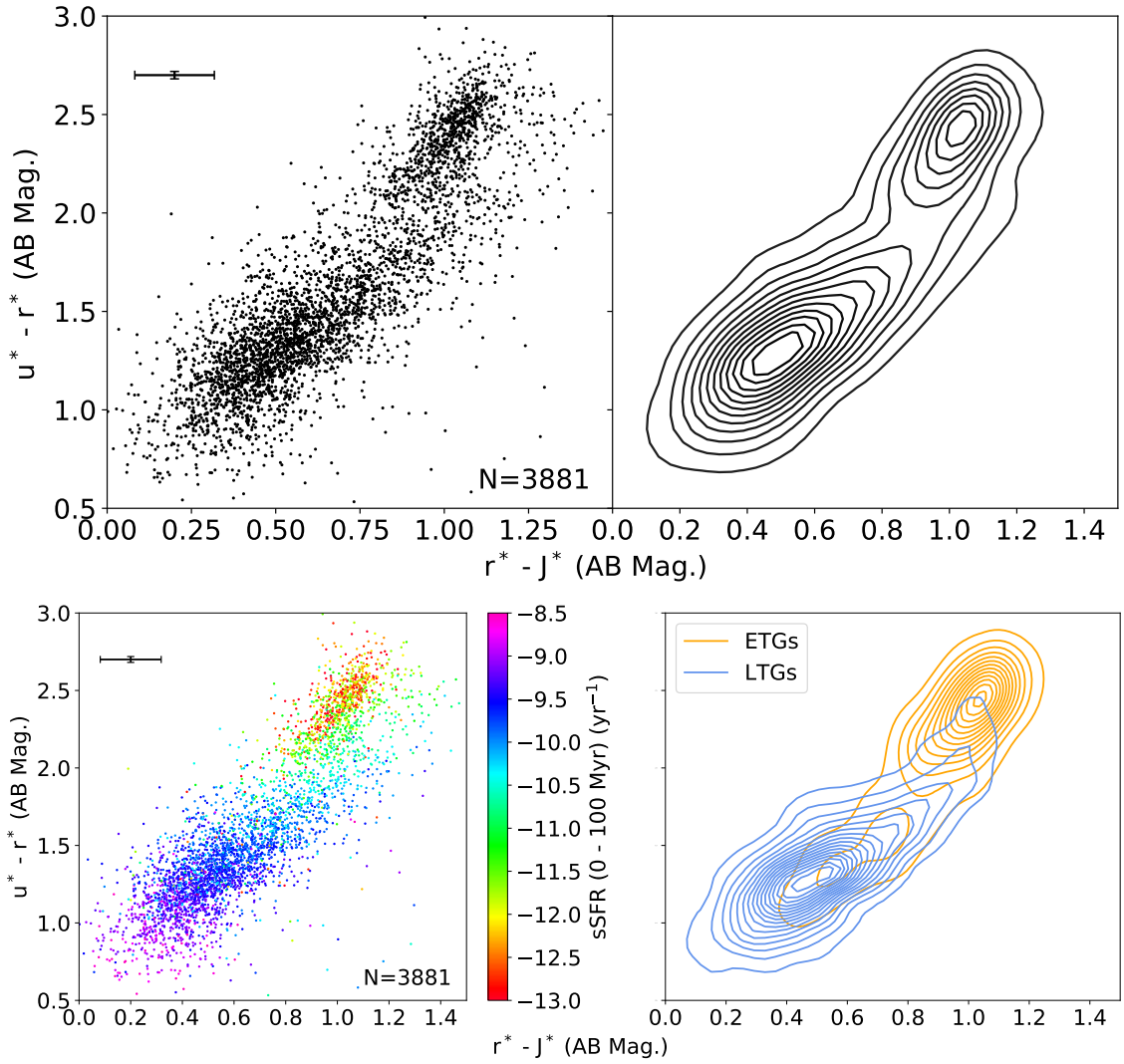

Figure 5.6: Galactic extinction corrected u^* - r^* colour versus r^* - J^* colour for (upper) the Parent Sample, (lower left) the Parent Sample with sSFR (0 - 100 Myr) highlighted, (lower right) ETGs and LTGs separately. Median uncertainties for the Parent Sample galaxy data are shown.

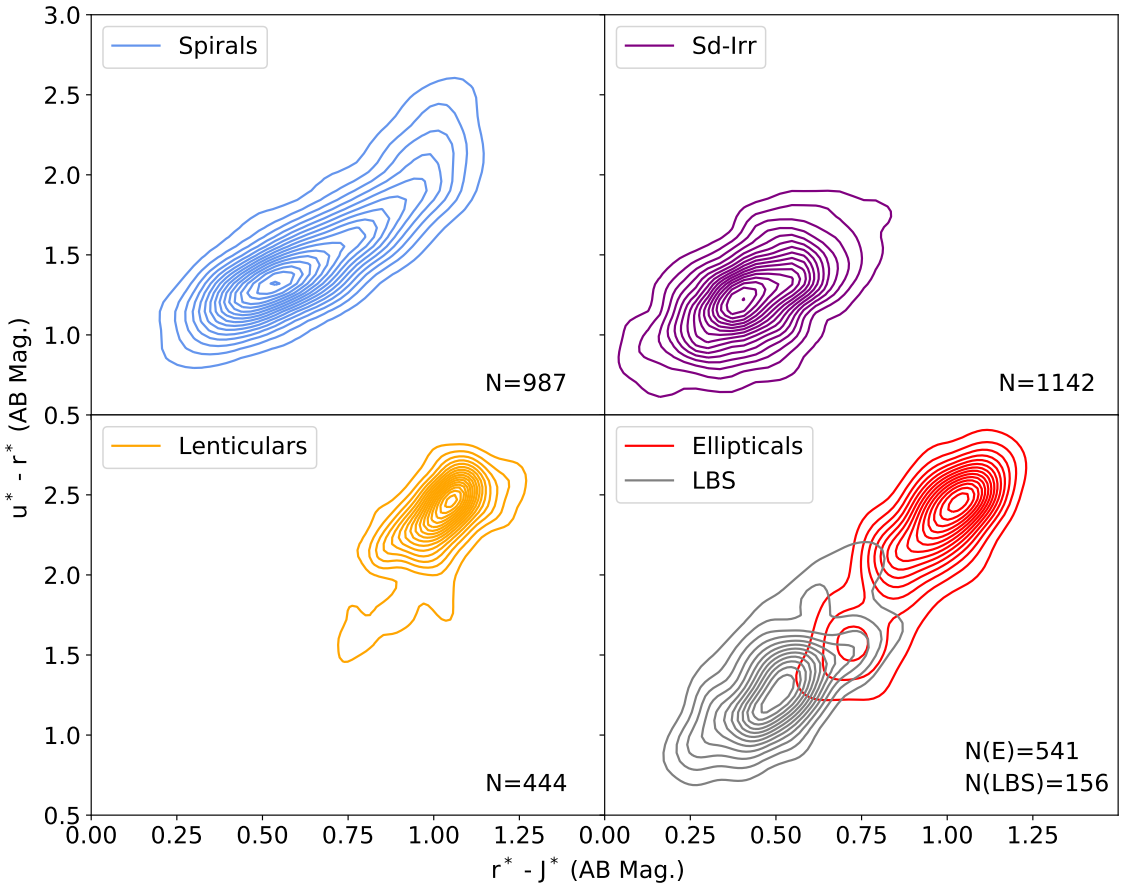

Figure 5.7: Galactic extinction corrected u^* - r^* colour versus r^* - J^* colour for morphological classifications.

in Figure 5.7.

5.4 r-Band Single-Component Sérsic Index versus Stellar Mass

Sérsic indices (see Section 3.2.2) for a single-component surface brightness model fitted to SDSS r-band images of GAMA galaxies are available in the GAMA II catalogue SersicCatSDSSv09. Of the 4,458 galaxies in the clean and complete Parent Sample, 4,330 have Sérsic indices (n) with absolute uncertainties <1. This threshold was chosen to include as many galaxies as possible without introducing those with very large uncertainties in Sérsic index. The selected galaxies were used to construct a plot of n versus stellar mass, shown in Figure 5.8. There is evidence of continuum behaviour in this plot, with galaxies clustering at around n = 1 and dispersing to higher n at greater stellar mass. There is a weak cluster apparent at around n = 4, which is where larger spheroidal galaxies and pressure-supported galactic bulges could be expected with a classical de Vaucouleurs surface brightness profile typical of these structures (de Vaucouleurs 1948). Figure 5.8 also shows a similar plot for ETGs and LTGs separately. The LTG sample has n clustering around 1, which represents an exponential surface brightness profile and is a characteristic of disc-like structure. The ETG sample extends into the LTG regime, but two dominant clusters are apparent at n $\sim$ 1.5 and n $\sim$ 4. These probably represent ETGs with disc-like components (n $\sim$ 1) or pseudobulges (n $\sim$ 1 - 2) (Kormendy & Kennicutt 2004), and bulge-dominated or elliptical galaxies with a de Vaucoleurs surface brightness profile (n = 4). This plot indicates similar findings to those presented in Figure 5.4, where LTGs have tighter relations in properties and ETG property trends are more distributed but link up with the LTGs.

Figure 5.9 shows the same plot but for individual morphological classifications. The LTGs and low-mass LTGs cluster around n = 1, whereas ellipticals and lenticulars show

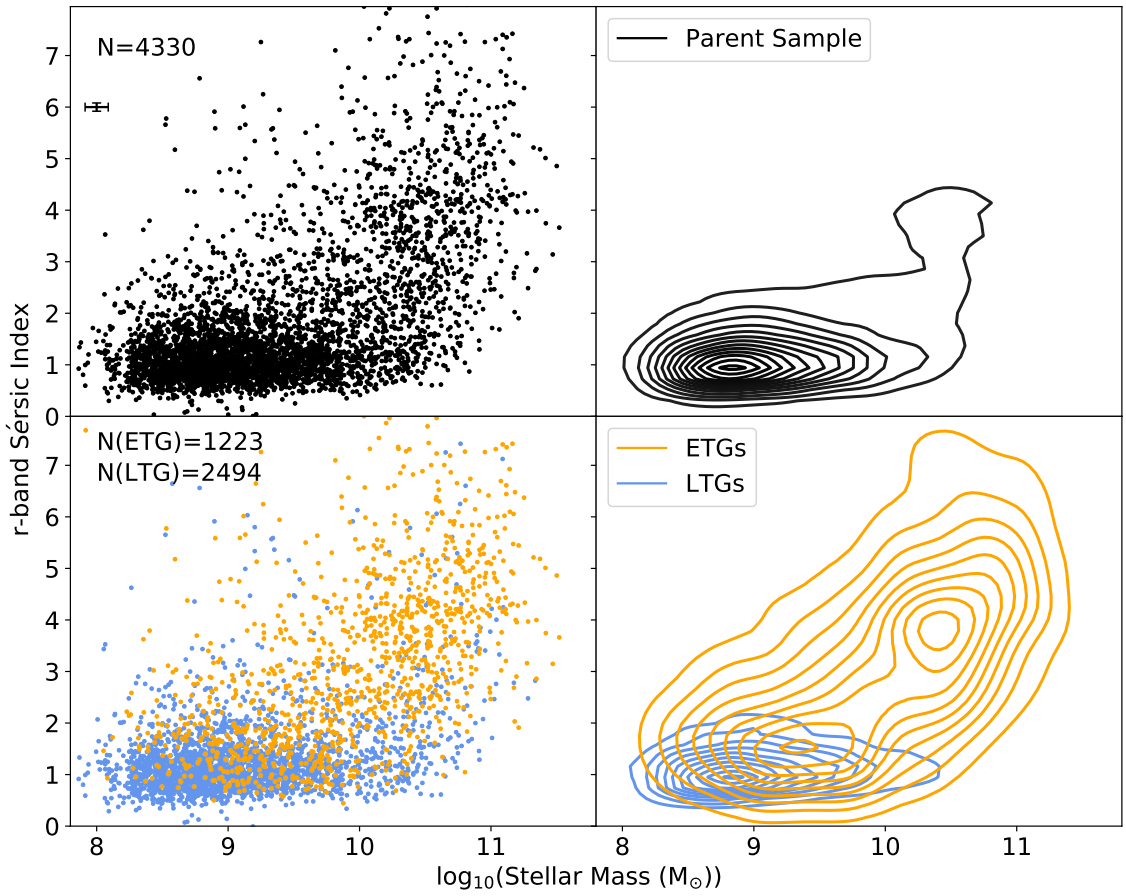

Figure 5.8: r-band Sérsic index (single component) versus stellar mass for (upper) the Parent Sample, (lower) LTGs and ETGs separately.

a wider spread of indices. Above a stellar mass of $\sim 10^{10}$ $M_{\odot}$, Ellipticals and Lenticulars display significantly higher n than Spirals and Sd-Irr. The Sérsic index therefore appears to be effective as a proxy for morphology at higher stellar mass. The Lenticulars show a cluster at higher stellar mass than the LTGs at n ∼3 - 4, indicating possible bulge dominance or a preference for the profile fitting software to select the bulge component. This could be more of an issue for galaxies at higher redshift, where a weaker disc would be more challenging to detect and fit with surface brightness profile, except possibly at higher stellar mass.

For the ETGs, there is some spread at lower stellar masses to lower Sérsic indices, consistent with LTGs. However, the Ellipticals show a cluster at stellar masses consistent with LTGs and n ∼1 - 2, indicating possible disc-like structure and central pseudobulges. The remaining Ellipticals show a spread of Sérsic indices with increasing stellar mass towards a weak cluster at n = 4, where pressure-supported spheroidal galaxies typically lie. A link with LBS and lower-mass Ellipticals is also apparent, as seen in previous plots, at n ∼1.5. LBS may therefore be either flattened spheroids or disc-like, but further investigation is needed to establish which morphology better represents LBS.

5.5 Bulge-Disc Decomposition from KiDS Images

A recently-published GAMA II catalogue, BDMODELSV04 (Casura et al. 2022), contains information on the fitting of multicomponent Sérsic surface brightness profiles to a selection of KiDS-observed galaxies from GAMA catalogues for g, r and i passbands. All 4,458 galaxies from the parent sample are referenced in the catalogue, although for some the model fits were not successful. Of those successfully fitted, 579 of 1,225 LTGs (47%) and 560 of 2,494 ETGs (22%) have two-component fits which relate to disc and bulge components. Single-component Sérsic profile fits were successful for 249 ETGs (20%) and 1043 LTGs (42%), dominated by 919 Sd-Irrs. The remainder had flags set within the catalogue that indicated problematic fitting (e.g. prior limits reached, insufficiently low χ^2) or failed fitting, e.g. due to excessively complex morphology from mergers or

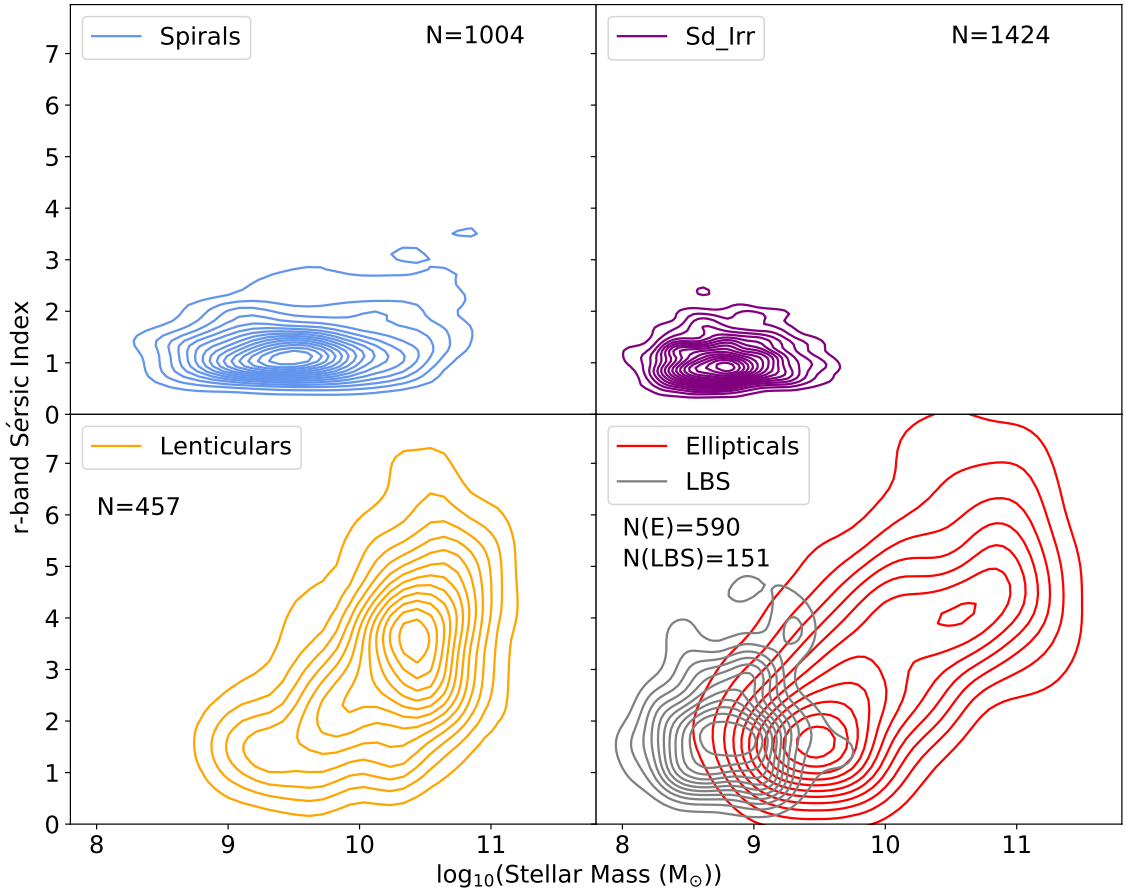

Figure 5.9: r-band Sérsic index (single component) versus stellar mass for morphological classifications.

interactions (Casura et al. 2022). The single-component fits are distinct from those in the GAMA II catalogue SersicCatSDSSv09 (Kelvin et al. 2012), which allowed the fits to include more of the outer regions of galaxies. The fits in BDModelsv04 concentrated more on the inner regions where signal-to-noise per pixel is maximised, which avoids fitting models to less well-defined outer features such as disc breaks and flares (Casura et al. 2022).

Figure 5.10 shows r-band B/T from 2-component profile fitting plotted against stellar mass for galaxies in the Parent Sample wih suitable data, and for ETGs and LTGs separately. A continuum is apparent, starting with a cluster at low B/T and stellar mass and a general increasing trend in both parameters. However, for a given stellar mass there is a considerable spread of B/T especially at larger stellar masses. Also plotted are galaxies for which fitting of single-component Sérsic profiles was most appropriate, with B/T assigned as zero for $0.5 \leq n \leq 1.5$ and one for $n > 1.5$. LTGs generally have a low B/T ratio, while ETGs have a greater spread of B/T but tend to have higher values. There is overlap between the two populations at lower stellar mass, as observed in previous plots. At lower stellar masses, B/T values of between 0.2 and 0.6 can be either ETGs or LTGs, while nearly all galaxies with $B/T > 0.6$ are ETGs. For the galaxies subject to single-component surface brightness profile fitting, LTGs are mostly disc-like ($B/T = 0$) with a few that are more spheroidal). The reverse is true for ETGs, with only a few shown as disc-like and the remainder more spheroidal. A spread towards higher stellar mass is also apparent for the spheroidal ETGs.

Figure 5.10 shows B/T plotted against stellar mass for galaxies in the Parent Sample wih suitable data, and for ETGs and LTGs separately. Also plotted are galaxies for which fitting of single-component Sérsic profiles was most appropriate, with B/T assigned as zero for $0.5 \leq n \leq 1.5$ and one for $n > 1.5$. A cluster at low B/T exists at lower stellar mass, but data are much more dispersed over the B/T range at higher stellar mass. LTGs generally have a low B/T ratio, while ETGs have a greater spread of B/T but tend to have higher values. There is overlap between the two populations at lower stellar mass, as

observed in previous plots. Nearly all galaxies with B/T > 0.6 are ETGs. For galaxies subject to single-component surface brightness profile fitting, LTGs are mostly disc-like (B/T = 0) with a few that are more spheroidal). The reverse is true for ETGs, with only a few shown as disc-like and the remainder more spheroidal. A spread towards higher stellar mass is also apparent for the spheroidal ETGs.

The findings from the plot suggest that while existing as LTGs, galaxies have smaller bulges but bulge and mass growth within galaxies occurs during their evolution to become ETGs (Section 1.2.2). Morphological quenching (Martig et al. 2009) is a known phenomenon where conditions towards the centre of the disc of a star-forming galaxy becomes progressively more pressure-supported rather than rotationally-supported (and hence bulge-like) with increasing radius over time (see also Section 1.2.1). The process stabilises the molecular gas present against collapse to form new stars, effectively driving a spiral galaxy towards lenticular morphology and quiescence. Major mergers can also lead to giant spheriodal ETGs (Xilouris et al. 2004).

Figure 5.11 shows that Lenticulars cluster at higher stellar mass than most LTGs, with a spread of B/T from low (disc-dominated) to high (bulge-dominated). This is in line with the findings of Kormendy & Bender (2012), who showed that Lenticulars exist with a range of B/T ratios. Ellipticals were selected originally to be single component from the SDSS images used in GAMA for morphological classification (Section 4.6.1), but from model fitting of deeper KiDS images it is apparent that a number of them have lower B/T than expected, possibly heading towards disc dominance. It is generally acknowledged that separating Ellipticals from Lenticulars in optical images can be challenging, especially at low observed galaxy inclinations. Also studies of stellar and ionised gas kinematics using IFU observations have shown that visually-classified Ellipticals can be sub-divided into fast rotators (more like discs) at higher ellipticities, and rounder, slow rotators which are more pressure-supported (e.g. Cappellari et al. 2011). In spite of these challenges, it is acceptable to treat these galaxies as ETGs generally because of a lack of apparent spiral structure in KiDS images (Section 4.6.2).

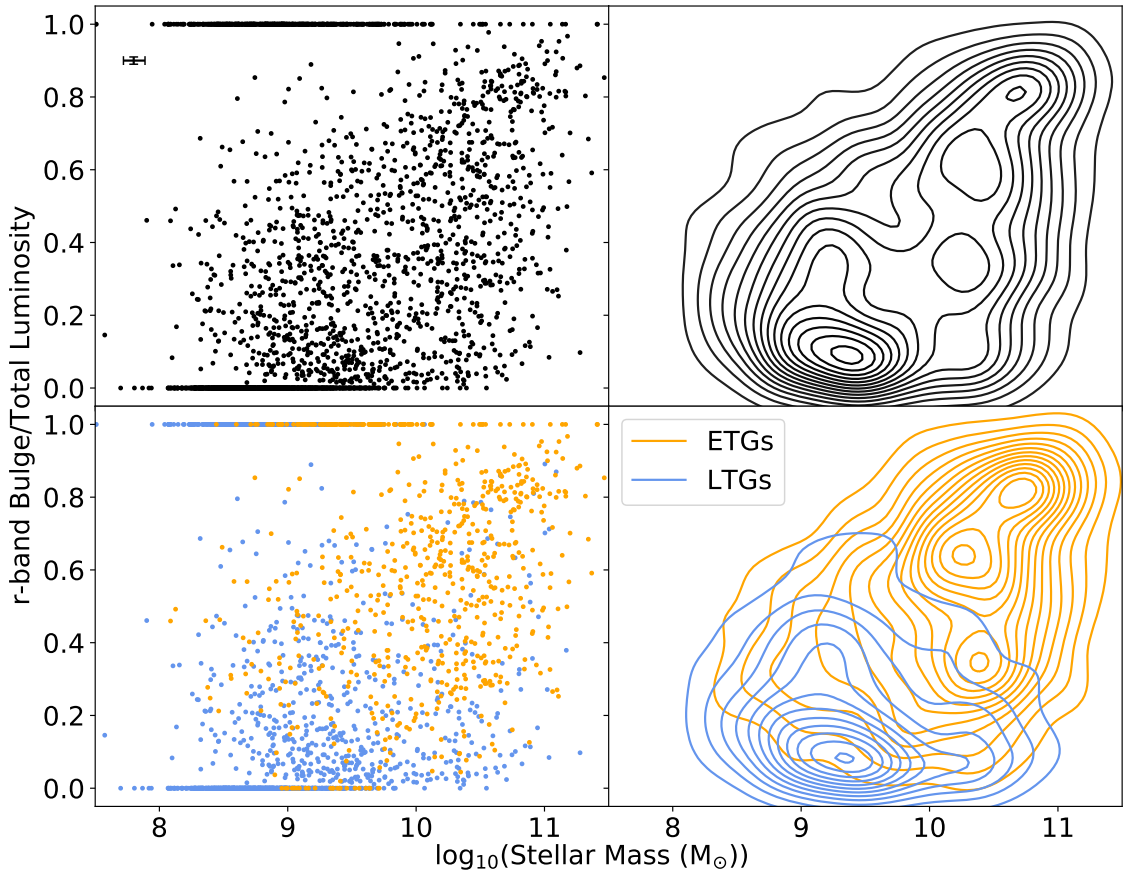

Figure 5.10: r-band bulge/total light ratio versus stellar mass for the Parent Sample and for ETGs/LTGs. Galaxies with single Sérsic profile fits are included, with n≤1.5 shown as B/T = 0 and n>1.5 shown with B/T = 1.

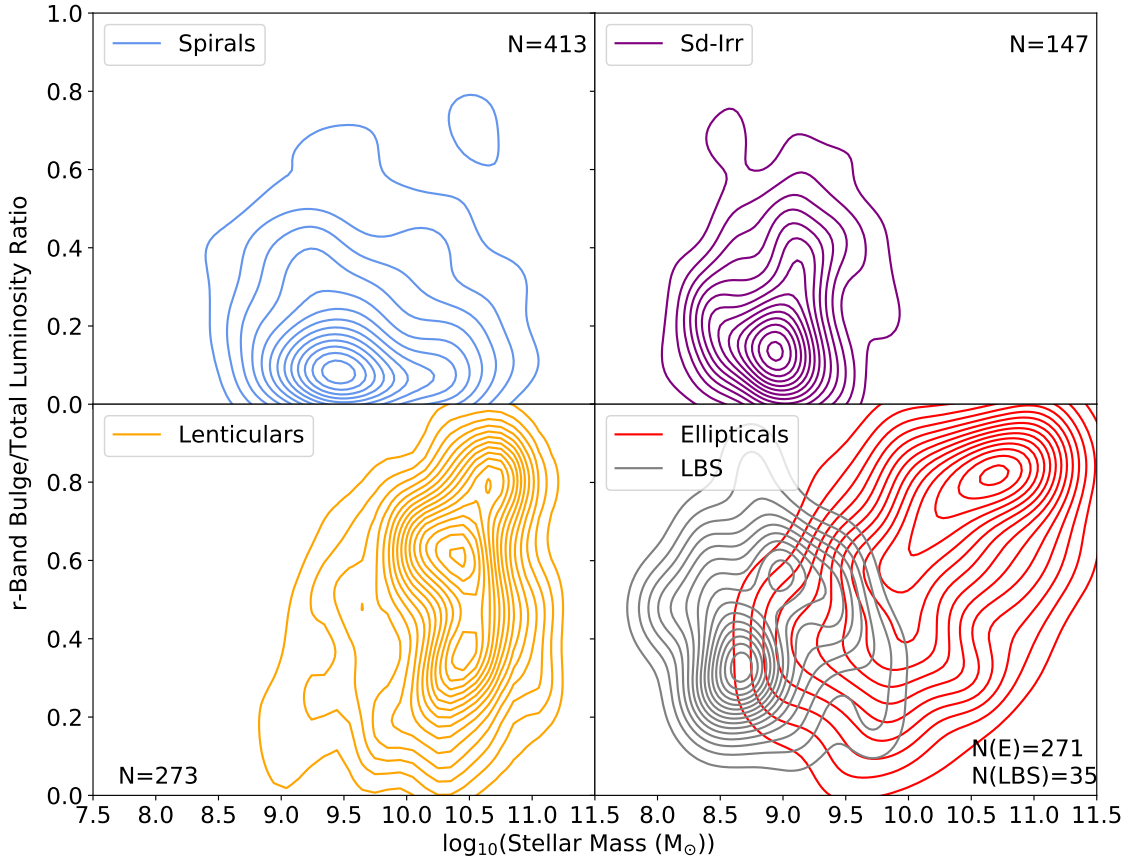

Figure 5.11: r-band bulge/total light ratio versus stellar mass for morphological classifications.

5.6 Impact of removing Galaxies with AGN from the Parent Sample

As stated in Section 1.2.2, removal of galaxies with strong AGN from a sample may deepen the GV in at least some of the plots presented in this Chapter. This effect could mask continuum behaviour across a parameter space, and make pile-ups in plotted data due to property limits more apparent. To investigate this, the effect of adding previously removed galaxies with AGN back into the Parent Sample on the findings presented in this Chapter is investigated below.

Figure 5.12 shows where the galaxies thought to contain strong AGN lie compared to the Parent Sample, on a plot of SDSS g - r colour (corrected for Galactic extinction) versus estimates of stellar mass from fitting of photometry using MAGPHYS (Section 2.7.3), similar to those presented in Section 5.1. In this plot, only the radio-quiet galaxies identified as having AGN are included, because it is possible that some radio-quiet galaxies are mis-identified as having AGN by the diagnostics employed. Not all galaxies have suitable photometry for plotting, hence a further slight reduction in plotted galaxy numbers compared to those quoted earlier. Galaxies with strong AGN are generally within the GV at higher stellar mass, concentrated more towards the Red Sequence where many ETGs exist. At lower stellar mass, a small proportion of the galaxies with strong AGN are mixed with the Blue Cloud, where LTGs predominantly exist.

Figure 5.13 shows plots for the parameter spaces discussed above, with and without radio-quiet AGN removal. In all cases, the same clustering of data or continuum behaviour across the parameter space are apparent with and without AGN removal. Therefore, the findings of this Chapter are unaltered by the removal of AGN to form the Parent

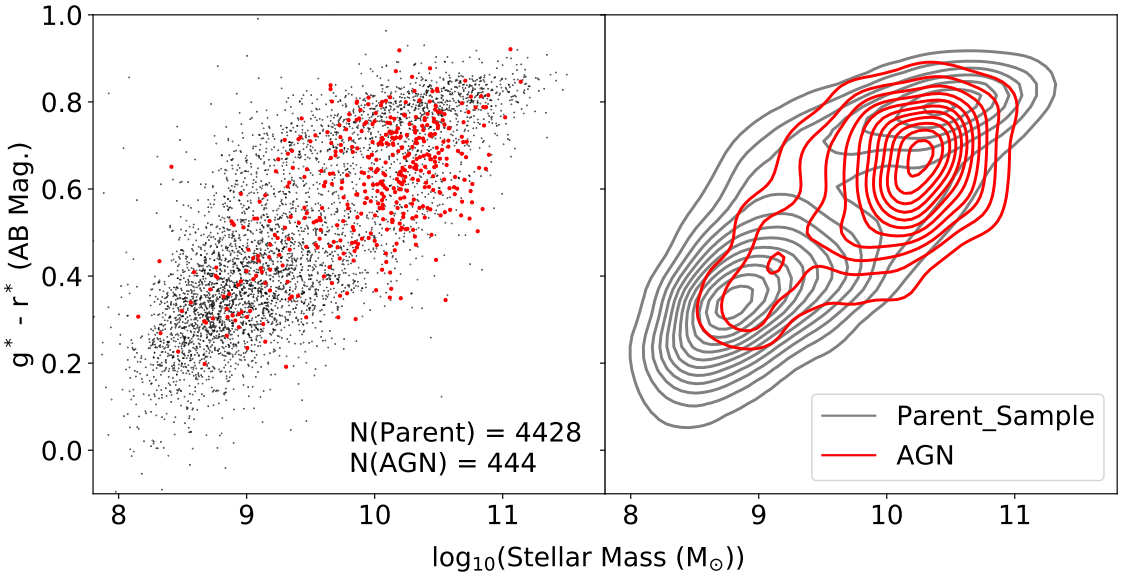

Figure 5.12: SDSS g - r (corrected for Galactic extinction) versus stellar mass from MAGPHYS, for the Parent Sample and "radio-quiet" galaxies with AGN.

Sample.

5.7 Relative Behaviour of Numeric Morphology Indicators

From the analysis above, it appears that r-band Sérsic index from a single-component surface brightness model is a reasonable numeric indicator of visual morphology for some ETGs with high Sérsic index (Figure 5.4). This is less the case with B/T and sSFR, which display some continuum behaviour but are only partially successful at constraining visual morphology. In this Section, these measures of morphology are examined further to see if any trends emerge that may assist in constraining the morphology of galaxies.

Figures 5.14 and 5.15 show r-band Sérsic indices from single-component fits to

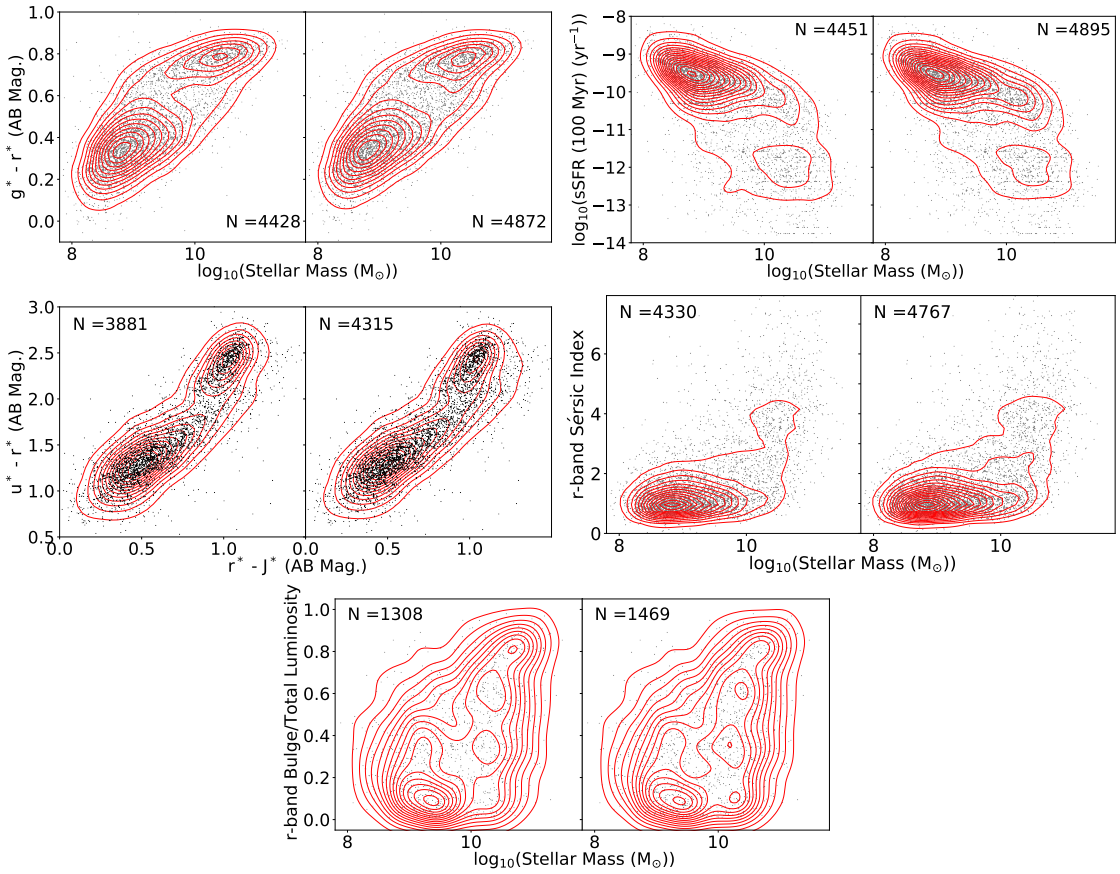

Figure 5.13: Plots of parameter spaces discussed in Sections 5.1 - 5.5, with radio-quiet, strong AGN removed *(left)* and retained *(right)* within each pair of plotted samples.

SDSS images (from GAMA II SersicCatSDSSv09) plotted against sSFR for galaxies in the Parent Sample, for ETGs/LTGs separately and for visual morphology classifications. A cluster is apparent at high sSFR and n∼1 in Figure 5.14, with galaxies diffusing away from this towards higher n and lower sSFR. Some clustering is apparent at $\log_{10}$(sSFR)∼-12 and n∼4, as discussed in Section 5.2. In Figure 5.15, LTGs are clustered around $\log_{10}$(sSFR)∼-9.7 and n∼1, while ETGs spread away from this to a weak cluster at $\log_{10}$(sSFR)∼-12 and n∼4. The presence of star-forming ETGs with lower n (∼1.5) is also apparent. Overall, these plots support the finding of continuum behaviour for these proxies for morphology. LTGs show a concentration at n∼1 and sSFR∼$10^{-9.5}$ yr^{-1}, while ETGs spread away from this.

Figures 5.16 shows the relationships between sSFR and B/T. for suitably fitted galaxies from the Parent Sample, for ETGs/LTGs separately and for the individual morphological classifications. When combined in this way, LTGs form a cluster which is separate from most ETGs, and also shows some separation from the low-mass, star-forming ETGs discussed earlier and in the next section.

5.8 Low-Mass ETGs with LTG Properties ("ETG Misfits")

All of the parameter spaces explored above show a population of visually-classified, ETG-like galaxies with properties more aligned to LTGs and distinct from LBS, specifically optical colour, sSFR and Sérsic index (Figures 5.3, 5.5 and 5.9). To study these "ETG Misfits" further, a proportion of these galaxies were isolated from the ETG sample based on limits apparent in the plots presented in previous sections, i.e. sSFR (best fit) ≥ $10^{-10.2}$ yr^{-1}, stellar mass (best fit) ≤ 10^{10} $M_{\odot}$, Sérsic index ≤ 2.4. These limits isolate 90 galaxies out of 1069 ETGs in total. Figure 5.17 shows the distributions of the ETG Misfits in a selection of the parameter spaces explored in the previous sections. Some distributions are produced by the selection criteria for ETG Misfits and therefore conform

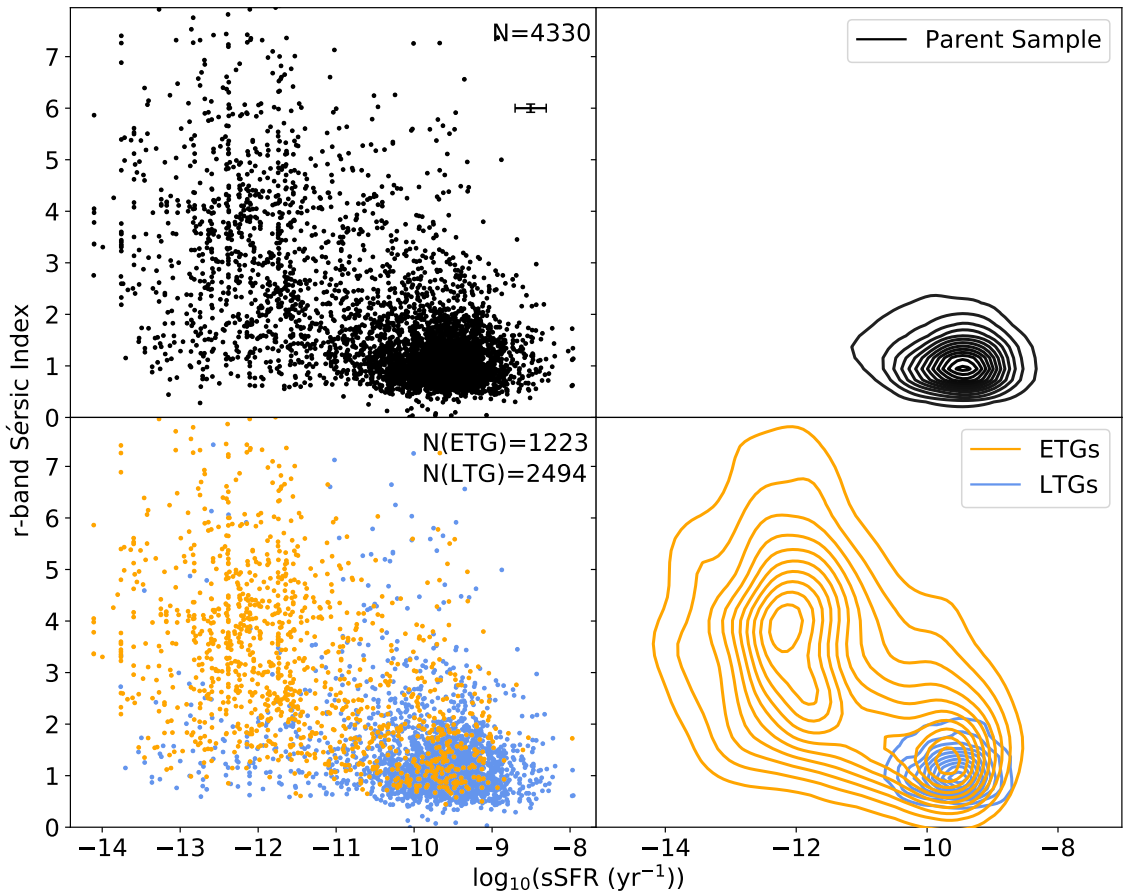

Figure 5.14: r-band Sérsic index versus sSFR for the Parent Sample, from single-model fits to SDSS images for the Parent Sample. Median uncertainties are shown for the plotted galaxies.

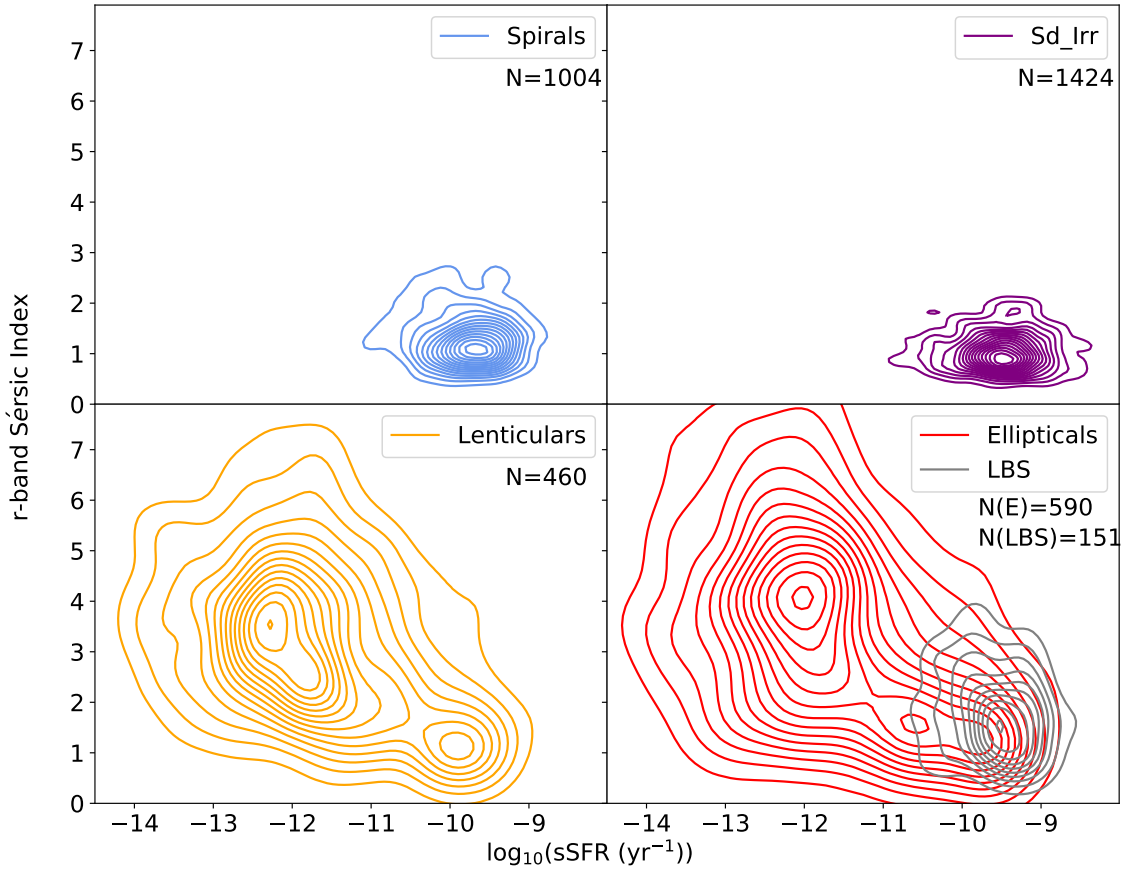

Figure 5.15: r-band Sérsic index versus sSFR for morphological classifications, from single-model fits to SDSS images.

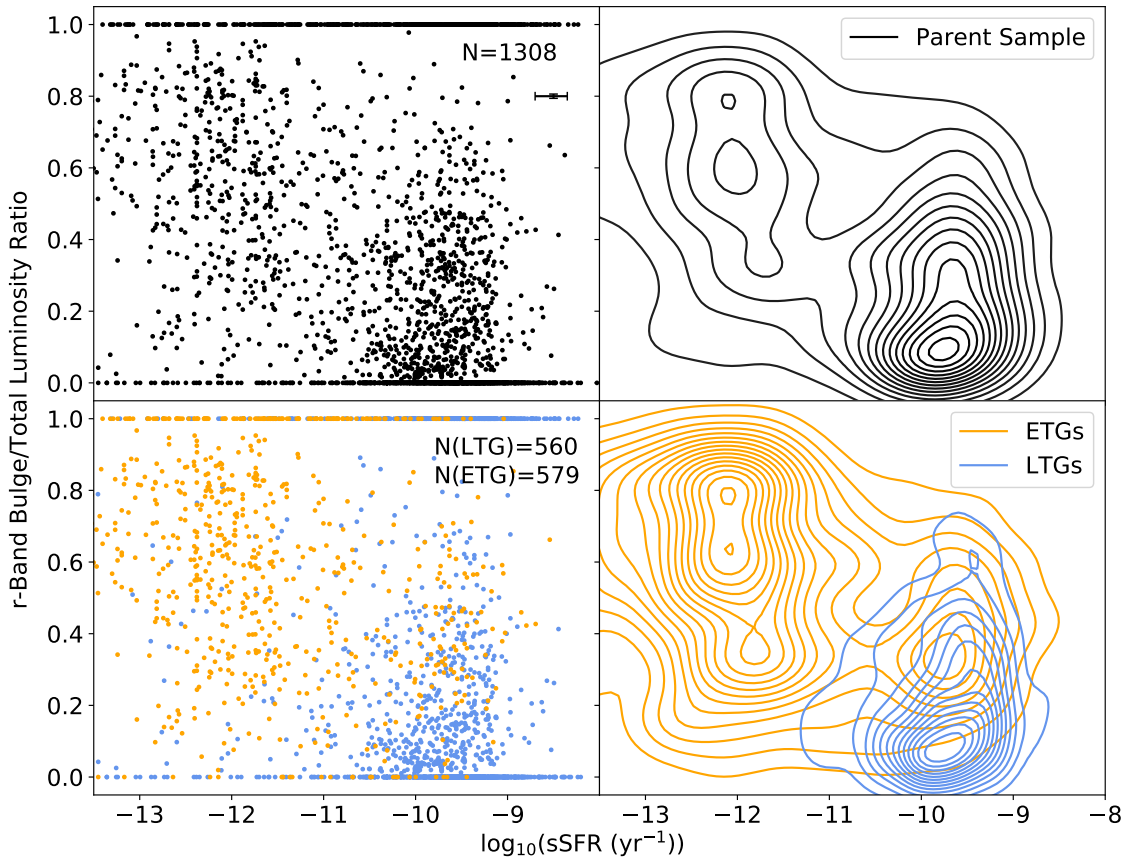

Figure 5.16: B/T versus sSFR for the Parent Sample. Galaxies with single Sérsic profile fits are included, with n≤1.5 shown as B/T = 0 and n>1.5 shown with B/T = 1. Median uncertainties are shown for the plotted galaxies with double-component model fits.

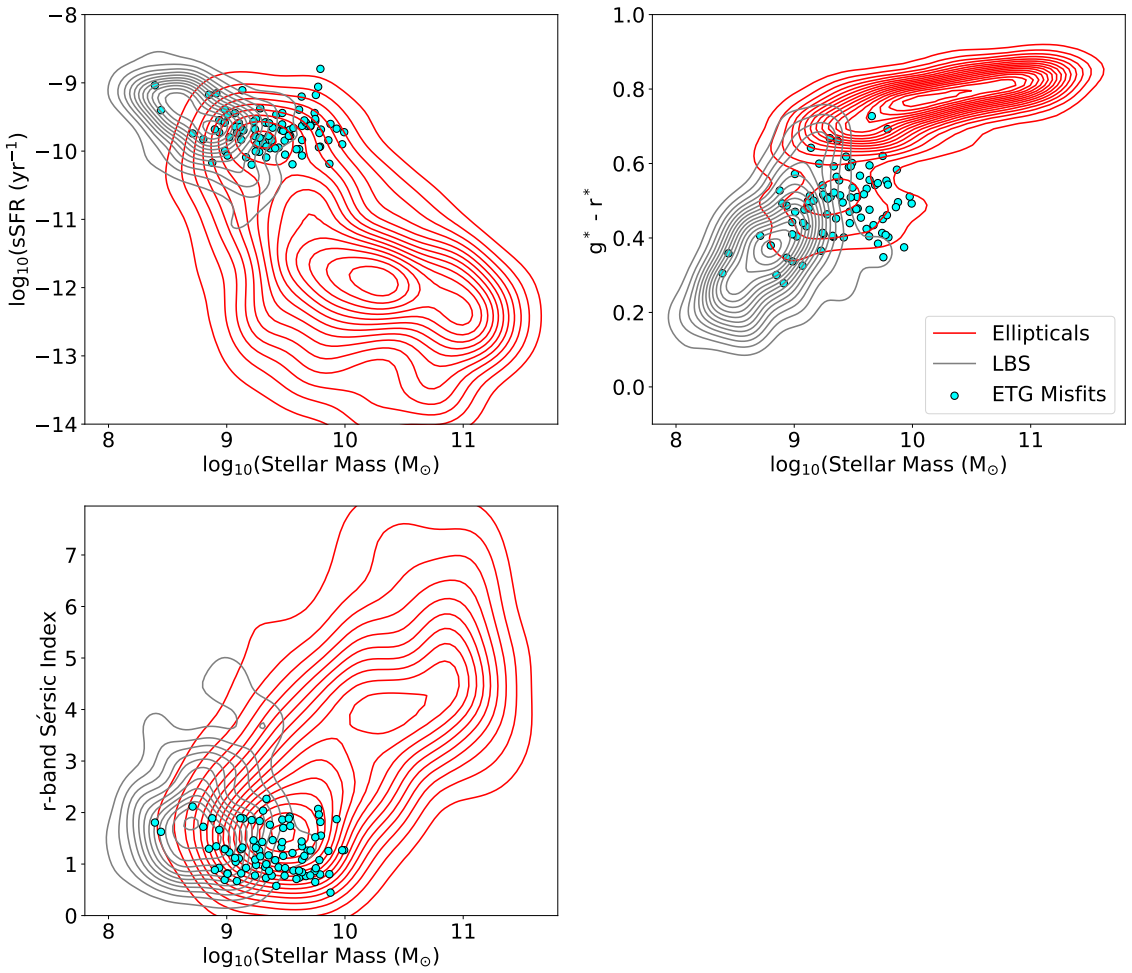

Figure 5.17: ETG Misfit distributions in various parameter spaces, compared with distributions of Ellipticals and LBS from the Parent Sample.

to expectations. The distribution of g^* - r^* colour versus stellar mass is mostly compliant with the zone where ETG misfits appear to exist, in spite of not using colour as a selection criterion.

Figure 5.18 shows that the distribution of these galaxies in terms of redshift is broadly similar to the distribution of the ETG sample. A k-sample, midrank Anderson-Darling test (Scholz & Stephens 1987) using the PYTHON function SCIPY.STATS.ANDERSON_KSAMP shows that the ”null hypothesis” of both samples being drawn from the same distribution can

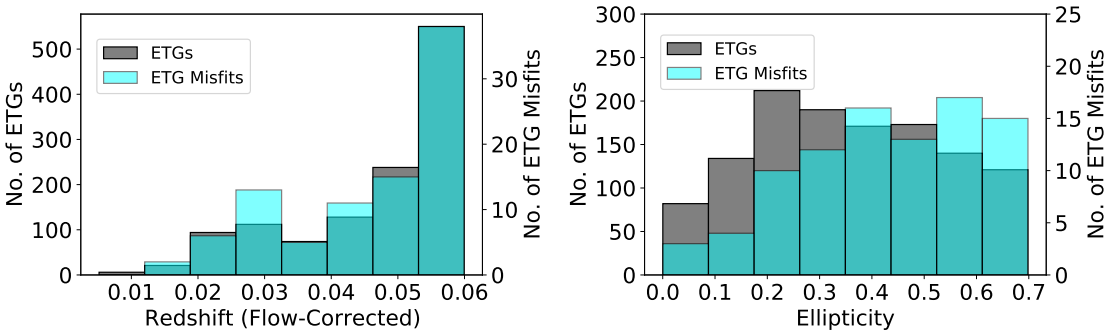

Figure 5.18: ETG Misfit distributions of redshift *(left)* and ellipticity *(right)* compared to the overall ETG sample.

only be rejected at a confidence level >25%, which means the hypothesis can be maintained. The selection of the ETG misfits as ETGs is therefore not affected by redshift. Figure 5.18 also shows the distribution of ellipticities (from the GAMA II catalogue SersicCatSDSSv09), derived from fitting of single Sérsic profiles. The ETG Misfits appear to be distributed with higher ellipticities than the ETG sample. A k-sample, midrank Anderson-Darling test shows that these ellipticity distributions are significantly different, with <0.01% significance of being the same. Assuming that the ETG Misfits have no special orientation compared to the ETGs, this implies that ETG Misfits are more elongated than the overall ETG population , e.g. disc-like or elongated spheroids.

Visual examination of KiDS gri images for the ETG misfits (Section 4.6.6) shows that five of them had residual spiral features, 34 are irregular or flocculent (38% of ETG misfits, and 39% of all Sd/Irrs classified visually in Section 4.6.6), and one could not be classified. The remainder (50) were smooth ETGs (Ellipticals or Lenticulars). Figure 5.19 shows examples of ETG misfits that are smooth, or irregular or flocculent.

Figures 5.20 and 5.21 show r-band effective radii (R_e, containing 50% of galaxy light) from GAMA II SersicCatSDSSv09 plotted against stellar mass from GAMA II MagPhysv06, both as a scatter plot and as a contour plot to indicate the locations of galaxy morphologies. Effective radii in kpc were calculated using the Astropy.Cosmology function kpc_proper_per_arcmin, using flow-corrected redshift as an input. The plot shows

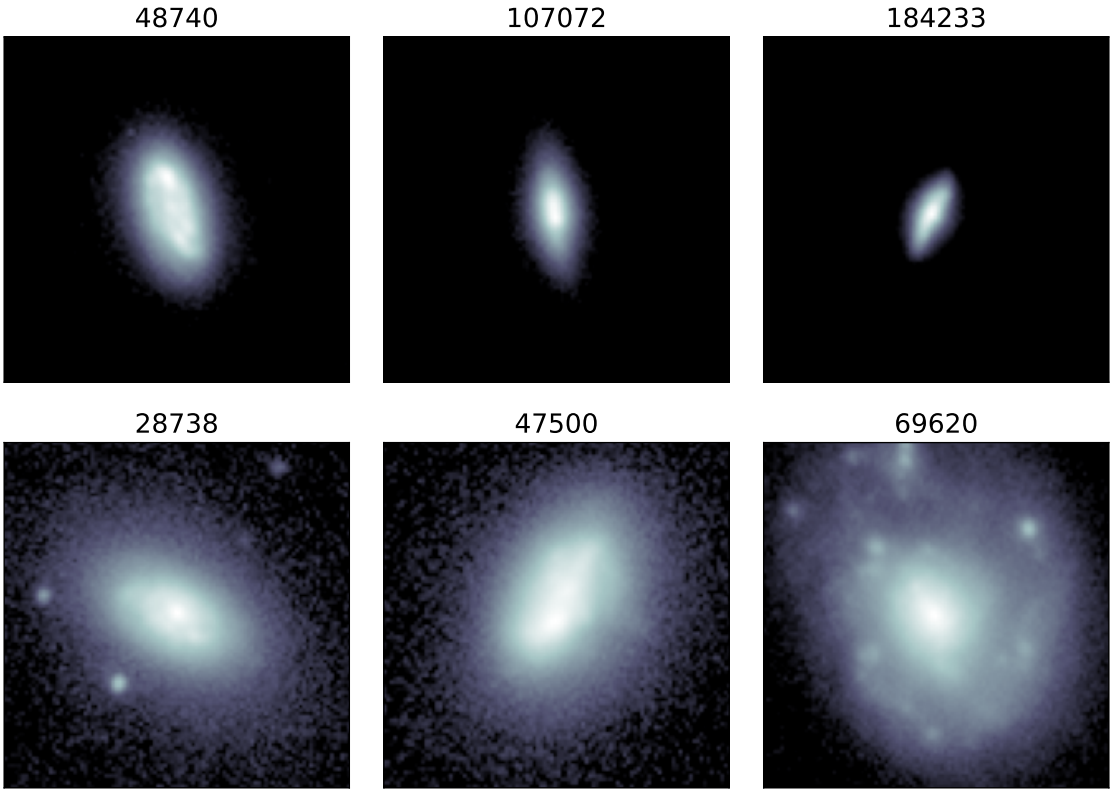

Figure 5.19: Example KiDS r-band images (20 arcsec × 20 arcsec, log-normalised) of ETG misfits. *Upper row*: Smooth. *Lower row*: Irregular/flocculent.

that the galaxies conform to a ”Zone of Avoidance” (Misgeld & Hilker 2011), in which dynamically-hot galaxies with given stellar masses cannot have radii as low as these. Addition of further stellar mass to an already compact galaxy must lead to an expansion of the galaxy out of the zone. The slope of the zone demarcation line in logarithmic space (0.8) is as given by Misgeld & Hilker (2011), but their $\log_{10}(R_e)$ intercept is increased by a factor of ∼2. r-band data are used in this work instead of the average of SDSS g and z passbands used by Misgeld & Hilker (2011), which appears to have caused an increase in measured radius in this work. The left-hand plot in Figure 5.20 shows a continuous distribution. In the right-hand plot of Figure 5.20 and in Figure 5.21, E and S0 galaxies are shown as being relatively compact compared to the LTGs. LBS are also shown as relatively compact, following the trend of the ETGs. The ETG Misfits nearly all follow the ETG and LBS trend for compactness in relation to stellar mass, apart from two which may be mis-identified LTGs. Given that all of them have been classified visually as ETGs, it is logical to classify these galaxies as low-mass, compact, star-forming ETGs that are possibly related to LBS and form a link with the Ellipticals. It is possible that they form an intermediate step between low-mass, compact galaxies, which may be the progenitors of larger galaxies before growth e.g. by mergers, and higher-mass galaxies which evolve across the GV. They can be retained in the visually-classified ETG sample, but can be isolated and removed if required using the criteria for stellar mass, SFR and single-model Sérsic index stated above.

5.9 Discussion of Chapter

In this Chapter, a clean and complete Parent Sample of 4,458 galaxies in the GAMA equatorial regions has been constructed, and 3,722 of these have morphologies visually classified as sub-classes of LTG or ETG. The ETG and LTG populations are generally distinct, except for some low-mass, star-forming ETGs that overlap with LTGs. This classification has allowed the study of the distribution of LTGs, ETGs and sub-classes

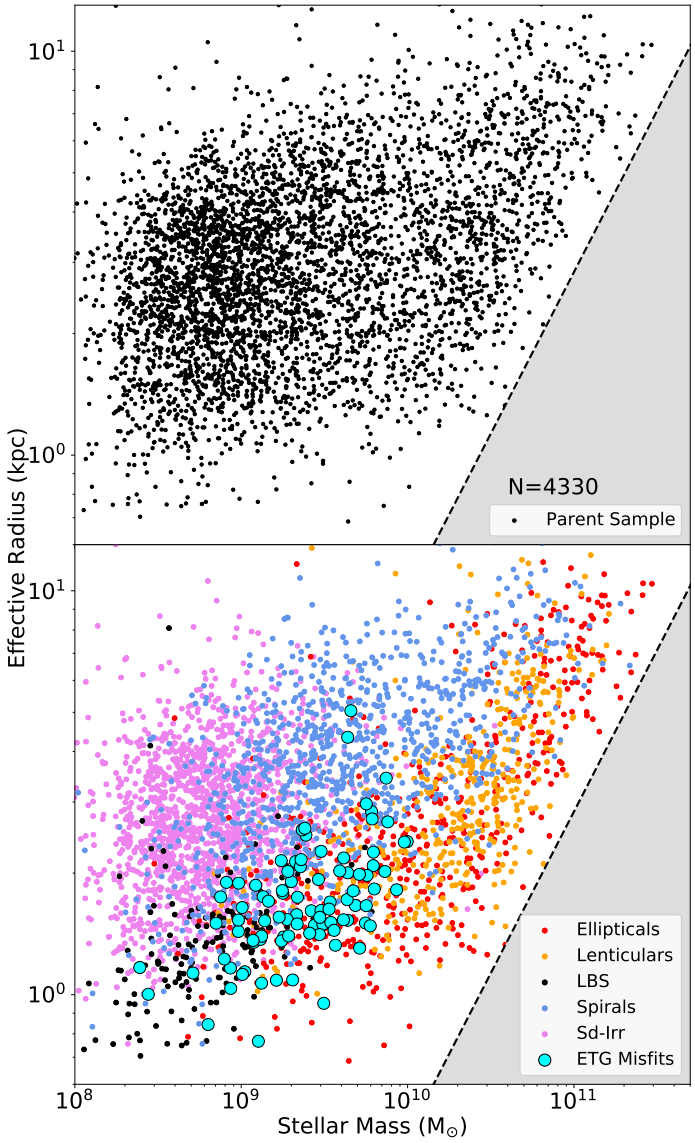

Figure 5.20: Effective r-band radius versus stellar mass for the Parent Sample and for morphological classifications. Grey shaded region is a ”Zone of Avoidance” representing a limit on the compactness of dynamically-hot galaxies (Misgeld & Hilker 2011)

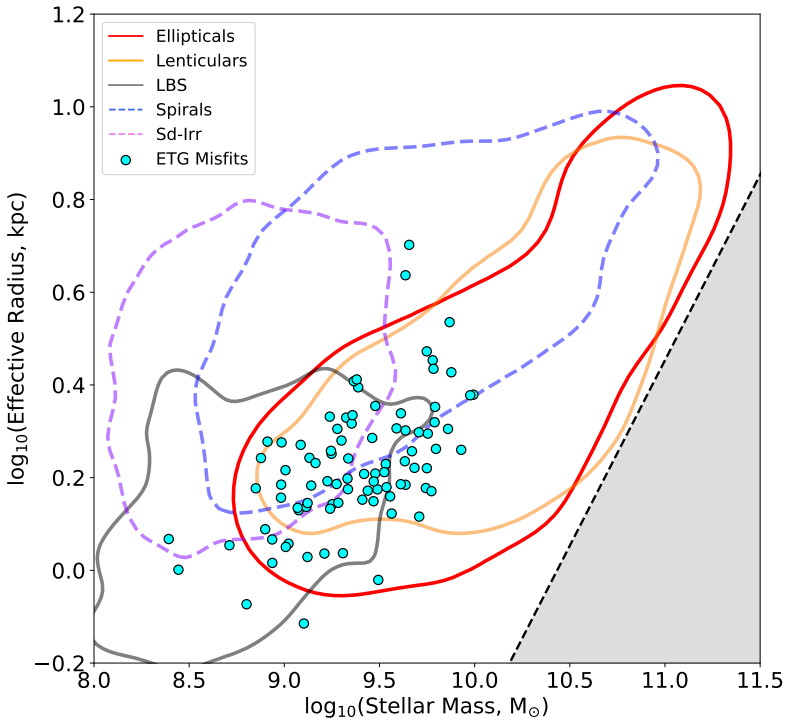

Figure 5.21: Effective r-band radius versus stellar mass for morphological classifications, shown as contours to 20% of peak density for each classification.

across various parameter spaces, with the aim of identifying smoothly-varying or discontinuous behaviour across parameter spaces as morphology changes. The removal of galaxies containing strong AGN to create the Parent Sample does not alter the findings from this Chapter. These galaxies all lie within low-density environments, so the more extreme effects of cluster environments on galaxy evolution are excluded.

The analyses above show that for most of parameter spaces considered, the distributions of morphologies show clustering at upper and lower limits. For example, Eales et al. (2018) demonstrated that clustering in the colour-stellar mass plane is due to limits on redder and bluer colours with changing star formation rate. However, continuum behaviour is apparent in certain parameter spaces considered. The plot of sSFR versus stellar mass shows continuum behaviour if morphology is neglected. However, when considered alone a subset of the ETGs form a cluster at a sSFR of $\sim 10^{-12}$ yr^{-1}. This could be due to ongoing, low-level star formation over long durations due to stochastic events including re-introduction of ISM. Continuum behaviour is also apparent in the r^* - J^* versus u^* - r^* plane in terms of sSFR through this space. If photometry is available for a galaxy, it should be possible to obtain an estimate of its sSFR by locating the galaxy on this plot. This behaviour is the same as that shown by Wang et al. (2017).

The Sérsic index - stellar mass plane also shows continuum behaviour away from the region occupied by LTGs when using single-component model fitting (Kelvin et al. 2014). Figures 5.8 and 5.9 show that LTGs typically have r-band Sérsic indices of ∼1, whereas ETGs spread away from this with some clustering around ∼2 or ∼4. This clustering could simply be due to the natural structure of discs and bulges. Indices of 1 are associated with discs with exponentially declining radial surface brightness profiles. Indices of ∼2 are indicative of pseudo-bulges, which could include nuclear rings and bars (e.g. Kormendy & Kennicutt 2004), while indices of 4 indicate classical bulges with a de Vaucouleurs surface brightness profile (de Vaucouleurs 1948).

Continuum behaviour can also be seen in the relation between bulge/total r-band light (B/T) and stellar mass for Lenticulars (Figure 5.11). A spread of B/T values almost from

~0.2 to ~0.8 can be seen. Bulge growth is a known mechanism for quenching of star-forming disc galaxies (morphological quenching, see Section 1.2.1), so this spread could indicate a wide range of bulge growth and evolutionary progress towards fully-passive galaxies within the Lenticular classification. The large spread of B/T with varying stellar mass means that it cannot isolate morphology uniquely. However, by inspection of Figure 5.10 B/T $\geq$0.65 may indicate a subset of early-type morphology.

The plot of sSFR versus stellar mass in particular (Figure 5.4) shows that the LTGs mostly follow a star-forming main sequence which is relatively tight in terms of sSFR, but the decline in sSFR away from SFMS due to quenching is occurring largely in the identified ETGs, along with growth towards the most massive galaxies in the sample. The behaviour shown in the plot has been demonstrated in other studies (e.g. Brinchmann & Ellis 2000; Salim et al. 2007; Peng et al. 2010; Saintonge et al. 2016, 2018). Unlike other studies which select ETGs based on having low sSFR (e.g. Croom et al. 2021b), this study has focussed on smooth visual morphology as an indicator of ETG status. As a result, ETGs with star formation have been retained in the ETG sample. Given the link between star formation and the presence of cool ISM (dust and molecular gas), this ensures that ETGs containing ISM are retained for study in this work.

In addition, a population of low-mass, star-forming ETGs has been identified in various parameter spaces that are related to both Ellipticals/Lenticulars and LBS, and appear to provide a link between these two classifications in terms of their properties. It is possible that these ETGs are an intermediate step between less massive galaxies and more massive galaxies which evolve via interactions and mergers with the smaller ones.

Overall, the analysis of the Parent Sample and morphologically-classified subsets shows that that the continuum behaviour in galaxy properties for galaxy evolution proposed by Eales et al. (2017) is apparent in some parameter spaces, and is probably masked by clustering due to physical limits within others. Further work on this topic could make use of additional galaxy properties recently published as part of GAMA DR4 (Section 2.8.1).

Chapter 6

Properties of Cool Interstellar Dust in Local Galaxies

6.1 Introduction

In this chapter, the fitting of a dust thermal emission model to measured sub-mm wavelength spectra from the H-ATLAS survey (Section 2.8.7) is used to obtain dust properties for all galaxies with suitable sub-mm detections in the Parent Sample created in Chapter 3. The behaviour of dust properties with changes in morphology and other galaxy properties from GAMA II is then explored. A description of the thermal emission model for cool dust is provided, along with a description of the methods used to fit the model to the data.

6.2 Spectra of Cool Dust Thermal Emission

Interstellar dust within a galaxy consists of fine solid particles (diameter ~0.5 μm or less) typically consisting of carbon, silicon, iron and ice (Whittet 2003). The sources of internal production of dust in a galaxy include supernovae and winds from Asymptotic Giant Branch (AGB) stars (Whittet 2003; Lamperti et al. 2019, and references therein). Significant quantities of dust can also be supplied to a galaxy externally, by acquisition of ISM from other galaxies by merger or interaction (e.g. Smith et al. 2012). Once in place, dust particles are subject to conditions that change their mass, structure and composition or destroy them, such as accretion of metals from surrounding gas, shockwaves from supernovae or sputtering by cosmic rays or high-energy photons. The dust population in a galaxy can therefore have different compositions and temperatures in different locations, depending on its formation history and subsequent evolution. The spectral fitting tool MAGPHYS (Section 2.7.3) considers this, as discussed in Section 6.4.4. However, it is possible to approximate the bulk properties of the dust by assuming a single dust population with a single temperature and composition. A thermal emission model that is a function of dust mass, dust temperature and emissivity coefficient (dependent on dust structure and composition), referred to as a Single Modified Blackbody (SMBB) model, can be fitted to a measured emission spectrum at sub-mm wavelengths (e.g. 60 - 1000 μm) to recover these parameters (e.g. Smith et al. 2012; Lamperti et al. 2019). Lamperti et al. (2019) explored more complex models with more free parameters such as two coexistent dust populations each with different properties, but they used additional flux density measurements to those from the Herschel for model fitting. There is a limit on the number of free parameters that can be fitted to a model using only flux densities at five wavelengths provided by H-ATLAS. This work focusses solely on the SMBB model with three free parameters, namely dust mass (M_d), dust temperature (T) and dust emissivity coefficient (β), along with known galaxy luminosity distance (D_L), mass absorption coefficient (κ_ν, m^2 $kg^{-}1$) and redshift (z) (Hildebrand 1983; Calura et al. 2017). These parameters are used to determine the observed flux density $S_{\nu,obs}$ from conditions in the galaxy frame:

$$S_{\nu,obs} = M_d \left(\frac{\kappa_{\nu,rest} B_{T,\nu,rest}}{D_L^2} \right) (1+z) \tag{6.1}$$

where $B_{T,\nu}$ is the Planck function for blackbody emission, with c, h and k as the speed of light, the Planck constant and the Boltzmann constant:

$$B_{T,\nu} = \frac{2\pi\nu^3}{c^2} \left(e^{\frac{h\nu}{kT}} - 1 \right)^{-1} \tag{6.2}$$

This relation is an expression of Kirchhoff's Law of thermal radiation, which implies that the dust is at thermal equilibrium with its surroundings and absorption and emission of thermal radiation by the dust are equal. In this work, all model fitting is performed in the galaxy rest frame, so wavelengths and flux densities from H-ATLAS observations are adjusted by dividing them both by $(1 + z)$. The mass absorption coefficient κ_ν for interstellar dust at any observed emission frequency is determined as follows (Hildebrand 1983, their Section 2):

$$\kappa_\nu = \kappa_0 \left(\frac{\nu}{\nu_0} \right)^\beta \tag{6.3}$$

where κ_0 is a reference mass absorption coefficient at frequency ν_0 and β is the emissivity coefficient. The value of κ_0 is highly uncertain, and estimates normalised to the same ν_0 have a spread of up to three orders of magnitude (Clark et al. 2016, their Figure 1). It also varies to some extent with dust composition and temperature (Lamperti et al. 2019, and references therein). In this work a constant value for the reference mass absorption coefficient (κ_0) of 0.89 $m^2\ kg^{-1}$ at a reference wavelength of 250 μm (ν_0 = 1.991 THz) is selected, as used by Dunne et al. (2011). This value is derived from an earlier value of 0.077 $m^2\ kg^{-1}$ at 850 μm (Dunne et al. 2000), adjusted to a reference wavelength of 250μm using Equation 6.3 and assuming a value for β of 2. The estimate was selected by Dunne et al. (2000) as being intermediate between mass absorption coefficients for graphites and silicates (Draine & Lee 1984; Hughes et al. 1993). The same value (0.077

m^2 kg^{-1}) and reference wavelength (850 μm) are also used for SED fitting for the GAMA II MagPhysv06, so the dust SMBB model fitting presented here should be consistent with results from SED fitting within GAMA II MagPhysv06 provided that values of β remain close to 2. Selection of a reference frequency for κ of 250μm also places the reference wavelength at the centre of the range for H-ATLAS photometry for fitting.

6.3 Fitting of Dust Emission Models to Data

The catalogue data from H-ATLAS for the ETGs in the Parent Sample were fitted with the SMBB model using a Hamiltonian Monte-Carlo (HMC) approach based on Bayes' theorem. All fitting used Python code adapted by this author from scripts donated by Dr Isabella Lamperti, formerly of University College London, created for the analysis of dust masses and properties of local galaxies within the JINGLE galaxy sample (Section 2.8.7). These scripts used PyStan for fitting, which is a Python implementation of the STAN statistical language[1]. Two approaches to model fitting were used, referred to as non-hierarchical and hierarchical. The non-hierarchical approach fits each galaxy separately, while the hierarchical approach draws values to fit for each galaxy from "hyperparameters" with distributions of known shape. The parameters defining the hyperparameter distributions are themselves fitted to data for the whole galaxy population of interest. The hierarchical approach makes an assumption that the properties of dust in the whole fitted population form distributions arising from an underlying similarity. The approach has been shown to break (or at least minimise) a known degeneracy between dust temperature and emissivity coefficient β (Shetty et al. 2009a,b; Lamperti et al. 2019) which can skew the fitted results when fitting models to sub-mm dust emission spectra, as illustrated later in Section 6.4.2.

[1] https://mc-stan.org/

6.3.1 Non-Hierarchical Model Fitting

Non-hierarchical model fitting in this work is based on Bayes' theorem, reviewed in Lamperti et al. (2019), which in this case provides a posterior probability as a measure of how well a combination of model parameters fits the data:

$$p\left(\theta|S_{obs}\right) = \frac{p\left(S_{obs}|\theta\right)}{p\left(S_{obs}\right)} p\left(\theta\right) \propto p\left(S_{obs}|\theta\right) p\left(\theta\right) \tag{6.4}$$

where θ are fitted parameters, S_{obs} are observed flux densities, $p\left(\theta\right)$ is the prior probability assumed for the fitted parameters and $p\left(\theta|S_{obs}\right)$ is the posterior probability. The aim is to find the distribution and optimum (maximum) for the posterior probability by repeatedly sampling the assumed prior distribution and applying it to the model $p\left(S_{obs}|\theta\right)$. The term $p\left(S_{obs}\right)$ is a constant for given observations, and is set to 1 so that the equation calculates a measure of likelihood which can be explored in the same way as the posterior probability. By calculating the likelihood distribution using an appropriate algorithm to sample from the prior distribution repeatedly, it is possible to build up a likelihood probability density function (PDF) for each fitted parameter. Once sufficient samples have been taken to form sufficiently robust PDFs (see discussion on convergence below), optimum values of the fitted parameters (50th percentile) and uncertainty estimates (16th and 84th percentiles for 1σ) can be derived from the PDF.

It is appropriate to work with log-likelihood when performing this calculation, because the calculation of the log posterior probability is straightforward for uncertainty distributions such as Gaussian (Wall & Jenkins 2003). In this case a multivariate form was used to account for the fact that the uncertainties in flux densities from Herschel are not independent of each other. For example, a common calibration source with uncertainty in emission strength may have been used to convert signals from PACS or SPIRE to flux densities. The multivariate expression for log-likelihood, based on Gaussian noise distribution for the data, includes a covariance matrix which includes information on these correlated errors (Wall & Jenkins 2003):

$$l = -\frac{1}{2}\left(d\ ln(2\pi) + ln\left(|C|\right) + \sum_{i=1}^{d}\left(x_i - x_\mu\right)^T C^{-1}\left(x_i - x_\mu\right)\right) \tag{6.5}$$

where l is the log likelihood, d is the number of data points to be fitted, C is a covariance matrix, x_i are the data points and x_μ are the model predictions for the data points. The covariance matrix used in this instance is constructed from two components, a d × d calibration covariance matrix (d is the number of passbands) covering the correlated and uncorrelated uncertainties in calibration, and a d × d measurement covariance matrix which is essentially a diagonal matrix containing the individual measurement uncertainty per passband. The calibration covariance matrix is set up using values from Gordon et al. (2014) and Lamperti et al. (2019), and is shown in Equation 6.6. The clustering of non-zero values in the calibration covariance matrix reflects the two passbands in the PACS instrument and the three in the SPIRE instrument, in terms of correlated uncertainties.

$$C_{Cal} = \begin{bmatrix} 0.02^2 & 0.02^2 & 0 & 0 & 0 \\ 0.02^2 & 0.02^2 & 0 & 0 & 0 \\ 0 & 0 & 0.04^2 & 0.04^2 & 0.04^2 \\ 0 & 0 & 0.04^2 & 0.04^2 & 0.04^2 \\ 0 & 0 & 0.04^2 & 0.04^2 & 0.04^2 \end{bmatrix} + \begin{bmatrix} 0.05^2 & 0 & 0 & 0 & 0 \\ 0 & 0.05^2 & 0 & 0 & 0 \\ 0 & 0 & 0.015^2 & 0 & 0 \\ 0 & 0 & 0 & 0.015^2 & 0 \\ 0 & 0 & 0 & 0 & 0.015^2 \end{bmatrix} \tag{6.6}$$

The full covariance matrix is then formed using the flux density measurements and uncertainties for the ETG of interest:

$$C = C_{cal}\overline{Y} + \delta\overline{Y} \tag{6.7}$$

where $\overline{Y}$ is a d × d matrix formed from products of the measured flux densities and δY is a diagonal d × d matrix formed from the flux density measurement variances per passband.

Table 6.1: Flat priors used for SMBB model fitting.

Parameter	Prior Range (Hierarchical)	Prior Range (Non-Hierarchical)
Log_{10}(Dust mass ($M_\odot$))	5 - 10	5 - 10
Dust temperature (K)	10 - 45	10 - 60
Dust emissivity coefficient (β)	0.5 - 4.5	0.1 - 4.5

Identical flat priors with defined ranges (probability = 1 inside, 0 outside) were used for the three fitted parameters for each ETG, with wide but physically realistic limits as shown in Table 6.1. The initial range used for hierararchical fitting was extended for non-hierarchical fitting, to accommodate a wider range of fitted parameters.

6.3.2 Hierarchical Model Fitting

A hierarchical MCMC approach to fitting the SMBB model to the H-ATLAS data was also used, which involves fitting to data for individual galaxies and to the whole set of galaxies to be fitted. Fitting in this way makes use of hyperparameters, where the model parameters to be fitted are assumed to follow a known form of distribution and hyper-parameters control the actual shape of the distribution. Fitting a hierarchical model to data involves drawing hyperparameters from defined prior distributions, setting up the model parameter distributions using the drawn values, and then fitting the model to data for individual galaxies using non-hierarchical MCMC described earlier. The drawing of hyperparameters is performed repeatedly using an appropriate algorithm to select subsequent draws, until sufficient fits have been performed to define the posterior likelihood distributions of the hyperparameters. The likelihoods from fits of individual galaxies are also used to define posterior likelihood distributions for individual galaxy parameters, allowing median values and uncertainties for parameters to be determined. Bayes' theorem is written as follows, to reflect the linkage between the fitted parameters for an individual

galaxy θ_i and the hyperparameter distributions characterised by hyperparameter means μ_i and a covariance matrix Σ describing the varances and covariances for fitted parameters in θ (Lamperti et al. 2019, their equation 10):

$$p\left(\theta_i|S_{obs,i},\mu,\Sigma\right) = \frac{p\left(S_{obs,i}|\theta_i\right)}{p\left(S_{obs,i}\right)} p\left(\theta_i|\mu,\Sigma\right) \propto p\left(S_{obs,i}|\theta_i\right) p\left(\theta_i|\mu,\Sigma\right) \tag{6.8}$$

When fitting of models to the whole galaxy sample is considered, the posterior distribution for all parameters and the hyperparameters is expressed as (Lamperti et al. 2019, their equation 11):

$$p\left(\theta,\mu,\Sigma|S_{obs}\right) \propto \prod_{i=1}^{n} p\left(S_{obs}|\theta_i\right) p\left(\theta_i|\mu,\Sigma\right) \cdot p\left(\mu\right) \cdot p\left(\Sigma\right) \tag{6.9}$$

For hierarchical fitting, priors and prior distributions are needed for both the hyperparameters and the parameters drawn using the hyperparameters, and a suitable distribution for the noise within the data is assumed. This work follows the approach used by Lamperti et al. (2019), which is based on Kelly et al. (2012), Galliano (2018) and the STAN authors (Stan Development Team 2022a). Lamperti et al. (2019) describe the various priors and prior distributions used for terms in Equation 6.8, which were adopted for this work. For parameters for individual galaxies whose distribution is defined by the hyperparameters, two prior distributions are considered. A multivariate Student t-distribution is used with eight degrees of freedom:

$$p\left(\theta_i|\mu,\sigma\right) = \frac{\Gamma\left((f+m)/2\right)}{\Gamma(f/2)} \frac{1}{(\pi f)^{m/2}} \frac{1}{\sqrt{\Sigma}} \left(1 + \frac{1}{f}(\theta_i-\mu)^T\Sigma^{-1}(\theta_i-\mu)\right)^{-\frac{f+m}{2}} \tag{6.10}$$

where m is the number of measured flux densities per galaxy (5 passbands) and f is the number of degrees of freedom for the distribution (8 in this instance). Usually, the number of degrees of freedom is defined as one less than the sample size of interest, but in this instance it was simply used to control the shape of the distribution and the extent of

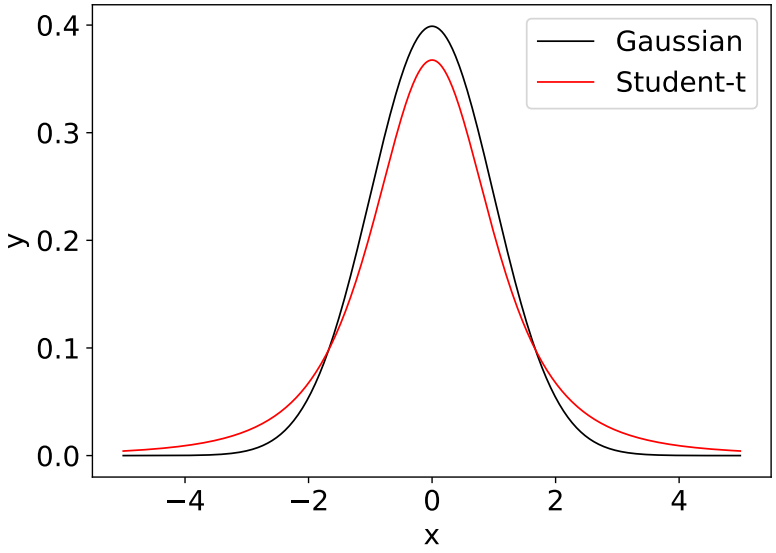

Figure 6.1: Comparison of Gaussian and Student-t (3 degrees of freedom) distributions (y) for input values of x. $\mu = 0$, $\sigma = 1$.

its outlying regions. Lamperti et al. (2019) report that varying the number of degrees of freedom did not alter their results significantly, so eight degrees of freedom are retained for use in this work. A Gaussian prior distribution is also used for comparison (Feigelson & Babu 2012):

$$p\left(\theta_i|\mu,\sigma\right) = \frac{1}{(2\pi)^{\frac{m}{2}}}\frac{1}{\sqrt{|\Sigma|}}exp\left(-\frac{1}{2}\left(x-\mu\right)^T\Sigma^{-1}\left(x-\mu\right)\right) \tag{6.11}$$

where m is the dimension of the vector x in the Equation. Both form symmetrical priors, but the Student t-distribution is narrower than an equivalent Gaussian distribution and has "wings" which capture more outliers (Figure 6.1). The Student-t distribution is therefore somewhat less dependent on the assumption of common dust property (hyperparameter) distributions (Lamperti et al. 2019). For comparison, both Gaussian and Student-t distributions were used for fitting in this work.

For use in Equation 6.9, the hyperparameter means (μ) are assigned flat priors with large ranges (p = 1 within the range, 0 outside), shown in Table 6.1. The covariance

matrix Σ is constructed as described in Lamperti et al. (2019), to achieve uniform prior distributions of correlations between the fitted parameters in the range [-1, 1] (all equally likely) using the ”separation strategy” defined by Barnard et al. (2000). This combines two defined matrices to form Σ. The first, τ, is a diagonal matrix containing the hyper-parameter standard deviations, and the second is the correlation matrix Ω which must be positive-definite and symmetric. These are combined using a defined expression to form the covariance matrix:

$$\Sigma = \tau\Omega\tau \tag{6.12}$$

The probability distribution of the hyperparameters to be fitted can be written as follows (Lamperti et al. 2019), for direct use in Equation 6.9:

$$p(\mu) \cdot p(\Sigma) \propto p(\mu) \cdot p(\tau) \cdot p(\Omega) \tag{6.13}$$

Lamperti et al. (2019) used the following prior probability distributions for τ and Ω, in line with guidance from the STAN authors (Stan Development Team 2022b). For priors on τ for each free parameter in the model, half-Cauchy distribution is used because of its useful shape as a weakly informative, symmetrical prior with a relatively flat ”centre” and sharp decreases in probability at the edges, to form a diagonal matrix. The scale factor σ_C is 2.5 in this instance.

$$p\left(\tau_{jj}\right) = \frac{1}{\pi\sigma_C} \frac{1}{1 + \left(\tau_{jj}/\sigma_C\right)^2} \tag{6.14}$$

where j runs over the number of free parameters and τ_{ij} is zero for off-diagonal elements. For Ω, a Lewandowski-Kurowicka-Joe (LKJ) correlation distribution is used (Lewandowski et al. 2009) with shape factor $\nu_{LKJ} = 2$. This form of matrix is designed to become more diagonal as ν increases. Its determinant is then used as follows (Lamperti

et al. 2019, their Equation 21):

$$p\left(\Omega\right) \propto det\left(\Omega\right)^{\nu_{LKJ}-1} \tag{6.15}$$

An additional set of hyperparameters dealing with calibration offsets is also fitted. This fits a single multiplying correction factor $(1 + \delta_i)$ to passband i of the five used for H-ATLAS. Either multi-normal or multi-Student-t prior distributions with 3 degrees of freedom were used as priors for these. It is possible to use these parameters for hierarchical fitting because of the large number of data points to be fitted across the whole galaxy sample. For non-hierarchical fitting of a single galaxy, with five data points and three parameters for an SMBB model, there are insufficient degrees of freedom to fit these extra parameters. These offsets are fitted for completeness when using hierarchical fitting, so that their effect is accounted for in the final posterior distributions. Ideally their values should be consistent with zero.

6.3.3 Noise Modelling

PySTAN requires definitions of the noise distributions in the measured data. For non-hierarchical fitting, a Gaussian distribution for noise on a measurement y using the 1σ uncertainty σ provided in the H-ATLAS catalogue was used:

$$p\left(y|\mu,\sigma\right) = \frac{1}{\sqrt{2\pi}\sigma}\exp\left(-\frac{1}{2}\left(\frac{y-\mu}{\sigma}\right)^2\right) \tag{6.16}$$

For hierarchical fitting, a Student-t distribution (Equation 6.17) is used with three degrees of freedom for the noise distribution (Lamperti et al. 2019). The ”wings” of this distribution allow more flexibility in fitting models with parameters constrained by hyperparameters than a Gaussian distribution. Lamperti et al. (2019) only used a Gaussian distribution throughout for noise, but this was to address a specific issue with fitting

additional measured flux densities at 850μm which is not relevant in this case.

$$p\left(y|\mu,\sigma,f\right)=\frac{\Gamma\left(\left(f+1\right)/2\right)}{\Gamma\left(f/2\right)}\frac{1}{\sqrt{f\pi\sigma}}\left(1+\frac{1}{f}\left(\frac{y-\mu}{\sigma}\right)^{2}\right)^{-\frac{f+1}{2}} \tag{6.17}$$

6.3.4 Implementation of Fitting

The STAN statistical programming language was used for all fitting of SMBB spectra to H-ATLAS flux densities. STAN was implemented in Python using PyStan2, which allowed data input, model fitting and processing of results within the same script. Colour and flux bias correction may cause problems if implemented on-the-fly during model fitting with STAN, especially for hierarchical model fitting (Lamperti et al. 2019), so a similar approach used by Lamperti et al. (2019) was adopted where colour and flux bias corrections were applied successively over three rounds of model fitting, as follows. The first round of fitting used H-ATLAS catalogue flux densities, adjusted using colour correction (Section 2.7.4) to initial estimates for dust temperature of 20K and β of 2. This gave revised estimates of temperature and β, which were used to revise H-ATLAS catalogue data with new colour and flux bias corrections, and a second round of fitting was performed. The new estimates of temperature and β were then used to update the H-ATLAS catalogue flux densities a third time, and a third round of fitting was performed. This approach was found to achieve satisfactory convergence of parameters (see Section 6.4.1).

STAN includes a No-U-Turn Sampler (NUTS, Hoffman & Gelman 2014) to perform sampling of the prior distributions and home in on an optimum fit. This is based on a Hamiltonian Monte-Carlo (HMC) method, which uses the derivatives of the density function being generated to explore the parameter space more efficiently than more straightforward sampling techniques (e.g. Metropolis) (Betancourt & Girolami 2013). In essence, it optimises the exploration of a parameter space by detecting u-turns into previously explored territory, and then selects an appropriate new starting point for further

exploration. This step avoids excessive computational effort while ensuring sufficiently detailed exploration of the parameter space. The PYTHON code to implement STAN was run mostly on a desktop computer with four available processor cores. Consequently, four parallel sampling chains (arrays of consecutively sampled parameter values) were used for fitting because PYSTAN2 assigns one chain per core. A typical fitting run for ~450 galaxies required approximately 8-9 hours to complete. Better performance could be achieved with an upgrade to PYSTAN3, which has improved capabilities for parallel processing. However, the PYTHON calls to run the STAN scripts and obtain the results are not backwards-compatible. Conversion of the existing code to PYSTAN3 is left for future work.

An essential step in using sampling-based methods to fit models to data is to ensure that the parameter space has found a solution and has been adequately sampled, to build meaningful posterior distributions from the results. This normally means that individual parallel chains of drawn samples are effectively sampling the same parameter space around an optimum. STAN returns two results that are useful for checking that this convergence has been achieved. The first is a measure of the effective sample size (N_{eff}), which estimates an equivalent number of sample values with the same ability to estimate the results as the total number of samples taken, N. N_{eff} is calculated using the definition of an autocorrelation parameter ρ_t for sample t out of the total N (Stan Development Team 2022b):

$$\rho_t = \frac{1}{\sigma^2} \int_\theta \left(\theta^{(n)} - \mu\right)\left(\theta^{(n+t)} - \mu\right) p\left(\theta\right) d\theta \tag{6.18}$$

where $\theta^{(n)}$ is the value within a chain at position n, μ is the arithmetic average of chain values and $p(\theta)$ is the prior probability for theta (which can be set to 1). The effective sample size is then (Stan Development Team 2022b):

$$N_{eff} = \frac{N}{1 + 2\sum_{t=1}^{\infty} \rho_t} \tag{6.19}$$

If $N_{eff} > 10$, the sampling is usually sufficient to estimate fitted parameters and uncertainties from prior distributions (Gelman & Rubin 1992). The second convergence check is the scale reduction factor, $\widehat{R}$. This is the ratio of the average samples within each parallel chain to the ratio of the pooled samples across all chains (Stan Development Team 2022b). If the chains have reached equilibrium, i.e. they are sampling around a stable solution, then $\widehat{R} = 1$. Typically, $\widehat{R} \leq 1.1$ is satisfactory for convergence (Gelman & Rubin 1992).

6.4 Results

Galaxies for fitting SMBB spectra were selected from the Parent Sample derived in Chapter 3, based on a minimum of 3σ detection within H-ATLAS at 160, 250 and 350μm. Of the 4,458 galaxies in the Parent sample, 445 galaxies meet this criterion. These include galaxies which have not been classified morphologically in Chapter 3 because they have an ellipticity >0.7. The other galaxies in the Parent Sample may still contain cool dust, but their H-ATLAS photometry is not suitable for fitting in this work. The galaxies fitted are predominantly LTGs or not classified due to high ellipticity, as discussed in Section 6.4.5, with proportionally more ETGs not fitted compared to those fitted. This behaviour can be expected if ETGs have less dust per unit stellar mass than LTGs (e.g. Smith et al. 2012).

6.4.1 Application of Colour and Flux Bias Corrections

Figures 6.2 and 6.3 show how the changes in parameter values over the three rounds of model fitting reduces sharply between the second and third rounds compared to the first and second. A parameter ζ is used as a measure of the changes per galaxy, which for a given galaxy parameter is the change in a parameter between model runs as a fraction of the 1σ uncertainty in the parameter from the later run. For hierarchical fitting, values of

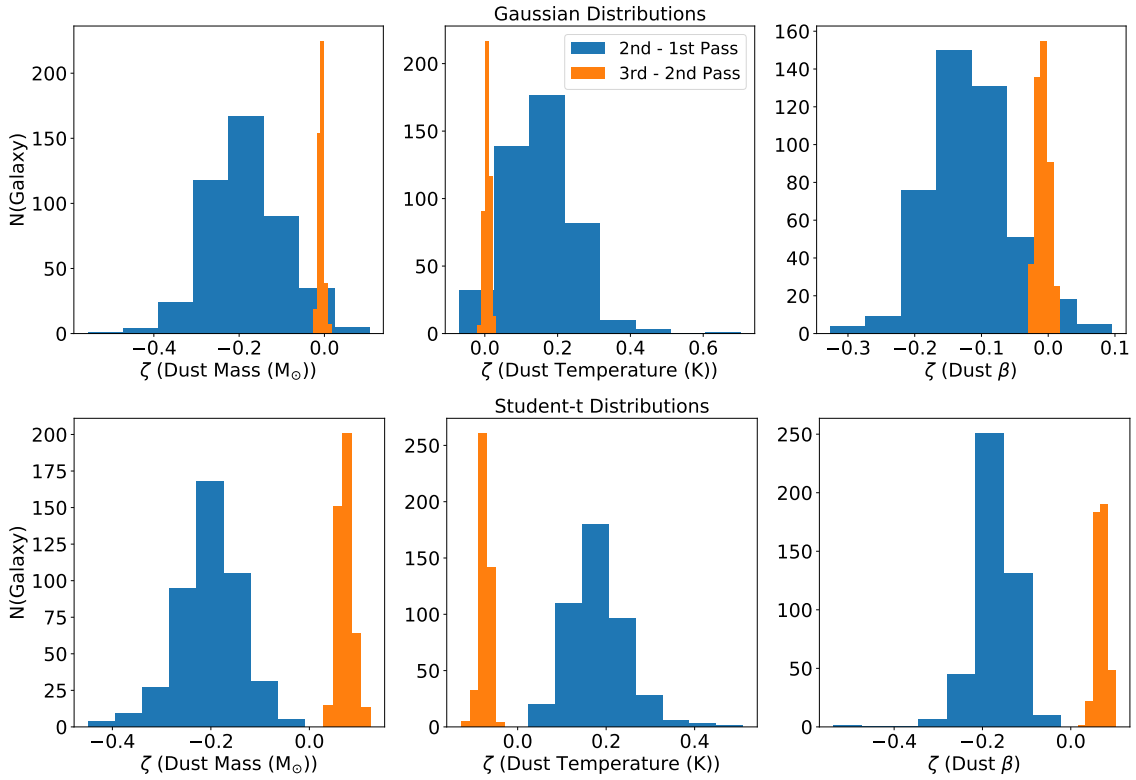

Figure 6.2: Convergence measures (ζ) for hierarchical fitting of SMBB models to ETGs and LTGs.

ζ are below 5% at the third round of fitting, which is considered to be a small enough change for satisfactory convergence. For non-hierarchical fitting, most galaxies achieve $\zeta < 5\%$ but a few outliers have ζ <10%. This is also considered adequate to proceed, because the incremental improvement in parameters with further fitting runs would only be a small fraction of the uncertainty.

6.4.2 Results of Fitting and Comparison of Fitting Methods

Convergence of the sampling chains as described in Section 6.3.4 was achieved with both fitting methods for all galaxies with $N_{eff} > 100$ (target > 10) and $\widehat{R}$ very close to 1 (target <1.1), using a total of 20,000 samples in four independent sampling chains. Figure 6.4 show the fitted spectra from non-hierarchical and hierarchical fitting for GAMA7836,

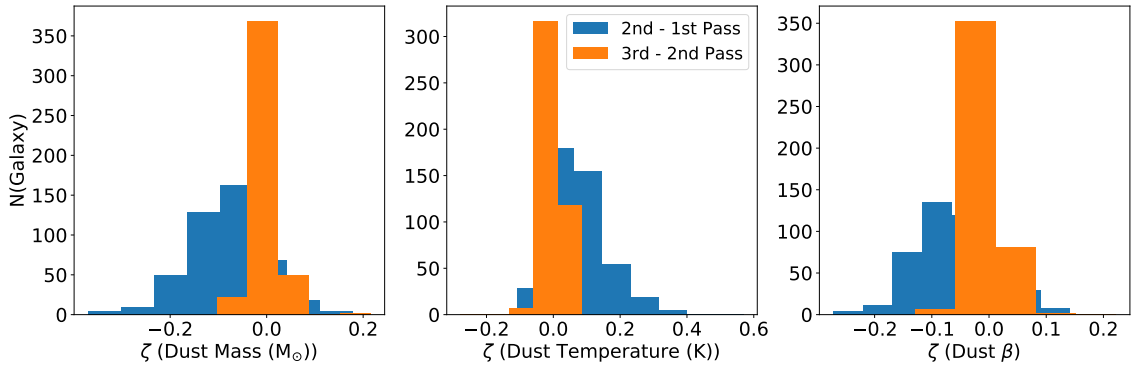

Figure 6.3: Convergence measures (ζ) for non-hierarchical fitting of SMBB models to ETGs and LTGs.

with relatively weak emission compared to other galaxies in the fitted sample and greater measurement uncertainty for the flux densities. The constraints on parameters imposed by hierarchical fitting mean that there is less spread in the uncertainty within the fitted spectrum at shorter and longer wavelengths, at the expense of greater uncertainty at the centre. Table 6.2 shows the fitted values of the hyperparameters (which define the overall distributions for the whole sample) for $\log_{10}$(dust mass), dust temperature and dust β from hierarchical fitting using Gaussian and Student-t distributions as described earlier. The results from both methods are in agreement within uncertainties.

Figure 6.5 compares the results of hierarchical fitting for individual galaxies based on Gaussian and Student-t distributions. Results for fitted parameters for all galaxies fitted are similar, given the prevailing levels of uncertainty, so results from both methods can be regarded as equivalent. Figure 6.6 shows the comparison of results from non-hierarchical fitting and hierarchical fitting. Dust masses are similar within levels of uncertainty, with uncertainty levels significantly greater for non-hierarchical fitting than hierarchical. For temperature and β, results from hierarchical fitting are concentrated in smaller ranges than those from non-hierarchical, which can be expected due to the fitting of a hyperparameter distribution. Comparing these results with those from Lamperti et al. (2019), their Figure 4, values of temperature and β are more constrained in this work than those from

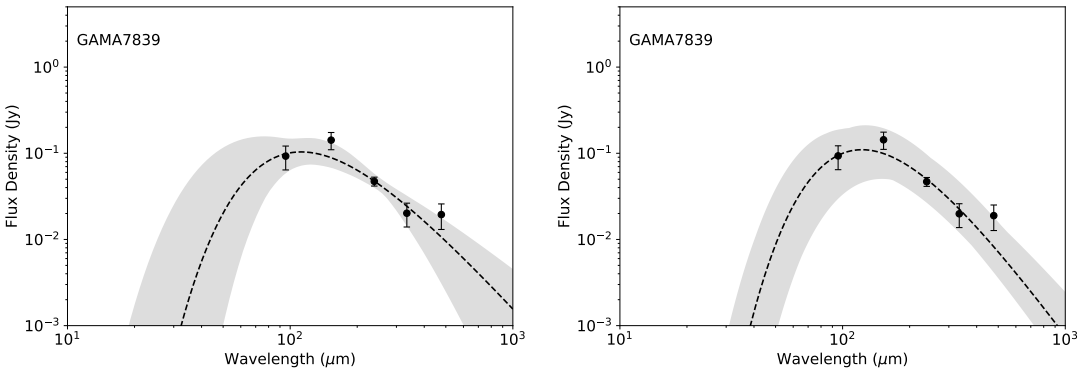

Figure 6.4: Example fitted spectra for GAMA7839. *Left:* non-hierarchical fitting, *Right:* Hierarchical fitting (Student-t distribution). Grey regions represent 1σ uncertainty.

Table 6.2: Hyperparameter values from hierarchical fitting of SMBB models to 445 dusty galaxies from the Parent Sample. Uncertainties are 16th and 84th percentiles from the posterior distributions.

Hyperparameter	Value
Gaussian Distributions	
Log_{10}(Dust Mass ($M_\odot$))	6.95 ± 0.49
Temperature (K)	23.98 ± 2.52
β	1.83 ± 0.33
Student-t Distributions	
Log_{10}(Dust Mass ($M_\odot$))	6.95 ± 0.42
Temperature (K)	24.35 ± 1.71
β	1.79 ± 0.22

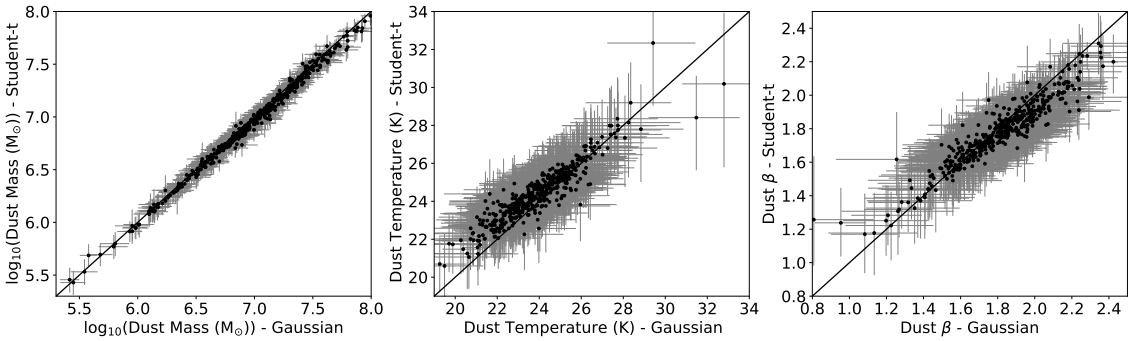

Figure 6.5: Comparison of results from hierarchical fitting methods using Gaussian and Student-t distributions.

hierarchical model fitting presented by Lamperti et al. (2019). This is discussed further in Section 6.4.3.

Use of hierarchical fitting has reduced the degeneracy between these parameters compared to non-hierarchical, as expected (Section 6.3). Figure 6.6 examines the degeneracy between dust temperature and β for non-hierarchical and hierarchical fitting with Gaussian and Student-t distributions. Irrespective of which method is used for hierarchical fitting, the spread of results for dust temperature and β is significantly less with hierarchical fitting than non-hierarchical. Figure 6.7 highlights the relation between fitted values of dust temperature and β from non-hierarchical and hierarchical fitting using Gaussian and Student-t distributions. The degeneracy between temperature and β arising from non-hierarchical fitting is apparent by the "banana" shape of the plot in Figure 6.7, which is an artefact of the degeneracy in fitting temperature and β. The absence of this artefact in the results from hierarchical fitting is clear. The degeneracy has been shown to arise naturally because of noise effects (Shetty et al. 2009a,b), and the benefits of using hierarchical fitting to reduce this problem are illustrated within this Figure. This is the same result as was demonstrated by Lamperti et al. (2019). The fitted dust masses from non-hierarchical and hierarchical fitting are generally in agreement within uncertainties,

indicating that dust masses are not particularly sensitive to degeneracy between dust temperature and β. Similar behaviour is also apparent in results from Lamperti et al. (2019), their Figure 4.

6.4.3 Comparison of Results with JINGLE

Before using the results of fitting of SMBB emission models to H-ATLAS data for analysis against other galaxy properties, the results are compared with those from JINGLE (Lamperti et al. 2019, Section 2.8.5) to investigate any possible issues with using H-ATLAS data alone for model fitting. Lamperti et al. (2019) used flux densities from JCMT (Section 2.5) at 850μm in addition to H-ATLAS photometry when performing non-hierarchical and hierarchical fitting of SMBB models.

Figure 6.8 shows a plot of stellar mass versus dust mass for SMBB model fitting to H-ATLAS data in this work alongside the equivalent data from Lamperti et al. (2019). Stellar masses and SFRs derived using MAGPHYS are selected from data provided in Saintonge et al. (2018). The alignment of data from this work and JINGLE is good at stellar masses above $\sim 10^{9.5}$ $M_{\odot}$, although results from JINGLE appear to be offset towards higher dust masses. JINGLE focussed primarily on star-forming galaxies, so ETGs with lower specific dust masses may not be included in their sample to the same extent as in this work. However at stellar masses less than $\sim 10^{9.5}$ $M_{\odot}$, dust masses appear to be lower for galaxies from this work compared with those from JINGLE which used additional photometry from JCMT. Trend lines are shown for both sets of data, with similar slopes and an offset towards higher dust masses for JINGLE.

Figure 6.9 shows plots of dust temperature and β from hierarchical fitting to H-ATLAS data and for the JINGLE results, plotted against stellar mass, star formation rate and dust mass. Agreement between the two datasets for dust temperature is qualitatively reasonable. However, the results for β from JINGLE show a downturn compared to the results from this work at lower stellar mass, SFR and in particular dust mass at $\sim 10^{6.5}$

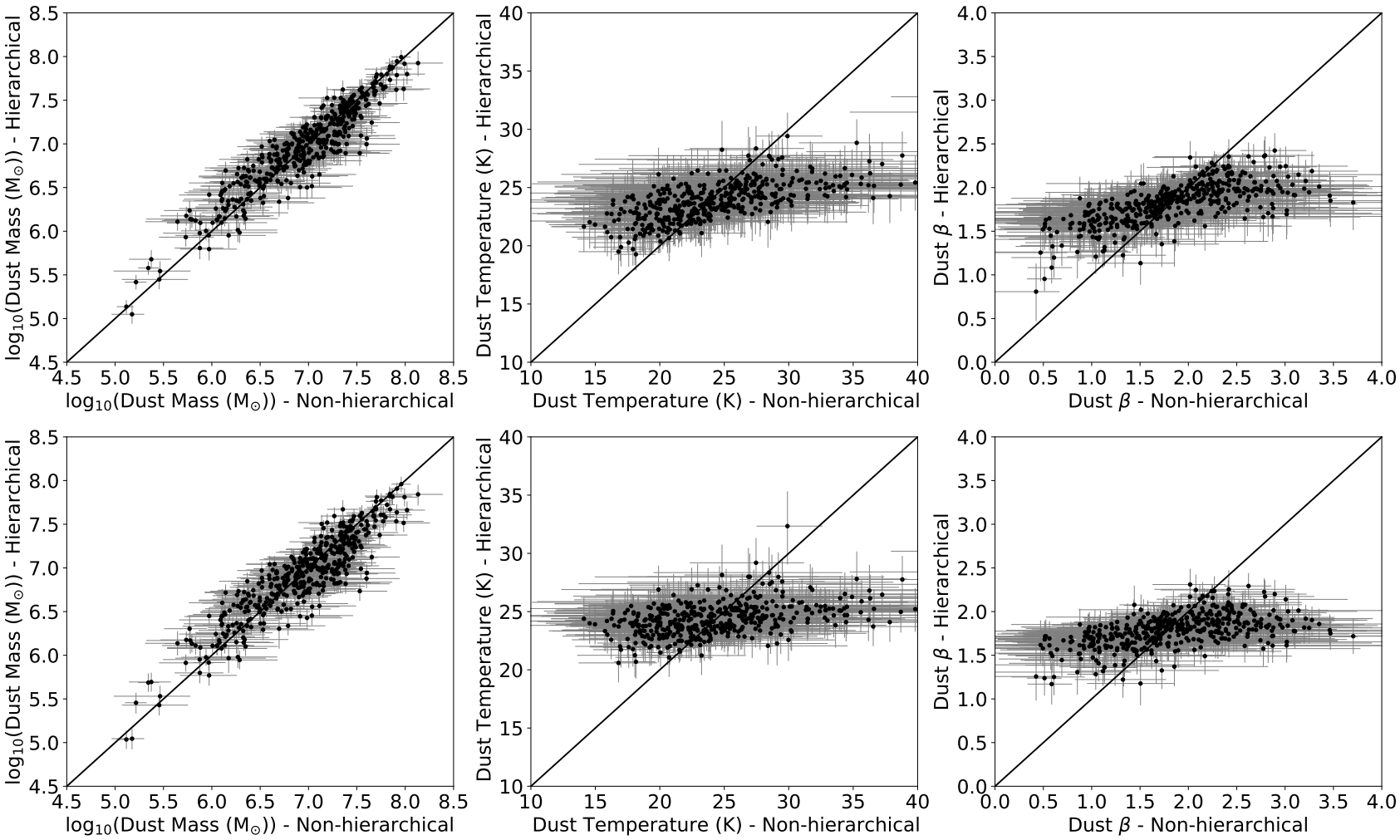

Figure 6.6: Comparison of non-hierarchical fitting results with hierarchical fitting using *upper:* Gaussian distributions, *lower:* Student-t distributions.

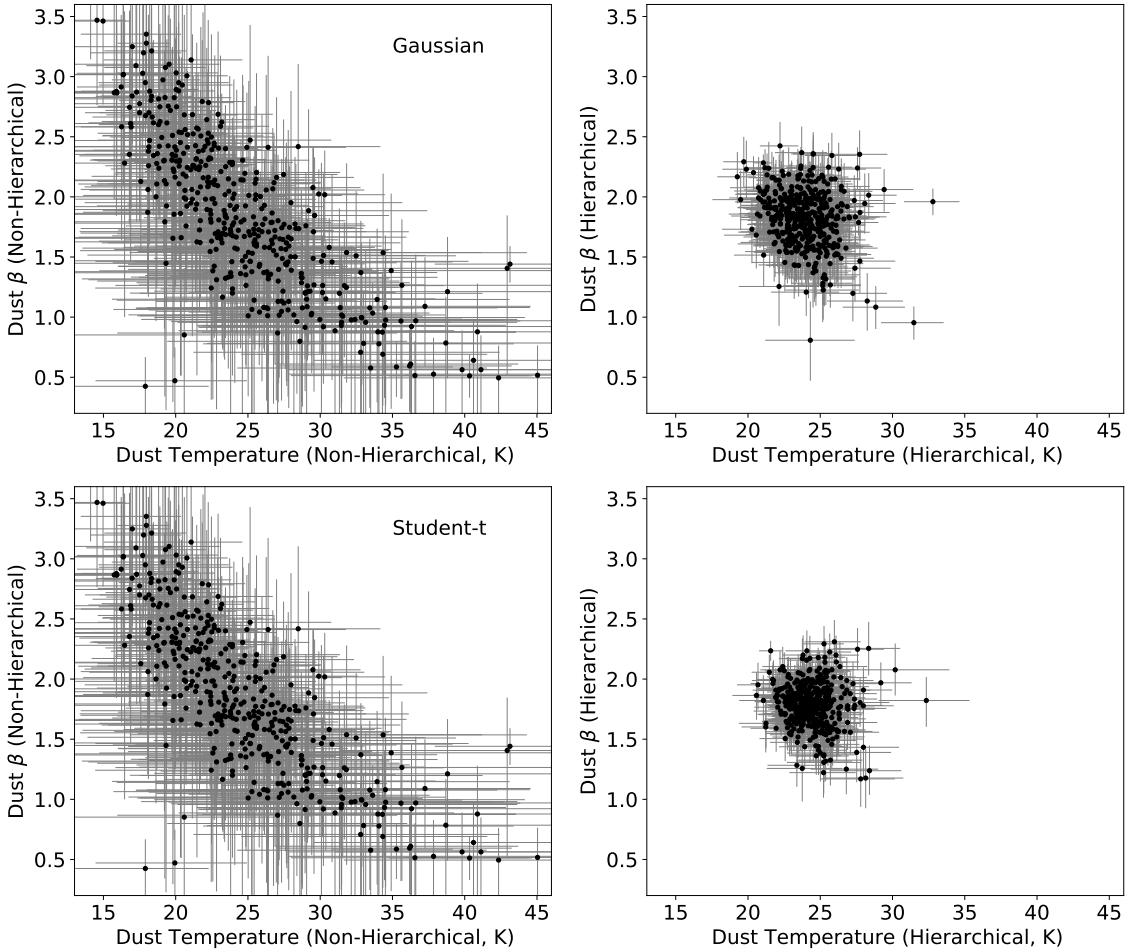

Figure 6.7: Dust β versus temperature arising from non hierarchical fitting and hierarchical fitting using *upper:* Gaussian distributions, *lower:* Student-t distributions.

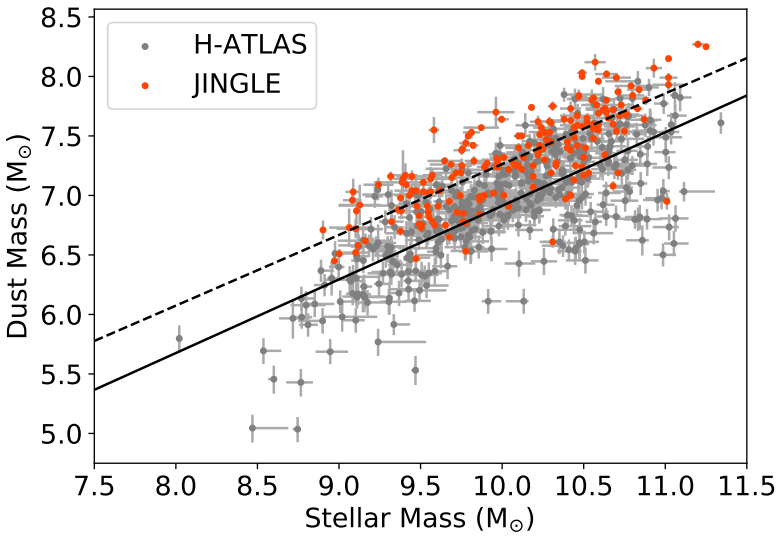

Figure 6.8: Dust mass versus stellar mass for Parent Sample galaxies with valid H-ATLAS data for fitting to SMBB models, and for galaxies from the JINGLE survey. The trendline (fitted to all H-ATLAS points) is $\log_{10}$(Dust mass, $M_\odot$) = (0.73 ± 0.43) + (0.62 ± 0.04) $\log_{10}$(Stellar mass, $M_\odot$), and for JINGLE $\log_{10}$(Dust mass, $M_\odot$) = (1.31 ± 0.31) + (0.59 ± 0.03) $\log_{10}$(Stellar mass, $M_\odot$)

$M_\odot$. The key difference between the two datasets is the use of longer-wavelength photometry in JINGLE (at 850μm) for model fitting. Lamperti et al. (2019) discuss how the additional photometry assists with quantifying a "sub-mm excess" in flux density that can occur at 850μm and remains poorly understood. It is associated with early-type galaxies and lower-mass, lower metallicity galaxies (Lamperti et al. 2019, and references therein). Without photometry at these longer wavelengths, fitted dust spectra from this work could have steeper slopes and hence greater fitted values of β. One possible cause of the sub-mm excess is a mass of colder dust within the galaxies (e.g. 10K, Galametz et al. 2011), which would have a peak sub-mm emission at longer wavelengths than those for the fitted galaxies (Figure 6.4). Adding emission at wavelengths >500μm would flatten the overall spectrum at in the Rayleigh-Jeans region, decreasing fitted values of β and increasing the fitted dust mass. Overall, results and inferences from the plots presented in subsequent sections need to be treated with caution for stellar masses below $\sim 10^{9.5}$ $M_\odot$ or dust masses below $\sim 10^{6.5}$ $M_\odot$.

6.4.4 Comparison with Results from GAMA II (MAGPHYS)

The GAMA II catalogue MagPhysv06 contains estimates of total dust masses for a combination of cool dust at ~15K and warm dust at over ~50K) for galaxies derived to SED fitting using MAGPHYS, and the results can be compared with the dust masses from SMBB fitting to H-ATLAS data. Figure 6.10 compares the two sets of dust masses, for the whole sample subject to SMBB fitting and for subsets identified morphologically as ETG or LTG, for both non-hierarchical and hierarchical fitting. The results for non-hierarchical fitting are more scattered with larger error bars, as expected. In general, dust mass estimates from MAGPHYS are greater than those from SMBB fitting in this work, in spite of both methods using the same dust mass absorption coefficient (da Cunha et al. 2008). For the comparison with data from hierarchical fitting, linear regression indicates that overall a subtraction of $\log_{10}$(Dust mass ($M_\odot$)) of 0.277 ± 0.04 aligns dust masses from MAGPHYS with those from SMBB fitting, implying that overall the galaxies in the

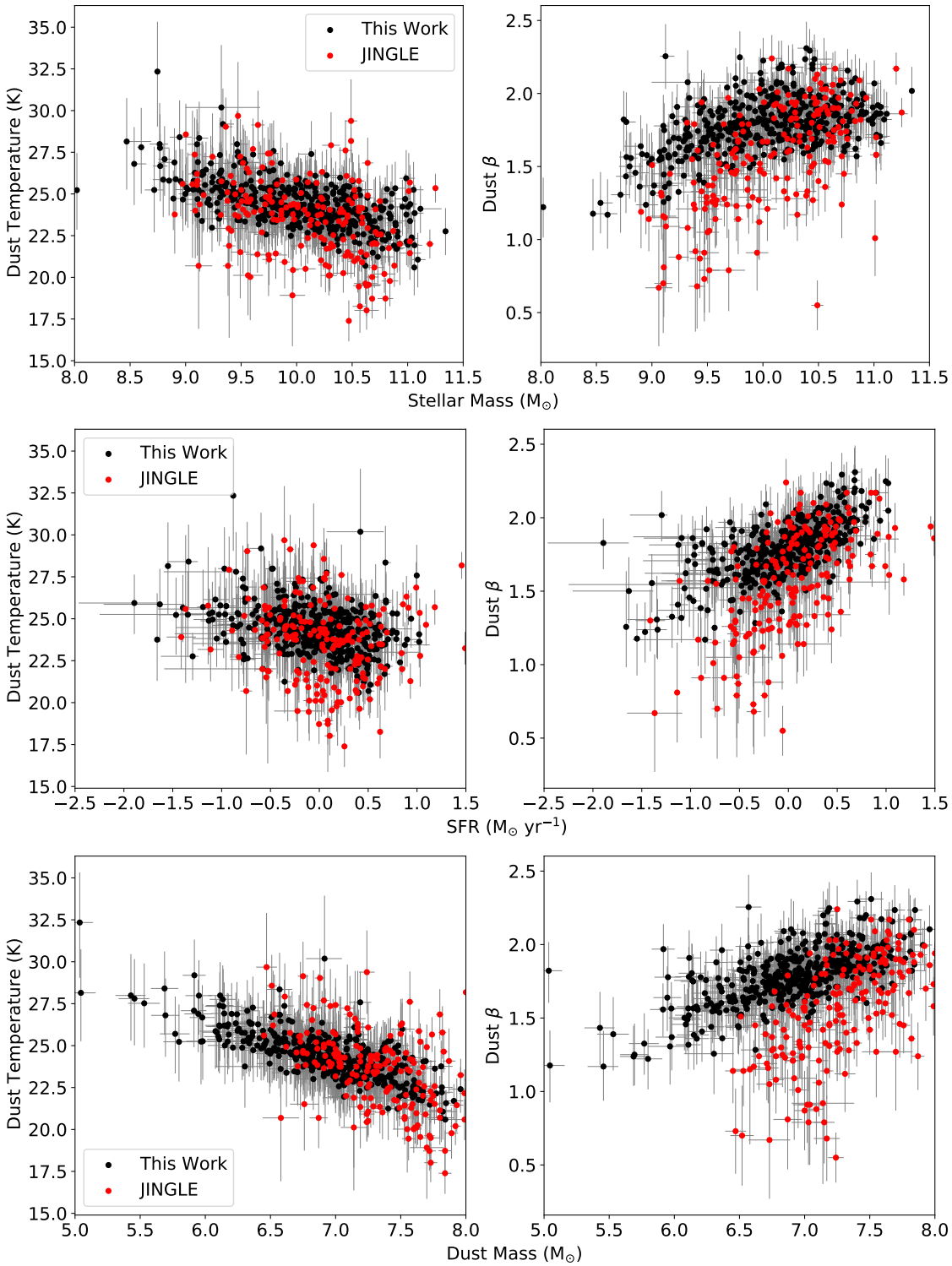

Figure 6.9: Dust temperature and β versus stellar mass, SFR and dust mass for H-ATLAS hierarchical model fits and JINGLE results.

sample contain additional dust at ~90% of the mass of cool dust. Similar linear regression was applied to the LTG and ETG subsets shown in figure 6.10 (right). For LTGs alone, a subtraction of 0.287 ± 0.047 aligns the MAGPHYS results from those of SMBB fitting, whereas for ETGs the subtraction is reduced to 0.177 ± 0.061. These trends are also apparent in Figure 6.10 when compared to the lines representing ±0.3 dex offsets from a 1:1 relation.

The increased dust masses from MagPhysv06 compared to SMBB fitting can be accounted for by the method used to estimate dust masses by MAGPHYS, which fits warm and cold dust components to the photometry data. MAGPHYS makes use of the same five passbands from Herschel provided for H-ATLAS for sub-mm photometry to be fitted. The mean dust temperature for SMBB fitting in this work is ~24K. When cold and warm masses are added to give a total, the result can be greater than that from SMBB fitting. To illustrate this, Figure 6.11 shows the effect of combining spectra from warm and cold dust components to give an overall fit to a calculated SMBB spectrum for a galaxy with dust mass = $10^7 M_\odot$ dust temperature = 22K and β = 2.0 at a redshift of 0.04. Cold (10K) and warm (50K) dust masses of $10^{7.25}$, and $10^{5.25} M_\odot$ (total mass $10^{7.254} M_\odot$), temperatures of 18K and 50K and a fixed β of 2 create a similar spectrum within the range 100 - 500μm to the SMBB example. The additional modelled flux in the range 50 - 100μm in Figure 6.11 would require photometry in this range to fully explore the properties of warm and cold gas, but this is not available in LambdarCatv01 used for input to MAGPHYS. Only photometry from WISE W4 at 22μm is available, which could be affected by line emission from higher hydrocarbon molecules associated with dust. In this Chapter, dust masses from SMBB fitting directly or dust masses from GAMA II scaled down to match SMBB dust massed are used for subsequent analyses where required. Overall, these results suggest that LTGs could contain more, colder dust than ETGs because of the smaller increments for GAMA dust masses compared to results of fitting to H-ATLAS data for ETGs.

It is also important to note that the template spectra used by MAGPHYS are based

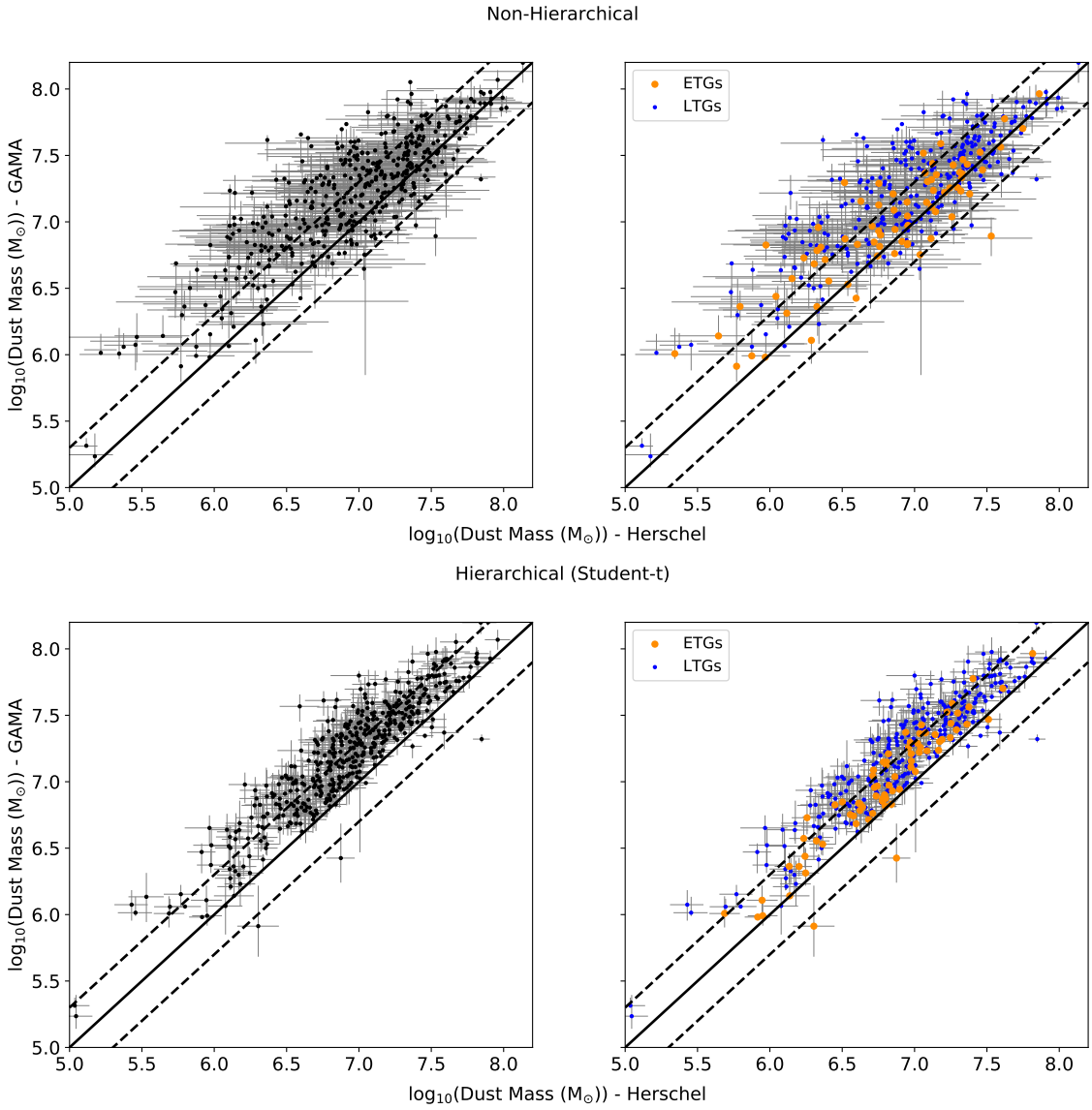

Figure 6.10: Comparison of fitted dust masses from hierarchical fitting (Student-t distribution) with dust masses from GAMA II. ±0.3dex dotted lines are shown around the solid 1:1 line.

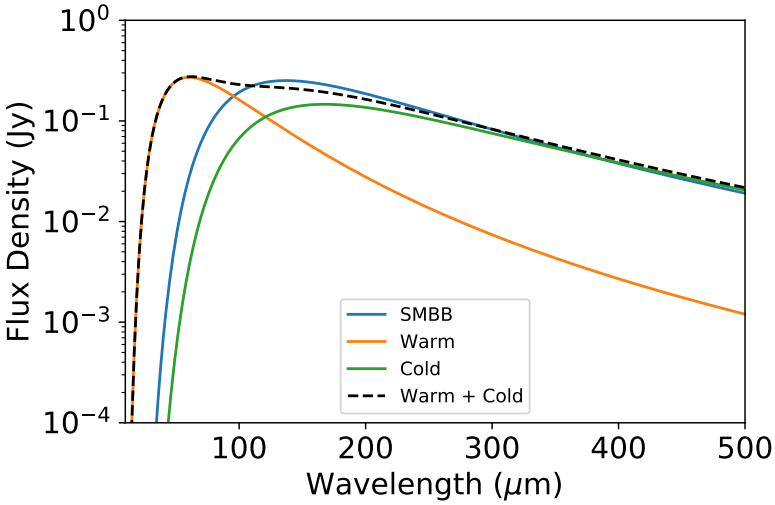

Figure 6.11: Comparison of spectra produced by SMBB ($10^7 M_\odot$, T=22K) with a two component model with cold dust ($10^{7.25} M_\odot$, T=18K) and warm dust ($10^{5.25} M_\odot$, T=50K). A fixed value of β=2 is used throughout.

on dust emission with β=2 (da Cunha et al. 2008). The relationship between these dust masses from GAMA II and those from hierarchical fitting in this work appears not to have been affected by any differences in β values, with linear trends apparent between the data (Figure 6.10). However, β values are more spread towards lower values in the results from Lamperti et al. (2019) at lower stellar mass, so total dust masses from GAMA II should also be interpreted with caution at stellar masses below $\sim 10^{9.5}$ $M_\odot$ or dust masses below $\sim 10^{6.5}$ $M_\odot$.

6.4.5 Relationship between Galaxy Dust Properties and Morphology

Using the dust mass, temperature and β results from hierarchical fitting, it is also possible to examine differences between these properties for samples of galaxies with different morphological classifications. Only galaxies with stellar masses $\geq 10^{9.5} M_\odot$ are considered in this Section, to avoid issues with overestimation of β at lower stellar mass discussed in Section 6.4.3. Within the sample of galaxies from the Parent Sample subject

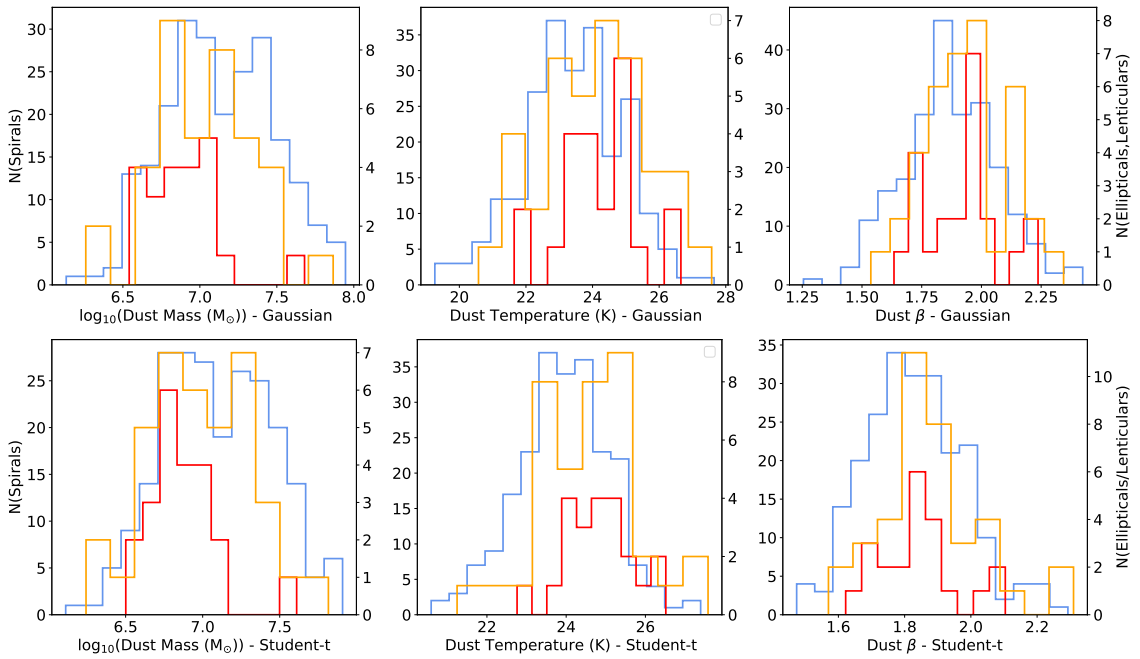

Figure 6.12: Histograms of $\log_{10}$(dust mass ($M_\odot$)), dust temperature (K) and dust β for morphological classifications from hierarchical fitting with Gaussian and Student-t distributions. Colours are blue: Spirals, orange: Lenticulars, red; Ellipticals.

to hierarchical fitting, this creates samples of 227 Spirals, 38 Lenticulars and 22 Ellipticals based on the morphological classifications presented in Chapter 3. Figure 6.12 shows distributions of the galaxy fitted properties from hierarchical fitting of SMBB models, for Ellipticals, Lenticulars and Spirals. Table 6.3 shows the median values and uncertainties of these fitted parameters.

Given the levels of 1σ uncertainty for all of the parameters in Table 6.3, it is difficult to draw firm conclusions about differences in dust properties. There is a suggestion that as a population, Ellipticals are less dusty than Lenticulars and Spirals, which has been observed before (Smith et al. 2012). The median reduction from LTG to ETG from the results in Table 6.3 is about 30%. There is also a suggestion that dust temperatures and β are increased in early-type galaxies compared to Spirals, with Ellipticals showing

Table 6.3: Median parameter values and median uncertainties (16th and 84th percentiles) for SMBB model parameters from hierarchical fitting of SMBB models, for Ellipticals, Lenticulars and Spirals. Galaxies with dust masses $\geq 10^{9.5} M_{\odot}$ only are considered (Section 6.4.3)

Parameter	Ellipticals	Lenticulars	Spirals
Gaussian Distributions			
Log_{10}(Dust Mass ($M_{\odot}$))	6.89±0.11	7.02±0.10	7.11±0.11
Temperature (K)	$24.13^{+1.93}_{-2.08}$	$24.18^{+1.89}_{-2.02}$	$23.42^{+1.89}_{-2.05}$
β	$1.94^{+0.25}_{-0.26}$	$1.92^{+0.23}_{-0.24}$	$1.86^{+0.24}_{-0.25}$
Student-t Distributions			
Log_{10}(Dust Mass ($M_{\odot}$))	6.82±0.09	6.99±0.09	7.08±0.09
Temperature (K)	$24.81^{+1.52}_{-1.65}$	$24.74^{+1.55}_{-1.64}$	$23.91^{+1.53}_{-1.63}$
β	$1.85^{+0.17}_{-0.18}$	1.85±0.17	1.82±0.17

slightly greater increase in these parameters. In order to explore relationships between differences in distributions more formally, k-sample midrank Anderson-Darling tests using the PYTHON function SCIPY.STATS.ANDERSON_KSAMP were used to highlight any differences across morphologies for galaxies with stellar mass $\geq 10^{9.5}$ $M_{\odot}$. As a guide, if the significance level is high (capped at 0.25 by the routine), then the samples could be from the same parent distribution. If the significance level is low (minimum 0.001 within the routine), the samples are unlikely to be from the same distribution. Table 6.4 shows the significance levels at which results for different morphological classifications are considered to be drawn from the same distribution, derived from hierarchical model fitting with both Gaussian and Student-t distributions. The results show that dust temperature and β values for Ellipticals and Lenticulars are indistinguishable. Dust temperatures are distinct for Spirals compared to Ellipticals and Lenticulars, as are β values when using Student-t distributions, but β values are less distinct when using Gaussian distributions. Lamperti et al. (2019) review and discuss why dust properties for early-type galaxies can be distinct from late types. Increased values of β could be expected in early-type galaxies rather than

Table 6.4: Significance levels for k-sample midrank Anderson-Darling tests comparing properties of dust within morphology classifications. Galaxies with dust masses $\geq 10^{9.5} M_{\odot}$ only are considered (Section 6.4.3)

Comparison	Dust Temperature	Dust β
Gaussian Distributions		
Spirals-Ellipticals	0.02	>0.25
Spirals-Lenticulars	0.04	0.09
Lenticulars-Ellipticals	>0.25	>0.25
Student-t Distributions		
Spirals-Ellipticals	<0.001	> 0.25
Spirals-Lenticulars	0.002	0.02
Lenticulars-Ellipticals	>0.25	>0.25

late-types, because dust ageing and a lack of introduction of new dust from star formation causes existing dust to become more amorphous with an increased silicon content. These properties are associated with higher values of β. Also, higher-metallicity galaxies are associated with a lower fractions of carbon stars within stellar populations, which reduces the overall carbon content of new dust from stellar processes.

Overall, the results from hierarchical SMBB fitting to H-ATLAS data have yielded plausible dust masses for galaxies within the constraints of the model inputs, for galaxies with stellar mass $\geq 10^{9.5}$ $M_{\odot}$. Extraction of dust properties (temperature, β) from SMBB fitting using H-ATLAS data alone may not indicate subtle differences between ETGs and LTGs in the same mass range expected from previous studies. The results so far also highlight the need for photometry at longer wavelengths than provided by H-ATLAS when fitting dust emission models for galaxies with stellar masses below $10^{9.5}$ $M_{\odot}$, to account for the additional emission at these wavelengths compared to expectations from model fitting using H-ATLAS data alone.

6.4.6 Variation of Galaxy Properties with Dust Mass

Section 6.4.4 showed that with the application of a correction offset, logarithmic dust masses from GAMA II can align with the results from hierarchical SMBB fitting. This allows the larger pool of results from GAMA II to be used to explore how dust mass is related to galaxy properties, including morphology proxies. The dust mass results from fitting of the SMBB model to data from H-ATLAS are overlain where appropriate, for comparison. It is emphasised that dust masses derived from MAGPHYS for GAMA II were derived using H-ATLAS data only for sub-mm emission, and therefore may be affected by the failure to account for sub-mm excess emission in lower-mass galaxies described in Section 6.4.3. Results for galaxies with stellar masses below $\sim 10^{9.5}$ $M_{\odot}$ should therefore be viewed with caution, but can still be regarded as lower limits.

Figure 6.13 shows plots of dust mass versus stellar mass for the Parent Sample, and for ETGs and LTGs separately. An upper sequence is apparent for dusty galaxies across the stellar mass range, with some galaxies at higher stellar mass falling away from the sequence with reduced dust masses. This behaviour was reported previously by Smith et al. (2012), their Figure 8, for galaxies above $\sim 10^{9.5}$ $M_{\odot}$. However, the upper sequence appears to spread downwards at lower stellar masses (below $\sim 10^{9}$ $M_{\odot}$). It is possible that dust masses in some galaxies at lower stellar mass are under-predicted because the template spectra used by MAGPHYS use a fixed β of 2 and sub-mm excess flux is not accounted for appropriately when fitting to the available photometry (Section 6.4.3). The same behaviour was reported by Nersesian et al. (2019) for Sd-Irr galaxies compared to spirals, also using spectral fitting to multi-passband photometry to obtain dust masses. It is possible that their results are also affected by not accounting for sub-mm excess emission from cool dust in lower-mass galaxies. With photometry available at wavelengths longer than 500 μm, e.g. from JCMT as used by JINGLE. it is likely that the dust mass results for lower-mass galaxies would align with those for galaxies of higher stellar mass. However, this should be verified by further research.

At higher stellar mass, the LTGs lie almost exclusively within the upper sequence. ETGs are present both on the sequence but mostly below it, irrespective of stellar mass. The results from model fitting with H-ATLAS data are overlain, and show the same trend as the data from GAMA II but with less scatter. The trend line shown is the same as that for Figure 6.8. Such a trend can be expected if power law relations exist between both SFR and dust mass with stellar mass, because both affect sub-mm emission. The trends for these galaxies are similar to the upper sequence for the Parent Sample, although the data covers a higher dust mass range. In particular, the sharper downward trend in GAMA dust masses at low stellar mass is also apparent in a few galaxies modelled using H-ATLAS data alone.

A plot of SFR versus dust mass (Figure 6.14) shows a sequence containing most LTGs, and a scatter to lower SFR for ETGs across the dust mass range. A trendline fitted to data for galaxies subject to hierarchical SMBB fitting to H-ATLAS data (Student-t distributions) is also shown. Figure 6.15 shows the same plot as used in Figure 6.14 but colour coded according to stellar mass, and a density plot showing the distributions of galaxies above and below a stellar mass of $10^{9.5}$ $M_{\odot}$. Galaxies with lower stellar mass, especially $< 10^{9.5}$ $M_{\odot}$, can be seen to be responsible for the upturn, which is probably due to the underestimation of dust mass from SMBB fitting using H-ATLAS data alone which does not account for sub-mm excess flux from galaxies at lower stellar mass. If dust masses for these galaxies were adjusted upwards, they could lie on the same trend as the higher-mass galaxies.

The Sérsic index from fitting a single-model surface brightness profile to r-band galaxy images was found in Section 5.4 to have a relationship with galaxy morphology. Figure 6.16 shows GAMA II r-band Sérsic indices plotted against corrected GAMA II dust masses from this work, for the Parent Sample and LTGs/ETGs separately. The LTGs form a tight sequence at a Sérsic index of ~1, while ETGs spread away from the sequence towards higher indices with no correlation between Sérsic index and dust mass across the whole dust mass range considered. This behaviour is expected if dust mass and SFR are

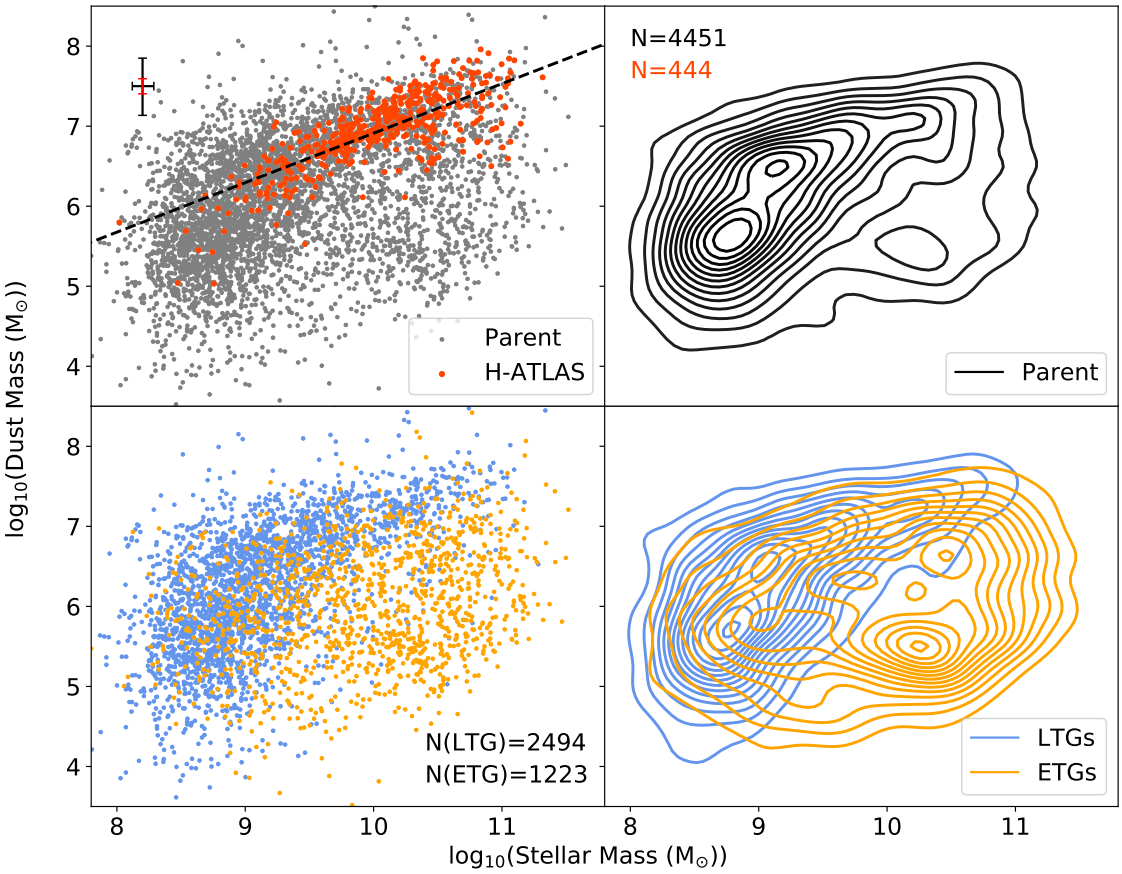

Figure 6.13: Dust mass versus stellar mass for Parent Sample galaxies, and LTGs/ETGs separately. GAMA II dust masses for the Parent Sample are corrected to align with H-ATLAS results. The dashed trendline is the same as that shown in Figure 6.8.

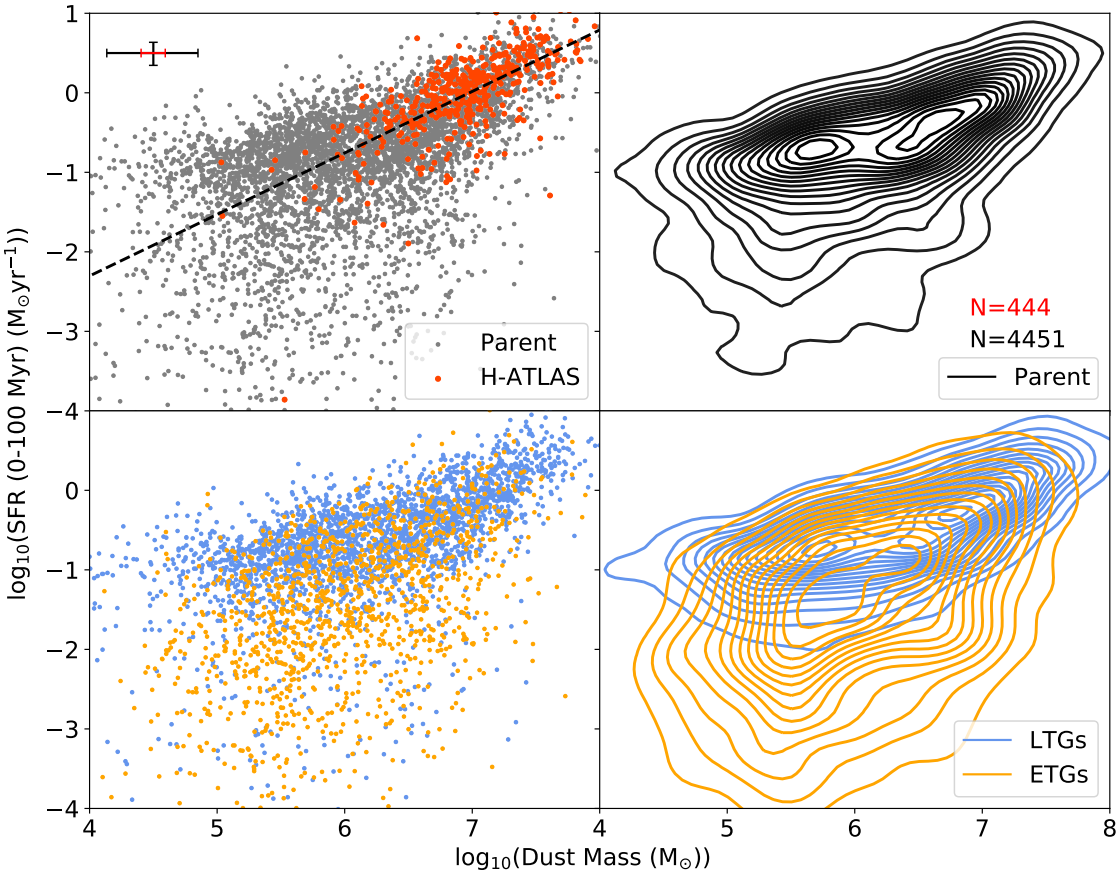

Figure 6.14: Star formation rate (0 - 100 Myr) versus dust mass corrected to align with results from hierarchical SMBB fitting to H-ATLAS data. The trend line has a slope of 0.77 ± 0.03 and an offset of -5.40 ± 0.25.

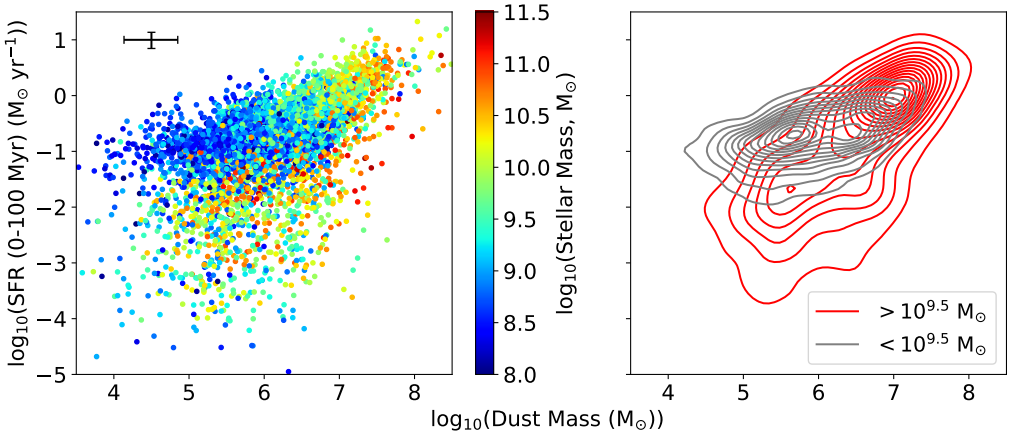

Figure 6.15: *Left*: Star formation rate (0 - 100 Myr) versus GAMA II dust mass corrected to align with results from hierarchical SMBB fitting to H-ATLAS data, colour-coded according to GAMA II stellar mass. *Right*: density plots derived from the plot on the left, for galaxies with stellar masses above and below $10^{9.5}$ $M_{\odot}$.

linked, and the trends apparent in Figure 6.16 reflect those in Figure 5.14.

6.5 Discussion of Chapter

The aim of this Chapter was to provide cool dust masses and properties (temperature, β) for galaxies in the Parent Sample with relevant sub-mm detections in H-ATLAS using hierarchical SMBB model fitting. The results were used to search for trends with other galaxy properties. The use of H-ATLAS data alone has been shown to restrict meaningful analyses to galaxies with stellar masses $>10^{9.5}$ $M_{\odot}$ or dust masses $>10^{6.5}$ $M_{\odot}$, because of issues with sub-mm excess emission that could not be characterised with H-ATLAS photometry alone.

Power-law relations are found between dust mass and stellar mass and between dust mass and SFR for LTGs with stellar masses $>10^{9.5}$ $M_{\odot}$. The relations could be expected, because both star formation and cool dust affect sub-mm emission. These power laws

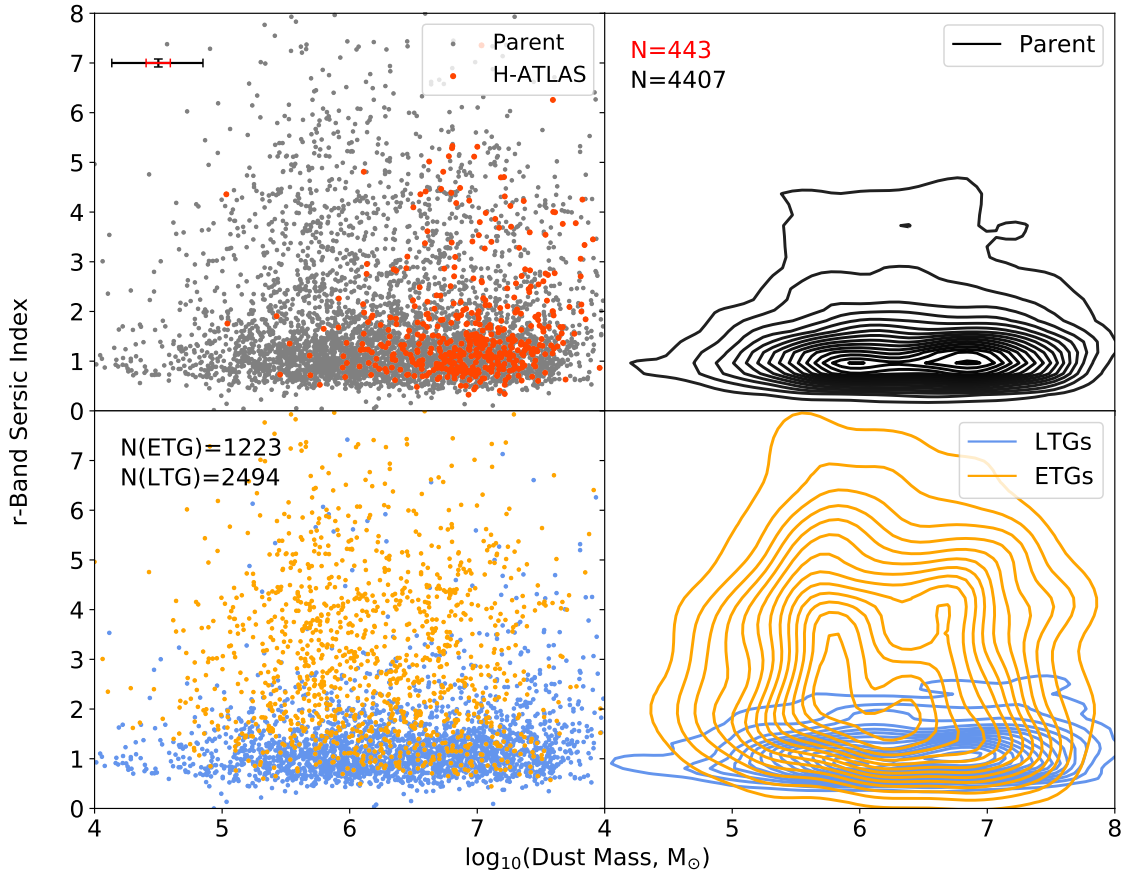

Figure 6.16: GAMA II dust mass corrected to align with results from hierarchical SMBB fitting to H-ATLAS data versus r-band single-model Sérsic index, for the Parent Sample.

might form part of a multivariate scaling relation for LTGs, linking star formation, dust mass, and molecular gas mass with stellar mass which is considered in Chapter 5. Establishment of such a relation is left for further research. The power-law exponent for dust mass versus stellar mass was found to be 0.61 ± 0.04, and for SFR versus dust mass 0.77 ± 0.03 for galaxies subject to hierarchical model fitting to H-ATLAS photometry. ETGs can be seen to lie on or fall away from these trends, with lower dust masses for the same stellar mass. Cortese et al. (2012) discuss the relationship between dust mass and star formation, and the trends seen in this work can be explained in a similar way. For LTGs, sSFR and dust masses (as the balance of dust formation and destruction) are linked by star formation and follow similar trends. However, once star formation declines as galaxies traverse the GV, star formation and associated dust production decline leading to reductions in dust mass with respect to stellar mass. The scatter in dust masses of ETGs for a given stellar mass has been reported previously (Smith et al. 2012), and has been attributed to random external addition of dust (e.g. acquisitions of ISM from interactions or minor mergers) as the most likely cause. The plot of single-model r-band Sérsic index versus dust mass only reveals the expected spread of Sérsic index with changing morphology, because of the wide range of dust masses present in each morphology category.

Further work on this topic should concentrate on extending the available photometry for sub-mm spectra of galaxies in the Parent Sample, to allow more complex models to be fitted. In particular, the sub-mm excess emission could be characterised further by photometry at multiple wavelengths beyond 500μm (Lamperti et al. 2019), and fitting more complex emission models could allow colder dust masses to be identified and studied. Although more challenging observationally due to their lower dust luminosities, further observational studies could also concentrate on galaxies with lower stellar masses ($<10^{9.5}$ $M_{\odot}$). Telescopes such as JCMT and the IRAM 30m telescope, with instruments such as SCUBA2 and NIKA2, can provide photometry at additional wavelengths to Herschel and constrain more complex dust thermal emission models. It may also be possible to use additional data within the GAMA II catalogue MagPhysv06 to characterise warm and cold dust components separately and recover dust masses for each component to compare with

the results of SMBB fitting. The Herschel Reference Survey and ATLAS3D surveys and the DustPedia catalogue (Section 2.8.7) also have dust masses for their surveyed galaxies, and these could be used for further comparisons provided that galaxy properties such as stellar mass and star formation rate are available for them or can be derived.

The next Chapter describes new observations of cool molecular gas using the IRAM 30m telescope for 32 Dusty ETGs selected from the Parent Sample. The aim is to investigate how cool molecular gas content and gas-to-dust mass ratio are influenced by morphology and other galaxy properties.

Chapter 7

IRAM 30m Telescope Observations of Dusty Early-Type Galaxies

As well as cool dust, the cool ISM of a galaxy contains cool molecular hydrogen (H_2), helium, metals and other compounds in the form of molecular gas. This is the main ingredient for the formation of new stars given the right conditions of temperature, density and instability leading to star formation by gravitational collapse. Its presence in ETGs, in terms of both content and distribution, can be used as an indicator of the evolutionary mechanisms responsible for the formation of ETGs, as shown in Chapter 2.

In this Chapter, the acquisition and results of observations of CO emission from 32 Dusty ETGs with the IRAM 30m telescope are presented. These are used to explore the molecular gas masses and kinematics within these ETGs, in relation to other galaxy properties and the results from similar observations performed by others. Possible interpretations of evolutionary mechanisms are discussed based on the findings. The Chapter covers observation planning, acquisition of observations, data reduction and data analysis.

7.1 Cool Molecular Gas and CO Emission

Molecular hydrogen is the essential ingredient for the formation of new stars, but it is challenging to study directly by observation in cool ISM (20 - 30K) because it does not have observable emission mechanisms at suitably low temperatures (see Naslim et al. (2015) for a review). However, alternative molecules do emit strongly at these temperatures, and this emission can be used as a proxy for molecular hydrogen. One of these molecules is CO which, unlike molecular hydrogen, has a finite dipole moment. Molecular rotation of CO causes oscillation of the charge about the centre of mass and emission of photons at mm wavelengths, at temperatures relevant to the study of cool ISM. Two rotation-based emission lines are of interest in this work, one of which was used in Chapter 2. These are ^{12}CO[1-0] at a frequency of 115.27 GHz (2.6mm), and the other is ^{12}CO[2-1] at a frequency of 230.54 GHz (1.3mm). The atomic mass of oxygen is fixed at 16 throughout this work. Conversion of CO line emission to molecular hydrogen (or molecular gas) mass requires a conversion factor, which is discussed later in this section.

7.2 Sample Selection and Observation Planning

Initial targets for observation were selected from the clean and complete dusty early-type galaxy (ETG) sample described in Chapter 4. Estimates of the ^{12}CO[1-0] line emission strength (in Jy km s^{-1}) were derived from estimates of cool dust masses, by assuming a constant molecular gas-to-dust mass ratio and that the ratio of this line emission to molecular hydrogen column density X_{CO} was similar to that of the Milky Way Galaxy (MWG).

The dust mass in each galaxy was estimated for observation planning from the 250μm emission shown in the Herschel-ATLAS DR1 catalogues (see Chapter 4), using the expression provided by Dunne et al. (2011) adapted to use luminosity distance rather than comoving distance. SI units are used throughout.

$$M_{dust} = \frac{S_{250} D_L^2 K}{\kappa_{250} B(\nu_{250}, T)(1+z)} \tag{7.1}$$

where M_{dust} is dust mass, S_{250} is flux density measured at 250μm, D_L is luminosity distance, κ_{250} is mass absorption coefficient at 250μm, $B(\nu_{250}, T)$ is the Planck function evaluated at a dust temperature T and frequency corresponding to 250μm, and z is flow-corrected redshift from GAMA II DistancesFramesv14. This is consistent with the SMBB model for dust thermal emission (Equation 6.1), but with a K-correction term which adjusts for the observed spectral shape of the emission as redshift varies (Dunne et al. 2011):

$$K = \left(\frac{1}{1+z}\right)^{3+\beta} \left(\frac{e^{(h\nu_{rest}/kT)} - 1}{e^{(h\nu_{obs}/kT)} - 1}\right) \tag{7.2}$$

where β is the dust emissivity coefficient, ν_{obs} is the frequency of measurement and ν_{rest} is the frequency of emission in the galaxy rest frame. A dust temperature of 22K and β of 2 were assumed for planning purposes. Figure 7.1 compares these dust mass estimates based on 250μm flux densities with estimates from GAMA II MagPhysv06 derived from MAGPHYS (Section 2.7.3), without the adjustments discussed in Chapter 4. The mass absorption coefficient used was that used in Chapter 4 (0.89 m^2 kg^{-1}) Both estimates agree reasonably well (within a factor of 3), so this approximate method of dust mass estimation was adequate for observation planning.

Molecular gas mass estimates were calculated from dust masses estimated using Equation 7.1 for each ETG, based on a conservatively low molecular gas to dust mass ratio of 50. This ratio is selected from lower values derived from previous observations of molecular gas in ETGs subject to merger activity (Davis et al. 2015; Sansom et al. 2019). The antenna temperatures measured by the IRAM 30m telescope were then estimated, by calculating the expected ^{12}CO[1-0] line emission flux in Jy km s^{-1}, converting this to to flux density by dividing flux by an estimated velocity line width of 150 km/s (Davis

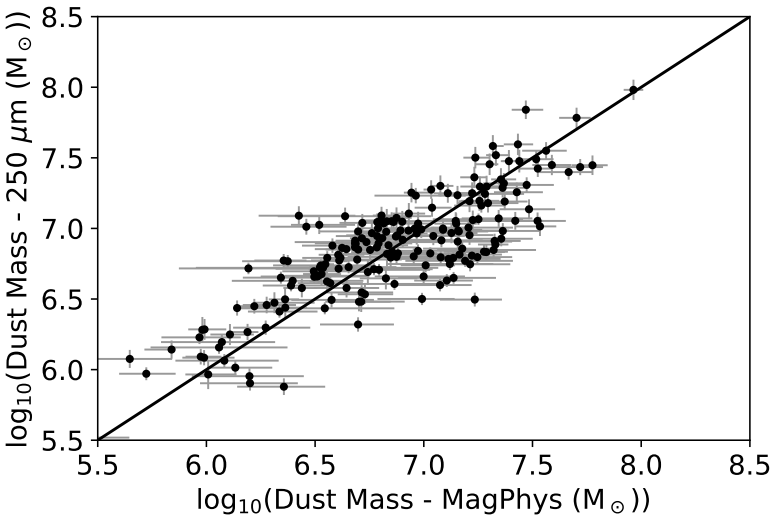

Figure 7.1: Comparison of MAGPHYS-derived dust mass estimates from GAMA II and calculation from H-ATLAS 250μm emission. 1:1 line shown in black.

et al. 2015) and applying a published factor for the telescope (6.0 Jy (K T_A^*)$^{-1}$)[1]. Measurement sensitivities (noise in a velocity bin of specified width) were then obtained using a signal to noise ratio of 3 in 50 km s^{-1} bins. These sensitivities were used to estimate observation times for galaxies, as outlined below. Note that this calculation requires the emitting CO to be optically thin, which would not be the case for larger masses of CO in a galaxy. However, many smaller masses emitting together create an emission which is approximately optically thin, and it is assumed that the CO in the observed galaxies is structured into small clouds according to the "mist model" (Bolatto et al. 2013, their Section 2.2). The observations are therefore assumed to capture CO emission from all available molecular gas within the telescope beam.

Measurement of CO emission from a galaxy with the IRAM 30m telescope follows radio astronomy conventions. The flux density from the source is reported as an equivalent brightness temperature, derived using the Rayleigh-Jeans law for blackbody emission at low frequency (long wavelength):

[1]https://publicwiki.iram.es/Iram30mEfficiencies

$$T_B = \frac{\lambda^2 I_\nu}{2k_B} \tag{7.3}$$

where T_B is brightness temperature, λ is wavelength, I_ν is spectral intensity and k_B is the Boltzmann constant. For a given radio telescope, with beam solid angle Ω, the integrated flux density recorded within the beam area is (e.g. Wilson et al. 2009):

$$S_\nu = \frac{2k_B}{\lambda^2} \iint_{source} T_B d\Omega = \frac{2k_B}{\lambda^2} T_{beam} \Omega_{beam} \tag{7.4}$$

The ^{12}CO[1-0] line flux (in Jy km s^{-1}) can be calculated using a conversion factor X_{CO}, defined as follows (Bolatto et al. 2013):

$$X_{CO} = \frac{N_{H2}}{\int T_B dv} \tag{7.5}$$

where N_{H2} is the molecular hydrogen column density (particles per unit area) and v is velocity of the source emission given by:

$$v = c \frac{(\nu_{rest} - \nu_{obs})}{\nu_{rest}} \tag{7.6}$$

where ν_{rest} is the rest emission frequency, ν_{obs} is the observed frequency and c is the speed of light. Note that Equation 7.5 uses molecular hydrogen column density, so a conversion to molecular gas mass is needed. Applying Equation 7.4 to the definition of X_{CO}, and recognising that the total number of hydrogen molecules in the beam is the column density multiplied by the beam area ΩD_L^2, gives an expression for the molecular hydrogen mass within the beam (Davis et al. 2015, adapted from their Equation 1):

$$M_{H2} = 2m_H \frac{\lambda_{rest}^2}{2k_B} D_L^2 X_{CO} (1+z)^{-1} \int S_\nu dv \tag{7.7}$$

where M_{H2} is molecular hydrogen mass, m_H is the mass of a single hydrogen atom, $S_\nu \Delta v$ is the velocity-integrated emisson line flux density, z is redshift, and λ_{rest} is the emission rest wavelength. Converting the variables to practical units for observations leads to the following expression (Davis et al. 2015, adapted from their Equation 2):

$$\left(\frac{M_{H2}}{M_\odot}\right) = 3.93 \times 10^{-17} X_{CO} \left(\frac{D_L}{Mpc}\right)^2 \left(\frac{S_{CO}\Delta v}{Jy\ km\ s^{-1}}\right)(1+z)^{-1} \tag{7.8}$$

Luminosity distances were estimated using flow-corrected redshifts from GAMA II DistancesFramesv14 (see Chapter 3) and the appropriate Astropy.Cosmology function for obtaining luminosity distance from redshift using the default cosmology for this work. A divisor of 1.36 is used to convert the molecular gas mass, calculated from the dust mass and molecular gas-to-dust mass ratio as outlined above, to molecular hydrogen mass for use in equation 7.8. This value is based on a typical content of helium in molecular gas (e.g. Bolatto et al. 2013), and is based on the combined mass fractions of hydrogen, helium and metals (total 1) divided by the mass fraction of hydrogen (~0.74). The value of X_{CO} used for observation planning is that used by Young et al. (2011) and Davis et al. (2015) for studies of ETGs, i.e. 3×10^{20} cm^{-2} (K km s^{-1})$^{-1}$. For data reduction, an alternative approach for estimating molecular gas masses is used with galaxy-specific conversion factors (Section 7.4.4).

The estimated ^{12}CO[1-0] emission line fluxes were then used to obtain estimated flux densities for emission, using an estimate of velocity width for the lines of 150 km/s from (Davis et al. 2015), and conversion of flux densities to IRAM 30m telescope corrected antenna temperatures (T_A^*) using the conversion factor of 6.0 Jy (K T_A^*)$^{-1}$ discussed previously. The target sensitivities for observation of each galaxy were then derived based on a signal (i.e. calculated T_A^* to RMS noise of 3 with 50 km s^{-1} binning (allowing a minimum of three bins per emission line).

Targets for observation were shortlisted initially based on the ability to achieve a

suitable sensitivity for detection in under four hours' total observing time per target, including overheads such as telescope pointing and focussing. The IRAM 30m telescope exposure time calculator[2] was used to establish an achievable sensitivity for 4 hours' observing (including overheads) in average (worst-case) Summer weather (higher atmospheric moisture content) at a typical measured line frequency (109 GHz). A suitable minimum sensitivity was found to be was 0.77 mK. Targets for observation were therefore shortlisted if their required sensitivity was greater than this value. A total observation time for the project of 40 hours was selected, on the understanding that if the observations were successful a further proposal would be made for more galaxies based on refined input parameters for observation planning. All targets were also checked to ensure that their r-band effective radii (from GAMA II SersicCatSDSSv09) were less than half the telescope beam width for ^{12}CO[1-0] emission (~22 arcsec FWHM), to increase the likelihood that molecular gas distributions lie within the telescope beam.

A total of 16 target Dusty ETGs were shortlisted for observation to achieve the planned 40 hours total observation time, based on the methods presented above. Definitive observation times were then obtained for the shortlisted targets using the IRAM 30m online exposure time calculator, but taking care to calculate times at the observed frequencies of emission obtained by adjusting the expected emission frequency using the heliocentric redshifts of the ETGs. This step is important because the Earth's atmosphere has a strong absorption line around the frequencies of observation for ^{12}CO[1-0] emission (Figure 2.6), and atmospheric absorption is therefore particularly sensitive to frequency. All shortlisted galaxies were found to be suitable for observation. The calculated observed frequencies were specified within the observation scripts along with zero additional radial velocity correction, on advice from duty astronomers during planning. The alternative approach of providing a rest frequency for emission and radial velocity was not recommended with the typical recession velocities of these galaxies.

A proposal was submitted in March 2019 to observe these Dusty ETGs for both

[2]https://www.iram.es/nte/

^{12}CO[1-0] and ^{12}CO[2-1] emission, because it was straightforward to obtain the latter while achieving the primary goal of measuring ^{12}CO[1-0] emission. This proposal was accepted (project 070-19, PI: Glass), with observations scheduled for Summer 2019. Table 7.1 shows details of the galaxies actually observed in June - July 2019. Shortly before observations commenced, one target (GAMA3907174) was confirmed as having been observed already with this telescope (Davis et al. 2015), and was replaced by GAMA509508 which was the next most suitable target. This is in spite of checking all targets for previous observations with the IRAM 30m Telescope, and probably occurred due to human error in searching the IRAM database[3].

From the 2019 observations, ^{12}CO[1-0] emission was detected in all 16 Dusty ETGs and ^{12}CO[2-1] was detected in all but one of them. On this basis, a second proposal was prepared and submitted in September 2019 for observations early in 2020. For observation planing for this new proposal, line velocity widths and molecular gas to dust mass ratios were adjusted to reflect the findings of the 2019 observations. The emission line width was increased to 300 km/s, which was the lowest value obtained in the 2019 observations, and the molecular gas to dust mass ratio was increased to 110 based on early data reduction using Equations 7.8 and the dust masses used for observation planning. A reduced target sensitivity of 0.68 mK was also used, based on the performance of the telescope actually achieved (in Summer weather, which is normally less favourable than in Winter). A total of 16 more Dusty ETGs were found to be suitable for observation on this basis. The second proposal was accepted with lower priority, and pool observations were scheduled for January 2020 (project 203-19, PI: Glass). Table 7.2 shows details of the 16 additional ETGs selected for observation in 2020. GAMA272990 was a late change to the schedule, to replace a backup galaxy with longer planned observation time (GAMA3603677) and to provide a check of the ALMA-observed ^{12}CO[2-1] spectrum and calculated molecular gas mass discussed in Chapter 2.

Figure 7.2 shows r-band tiles for the 32 observed Dusty ETGs. The tile for

[3]https://tapas.iram.es/tapas

Table 7.1: Dusty ETGs selected for observation with the IRAM 30m telescope in Summer 2019. GAMA509508 was a late change to the schedule so sensitivities and observation times were not estimated.

GAMA ID	RA(°)	DEC(°)	Redshift (helio.)	^{12}CO[1-0] Observed Frequency (GHz)	^{12}CO[1-0] Sens. (mK T_A^*)	Obs. Time (hr)
78425	217.0686	0.0023	0.053	109.2	0.82	3.2
79849	223.4286	0.0301	0.0452	110.0	0.88	2.9
85416	182.3694	0.5333	0.0194	112.8	1.58	1.3
99687	183.8668	1.0173	0.048	109.7	0.80	3.6
136847	176.3126	-1.7028	0.0277	111.9	0.81	3.3
227607	214.3244	1.1562	0.0535	109.2	2.01	0.5
296638	212.6745	1.4805	0.0258	112.1	1.38	1.5
298980	222.7181	1.1657	0.0271	112.0	0.91	3.4
422436	130.9628	2.7139	0.0259	112.1	0.79	3.6
509508	221.5713	-1.5729	0.0570	109.1	—	—
514212	140.4301	2.6909	0.0246	112.2	0.84	3.2
546040	222.6773	-0.8758	0.0266	112.0	0.88	3.7
560238	179.8037	-0.5238	0.0213	112.6	1.11	2.5
569555	219.4072	-0.5837	0.0568	108.8	1.29	1.3
570227	222.8017	-0.4569	0.0433	110.2	0.90	2.9
3576053	129.6038	-1.6062	0.052	109.3	1.34	1.2

Table 7.2: Dusty ETGs selected for observation with the IRAM 30m telescope in January 2020. Observation time for GAMA272990 was not evaluated because it was a late introduction.

GAMA ID	RA(°)	DEC(°)	Redshift (helio.)	^{12}CO[1-0] Observed Frequency (GHz)	^{12}CO[1-0] Sens. (mK T_A^*)	Obs. Time (hr)
16026	217.5345	0.7035	0.0538	109.4	0.75	3.5
63210	215.0195	-0.3148	0.0517	109.6	0.71	3.6
64087	218.092	-0.2267	0.0553	109.2	0.98	1.8
215579	134.2533	0.5055	0.0531	109.5	0.9	2.2
227264	212.8239	1.2753	0.0249	112.5	1.04	2.2
227266	212.8593	1.2865	0.0249	112.5	0.92	2.8
252021	221.8654	1.9181	0.0339	111.5	0.76	3.6
263044	222.5917	2.192	0.0449	110.3	0.93	2.1
272990	221.5713	-1.5729	0.0570	110.7	1.21	–
296934	214.0442	1.5414	0.0531	109.5	0.95	1.9
323854	133.4053	1.7177	0.0582	108.9	0.78	2.8
324349	135.7144	1.6811	0.0571	109.0	1.02	1.6
463434	213.0345	-1.3268	0.0538	109.4	1.07	1.5
549251	130.9384	-0.5346	0.0295	112.0	1.14	1.7
601255	139.0381	0.2965	0.0566	109.1	0.73	3.2
3616590	138.8673	-1.4902	0.0554	109.2	0.81	2.6

GAMA514212 is from SDSS, the remainder are from KiDS. Their generally smooth morphology is apparent. Figure 7.3 shows the ETG emission at 250 μm from Herschel, presumed to be from cool dust, with approximately the same beam FWHM as the IRAM 30m telescope when observing ^{12}CO[1-0] emission. The beam FWHM for the IRAM 30m telescope observing ^{12}CO[1-0] emission is also shown in both Figures for comparison. The 250 μm emission lies approximately within the telescope beam for many of the galaxies, with a few having emission beyond this. Section 7.4.3 describes how aperture correction is used to account for possible emission beyond the telescope beam.

Figure 7.4 shows the 32 observed Dusty ETGs on a plot of SFR versus stellar mass (from GAMA II MagPhysv06), with the Parent Sample galaxies also shown for context. Also shown is an empirical fit to the SFMS by Saintonge et al. (2016), to illustrate which ETGs are associated with it. The observed Dusty ETGs can be seen to follow the SFMS from low to high stellar mass, and then fall below it with further increase in stellar mass. The ETGs on the main sequence have lost most or all of their LTG-like morphology, but have recent star formation in line with expectations with LTGs. One, GAMA64087, has its SFR above the SFMS. The lowest SFR is found in GAMA227266, which is one of a pair of galaxies with GAMA227264 and is relatively close (redshift 0.0249). The most massive ETG in the sample, GAMA3616590, also has a low SFR in spite of having sufficient ISM to qualify for observation.

Because the Dusty ETG sample was selected on the basis of a minimum sensitivity for detection of CO emission, the sample is flux-limited. This is illustrated by Figure 7.5, which shows dust masses from GAMA II plotted against GAMA II stellar masses with the IRAM 30m target ETGs highlighted. All the Dusty ETGs have dust masses above $\sim 10^{6.6}$ $M_\odot$. At lower stellar masses, the ETGs for observation are therefore relatively dustier than those at higher stellar mass.

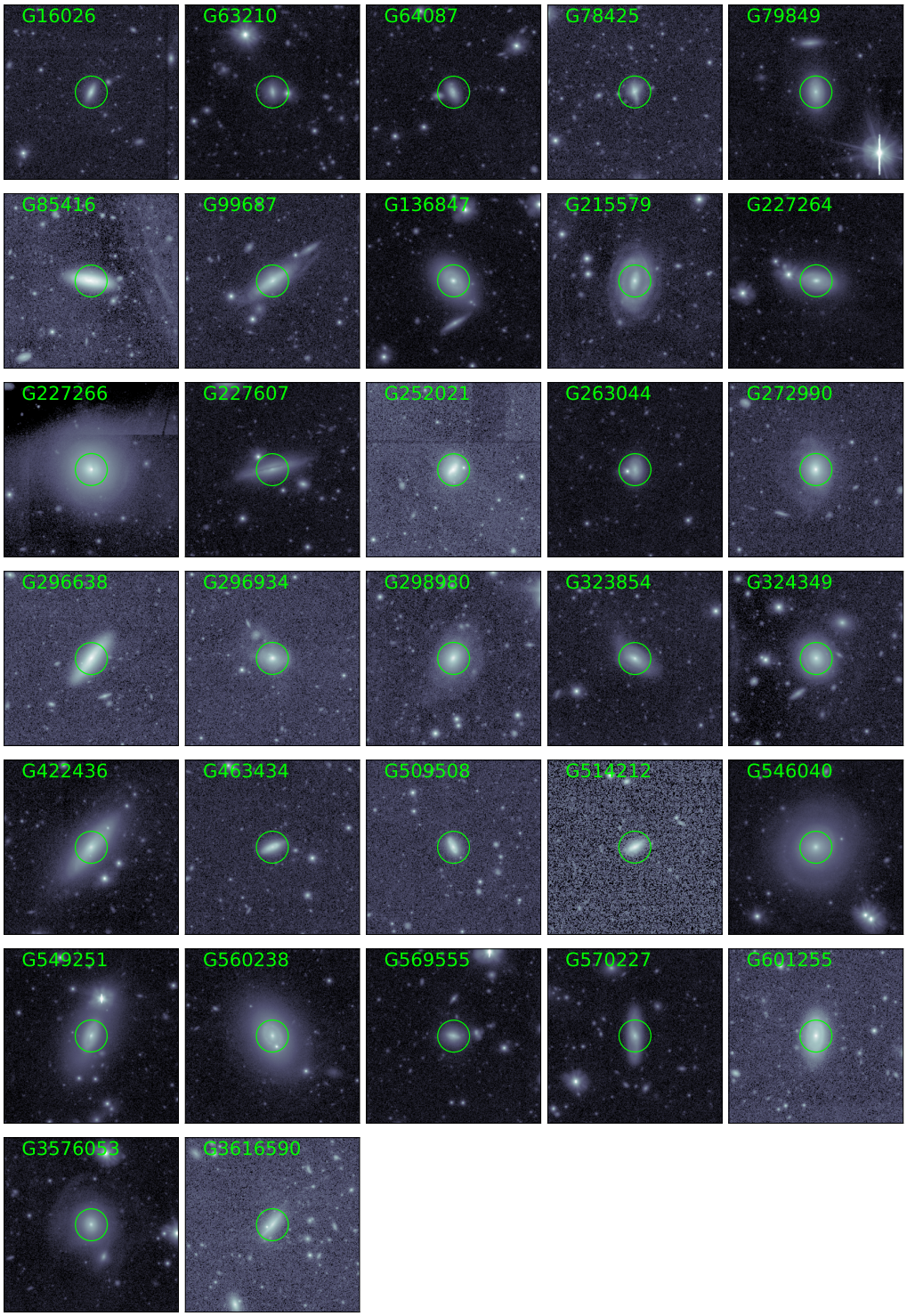

Figure 7.2: r-band log-normalised tiles (2 arcmin × 2 arcmin) of the 32 ETGs selected for observation with the IRAM 30m telescope. Image for GAMA514212 is from SDSS, the remainder are from KiDS. The telescope beam FWHM for ^{12}CO[1-0] observation is shown in green for comparison.

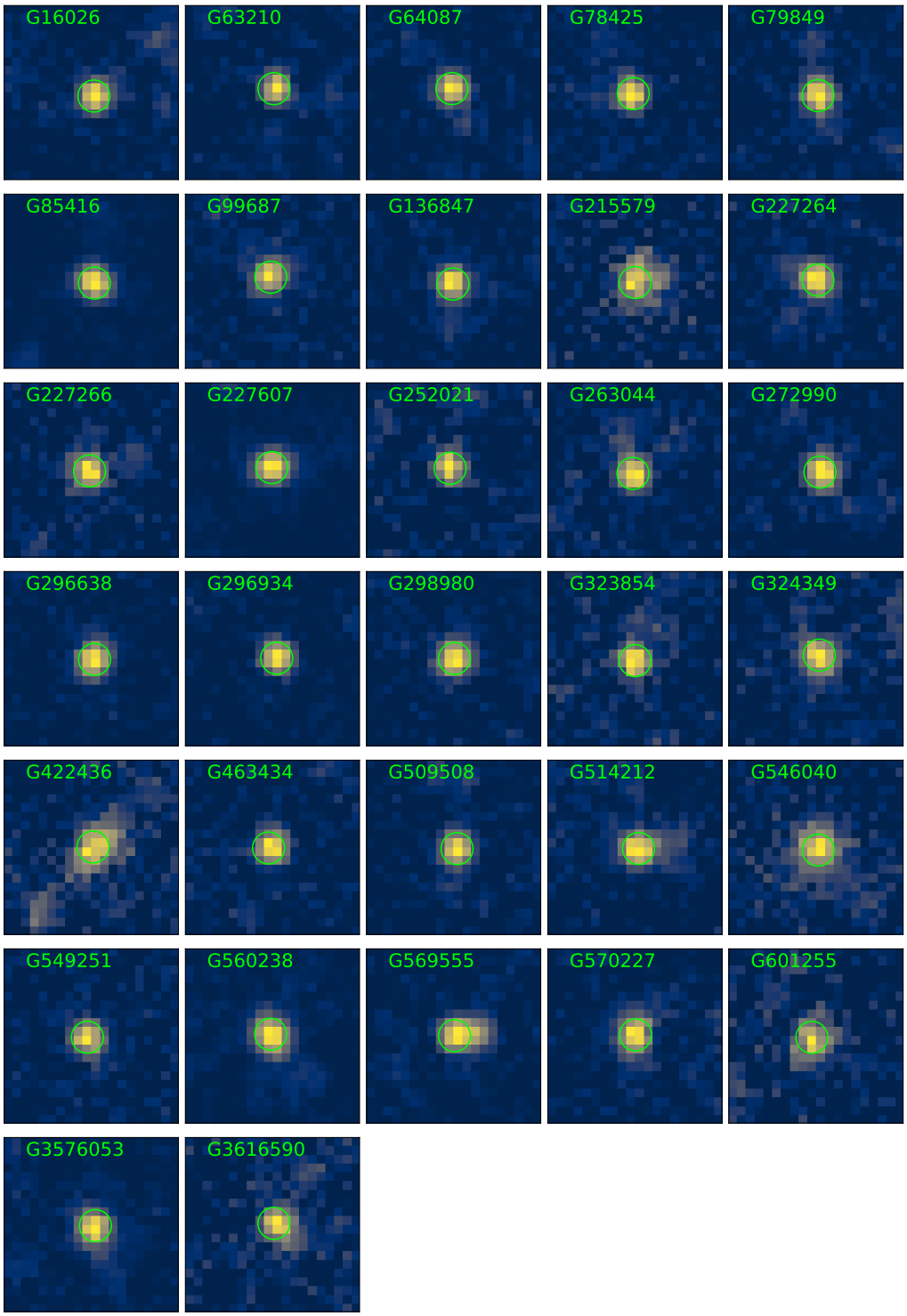

Figure 7.3: Herschel SPIRE 250μm tiles of the 32 ETGs selected for observation with the IRAM 30m telescope. The telescope beam FWHM for ^{12}CO[1-0] observation is shown in green for comparison.

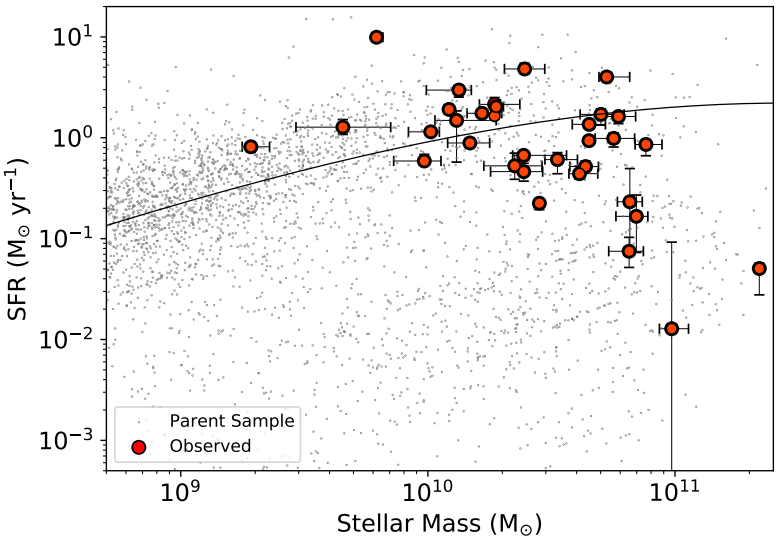

Figure 7.4: Star formation rate versus stellar mass for the Parent Sample and the IRAM 30m observed Dusty ETGs. Median uncertainties are shown for illustration. Trendline is the SFMS as determined by Saintonge et al. (2016).

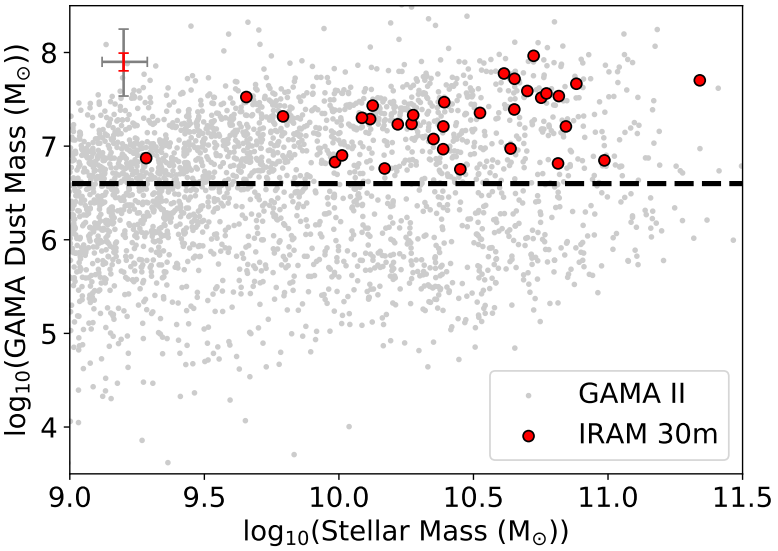

Figure 7.5: GAMA II dust mass versus stellar mass for the Parent Sample, and the Dusty ETGs selected for observation with the IRAM 30m telescope. A lower limit on dust mass of $10^{6.6}$ $M_\odot$ is shown.

7.3 Observations

Observing scripts using PAKO commands (Section 2.3) were prepared in advance for each Dusty ETG to be observed and reviewed by duty astronomers at the telescope. These were based on standard templates provided by the duty astronomers. The templates created for project 070-19 could be used effectively, but were prone to human error because the correct emission line frequency and setup for the observation had to be uncommented within a file with the remainder commented out. On one occasion the wrong emission line frequency was selected by a pool observer, and only part of the line was detected. This observation was repeated. For 203-19, a new style of script were created by this author with detailed setup scripts per ETG in a subdirectory, such that the observer could simply use the commands in sequence from one main script per ETG without having to modify any command lines. No further errors occurred when using the scripts.

All observations followed a standard pattern. The frontend and backend were set up based on the expected emission frequency of the target and if necessary tuning the LO by the telescope operator. An initial telescope pointing check was performed using a bright millimetre-wavelength source (various planets and quasars) followed by focussing. The telescope pointing was then re-checked using a millimetre-wavelength source closer to the target. Once satisfactory pointing and focus had been achieved, the telescope was directed onto the target and observations could commence.

Observations consisted of batches of individual scans. Each batch of scans consisted of an initial calibration using an internal hot source and three scans with a total duration of ~10 minutes each. This ensures that a calibration is performed approximately every 10 minutes, to follow atmospheric variations. Typically three batches of scans were initiated to start with (~30 minutes duration). A rapid reduction of the results using the CLASS program within IRAM's GILDAS software suite was performed typically after observing for an hour, after initiating a further three batches of scans. This reduction allowed the achieved baseline noise level to be assessed (with 50 km/s binning), and the presence of

any emission line to be examined. Further scans were initiated if the target baseline noise from observation planning had not been achieved, unless the uncertainty of detection of the intended emission line (mostly peak signal/RMS noise >3, but sometimes integrated flux/uncertainty >3) had been achieved. Pointing checks were repeated every 1.5 hours, and focussing every 2 hours approximately and after sunset. Care was taken throughout not to allow the telescope to pass through an azimuth of 60° clockwise, because this may reach the mechanical limits of the telescope cables. If this happens, eight minutes of observation would be lost while the telescope reverses 360° anticlockwise before observations can continue.

Observations for project 070-19 were performed using pool observing between 4th June 2019 to 23rd July 2019, where all pool observations are performed by observing project representatives when it is most suitable to perform them. Pool observing increases the chance of obtaining observations given the variations in weather compared to a shorter, fixed allocation of time. Consequently many of the Dusty ETGs were observed by others, and in return this author attended the telescope from 21st July - 28th July 2019 and observed some of the ETGs and targets for other observers. As a result, all 16 ETGs were observed. The weather generally was adequate, except for the week when this author attended the telescope. A heatwave was in progress, which led to high humidity (needing longer exposure times to achieve target sensitivities) and cumulus/cumulonimbus cloud in the direction of the targets which blocked incoming emission. There is also a chance that some of the scans performed were affected by anomalous refraction, with significant short-duration jumps in pointing due to pockets of moist air passing through the beam (Wilson et al. 2009).

Observations for project 203-19 were completed in three sessions. Only one complete observation (GAMA227264) and one partial observation (GAMA272990) were performed during pool observing on 21 - 28 January 2020 while this author attended the telescope, due to poor weather and heavy snowfall. Further time was therefore awarded to this author for remote observing from the UK on 24 - 26 April 2020 (9 hours). Although

this session was partially hampered by poor weather, the partial observation from January 2020 (GAMA272990) was completed. A further 49 hours remote observing time from the UK was then awarded to this author for 23 - 30 June 2020. This allowed all remaining observations for the project to be completed, in spite of restrictions on travel and personal movement in both the UK and Spain during the Covid-19 pandemic. The weather was generally good for these latter observations, and observations were only paused on the advice of operators when atmospheric issues arose (e.g. highly significant atmospheric refraction). A problem with an azimuth position sensor (reported late on by the telescope operator) meant that some larger than tolerable deviations between pointing corrections (>5°) may have been fictitious. Improved pointing performance was achieved later in the period by slewing the telescope 60° in azimuth and back before performing a pointing check.

Observations of four Dusty ETGs (GAMA215579, 251021, 422436 and 509508) were affected by high atmospheric water vapour levels and anomalous atmospheric refraction leading to large changes in pointing corrections midway through the observations. Although ^{12}CO[1-0] emission was detected from these ETGs, any fluxes quoted are regarded as lower limits because of sporadic beam deflection off the target. In general, fluxes determined from single-point observations such as these are at worst lower limits because of pointing accuracy, unquantified atmospheric fluctuations and the unknown extent of molecular gas compared to the beam size. This should be borne in mind when interpreting results.

7.4 Data Reduction

7.4.1 Line Detecton and Initial Flux Density Estimation

The immediate product from an observation is a number of individual scans, which are spectra from the target acquired over short time intervals as specified in the observation

script. The scans need to be cleaned, set to a common baseline and averaged to produce the definitive spectrum. Data reduction was performed using CLASS, a package within IRAM's GILDAS suite of software. This is a command-line driven package, which allows individual observation scans to be read in and identified, cleaned of spikes if required, set to a flat zero baseline and averaged, binned to a suitable channel width and plotted for inspection. Optionally, a spectral line profile (in this case, Gaussian) could be fitted to the averaged spectrum to obtain an indication of the line peak (in K T_A^*), line area (flux) and baseline RMS noise.

Definitive spectra for analysis were produced using more detailed steps within four scripts in the CLASS command language, provided by IRAM duty astronomers. A standard section of the scans covering the range -1000 to 1000 km s^{-1} (relative to the recession velocity of the observed galaxy) was selected for processing throughout, to avoid issues with any artefacts away from the emission line and provide sufficient baseline to identify and quantify the emission line. The first two scripts allowed individual scans to be inspected before and after binning to a specified channel width (typically 50 km s^{-1}). Scans with spikes (electronic noise causing a very large peak in a single unbinned channel) were identified and noted for action later. Also, scans with baseline RMS (excluding the emission line) significantly greater than the remainder or with artefacts such as large oscillations were noted for removal by inclusion in the next script. Scans with platforming (large steps within the spectrum) were also noted for correction if needed, for inclusion in the next script.

The third script was used to remove any spikes in scans by interpolating across neighbouring channels (using the FILL /INTER command in CLASS). Neighbouring channels around a spike were identified manually from an on-screen plot, and commands were included in the script to interpolate across them. Any scans found previously with excessive baseline RMS noise were removed from the analysis using the DROP command within CLASS. The baselines of the remaining scans were then fitted with polynomials of the lowest possible order (typically first order, but second order was needed for

GAMA227607) in order to set baselines for individual scans to an average of zero. The baselined scans were then written to a file for later processing. This script was also used to de-platform scans from FTS for GAMA272990 by calling a standard CLASS subscript (FtsPlatformingCorrection5.class) supplied by IRAM duty astronomers. Most observations of ^{12}CO[2-1] with FTS were affected by platforming, so ^{12}CO[2-1] observations from WILMA were used throughout where available. However, WILMA was not available during observations of GAMA272990 in April 2020.

The fourth script combined and averaged the baselined scans (using the AVER command in CLASS) to produce a definitive binned spectrum, and output a FITS file for later use and a plot for immediate inspection of the final spectrum. Averaging of scans used a weighting scheme based on the square of the baseline RMS noise for each scan. Bin sizes were typically ~50 km/s (i.e. ~90 channels/bin for FTS, ~15 channels/bin for WILMA). However if this failed to achieve a ratio of line flux to uncertainty of 3 in later analyses, the bin size was increased in 25 km/s increments to reduce the baseline RMS noise and try to recover an emission line. A minimum of three bins per spectrum was considered appropriate for detection of an emission line. Figures 7.6 and 7.7 show the spectra obtained for the 32 observed Dusty ETGs, with detected emission highlighted.

If an emission line was apparent in a spectrum, a Python script prepared by this author was used to isolate the bins with emission manually and provide an integrated flux for the line by summing the bins and multiplying by the bin velocity width. Channels for inclusion in integration were selected as being above the surrounding background channels. The remainder of the bins within a ±1000 km s^{-1} window were used to recalculate the baseline offset and re-zero the baseline. Symmetry about a relative velocity of 0 km s^{-1} was also used as a guide. The results were compared with Gaussian profile fitting to the spectral lines and integration, using tools available in CLASS. Figure 7.8 shows that with one exception, fitting Gaussian profiles to the spectra delivers integrated fluxes that are comparable within the levels of uncertainty. This even applies for spectra with double peaks, because the outer edges of the Gaussian profile extend beyond the

spectral lines and compensate for the lack of fitting of the tops of the peaks. The outlier is the ^{12}CO[2-1] line for GAMA227264, whose emission includes three dominant central bins where Gaussian fitting took place, but fitting did not account for the spectral shape adequately and recover the expected line flux. Davis et al. (2015) found a similar good comparison between the two methods. In this work, integrated fluxes from manually identified channels are used. Table 7.3 shows the line fluxes obtained. Uncertainties for line fluxes were calculated according to Young et al. (2011), their Equation 1:

$$\sigma_0^2 = \Delta v^2 \sigma^2 N \left(1 + \frac{N}{N_b}\right) \tag{7.9}$$

where σ_0 is the flux density uncertainty per velocity bin, Δv is the bin velocity width, σ is the baseline RMS noise, N is the number of bins in the line and N_b is the number of bins used to estimate σ. The uncertainty on the velocity width is taken to be ±0.5 bin widths. Uncertainties in Table 7.3 include calibration uncertainty at 8% of the measured line strength (Saintonge et al. 2017).

Table 7.3: Measured CO line fluxes (K(T_A^*) km s^{-1}) and velocity widths (km s^{-1}) for the Dusty ETGs observed with the IRAM 30m telescope.

GAMA ID	**^{12}CO[1-0] Line Flux**	**^{12}CO[1-0] Line Width**	**^{12}CO[2-1] Line Flux**	**^{12}CO[2-1] Line Width**	**I[2-1] / I[1-0]**
16026	0.74 ± 0.11	448 ± 50	1.59 ± 0.30	493 ± 49	2.15 ± 0.52
63210	0.54 ± 0.09	301 ± 50	1.29 ± 0.24	345 ± 49	2.38 ± 0.59
64087	0.84 ± 0.11	399 ± 50	0.88 ± 0.26	296 ± 74	1.04 ± 0.33
78425	0.57 ± 0.09	298 ± 50	0.70 ± 0.19	246 ± 49	1.22 ± 0.38
79849	1.37 ± 0.14	449 ± 50	1.86 ± 0.30	440 ± 49	1.36 ± 0.26
85416	2.56 ± 0.23	452 ± 50	2.72 ± 0.31	353 ± 50	1.06 ± 0.15
99687	0.75 ± 0.14	525 ± 75	—	—	—
136847	1.68 ± 0.16	401 ± 50	2.27 ± 0.31	406 ± 51	1.35 ± 0.22
			Continued		

Table 7.3 – Continued

GAMA ID	^{12}CO[1-0] Line Flux	^{12}CO[1-0] Line Width	^{12}CO[2-1] Line Flux	^{12}CO[2-1] Line Width	I[2-1] / I[1-0]
215579	0.48 ± 0.13	400 ± 100	0.63 ± 0.21	296 ± 49	1.31 ± 0.56
227264	0.76 ± 0.11	450 ± 50	1.23 ± 0.31	304 ± 101	1.61 ± 0.47
227266	0.73 ± 0.17	600 ± 100	1.15 ± 0.41	506 ± 101	1.58 ± 0.68
227607	2.16 ± 0.22	528 ± 75	3.63 ± 0.42	550 ± 50	1.68 ± 0.26
252021	0.71 ± 0.09	299 ± 50	—	—	—
263044	1.08 ± 0.11	299 ± 50	1.23 ± 0.24	342 ± 49	1.14 ± 0.25
272990	1.27 ± 0.13	352 ± 50	1.88 ± 0.27	350 ± 50	1.48 ± 0.26
296638	1.63 ± 0.15	350 ± 50	2.74 ± 0.32	355 ± 51	1.68 ± 0.25
296934	1.08 ± 0.11	249 ± 50	1.55 ± 0.22	246 ± 49	1.44 ± 0.25
298980	1.08 ± 0.11	250 ± 50	2.03 ± 0.25	254 ± 51	1.88 ± 0.30
323854	0.49 ± 0.08	250 ± 50	1.32 ± 0.40	495 ± 99	2.68 ± 0.92
324349	0.67 ± 0.10	350 ± 50	0.85 ± 0.23	346 ± 49	1.27 ± 0.39
422436	0.75 ± 0.17	600 ± 100	—	—	—
463434	1.07 ± 0.14	548 ± 50	1.44 ± 0.27	395 ± 49	1.35 ± 0.30
509508	0.41 ± 0.10	301 ± 75	0.68 ± 0.34	396 ± 99	1.66 ± 0.92
514212	0.74 ± 0.09	250 ± 50	1.01 ± 0.23	225 ± 75	1.36 ± 0.35
546040	0.54 ± 0.09	300 ± 50	0.86 ± 0.33	449 ± 75	1.61 ± 0.66
549251	—	—	—	—	—
560238	1.29 ± 0.13	299 ± 50	1.55 ± 0.26	353 ± 50	1.20 ± 0.23
569555	0.82 ± 0.10	349 ± 50	1.62 ± 0.26	346 ± 49	1.96 ± 0.40
570227	0.99 ± 0.12	399 ± 50	2.24 ± 0.31	440 ± 49	2.27 ± 0.42
601255	0.29 ± 0.06	150 ± 50	—	—	—
3576053	1.46 ± 0.15	452 ± 50	1.41 ± 0.46	503 ± 126	0.96 ± 0.33
3616590	0.50 ± 0.08	249 ± 50	—	—	—

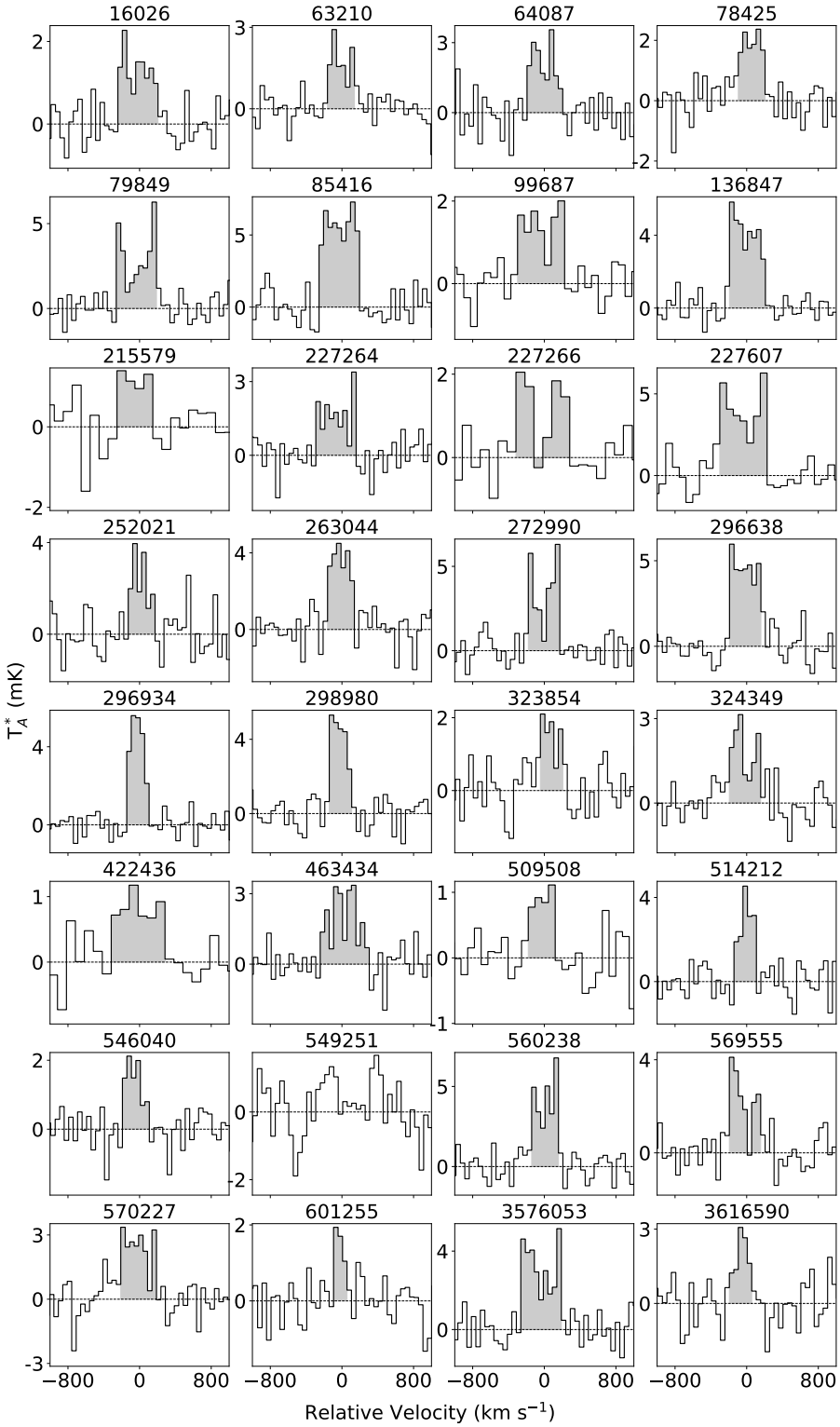

Figure 7.6: Emission spectra (~110 GHz) for 32 Dusty ETGs observed with the IRAM 30m telescope. ^{12}CO[1-0] emission lines are shown in grey. Velocities are relative to the recession velocity of the ETGs.

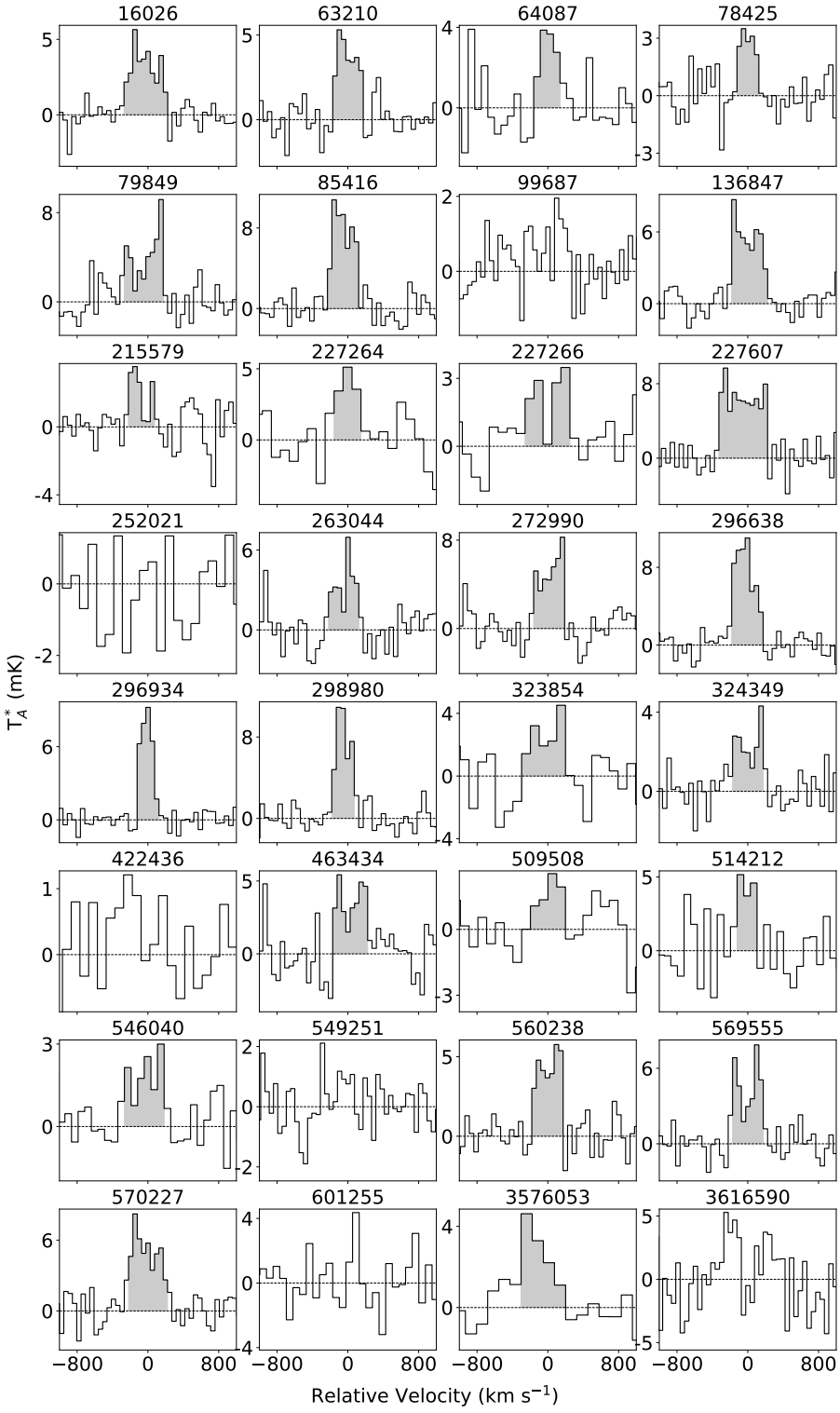

Figure 7.7: Emission spectra (~220 GHz) for 32 Dusty ETGs observed with the IRAM 30m telescope. ^{12}CO[2-1] emission lines are shown in grey. Velocities are relative to the recession velocity of the ETGs.

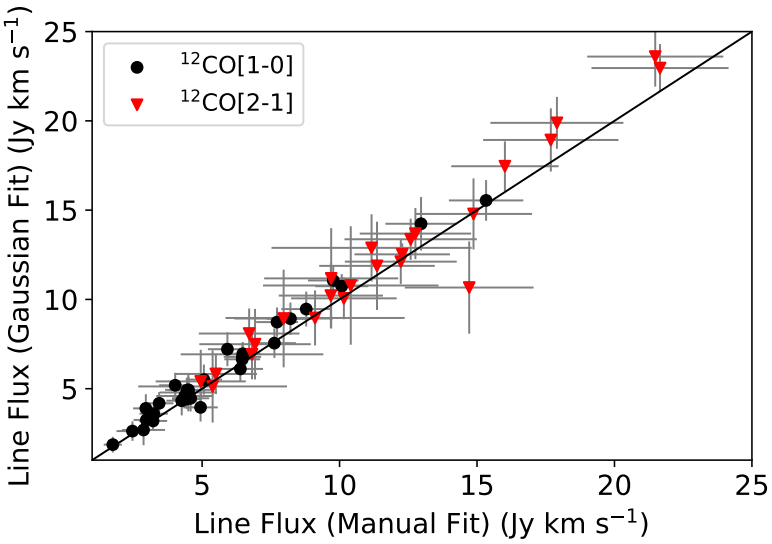

Figure 7.8: Comparison of integrated fluxes from integration of manually selected bins and Gaussian profiles fitted to spectral lines. Line fluxes are not aperture-corrected.

The ^{12}CO[2-1] line fluxes in all cases are greater than or equal to those for ^{12}CO[1-0]. As explained by Young et al. (2011), this is due to the extent to which the optically-thick CO emission fills the telescope beams for the emission frequencies of the two lines. If the emission fills the beam footprints, the antenna temperatures for both emission lines should be identical. However for highly compact emission an ^{12}CO[2-1]/^{12}CO[1-0] antenna temperature ratio of 4:1 can be expected. This is because the antenna temperature is an average over the beam, and the beam area for ^{12}CO[2-1] emission is a quarter of that for ^{12}CO[1-0]. Therefore, ratios of integrated line fluxes in units of K(T_A^*) km s^{-1} should be 1 if the emission source is at least as wide as the beams, and 4 if it is effectively a point source. Ratios greater than 1 are also dependent on gas temperatures being above the minimum temperature for significant ^{12}CO[2-1] line emission (~15K, Wilson et al. 2009). All the measurements for ETGs in Table 7.3 comply with these criteria, within uncertainties. Two ETGs, GAMA64087 and 3576053, have ratios close to 1 suggesting that the distribution of CO is beyond both beams. The remainder are between 1 and 4, suggesting that CO distributions are not point sources but are spread out to some extent less

than the beam width for ^{12}CO[1-0] emission (~22 arcsec FWHM). The absence of line emission ratios less than 1 is encouraging, because issues such as pointing inaccuracies or shifts during observations of ^{12}CO[2-1] emission can cause this.

The measured widths of the two spectral lines for each ETG shown in Table 7.3 are consistent within uncertainties for most of the observed Dusty ETGs. However, some variation exists, specifically for GAMA323854, 463434, 546040 and 570227. The noise levels within the ^{12}CO[2-1] spectra for these ETGs are such that it is challenging to identify the boundaries of the lines. The effect on the integrated fluxes is expected to be small, because this issue only affects the outer bins for a line which contribute significantly less emission than the inner bins.

7.4.2 ETG Optical Inclination and ^{12}CO[1-0] Spectral Shape

The spectra for ^{12}CO[2-1] emission shown in Chapter 2 (Figure 3.5) show a characteristic "double-horned" shape due to emission from rotating discs of CO with roughly exponential surface brightness and flat rotation velocity profiles with radius. The same features are apparent in the spectra for some of the ETGs shown in Figures 7.6 and 7.7. Many of the double-horned spectra are lopsided, which indicates more emission on one side of the rotating disc than the other (see discussion on GAMA272990 in Chapter 2). This is an indication of recent disturbance of ISM or introduction of new ISM, e.g. from a minor merger or other interaction with another galaxy. On the other hand, some are flat-topped or rounded, and have lower peak velocities than the double-horned spectra.

Based on the findings in Chapter 2 from kinematic modelling of rotating emission from molecular gas discs, double-horned spectra are associated with inclined rotating discs with approximately exponential radial surface brightness profiles. Rings and hollow discs can also produce double-horned spectra. A double-horned spectrum occurs when more flux (i.e. more surface emission) is associated with higher line-of-sight velocities than lower. If relative emission associated with lower velocities is increased, e.g. from

bright central emission, the valley between the horns is filled in. Decreased inclination decreases line-of-sight velocities across the disc needed to create the observed spectrum via Doppler shift. By examination of Figures 7.6 and 7.2, this appears to be the case for 12 of the observed Dusty ETGs. On the other hand, some of the remaining spectra are flat-topped or domed which may indicate inadequate velocity resolution to detect the horns or multiple kinematic features contributing to the spectrum (e.g. results for GAMA622429 in Section 3.3.1, for example). Optical thickness of the CO emission is also a possibility in these cases, resulting in a flat-topped spectrum and under-estimation of CO flux due to detection of flux from the emitting surface only. Other spectra are single-peaked and narrower in terms of velocity width, and it is possible that the CO observed is pressure-supported (with random orbits and an approximately Gaussian velocity profile) rather than rotation supported. The observed molecular gas in these instances could be concentrated towards the centre of the ETG in a bulge-like configuration, as originally assumed for planning of the ALMA observations discussed in Chapter 2 (Sansom et al. 2019). One interesting exception is the spectrum for GAMA227266, which has two strong and separate peaks at opposing velocities for both ^{12}CO[1-0] and ^{12}CO[2-1] emission, with little or no emission at lower velocities. Overall, the spectral shape information presented can be used to select galaxies for high-resolution observations of CO distribution using ALMA, to verify the spectral shapes observed in this study and explore the links between CO distribution and galaxy evolution. GAMA227266 is of particular interest because of its distinctive spectral shape, along with its low star formation rate in spite of the detectable presence of molecular gas.

7.4.3 Aperture Correction

A known problem with using single-dish radio telescopes for single-pointing observations is aperture effects. The telescope samples the on-sky emission via its beam, which is 2-dimensional Gaussian sensitivity profile with full-width at half-maximum (FWHM) dependent on dish diameter and observed wavelength. An example of a beam profile is

shown in Figure 7.11. An observed source is effectively vignetted by the beam, due to loss of sensitivity away from the beam centre. For an extended object, progressively less emission is measured further away from the centre of the beam and the total recorded emission over the whole beam is therefore reduced.

Figure 7.9 illustrates the aperture effects discussed above, using ^{12}CO[2-1] spectra obtained with the IRAM 30m telescope as part of this work and with ALMA (see Chapter 3) for GAMA272990. The ALMA observation shows the actual on-sky distribution of emission that was observed using the IRAM 30m telescope. The agreement between the IRAM 30m and ALMA spectra is good at low velocities corresponding to the central region of the rotating CO disc (as shown by the PV diagram in Figure 3.5), where beam sensitivity is strongest. However, the IRAM 30m telescope has not detected all of the ^{12}CO[2-1] flux at higher velocities, corresponding to spatial locations away from the beam centre where telescope sensitivity is lost. This is because the telescope beam for ^{12}CO[2-1] emission has a FWHM of ∼11 arcseconds, which is about the same diameter as the CO disc detected by ALMA (Figure 3.3). As a contrast, the IRAM 30m observed spectrum for ^{12}CO[1-0] emission is also shown in Figure 7.9. The telescope beam for this spectral line is ∼22 arcsec, so more of the flux at greater radius is captured and the double-horned spectrum expected from the ALMA observation is now apparent.

It is possible to compensate for the loss of emission at the beam edges if other information can be used to infer the actual distribution of CO, using a process called aperture correction (Lisenfeld et al. 2011; Saintonge et al. 2011). This makes use of a 2-dimensional model or image of proxies for the full distribution of CO emission within the galaxy in question, e.g. emission related to star formation which is associated with the presence of molecular gas. Examples of such images are exponential radial emission profiles with suitable effective radii, star formation maps, e.g. from IFU observations, maps from line emission surveys (e.g. Hα) or images using passbands where continuum emission can be used as a proxy for star formation (e.g. far ultra-violet). Map values need to be proportional to CO emission, but the units are not important. This model or

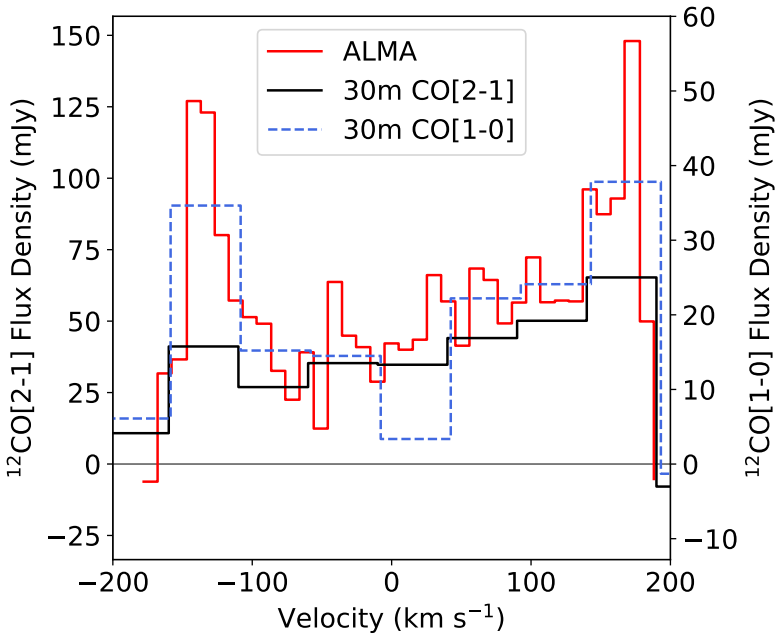

Figure 7.9: Comparison of ^{12}CO[1-0] and ^{12}CO[2-1] spectra from the IRAM 30m telescope and ALMA (see Chapter 2) for GAMA272990.

map is convolved with a 2-dimensional image representing the relevant telescope beam footprint at the location of the centre of the telescope beam, and the total emission from the distribution with and without beam convolution is found. The ratio of the two fluxes (without/with beam convolution) is a correction factor that can be applied to the actual measured flux within the beam, to scale it to the expected level.

In this instance, convolution involves multiplying corresponding pixels within the expected CO distribution map with a 2D image representing the IRAM 30m telescope beam of the same map size and scale, with 1 at the beam centre decaying to zero at the outer edges. The centre of the beam needs to be centred on the coordinate of observation. This operation effectively treats the telescope as a single-pixel camera, with emission captured only within the beam (ignoring sidelobe effects), and in effect creates an image vignetted by the beam profile. If the model and the beam are expressed as functions of map coordinates x and y with origin at the coordinate of observation, then the operation can be expressed as follows:

$$S_{\nu,c} = \int_0^\infty \int_0^\infty S_\nu(x,y)\, b(x,y)\, dxdy \tag{7.10}$$

where $S_{\nu,c}$ is the convolved flux density of the source at the pixel of observation. When applied to 2-dimensional pixels (i,j) in an image with known flux density $S_{\nu,ij}$ and a pixelated beam image of the same spatial dimensions b_{ij}, this becomes:

$$S_{\nu,c} = \sum_i \sum_j S_{\nu,ij} b_{ij} \tag{7.11}$$

One possible model that could be used for molecular gas distribution in a galaxy is a map of SDSS u-band emission with sufficiently high resolution. Star formation within LTGs is known to be traced by light in u-band images (e.g. Hopkins et al. 2003; Davies et al. 2016). New star formation generates emission at shorter wavelengths due to the presence of OB stars, and requires the presence of cool molecular gas. It should therefore be possible to use high-resolution u-band images to trace the distribution of star formation and hence estimate the distribution of molecular gas responsible for star formation. The KiDS survey (Section 2.6.4) provides seeing-limited (~0.7 arcsec FWHM) u-band images which can be used directly for this. However, some of the ETGs selected for observation with the IRAM 30m telescope are more passive, and it is possible that the relation between star formation and u-band emission is not applicable to them. In particular, UV emission from ETGs has stronger contributions from older stellar populations, (e.g. white dwarfs, AGB stars) than LTGs (Stasińska et al. 2008, and references therein, see also Section 4.3.2).

To investigate whether this principle can be applied to the observed Dusty ETGs, u-band luminosity densities for the early-type and late type galaxy samples discussed in Chapter 3 were calculated from extinction-corrected flux densities in GAMA II 21BandPhotomv03 and were plotted against MAGPHYS-derived star formation rates from GAMA II MagPhysv06 (see Chapter 3). The results (Figure 7.10) show that the LTGs follow a trend as expected, with a slope similar to those found by Davies et al.

(2016). However, many ETGs at lower star formation rates appear to show higher luminosities than the LTG trend would indicate, because of stronger contributions to u-band emission from older stellar populations compared to LTGs. Of the 32 observed Dusty ETGs, 30 are also shown on Figure 7.10. GAMA514212 a non-detection for CO and is not shown, and GAMA3576053 has no u-band photometry within GAMA II 21BandPhotomv03 for plotting. All but five of the 30 ETGs plotted follow the trend for LTGs. GAMA78425 has a lower u-band luminosity density than its relatively high SFR would suggest. GAMA227264, 227266, 422436 and 546040 lie in the ETG distribution, above the LTG trend line, and light from older stellar populations within these could be contributing more strongly to u-band emission. The strategy followed in this work was therefore to calculate aperture corrections for all ETGs with detected CO emission, and if they are sufficiently small or are generally within the distribution of the other calculated correction factors then they are suitable for use. CO emission is then either mostly contained within the relevant beam, or the correction factors are not overly distorted by u-band emission from older stellar populations.

Aperture correction factors (multipliers) for each observed ETG were determined by multiplying 2 arcmin x 2 arcmin KiDS u-band cutouts in FITS format from the SAMI cutout service[4], or from the ESO portal[5] if images from SAMI were not available, with a 2D Gaussian beam map created with astropy.modeling.functional_models.Gaussian2D. Correction factors obtained were found to be very sensitive to the sum of the background noise beyond the galaxy included in the calculation, and hence the image region used to calculate the correction factor. To create justifiable estimates of correction factors, a method based on aperture photometry was used to optimise the region sampled. The Python function SEP[6] was used to produce an image in which the galaxy of interest was identified, and background was subtracted as far as possible. The fitted galaxy shape parameters from SEP (major/minor axis lengths and position angle) were then used to

[4]https://datacentral.org.au/services/cutout/

[5]https://archive.eso.org/scienceportal/home

[6]https://github.com/kbarbary/sep

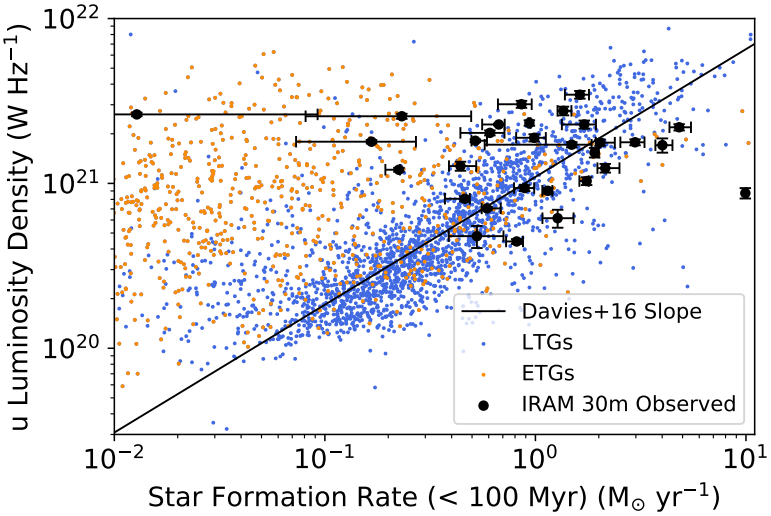

Figure 7.10: u-band luminosity density versus MAGPHYS-estimated SFR (<100 Myr) for the Spirals (LTG) and Ellipticals/Lenticulars (ETG) samples derived in Chapter 3. The 30 IRAM 30m ETGs with ^{12}CO[1-0] detections and suitable u-band photometry are also shown. Error bars are shown for the observed galaxies only.

create an elliptical mask which is applied to the image and the beam map to calculate the aperture correction ratio. A multiplier was found for the major/minor axis lengths which maximised the correction factor while minimising the sampled area and avoided background sources. Figure 7.11 illustrates the derivation of the aperture correction factor for GAMA272990.

Table 7.4 summarises the aperture corrections used and the corrected line fluxes which are used to calculate molecular gas masses in the next Section. Aperture correction factors for ^{12}CO[1-0] emission for the five ETGs with brighter u-band emission than expected from the LTG trend (Figure 7.10) are in the range 1.1 - 1.4, with two galaxies at the higher end of this range. Overall, the values obtained were not significantly different from those found for the remaining ETGs, so the aperture corrections were applied to these ETGs. For comparison, Domínguez-Gómez et al. (2022) convolved their IRAM 30m telescope observations of Void galaxies with with exponential r-band radial surface brightness models, and obtained aperture correction factors of between 1.1 and 1.5. Factors for ^{12}CO[2-1] observations are greater, because of the smaller beam size.

The results of this process for GAMA272990 illustrate the benefits of using aperture correction in this way. The ^{12}CO[2-1] line flux for this ETG reported in Table 7.3 is 1.88 ± 0.27 K(T_A^*) km s^{-1}, which converts to 14.9 ± 2.1 Jy km s^{-1} using the conversion factor discussed earlier of 7.9 Jy K(T_A^*)$^{-1}$. This falls short of the value of 21.0 ± 1.4 Jy km s^{-1} derived from the ALMA observation discussed in Section 2. When the aperture correction factor from Table 7.4 is applied, a flux of 19.71 ± 2.82 Jy km s^{-1} is obtained. This now agrees with the ALMA-derived value.

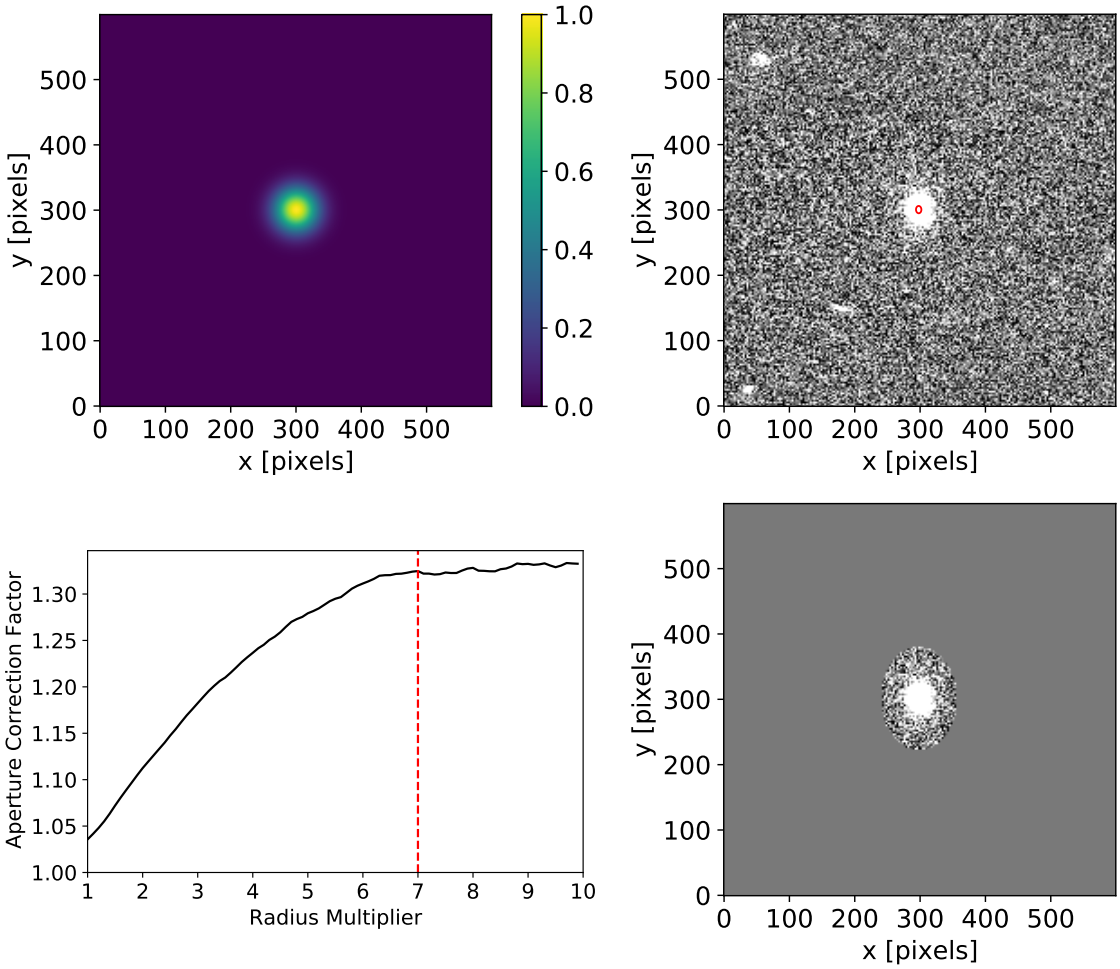

Figure 7.11: KiDS u-band aperture correction estimation for GAMA272990, ^{12}CO[2-1] observation. *Top left*: IRAM 30m telescope Gaussian beam map, 11 arcsec FWHM. *Top right*: selected galaxy from image (at centre coordinates) and overplotted ellipse (red) showing fitted shape parameters from SEP. *Lower left*: Multipliers applied to fitted ellipse axis dimensions, and optimum multiplier selected to minimise the ellipse dimensions while maximising emission. *lower right*: Selected masked region showing central galaxy.

Table 7.4: u-band aperture correction factors and corrected flux densities (Jy) for ^{12}CO[1-0] and ^{12}CO[2-1] emission for the observed Dusty ETGs with detected ^{12}CO[1-0] emission.

GAMA ID	**CO[1-0] Aperture Corr.**	**CO[1-0] Flux**	**CO[1-0] Flux Err.**	**CO[2-1] Aperture Corr.**	**CO[2-1] Flux**	**CO[2-1] Flux Err.**
		Jy km s^{-1}			**Jy km s^{-1}**	
16026	1.058	4.71	0.72	1.150	14.47	2.77
63210	1.090	3.53	0.57	1.216	12.35	2.34
64087	1.052	5.33	0.71	1.201	8.32	2.43
78425	1.049	3.61	0.55	1.186	6.52	1.78
79849	1.136	9.33	0.99	1.493	21.97	3.50
85416	1.164	17.84	1.58	1.578	33.90	3.91
99687	1.120	5.04	0.97	—	—	—
136847	1.150	11.59	1.11	1.465	26.23	3.54
215579	1.334	3.83	1.06	1.862	9.22	3.05
227264	1.140	5.22	0.78	1.463	14.18	3.57
227266	1.234	5.39	1.30	1.682	15.32	5.48
227607	1.294	16.78	1.69	1.939	55.54	6.39
252021	1.075	4.58	0.61	—	—	—
263044	1.080	6.98	0.74	1.350	13.07	2.56
272990	1.097	8.37	0.86	1.325	19.71	2.82
296638	1.227	11.99	1.14	1.744	37.77	4.35
296934	1.054	6.81	0.69	1.192	14.64	2.07
298980	1.092	7.08	0.72	1.315	21.06	2.57
323854	1.076	3.18	0.51	1.260	13.11	4.02
324349	1.186	4.77	0.70	1.606	10.78	2.94
422436	1.414	6.36	1.50	—	—	—

Continued

Table 7.4 – Continued

GAMA ID	CO[1-0] Aperture Corr.	CO[1-0] Flux	CO[1-0] Flux Err.	CO[2-1] Aperture Corr.	CO[2-1] Flux	CO[2-1] Flux Err.
		Jy km s^{-1}			Jy km s^{-1}	
463434	1.071	6.85	0.89	1.260	14.32	2.65
509508	1.062	2.62	0.63	1.243	6.69	3.36
514212	1.061	4.71	0.57	1.235	9.84	2.21
546040	1.309	4.21	0.68	1.895	12.92	4.91
549251	—	—	—	—	—	—
560238	1.282	9.90	0.98	2.296	28.07	4.67
569555	1.057	5.23	0.67	1.220	15.57	2.47
570227	1.236	7.32	0.88	1.705	30.15	4.20
601255	1.254	2.20	0.42	—	—	—
3576053	1.126	9.89	1.03	1.415	15.80	5.15
3616590	1.155	3.43	0.54	—	—	—

7.4.4 Estimation of Molecular Gas Masses from ^{12}CO[1-0] Emission

The ^{12}CO[1-0] line fluxes presented in Table 7.4 can be used to estimate the mass of molecular gas responsible for the emission in each Dusty ETG. In this instance a metallicity-dependent mass-to-light ratio α_{CO} (with units of $M_\odot$ (K km s^{-1} pc^2)$^{-1}$) is used where available, as follows:

$$\left(\frac{M_{gas}}{M_\odot}\right) = \alpha_{CO}\left(\frac{L_{CO[1-0]}}{Kkms^{-1}pc^2}\right) \tag{7.12}$$

where $L_{CO[1-0]}$ is the line luminosity. Note that α_{CO} by convention should be the ratio

of molecular gas mass to luminosity, unlike X_{CO} which is normally based on molecular hydrogen column density (Bolatto et al. 2013). Care is needed when examining work using these conversion factors, because usage and terminology is not always consistent. A factor of 1.36 converts molecular hydrogen mass to molecular gas mass, including the primordial mass fraction of helium.

The line luminosity can be calculated from an observed line flux in Jy km s^{-1} using the following expression from Solomon & Vanden Bout (2005), their Equation 3, and was adapted by Sansom et al. (2019) as follows with constant rest emission frequency used instead of observed frequency:

$$L_{CO} = \left(\frac{c^2}{2k_B}\right) \nu_{rest}^{-2} D_L^2 (1+z)^{-1} \int S_{CO} dv \tag{7.13}$$

where L_{CO} is line luminosity in terms of brightness temperature , S_{CO} is the emission line flux density, v is velocity, ν_{rest} is the emission rest frequency and z is redshift. All variables are in SI units. Converting the variables to practical units for observations yields:

$$\left(\frac{L_{CO}}{K\ km\ s^{-1}\ pc^2}\right) = 3.25 \times 10^7 \left(\frac{\nu_{rest}}{GHz}\right)^{-2} \left(\frac{D_L}{Mpc}\right)^2 \left(\frac{S_{CO}\Delta v}{Jy\ km\ s^{-1}}\right) (1+z)^{-1} \tag{7.14}$$

This approach differs from that used for observation planning, which used Equation 7.8 based on X_{CO}. However, both approaches yield the same results as long as the values of α_{CO} and X_{CO} are compatible. Values for α_{CO} (or X_{CO}) are notoriously difficult to estimate for a specific galaxy (Eales et al. 2012), with wide variations in estimates from different studies. For the single example of the Milky Way Galaxy, the uncertainty in α_{CO} is around ±30% (Bolatto et al. 2013). One galaxy property which is known to influence the conversion factor is the gas-phase metallicity, which is linked to the ratio of molecular gas (H_2, He) to carbon present as gaseous CO. In this work the empirical relation derived by Accurso et al. (2017) is used to estimate α_{CO} from a measure of gas-phase metallicity based on oxygen abundance ($12 + \log_{10}$[O/H]), which in turn is found from a range of

empirical means. This choice allows direct comparison of results with those from the xCOLD GASS survey (Saintonge et al. 2017), which surveyed 532 galaxies for molecular gas content in the local Universe and used the conversion factors based on methods from Accurso et al. (2017, their Equation 25). The empirical relation between α_{CO} and 12 + $\log_{10}$[O/H] used in this work is as follows:

$$log_{10}(\alpha_{CO}) = 14.752 - 1.623\,(12 + log_{10}[O/H]) + 0.062 log_{10}\Delta(MS) \tag{7.15}$$

where $\Delta(MS)$ is a term representing the fraction of the measured specific star formation rate in a galaxy compared to expectation from the star-forming main sequence defined empirically by (Accurso et al. 2017, their Equation 6) as a function of redshift z:

$$log_{10}(sSFR_{MS}) = -1.12 + 1.14z - 0.19z^2 - (0.3 + 0.13z)\,(log_{10}M_* - 10.5) \tag{7.16}$$

Several means of estimating the gas-phase metallicity for a galaxy exist (e.g. Pettini & Pagel 2004; Marino et al. 2013; Steidel et al. 2014; Bian et al. 2018; Bellstedt et al. 2021), some of which are intended for use with galaxies at high redshift. The methods from Pettini & Pagel (2004) as used by Saintonge et al. (2017) and Accurso et al. (2017) are used here, to allow consistency of the results from the xCOLD GASS survey and this work. Pettini & Pagel (2004) define the following relation between gas-phase metallicity (expressed as 12 + $\log_{10}$[O/H]) and an expression based on ratios of emission line strengths, valid for -1 ≤ O3N2 ≤ 1.9:

$$O3N2 = log_{10}\frac{\left([OIII]\lambda5007/H_\beta\right)}{([NII]\lambda6583/H_\alpha)} \tag{7.17}$$

$$12 + log_{10}[O/H] = 8.73 - 0.32 \times O3N2 \tag{7.18}$$

Only emission lines detected at 3σ or greater are considered. This relation is appropriate where relatively strong ionisation sources are present to create the emission lines (e.g. star formation). However, some of the ETGs observed with the IRAM 30m telescope have weak absorption lines, with an absence of detected [OIII] and H_β emission. The strategy adopted for this study is to use another empirical relation from Pettini & Pagel (2004) to estimate gas-phase metallicity if Equation 7.18 cannot be used, based on [NII] and H_α emission alone and valid for -2.5 ≤ N2 ≤ -0.3:

$$N2 = log_{10}\left([NII]\lambda6583/H_\alpha\right) \tag{7.19}$$

$$12 + log_{10}[O/H] = 9.37 + 2.03N2 + 1.26N2^2 + 0.32N2^3 \tag{7.20}$$

If an ETG has no useable detected emission lines for the relations presented above, an empirical relation based on stellar mass (in Solar units) alone is used (Kewley & Ellison 2008):

$$12 + log_{10}[O/H] = 32.1488 - 8.51258log_{10}M_* + 0.976384log_{10}M_*^2 - 0.0359763log_{10}M_*^3 \tag{7.21}$$

Note that the mass-metallicity relation may cause α_{CO} to be under-predicted for ETGs where significant quantities of low-metallicity gas has been introduced by minor mergers or other interactions. The relation based on O3N2 is used in preference, if suitably detected emission lines are available (from GAMA II GaussFitSimplev05, see Chapter 3). The N2 relation is used as a second choice, if the relevant lines only are detected. If no suitable lines are detected, the stellar mass-based relation is used as a contingency. However, this last method introduces a possible issue when using derived stellar masses from the same source (in this case, the GAMA catalogue MagPhysv06, see Chapter 3). It is possible that a circular argument could arise when comparing molecular gas or other

properties calculated using stellar mass with the stellar mass. All molecular gas mass calculations were therefore repeated with a constant value of α_{CO}, to see if similar trends emerged to those with α_{CO} derived individually for each ETG.

Table 7.5 shows the results of calculations to estimate 12 + $\log_{10}$[O/H] for each observed ETG, including the choice of method based on the emission line line ratios available.

Table 7.5: O3N2 and N2 values (where they exist), selected method used for gas-phase metallicity calculation and estimated values of 12 + $\log_{10}$[O/H]. 0 = O3N2 used (Equation 7.18), 1 = N2 used (Equation 7.20), 2 = mass-metallicity relation used (Equation 7.21)

GAMA ID	**O3N2**	**N2**	**Method**	**12 + $\log_{10}$[O/H]**
16026	-0.077	-0.406	0	8.755
63210	-0.240	-0.401	0	8.807
64087	-0.199	-0.390	0	8.794
78425	0.609	-0.524	0	8.535
79849	—	0.150	2	8.776
85416	-0.207	-0.387	0	8.796
99687	—	0.150	2	8.779
136847	—	0.505	2	8.776
215579	—	—	2	8.776
227264	—	-0.173	2	8.761
227266	—	—	2	8.770
227607	—	-0.056	2	8.778
252021	0.050	-0.367	0	8.714
263044	-0.274	-0.407	0	8.818
272990	—	-0.212	2	8.768
296638	—	0.018	2	8.754
		Continued		

Table 7.5 – Continued

GAMA ID	O3N2	N2	Method	12 + $\log_{10}$[O/H]
296934	0.004	-0.484	0	8.729
298980	-0.031	-0.425	0	8.740
323854	—	-0.029	2	8.778
324349	—	0.315	2	8.779
422436	—	0.878	2	8.778
463434	0.021	-0.350	0	8.723
509508	0.017	-0.435	0	8.724
514212	0.295	-0.475	0	8.636
546040	—	—	2	8.778
549251	—	—	2	8.778
560238	—	0.534	2	8.754
569555	0.198	-0.400	0	8.67
570227	—	0.295	2	8.774
601255	—	—	2	8.776
3576053	—	-0.074	2	8.711
3616590	—	-0.408	1	8.730

The metallicities in Table 7.5 were used to calculate estimates of α_{CO} using Equation 7.15, along with specific star formation estimates (0 - 100 Myr) from GAMA II MagPhysv06 to compare with the expectation from SFMS using Equation 7.16. Table 7.6 shows the estimated values of α_{CO} and the resultant molecular gas masses. Also shown are molecular gas mass estimates with a constant value of α_{CO} of 4.36 $M_\odot$ (K km s^{-1} $pc^2)^{-1}$), consistent with estimates for molecular gas clouds in the Milky Way Galaxy (Accurso et al. 2017). These latter values can be used as an alternative to the molecular gas mass estimates with variable α_{CO} to ensure that trends with stellar mass are not affected

by the use of stellar mass to estimate gas-phase metallicity.

Table 7.6: Estimated values of α_{CO} based on gas-phase metallicity, and molecular gas mass estimates from aperture-corrected ^{12}CO[1-0] line fluxes in Table 7.4. Molecular gas masses calculated using a constant value of α_{CO} of 4.36 $M_\odot$ (K km s^{-1} pc^2)$^{-1}$) are also shown.

GAMA ID	α_{CO}	**M$_{mol}$**	**Uncert.**	**M$_{mol}$**	**Uncert**
				Constant α_{CO}	
		10^9 M$_\odot$		**10^9 M$_\odot$**	
16026	3.49	2.52	0.38	3.14	0.48
63210	2.63	1.31	0.21	2.17	0.35
64087	3.04	2.63	0.35	3.78	0.50
78425	9.21	4.94	0.76	2.34	0.36
79849	2.97	2.94	0.31	4.31	0.46
85416	2.88	1.09	0.10	1.66	0.15
99687	2.92	1.81	0.35	2.69	0.52
136847	2.88	1.35	0.13	2.05	0.20
215579	3.04	1.75	0.48	2.51	0.70
227264	2.95	0.49	0.07	0.73	0.11
227266	2.27	0.39	0.09	0.75	0.18
227607	3.20	8.15	0.82	11.11	1.12
252021	3.93	1.06	0.14	1.17	0.16
263044	2.76	2.02	0.21	3.19	0.34
272990	3.02	2.26	0.23	3.26	0.34
296638	3.19	1.31	0.12	1.79	0.17
296934	3.92	3.98	0.40	4.43	0.45
298980	3.69	0.97	0.10	1.15	0.12
323854	3.04	1.76	0.28	2.52	0.40
		Continued			

Table 7.6 – Continued

GAMA ID	α_{CO}	M_{mol}	Uncert.	M_{mol} Constant α_{CO}	Uncert.
		10^9 $M_\odot$		10^9 $M_\odot$	
324349	3.01	2.51	0.37	3.64	0.53
422436	2.61	0.57	0.13	0.95	0.22
463434	3.94	4.14	0.54	4.58	0.60
509508	4.07	1.84	0.44	1.97	0.47
514212	5.73	0.84	0.10	0.64	0.08
546040	2.67	0.40	0.06	0.66	0.11
549251	2.49	—	—	—	—
560238	3.27	0.81	0.08	1.08	0.11
569555	5.08	4.56	0.58	3.92	0.50
570227	2.87	2.04	0.25	3.10	0.37
601255	2.88	1.09	0.21	1.65	0.32
3576053	2.95	4.20	0.44	6.21	0.64
3616590	3.97	2.24	0.35	2.47	0.39

7.5 Relationships Between Galaxy Properties and Molecular Gas Mass

In this Section, molecular gas mass is plotted against other galaxy properties to investigate whether trends for the Dusty ETGs observed for this work with the IRAM 30m telescope. Molecular gas masses and other properties derived for other surveys are used for comparison, described in Section 2.8.7. The xCOLD GASS survey provides a large

sample for primarily star-forming galaxies, to show the overall range of properties varying with molecular gas mass. A survey by Davis et al. (2015) observed CO emission from more massive ETGs with prominent dust lanes (referred to as Dust-Lane ETGs) as evidence of significant recent minor merger activity. As a contrast to this, the CO-CAVITY survey of molecular gas in void galaxies observed lower-mass galaxies in very sparse environments which should have avoided significant interactions and mergers, referred to as Void galaxies. All of these surveys were undertaken using the IRAM 30m telescope and instrumentation described in this work, with similar observing strategies.

The analyses presented below use linear trendlines fitted to logarithms of data to highlight differences in behaviour of galaxy populations. These were obtained using SCIPY.OPTIMIZE.CURVE_FIT. Uncertainties in fitted parameters were mostly derived without using the errors on dependent variables and relying only on the scatter of the data points, because these were found by experiment to return larger (and therefore more conservative) estimates of uncertainty. Otherwise, the quoted fitting results make use of these errors where stated.

Molecular gas masses were re-calculated for the Dust-Lane and CO-CAVITY observations using the published line fluxes in Jy km s^{-1} and either metallicity-dependent α_{CO} using the mass-metallicity relation in Section 7.4.4 (Equation 7.21) or a fixed α_{CO} at an accepted value for the Milky Way Galaxy ($4.36\,M_{\odot}$ (K km s^{-1} $pc^2)^{-1}$). Molecular gas masses from xCOLD GASS with metallicity-dependent α_{CO} were already calculated using these methods (Accurso et al. 2017), and alternative molecular gas masses were calculated using published line fluxes and constant α_{CO}. The aim of using both metallicity-dependent and constant α_{CO} was to ensure that the use of stellar mass both to estimate gas-phase metallicity and molecular gas mass, and as a galaxy property for comparison with molecular gas mass, does not lead to a circular argument and false trends. Stellar masses and SFRs for the surveys presented in this work are derived using MAGPHYS and photometry

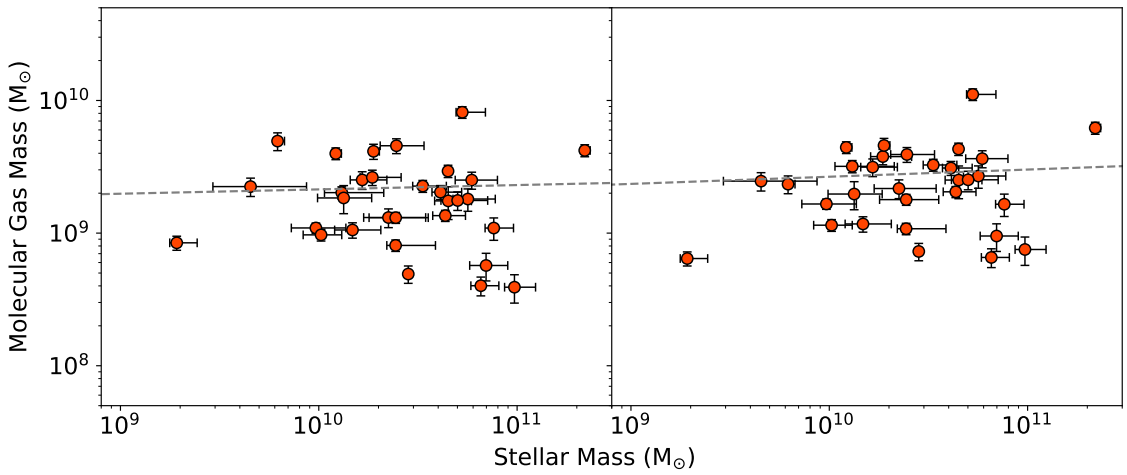

Figure 7.12: Molecular gas mass versus stellar mass for the Dusty ETGs. *Left*: Variable α_{CO}, *Right*: Fixed α_{CO}.

over multiple passbands for Dusty ETGs observed for this work and the Dust-Lane galaxies. Otherwise, they were derived from SDSS spectra and included in the MPA-JHU[7] data release relevant to the survey in question. Published line fluxes for xCOLD GASS and Void galaxies have been aperture corrected (Section 7.4.3) using various techniques, but line fluxes for Dust-Lane galaxies have not so their estimated molecular gas masses may be ~10-40% below actual values based on typical aperture corrections in Section 7.4.3.

7.5.1 Molecular Gas Mass versus Stellar Mass

Figure 7.12 shows the molecular gas mass estimates versus stellar masses from GAMA II MagPhysv06 for the Dusty ETGs. For both methods of estimating α_{CO}, the trends appear flat. Slopes of fitted lines to logarithms of stellar mass and gas mass using scipy.optimize.curve_fit, shown in the Figure, are 0.03 ± 0.2 when variable α_{CO} is used, and 0.05 ± 0.15 with constant α_{CO}, both of which are consistent with flat trends.

[7]https://wwwmpa.mpa-garching.mpg.de/SDSS/

Table 7.7: Coefficients for the trend lines in Figure 7.13.

	All Data	Stellar Mass $<10^{10}$ $M_\odot$
Variable α_{CO}		
a	3.24 ± 0.32	2.61 ± 0.90
b	0.57 ± 0.03	0.62 ± 0.09
Constant α_{CO}		
a	1.23 ± 0.55	-2.63 ± 0.78
b	0.77 ± 0.03	1.16 ± 0.08

Figure 7.13 shows molecular gas mass estimates plotted against stellar mass estimates for the four surveys of interest, including this work, calculated using variable and fixed α_{CO} estimates. The plot with variable α_{CO} (Figure 7.13, left) shows a trend with significant scatter, while the plot with constant α_{CO} (Figure 7.13, right) shows a relatively tight trend at lower stellar masses ($<10^{10}$ $M_\odot$) and a spread from the trend to lower molecular gas masses above this stellar mass. The Figure shows trendlines fitted using SCIPY.OPTIMIZE.CURVE_FIT for all data in the plots, and all data with stellar masses $<10^{10}$ $M_\odot$, of the form $\log_{10}(M_{gas}, M_\odot) = a + b \log_{10}(M_{stellar}, M_\odot)$. Coefficients and uncertainties are shown in Table 7.7. The slopes of the trends for variable α_{CO} are comparable, so the trend at lower stellar mass extends into the higher stellar mass region. This is not the case for the plot with constant α_{CO}, where line slopes are distinct based on their uncertainties.

The use of metallicity-dependent α_{CO} in the left-hand plot in Figure 7.13 has increased the scatter at the low stellar mass region of the plot, and the scatter at the high stellar mass region persists in both plots. The additional scatter in the left-hand plot has been introduced by the metallicity dependence of α_{CO}, and highlights a scatter in gas-phase metallicity. Davis et al. (2015) highlight the effect of minor mergers in causing this type of scatter at higher stellar mass, which introduce random masses of molecular gas at lower metallicity from less massive galaxies, e.g. dwarfs. Rémy-Ruyer et al. (2014) highlight the influence of minor mergers and dust growth on gas-phase metallicity and GDR

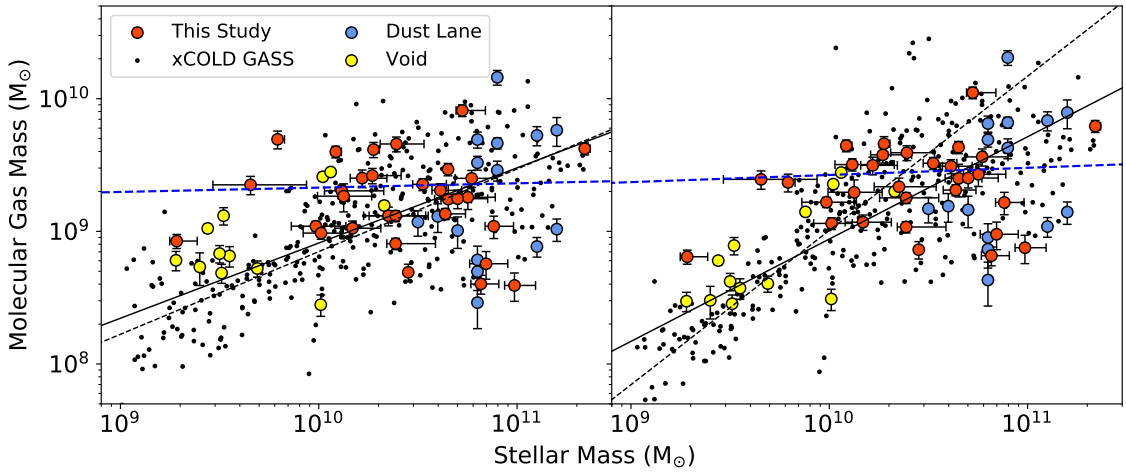

Figure 7.13: Molecular gas mass versus stellar mass for galaxies from this work and other surveys for comparison. *Left*: metallicity-dependent α_{CO} (Accurso et al. 2017), *right*: constant α_{CO} (Bolatto et al. 2013). Error bars are not shown for the xCOLD GASS data, but are comparable to those shown for the other surveys. Trendlines are shown for all galaxies plotted (solid line) and for galaxies with stellar mass $\leq 10^{10}$ $M_\odot$ (dashed line). The blue trendline is from Figure 7.12 for observed Dusty ETGs only.

in addition to minor mergers, by transferring metals from the gas phase to the solid phase. This effects could also introduce scatter in metallicity and α_{CO} at a given stellar mass. A downward spread of molecular gas masses at higher stellar mass can also be expected due to evolution of galaxies across the GV towards passivity (Section 1.2.2), with molecular gas reservoirs declining.

Irrespective of whether α_{CO} is fixed or variable, the Dusty ETGs follow a different trend to a more general population of primarily star-forming galaxies. They have increased molecular gas contents at lower stellar mass, and reduced contents at higher stellar mass. Given that interactions and minor mergers are known to be a mechanism for transfer of ISM and evolution of LTGs into ETGs (see discussions in Chapter 2), it is possible that this trend shows the deposition of proportionally more new molecular gas into the Dusty ETGs with lower stellar mass. This effect would occur if the same population of smaller, dusty and gas-rich galaxies are responsible for interactions and minor mergers across the mass range, which add proportionally more fresh ISM to the lower mass Dusty ETGs than the higher-mass ones. Such encounters can cause LTG-like morphology to be lost, by disturbing spiral structure to at least some extent. The Dust-Lane ETGs, selected specifically because of evidence of recent minor merger activity, have a similar scatter on the plots to the higher-mass Dusty ETGs, so it is possible that some of the Dusty ETGs with higher stellar mass have experienced similar recent minor mergers. At present there is no information to examine the properties of potential progenitor galaxies involved in mergers with the Dusty ETGs.

The Void galaxies follow the general trend for galaxies with lower stellar mass in both plots, suggesting that galaxies with lower stellar mass can contain expected levels of molecular gas without recent interactions or mergers. The few Dusty ETGs in this region of the plots appear to have increased molecular gas masses in comparison.

Table 7.8: Coefficients for the trend lines in Figure 7.14.

	Dusty ETGs	Dust-Lane ETGs
Variable α_{CO}		
a	2.00 ± 1.38	3.33 ± 1.61
b	0.57 ± 0.15	0.46 ± 0.17
Constant α_{CO}		
a	0.68 ± 1.42	3.32 ± 1.67
b	0.71 ± 0.15	0.46 ± 0.18

7.5.2 Dust Mass versus Molecular Gas Mass

Figure 7.14 shows plots of molecular gas mass versus dust masses for Dust-Lane ETGs estimated using MAGPHYS (Kaviraj et al. 2012; Davis et al. 2015) and the Dusty ETGs from GAMA II MAGPHYS results for compatibility. No dust masses are readily available for xCOLD GASS galaxies, and molecular gas masses for JINGLE galaxies are not yet available. The left-hand plot uses molecular gas masses based on metallicity-dependent α_{CO} estimates, while the right-hand plot uses molecular gas masses based on constant α_{CO}. Trend lines are shown for the Dust-Lane and Dusty ETGs separately, for both metallicity-dependent and constant α_{CO}, of the form $\log_{10}(M_{dust}, M_{\odot}) = a + b \log_{10}(M_{gas}, M_{\odot})$. Coefficients and uncertainties are shown in Table 7.8. Molecular gas mass and dust mass could be expected to be linked, because both are related to galaxy metallicity which in turn is known to generally increase with stellar mass (Equation 7.21). With more metals present overall in a galaxy, more gas and dust can both be expected. This also gives rise to increasing molecular gas mass and dust mass with increasing stellar mass, as shown elsewhere within this work.

Two trends are apparent in both plots, and comparison of the two plots indicates that the use of α_{CO} calculated from metallicity based on stellar mass is not influencing the apparent trends. The Dusty ETGs mostly form a trend following the fitted lines,

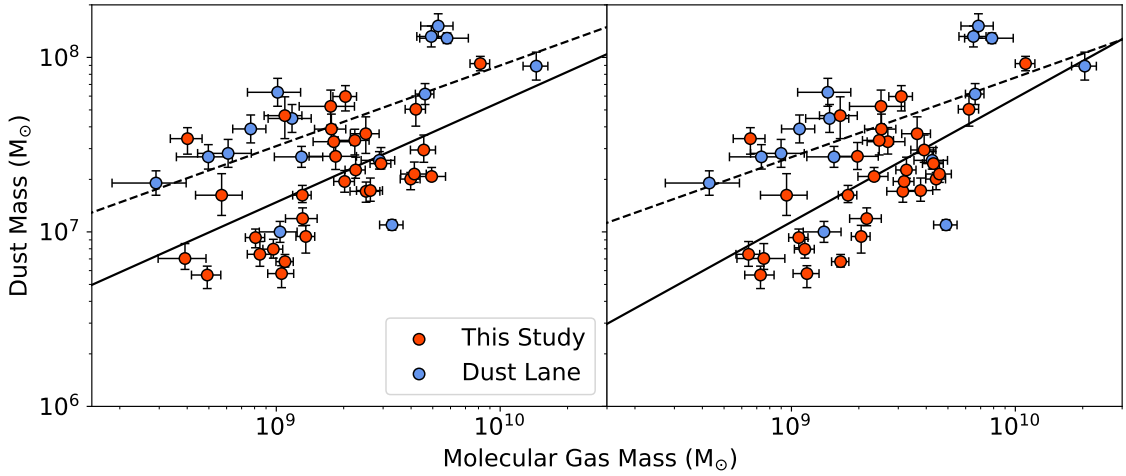

Figure 7.14: Dust mass versus molecular gas mass for galaxies from this work and Davis et al. (2015). Trend lines are fitted to the Dusty ETGs (solid) and the Dust-Lane ETGs (dashed). The left-hand plot is based on metallicity-dependent α_{CO}, while the plot on the right is based on constant α_{CO}.

with some drift upwards mostly at higher stellar mass. The Dust-Lane galaxies, selected because they appear to have undergone significant recent minor mergers, appear form a separate trend at higher dust mass which approaches that of the Dusty ETGs at higher molecular gas mass. However, the uncertainties on the slopes of the fitted lines indicate that they could be similar. A difference in slope might be explained if Dusty ETGs with lower molecular gas masses have not undergone significant merger events leading to the acquisition of significant quantities of additional dust, unlike the Dust-Lane ETGs of similar mass. At higher molecular gas masses, both set of ETGs could have acquired similar levels of dust through interactions.

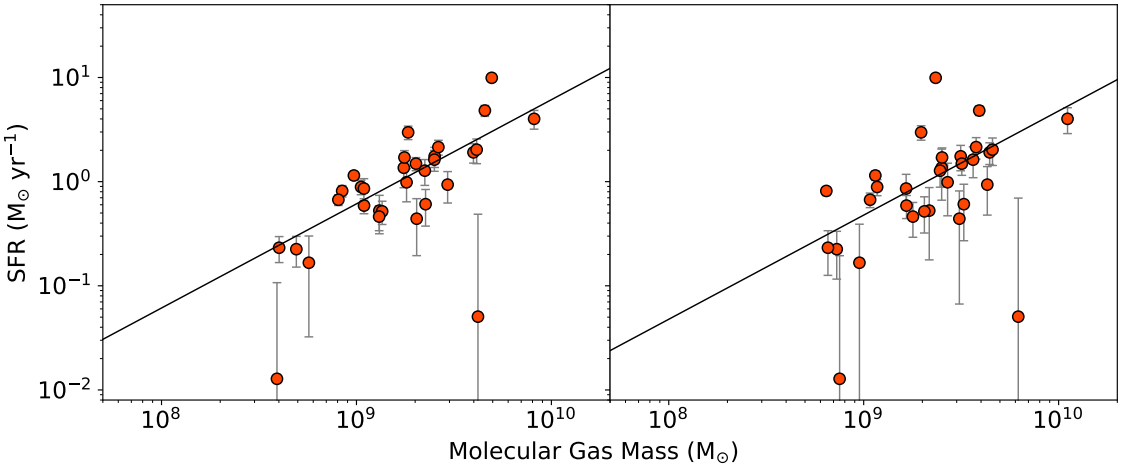

Figure 7.15: SFR versus molecular gas mass for the Dusty ETGs. The left-hand plot is based on metallicity-dependent α_{CO}, while the plot on the right is based on constant α_{CO}.

7.5.3 Star Formation and Molecular Gas Content

Figure 7.15 shows the relation between SFR and molecular gas mass for the Dusty ETGs, with metallicity-dependent and constant α_{CO}. Trends are apparent, with fitted linear equations (excluding the two low-SFR outliers GAMA227266 and 3576053) for logarithmic SFR ($M_\odot$ yr^{-1}) of (-9.92 ± 1.30) + (1.08 ± 0.14) $\log_{10}(M_{gas}, M_\odot)$ for metallicity-dependent α_{CO}, and (-8.20 ± 1.97) + (0.88 ± 0.21) $\log_{10}(M_{gas}, M_\odot)$ for constant α_{CO}. The slopes of the trendlines are consistent with unity as expected if star formation is directly linked to molecular gas mass, i.e. star formation from molecular gas is equally as challenging across the mass range for the Dusty ETGs. Linear trends can also be discussed in terms of a constant star formation efficiency, which is the ratio of SFR to molecular gas mass. The two Dusty ETGs significantly below the line have substantially reduced SFE. One possible cause of this is bulk gas motion post-minor merger which stabilises molecular gas against star formation (van de Voort et al. 2018).

Figure 7.16 shows the relation between SFR and molecular gas mass for the Dusty

ETGs, the xCOLD GASS sample, the Dust-Lane ETGs and the Void galaxies on the same plots. An immediately apparent feature of this plot is the scatter of the Dust-Lane ETGs away from the general trend dominated by xCOLD GASS galaxies. Davis et al. (2015) and van de Voort et al. (2018) discuss these low SFRs in terms of disturbance and bulk flows of molecular gas following minor mergers, which has yet to stabilise and allow molecular gas to form stars. Apart from the two exceptions discussed above, the Dusty ETGs do not exhibit the same behaviour. Trendlines for logarithmic SFR ($M_\odot$ yr^{-1}) versus logarithmic molecular gas mass ($M_\odot$) for xCOLD GASS galaxies, Void galaxies and Dusty ETGs combined are (-7.92 ± 0.35) + (0.87 ± 0.04) $\log_{10}(M_{gas})$ for metallicity-dependent α_{CO}, and (-6.4 ± 0.3) + (0.7 ± 0.03) $\log_{10}(M_{gas})$ for constant α_{CO}. Figure 7.15 indicates that the Dusty ETGs may have reduced SFR at low molecular gas mass compared to the overall trend. The Void galaxies generally have similar SFR to the general trend, as expected if conditions for star formation are in line with the majority of the galaxies plotted.

7.5.4 Gas-to-Dust Ratio versus Stellar Mass

GDR is useful as an indicator of processes taking place within a galaxy as it evolves. A roughly constant GDR with increasing stellar mass indicates that the ISM content is influenced more by secular (internal) process, whereas large scatter in GDR could indicate external processes at work. Higher values of GDR indicate processes that destroy dust (e.g. supernovae) or an absence of mechanisms that create new dust (e.g. carbon stars) are at work, while low values could indicate deposition of dust in favour of molecular gas or more effective transfer of metals from the gas phase into new dust. Based on simulations, particularly high GDR compared to star-forming galaxies might be expected in quiescent galaxies due to dust destruction and no effective means of replenishing it (Whitaker et al. 2021).

Figure 7.17 shows how the GDR (based on dust mass estimates from MAGPHYS

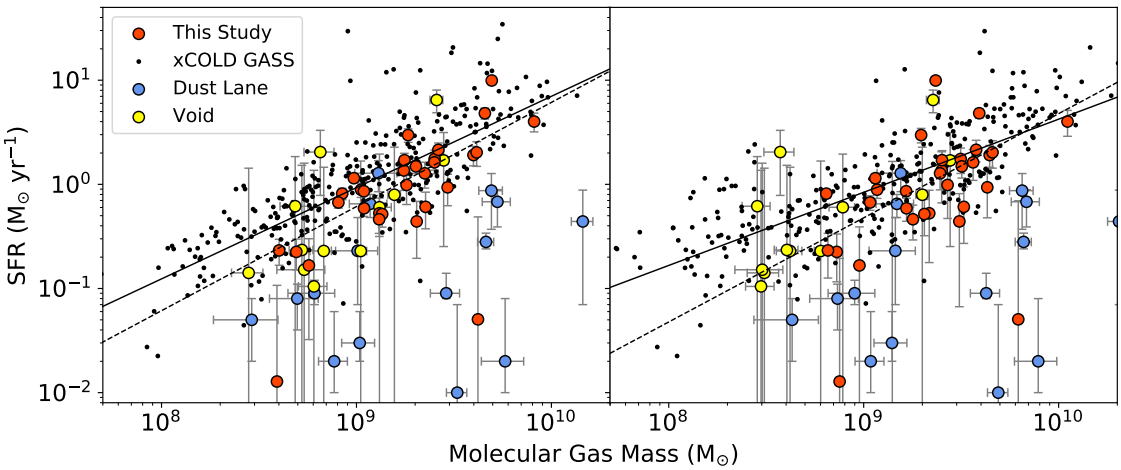

Figure 7.16: SFR versus molecular gas mass for galaxies from xCOLD GASS, Dusty ETGs observed for this work, Dust-Lane ETGs and Void Galaxies. The left-hand plot is based on metallicity-dependent α_{CO}, while the plot on the right is based on constant α_{CO}. The solid trend line is for xCOLD GASS, Void galaxies and Dusty ETGs, while the dotted lines are for Dusty ETGs only.

Table 7.9: GDR properties for Dusty ETGs observed for this work, binned above and below a stellar mass of 3×10^{10} $M_{\odot}$.

Stellar Mass	GDR Mean	GDR Standard Deviation	GDR Error on Mean
Variable α_{CO}			
$\leq 3 \times 10^{10}$ $M_{\odot}$	133	51	12
$>3 \times 10^{10}$ $M_{\odot}$	64	39	10
Constant α_{CO}			
$\leq 3 \times 10^{10}$ $M_{\odot}$	154	55	13
$>3 \times 10^{10}$ $M_{\odot}$	96	56	15

throughout) for the Dusty ETGs and the Dust-Lane ETGs vary with stellar mass, for metallicity-dependent and constant α_{CO}. Only the Dusty ETG on the far left of the plot (GAMA514212) may be affected by under-estimation of dust mass due to lack of sub-mm photometry at wavelengths longer than 500 μm (see Section 6.4.3).The plot using metallicity-dependent α_{CO} for Dusty ETGs appears to show a downward (albeit scattered) trend in GDR with increasing stellar mass, consistent with the trend in α_{CO} and metallicity with increasing stellar mass. Table 7.9 shows the mean, standard deviation and error on the mean for GDR in Dusty ETGs observed for this work, above and below a stellar mass of 3×10^{10} $M_{\odot}$ where the downward trend appears to begin in Figure 7.17. Mean GDR values above the threshold are lower than those below, which provides supporting evidence for a trend downwards at higher stellar mass. The results suggest that Dusty ETGs could be subject to different evolutionary processes at lower and higher stellar mass, causing this variation. Also of interest in the plots is an apparent "zone of avoidance" at lower stellar mass (below $\sim 3 \times 10^{10}$ $M_{\odot}$), where lower GDR (e.g. below ~40) does not appear to occur in Dusty ETGs with lower stellar mass.

The two Dusty ETG with the highest stellar mass, which appear to be more associated with the Dust-Lane ETGs within the plots, are confirmed as GAMA227266 and

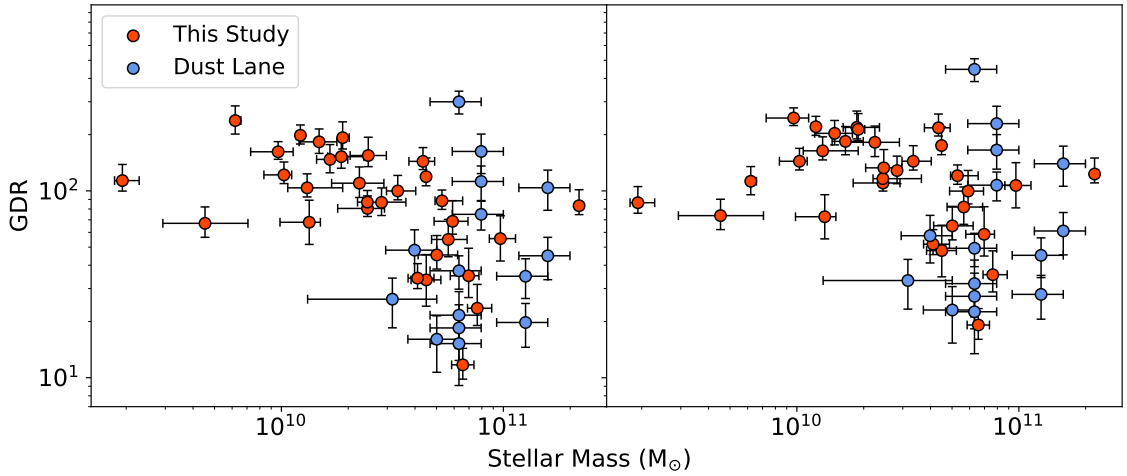

Figure 7.17: Molecular gas to dust mass ratio (GDR) versus stellar mass for Dusty ETGs and Dust-Lane ETGs *left*: metallicity-dependent α_{CO}, *Right*: fixed α_{CO}

GAMA3576053 which were identified earlier as having reduced SFR (Section 7.5.3). It is possible that the Dusty ETGs at lower stellar mass have either undergone a different evolutionary pathway to the Dust-Lane ETGs which does not involve acquisition of new ISM, or less molecular gas and dust have been introduced following an interaction or merger compared to the Dust-Lane ETGs. This would leave the existing ISM from secular evolution as dominant, with similar masses and ratios across the sample. However, it must be remembered that the selection of Dusty ETGs for observation with the IRAM 30m telescope for this study is flux-limited (Figure 7.5), and lower-mass ETGs with less ISM content may be under-represented in this analysis. At higher stellar mass, the Dusty ETGs appear to be richer in dust which reduces their GDR, and may have acquired this externally e.g. by merger, leading to an alignment with the dustier Dust-Lane ETGs.

7.6 Discussion of Chapter

The molecular gas masses derived for the Dusty ETGs (31 detections of ^{12}CO[1-0] emission) as a function of stellar mass appear to be broadly consistent with those from the previous observational studies conducted with the IRAM 30m telescope used for comparison. Aperture correction using high-resolution u-band images from the KiDS survey also appears to have been successful, and has yielded realistic corrections to observed line fluxes to account for possible CO emission beyond the telescope beam footprint.

The actual molecular gas masses quoted in this work are not to be taken as definitive, because of the significant uncertainties in the conversion factors from line flux to gas mass used and in the uncertainties in gas-phase metallicity estimates. However, the derived molecular gas masses can be used to examine relative changes in behaviour with variation in other galaxy properties. It is recommended that future work makes use of the aperture-corrected line fluxes in Table 7.4 and values for α_{CO} that represent best practice at the time.

In common with cool dust mass and SFR, molecular gas mass in the Dusty ETGs show a scaling behaviour at low stellar mass extending to higher stellar mass, with galaxies falling away from the low-mass trend at higher stellar mass (Figure 7.13). This behaviour indicates a multivariate relation between molecular gas mass, dust mass and SFR. The relationships between SFR and molecular gas mass (Section 7.5.3) and with dust mass (Section 6.14), reinforce this, although some galaxies can be seen to have reduced SFR compared to the trends.

At lower stellar mass, the evolutionary status of Dusty ETGs appears to be different to that of the Dust-Lane ETGs which have reduced SFR and more scattered GDR. Davis et al. (2015) and van de Voort et al. (2018) discuss the evolution of Dust-Lane ETGs in terms of minor mergers with smaller gas-rich galaxies, with the ISM still showing signs of flow and still settling into a stable configuration. The molecular gas is then not stable enough to allow star formation, and the introduction of quantities of new ISM with

different masses and compositions into each Dust-Lane ETG could explain the scatter in GDR. On the other hand, the evolutionary status of the Dusty ETGs at lower stellar mass appears to be different. The evolution of the Dusty ETGs appears to have involved the acquisition of lesser quantities of new molecular gas via interaction rather than merger, or just re-alignment of existing molecular gas by interaction, to explain the reduced scatter of GDR. This would also cause visual LTG morphology to be lost. The levels of SFR in most of the Dusty ETGs can be explained if the disturbance of the ISM has largely dissipated, leaving the ISM stable enough for star formation to occur. The two outlier Dusty ETGs, GAMA227266 and GAMA3576053, align more with the Dust-Lane ETGs in terms of GDR and SFR, and therefore are likely to be in a similar state to the Dust-Lane ETGs having undergone a minor merger. The overall finding that Dusty ETGs from a clean and complete sample are generally not undergoing evolution from LTGs in less dense environments as a result of more disruptive minor mergers except at higher stellar mass is significant, and can be used to verify the results of simulations.

Chapter 8

Discussion and Conclusions

8.1 Overall Findings

This work set out to address a number of research topics highlighted in Section 1.3, using a variety of data and techniques based on observations of Dusty ETGs in less dense environments in the local Universe, stated in Section 1.3. All of the research topics have been addressed, using a variety of methods for observation, data reduction and analysis within Chapters 3 - 7.

ALMA observations of cool molecular gas distribution in four Dusty ETGs (Chapter 3) show that two have molecular gas aligned with the stellar disc in ring-like structures, with a tidal stellar tail and a distorted stellar disc as evidence of gravitational interaction and subsequent settlement and re-alignment of ISM. A third, GAMA272990, has undergone an interaction which could be gravitational or a minor merger. The remaining dusy ETG, with a strong AGN, has undergone a minor merger and has molecular gas concentrated at the centre.

IRAM 30m Telescope observations of cool molecular gas in Dusty ETGs (Chapter 7) show that GDRs, while having a degree of scatter with stellar mass, are higher and

less scattered at stellar masses below $10^{10.5}$ $M_{\odot}$ than above (Figure 7.17). An incomplete sample of Dust-Lane ETGs which appear to have undergone recent minor mergers (Davis et al. 2015) are included in the Figure also at higher stellar mass. They also show a significant scatter of GDR consistent with addition of random masses of new ISM (e.g. Smith et al. 2012). Taken together, these findings indicate that interactions or minor mergers which do not alter ISM mass significantly are more relevant for Dusty ETG formation at lower stellar masses, while minor mergers which add various quantities of ISM to Dusty ETGs are more significant at higher stellar masses.

All but two of the Dusty ETGs observed with the IRAM 30m Telescope (Section 7.3) have similar estimated rates of star formation to LTGs and some ETGs in the xCOLD GASS galaxy sample (Figure 7.16). The remaining two observed Dusty ETGs have suppressed star formation relative to their molecular gas content, similar to findings for the Dust-Lane ETGs (Davis et al. 2015). The results indicate that most of the Dusty ETGs underwent their transformation sufficiently long ago for the ISM to settle into a stable configuration, allowing star formation to recommence. This is not the case for the Dust-Lane ETGs, where ISM is still largely stable against star formation. This finding is supported by the analysis of the ALMA observations of Dusty ETGs in Chapter 3, which show molecular gas configurations stable enough for star formation after tranformation to ETG visual morphology.

Results from the fitting of SMBB cool dust emission model to galaxies with appropriate H-ATLAS sub-mm photometry highlighted the importance of quantifying dust emission at wavelengths longer than 500 μm, i.e. beyond the wavelengths of passbands available from Herschel, for galaxies with stellar mass below $\sim 10^{9.5}$ $M_{\odot}$ or dust masses below $\sim 10^{6.5}$ $M_{\odot}$. Failure to do so means that dust masses from SMBB fitting could be under-estimated (Figure 6.8), and are then lower limits only. Above a stellar mass of $10^{9.5}$ $M_{\odot}$, the work showed no discernible difference between SMBB dust temperatures and emissivity coefficients (β) within visually-classified LTGs and Dusty ETGs . This similarity could arise because the dust is relatively undisturbed during the transition from LTG

to dusty ETG, or dust with similar properties (e.g. from a smaller star-forming galaxy) has been introduced as a result of gravitational interaction or minor merger. Both of these mechanisms are consistent with the evolutionary pathways discussed above, found by examining molecular gas in ETGs.

The work presented above also highlighted power-law relations between molecular gas mass, cool dust mass, stellar mass and star formation rate, which would be expected if these properties are linked (Figures 7.14, 6.8, 7.15 and 6.14). Further analysis of these trends, e.g. to explore which is the dominant driver of galaxy evolution to form ETGs, is left for future research.

The clean and complete, morphologically-classified samples of galaxies for the GAMA equatorial regions developed in Chapter 4 will be made available to the astrophysics community. The ETG sample derived from this was used to select Dusty ETGs for observation by the IRAM 30m telescope. The Parent Sample and morphologically classified samples were used to investigate whether galaxy properties exhibit continuum behaviour or are bimodal, as predicted by Eales et al. (2017). Bimodality is mostly apparent in the parameter spaces explored, due to physical limits on property values at two extremes. For some cases, namely r-band Sérsic index, specific star formation rate and r-band bulge/total mass ratio from two-component surface brightness model fitting, a physical limit exists at one extreme (n $\sim$1 for disc-like morphology) when plotted against stellar mass but the data then extend smoothly through the parameter space (Figures 5.4, 5.8 and 5.10). This finding provides evidence of continuum behaviour within certain parameter spaces for a large, clean and complete sample.

Classification of galaxies by visual morphology has achieved an effective separation of LTGs and ETGs, while preserving the classification as ETGs of dusty, star-forming examples (Chapter 5). Arising from this classification is a class of compact, star-forming galaxies with ETG-like visual morphology and at the low end of stellar mass range (labelled “ETG Misfits” in this work). The ETG Misfits sit between the properties of ETGs and LBS galaxies (Figures 5.3, 5.5, 5.7, 5.9 and 5.20). Understanding their evolutionary

history could be of interest in understanding how low mass galaxies develop into more massive galaxies, because the ETG Misfits could represent an intermediate step.

8.2 Future Work

Opportunities for further work to understand the behaviour of ISM in dusty ETGs are discussed below. These are presented as short-term projects, which could be carried out as soon as new data becomes available, and longer-term projects which require more planning.

8.2.1 Short-Term Projects

In the short term, the JINGLE project (Section 2.8.5) intends to deliver molecular gas masses as well as dust masses discussed in Section 6.4.3, obtained using the JCMT (Section 2.5). Once available, these additional molecular gas masses can be used alongside xCOLD-GASS results for comparison with results for the Dusty ETGs, in particular to expand the GDR data plotted in Figure 7.17. Results from other surveys of dust and molecular gas in the local Universe may also be introduced into the work. Results from the Herschel Reference Survey, the ATLAS3D survey and DustPedia (Section 2.8.7) are also candidates for inclusion alongside JINGLE and xCOLD GASS. There are also datasets available via GAMA DR4 (Section 2.8.1), with new parameters which could be used to further investigate continuum behaviour with galaxy evolution across the Parent Sample (Chapter 5).

It is possible that previous observations of dusty ETGs are available within the ALMA database[1], which could be analysed using the tools and techniques demonstrated in Chapter 3. Such analyses could extend the sample size from the five ETGs considered

[1] http://almascience.org

in this work, and test the conclusions drawn.

The power-law relations found in this work between stellar mass, SFR, dust mass and molecular gas mass for galaxies in the local Universe (Figures 6.8, 6.14, 7.14 and 7.15) can be explored in more detail, using better techniques for multivariate model fitting and more data. It is possible to test for overall relations in properties for all galaxies or subsets of morphological classifications, to explore the linkages between the properties and indicate which variable if any dominates galaxy evolution.

The GAMA-KiDS-GalaxyZoo catalogue provided for this work is preliminary, and at some point a final version will be produced. In addition to the voting categories used to classify galaxies from the Parent Sample morphologically (Figure 4.9), the catalogue also contains vote information for additional questions relating to detailed features such as bulge prominence and features such as dust lanes, mergers, rings and lenses. This information could be used to explore the evolution of ETGs from the Parent Sample in more detail, e.g. to explore the effect of stellar mass on the fractional occurrence of different features.

It may be possible to reverse-engineer data within GAMA II MagPhysv06 to recover warm and cold dust masses, by fitting the SMBB model (Equation 6.1) to the published dust temperatures and luminosities for warm and cold dust separately. If successful, the results would allow a better understanding of the differences in dust contents between galaxy morphologies and at different stellar and dust masses. Section 5.2 also discusses the possible reasons for the weak clustering of galaxies at low sSFR witin the sSFR-stellar mass plane. It is possible that UV light from evolved stars is misinterpreted as low-level star formation when fitting photometry from quiescent galaxies. SEDs which reflect this behaviour, with very low rates of star formation but light from evolved stars included, could be used within the library of spectra used by MAGPHYS to see if very low levels of star formation can be recovered by model fitting.

The “ETG Misfits” identified in Section 5.8, which are star-forming and have stellar

masses intermediate between ETGs and dwarf galaxies, are worthy of further study. They could be an intermediate step between these two populations of galaxies. For example, observational studies of their star formation histories, e.g. using optical spectroscopy, could highlight whether secular growth from gas accretion or growth via minor mergers are significant in their evolution. Further observations of their molecular gas content using the IRAM 30m telescope would also help to understand the origins of material needed for ongoing star formation.

8.2.2 Longer-Term Projects

Further opportunities for observations of Dusty ETGs would allow the findings presented above to be refined. Possible opportunities are discussed below.

Further observations with ALMA of the ^{12}CO[2-1] distribution within local Dusty ETGs would allow the conclusions presented above, i.e. Dusty ETGs formed largely from earlier disturbance or merger followed by settlement of ISM and resumed star formation, to be tested on a larger sample. Candidate targets can be drawn from the Dusty ETGs observed with the IRAM 30m Telescope (Section 7.4), because the presence of molecular gas for observation in many of these is confirmed. Of particular interest is GAMA227266, because of its unusual CO spectrum with all molecular gas at high positive or negative velocity (Figure 7.6). An ALMA observation would help to understand the nature of this emission. Also, GAMA3576053 is of interest because of its reduced SFR, which may be explained by asymmetry and other evidence of disturbance in its molecular gas distribution. However, resolved ALMA observations of continuum dust emission in Dusty ETGs are not feasible at present, because of long observation time requirements.

Additional observations of ^{12}CO[1-0] emission from Dusty ETGs using the IRAM 30m Telescope would also be of interest, to explore the parameter spaces discussed in Section 7.5 in more detail. Because of the high detection rate in the overall sample of 32 Dusty ETGs observed to date, a further selection for observation can be made using lower

predicted molecular gas masses (Section 7.2). In particular, The "zone of avoidance" at lower stellar masses for GDR apparent in Figure 7.17 can be explored further, along with the scatter of GDR at higher stellar mass.

Telescopes and detectors such as JCMT with SCUBA2, or the IRAM 30m telescope with NIKA-2, could provide photometry for continuum dust emission from LTGs and Dusty ETGs at wavelengths >500 μm. Such data, in conjunction with photometry from Herschel, would allow more more complex dust emission models to be fitted, such as those with two or more dust populations or a single population with a power-law change at a certain wavelength (Lamperti et al. 2019). A better comparison of dust properties between ETGs and LTGs could then be performed at lower stellar masses, and allow the issue of sub-mm excess emission in ETGs and galaxies with lower stellar mass to be explored in more detail.

It is acknowledged that the conversion factors used in this work to obtain dust masses from sub-mm photometry, and molecular gas masses from ^{12}CO[1-0] emission, are highly uncertain. Attempts by others have been made to simulate the formation and destruction of CO alongside molecular hydrogen in gas clouds (e.g. Gong et al. 2018; Keating et al. 2020) using detailed models of the chemistry, radiation effects (including shielding of molecular gas) and fluid dynamics involved, with some success claimed for the Milky Way environment. Such work needs to be extended to other galaxies, including Dusty ETGs. Additional modelling should also address dust formation and evolution, to understand how dust properties in LTGs and Dusty ETGs should differ. In both cases, comparisons of observational results with models for secular production and accumulation of these material should reveal practical details, in particular the role of mergers and interactions in introducing fresh ISM into a galaxy.

It is also possible to apply radiative transfer modelling to an ETG, to investigate whether the dust component of the ISM is in equilibrium with the prevailing radiation field. If not, the dust is likely to have been introduced relatively recently and could be from an external source. The approach to take would be similar to that applied recently to

M33 (Thirlwall et al. 2020). Multi-passband photometry is required for this, with as high a resolution as possible. In addition, a map of dust distribution is required. This work has indicated that there is an association between molecular gas and cool dust in the Dusty ETGs (see Figure 7.14), so a high-resolution map of 12CO[2-1] emission from ALMA would serve as a proxy for dust distribution. Candidates for such a study include the ALMA-observed ETGs from this work, specifically GAMA64646 and GAMA272990.

Bibliography

2010, AKARI/FIS All-Sky Survey Bright Source Catalogue Version 1.0 Release Note, https://lambda.gsfc.nasa.gov/data/foregrounds/akari/AKARI-FIS_BSC_V1_RN.pdf, accessed 22/3/22

Accurso, G., Saintonge, A., Catinella, B., et al. 2017, *MNRAS*, 470, 4750

Agius, N. K., di Serego Alighieri, S., Viaene, S., et al. 2015, *MNRAS*, 451, 3815

Agius, N. K., Sansom, A. E., Popescu, C. C., et al. 2013, *MNRAS*, 431, 1929

Agostino, C. J., Salim, S., Boquien, M., et al. 2023, *MNRAS*, 526, 4455

Alatalo, K., Davis, T. A., Bureau, M., et al. 2013, *MNRAS*, 432, 1796

Antonucci, R. 1993, *ARA&A*, 31, 473

Athanassoula, E. 1992a, *MNRAS*, 259, 328

Athanassoula, E. 1992b, *MNRAS*, 259, 345

Baars, J. W., Greve, A., Hein, H., et al. 1994, *Proc. IEEE*, 82, 687

Baldry, I. K., Glazebrook, K., Brinkmann, J., et al. 2004, *ApJ*, 600, 681

Baldry, I. K., Liske, J., Brown, M. J. I., et al. 2018, *MNRAS*, 474, 3875

Baldwin, J. A., Phillips, M. M., & Terlevich, R. 1981, *PASP*, 93, 5

Balm, P. 2012, in Astronomical Society of the Pacific Conference Series, Vol. 461, Astronomical Data Analysis Software and Systems XXI, ed. P. Ballester, D. Egret, & N. P. F. Lorente, 733

Barnard, J., McCulloch, R., & Meng, X.-L. 2000, *Statistica Sinica*, 10, 1281

Becker, R. H., White, R. L., & Helfand, D. J. 1994, in Astronomical Society of the Pacific Conference Series, Vol. 61, Astronomical Data Analysis Software and Systems III, ed. D. R. Crabtree, R. J. Hanisch, & J. Barnes, 165

Bell, E. F., Wolf, C., Meisenheimer, K., et al. 2004, *ApJ*, 608, 752

Bellstedt, S., Robotham, A. S. G., Driver, S. P., et al. 2021, *MNRAS*, 503, 3309

Bertin, E. & Arnouts, S. 1996, *A&AS*, 117, 393

Best, P. N., Kauffmann, G., Heckman, T. M., & Ivezić, Ž. 2005, *MNRAS*, 362, 9

Betancourt, M. J. & Girolami, M. 2013, arXiv e-prints, arXiv:1312.0906

Bialas, D., Lisker, T., Olczak, C., Spurzem, R., & Kotulla, R. 2015, *A&A*, 576, A103

Bian, F., Kewley, L. J., & Dopita, M. A. 2018, *ApJ*, 859, 175

Boardman, N., Zasowski, G., Seth, A., et al. 2020, *MNRAS*, 491, 3672

Boizelle, B. D., Barth, A. J., Darling, J., et al. 2017, *ApJ*, 845, 170

Bolatto, A. D., Leroy, A. K., Rosolowsky, E., Walter, F., & Blitz, L. 2008, *ApJ*, 686, 948

Bolatto, A. D., Wolfire, M., & Leroy, A. K. 2013, *ARA&A*, 51, 207

Boselli, A., Cortese, L., & Boquien, M. 2014, *A&A*, 564, A65

Boselli, A., Eales, S., Cortese, L., et al. 2010, *PASP*, 122, 261

Bregman, J. N., Hogg, D. E., & Roberts, M. S. 1992, *ApJ*, 387, 484

Brinchmann, J. & Ellis, R. S. 2000, *ApJL*, 536, L77

Bruzual, G. & Charlot, S. 2003, *MNRAS*, 344, 1000

Bryant, J. J., Croom, S. M., van de Sande, J., et al. 2019, *MNRAS*, 483, 458

Buckle, J. V., Hills, R. E., Smith, H., et al. 2009, *MNRAS*, 399, 1026

Buta, R. & Combes, F. 1996, *Fundam. Cosmic Phys.*, 17, 95

Buta, R. J. 2017, *MNRAS*, 471, 4027

Calura, F., Pozzi, F., Cresci, G., et al. 2017, *MNRAS*, 465, 54

Capaccioli, M., Mancini, D., & Sedmak, G. 2005, *The Messenger*, 120, 10

Cappellarao, E. 2005, *The Messenger*, 120, 13

Cappellari, M., Emsellem, E., Krajnović, D., et al. 2011, *MNRAS*, 413, 813

Carter, M., Lazareff, B., Maier, D., et al. 2012, *A&A*, 538, A89

Casella, G. & George, E. I. 1992, *The American Statistician*, 46, 167

Casura, S., Liske, J., Robotham, A. S. G., et al. 2022, *MNRAS*, 516, 942

Cavanagh, M. K. & Bekki, K. 2020, *A&A*, 641, A77

Chabrier, G. 2003, *ApJL*, 586, L133

Charlot, S. & Fall, S. M. 2000, *ApJ*, 539, 718

Cid Fernandes, R., Stasińska, G., Mateus, A., & Vale Asari, N. 2011, *MNRAS*, 413, 1687

Cid Fernandes, R., Stasińska, G., Schlickmann, M. S., et al. 2010, *MNRAS*, 403, 1036

Cimatti, A., Fraternali, F., & Nipoti, C. 2019, Introduction to Galaxy Formation and Evolution: From Primordial Gas to Present-Day Galaxies (Cambridge University Press)

Clark, C. J. R., Roman-Duval, J. C., Gordon, K. D., et al. 2023, *ApJ*, 946, 42

Clark, C. J. R., Schofield, S. P., Gomez, H. L., & Davies, J. I. 2016, *MNRAS*, 459, 1646

Cluver, M. E., Jarrett, T. H., Hopkins, A. M., et al. 2014, *ApJ*, 782, 90

Comerón, S., Salo, H., Laurikainen, E., et al. 2014, *A&A*, 562, A121

Condon, J. J. 1992, *ARA&A*, 30, 575

Condon, J. J. & Ransom, S. M. 2015, Essential Radio Astronomy, https://www.cv.nrao.edu/~sransom/web/xxx.html, accessed 05-10-2023

Cortes, P. C., Vlahakis, C., Hales, A., et al. 2023, ALMA Technical Handbook, Tech. Rep. ALMA Doc. 10.3, ver. 1.0, ESO

Cortese, L., Ciesla, L., Boselli, A., et al. 2012, *A&A*, 540, A52

Cowie, L. L., Songaila, A., Hu, E. M., & Cohen, J. G. 1996, *AJ*, 112, 839

Croom, S. M., Lawrence, J. S., Bland-Hawthorn, J., et al. 2012, *MNRAS*, 421, 872

Croom, S. M., Owers, M. S., Scott, N., et al. 2021a, *MNRAS*

Croom, S. M., Taranu, D. S., van de Sande, J., et al. 2021b, *MNRAS*, 505, 2247

da Cunha, E., Charlot, S., & Elbaz, D. 2008, *MNRAS*, 388, 1595

Daddi, E., Dickinson, M., Morrison, G., et al. 2007, *ApJ*, 670, 156

Dame, T. M. 2011, arXiv e-prints, arXiv:1101.1499

Darvish, B., Mobasher, B., Sobral, D., et al. 2016, *ApJ*, 825, 113

Davies, J. I., Bianchi, S., Cortese, L., et al. 2012, *MNRAS*, 419, 3505

Davies, L. J. M., Driver, S. P., Robotham, A. S. G., et al. 2016, *MNRAS*, 461, 458

Davis, T. A., Alatalo, K., Bureau, M., et al. 2013, *MNRAS*, 429, 534

Davis, T. A., Alatalo, K., Sarzi, M., et al. 2011, *MNRAS*, 417, 882

Davis, T. A., Nguyen, D. D., Seth, A. C., et al. 2020, *MNRAS*, 496, 4061

Davis, T. A., Rowlands, K., Allison, J. R., et al. 2015, *MNRAS*, 449, 3503

Davis, T. A. & Young, L. M. 2019, *MNRAS*, 489, L108

de Jong, J. T. A., Verdoes Kleijn, G. A., Boxhoorn, D. R., et al. 2015, *A&A*, 582, A62

de Vaucouleurs, G. 1948, Annales d'Astrophysique, 11, 247

de Vaucouleurs, G. 1960, *ApJ*, 131, 574

Deeley, S., Drinkwater, M. J., Sweet, S. M., et al. 2020, *MNRAS*, 498, 2372

Domínguez-Gómez, J., Lisenfeld, U., Pérez, I., et al. 2022, *A&A*, 658, A124

Dopita, M. A., Groves, B. A., Fischera, J., et al. 2005, *ApJ*, 619, 755

Draine, B. T. & Lee, H. M. 1984, *ApJ*, 285, 89

Dressler, A. 1980, *ApJ*, 236, 351

Driver, S. P., Bellstedt, S., Robotham, A. S. G., et al. 2022, *MNRAS*, 513, 439

Driver, S. P., Hill, D. T., Kelvin, L. S., et al. 2011, *MNRAS*, 413, 971

Driver, S. P., Norberg, P., Baldry, I. K., et al. 2009, *Astron. Geophys.*, 50, 5.12

Driver, S. P., Wright, A. H., Andrews, S. K., et al. 2016, *MNRAS*, 455, 3911

Duband, L., Clerc, L., Ercolani, E., Guillemet, L., & Vallcorba, R. 2008, *Cryogenics*, 48, 95

Dunne, L., Eales, S., Edmunds, M., et al. 2000, *MNRAS*, 315, 115

Dunne, L., Gomez, H. L., da Cunha, E., et al. 2011, *MNRAS*, 417, 1510

Eales, S., de Vis, P., Smith, M. W. L., et al. 2017, *MNRAS*, 465, 3125

Eales, S., Dunne, L., Clements, D., et al. 2010, *PASP*, 122, 499

Eales, S., Smith, M. W. L., Auld, R., et al. 2012, *ApJ*, 761, 168

Eales, S. A., Baes, M., Bourne, N., et al. 2018, *MNRAS*, 481, 1183

Edge, A., Sutherland, W., Kuijken, K., et al. 2013, *The Messenger*, 154, 32

Elbaz, D., Daddi, E., Le Borgne, D., et al. 2007, *A&A*, 468, 33

Emerson, J. P., Sutherland, W. J., McPherson, A. M., et al. 2004, The Messenger, 117, 27

Escoffier, R. P., Comoretto, G., Webber, J. C., et al. 2007, *A&A*, 462, 801

Faber, S. M., Willmer, C. N. A., Wolf, C., et al. 2007, *ApJ*, 665, 265

Feigelson, E. D. & Babu, G. J. 2012, Modern Statistical Methods for Astronomy: With R Applications (Cambridge University Press)

Feldmann, R. 2020, Communications Physics, 3, 226

Feldmann, R. & Mayer, L. 2015, *MNRAS*, 446, 1939

Foreman-Mackey, D., Farr, W., Sinha, M., et al. 2019, The Journal of Open Source Software, 4, 1864

Foreman-Mackey, D., Hogg, D. W., Lang, D., & Goodman, J. 2013, *PASP*, 125, 306

Fukugita, M., Ichikawa, T., Gunn, J. E., et al. 1996, *AJ*, 111, 1748

Gabor, J. M. & Davé, R. 2015, *MNRAS*, 447, 374

Galametz, M., Madden, S. C., Galliano, F., et al. 2011, *A&A*, 532, A56

Gallagher, John S., I. 1972, *AJ*, 77, 568

Galliano, F. 2018, *MNRAS*, 476, 1445

Garg, P., Narayanan, D., Byler, N., et al. 2022, *ApJ*, 926, 80

Gavazzi, G., Savorgnan, G., & Fumagalli, M. 2011, *A&A*, 534, A31

Gelman, A. & Rubin, D. B. 1992, Statistical Science, 7, 457

Giovanelli, R., Haynes, M. P., Kent, B. R., et al. 2005, *AJ*, 130, 2598

Glass, D. H. W., Sansom, A. E., Davis, T. A., & Popescu, C. C. 2022, *MNRAS*, 517, 5524

Gómez, P. L., Nichol, R. C., Miller, C. J., et al. 2003, *ApJ*, 584, 210

Gong, M., Ostriker, E. C., & Kim, C.-G. 2018, *ApJ*, 858, 16

González-Nuevo, J., Lapi, A., Fleuren, S., et al. 2012, *ApJ*, 749, 65

Gordon, K. D., Clayton, G. C., Misselt, K. A., Landolt, A. U., & Wolff, M. J. 2003, *ApJ*, 594, 279

Gordon, K. D., Roman-Duval, J., Bot, C., et al. 2014, *ApJ*, 797, 85

Greve, A., Panis, J. F., & Thum, C. 1996, *A&AS*, 115, 379

Griffin, M. J., Abergel, A., Abreu, A., et al. 2010, *A&A*, 518, L3

Gunn, J. E., Carr, M., Rockosi, C., et al. 1998, *AJ*, 116, 3040

Gunn, J. E., Siegmund, W. A., Mannery, E. J., et al. 2006, *AJ*, 131, 2332

Hart, R. E., Bamford, S. P., Willett, K. W., et al. 2016, *MNRAS*, 461, 3663

Heeschen, D. S. 1975, *Sky & Telescope*, 49, 344

Herbst, E., Chang, Q., & Cuppen, H. M. 2005, in Journal of Physics Conference Series, Vol. 6, Journal of Physics Conference Series, 18–35

Herpich, F., Mateus, A., Stasińska, G., Cid Fernandes, R., & Vale Asari, N. 2016, *MNRAS*, 462, 1826

Hickox, R. C., Mullaney, J. R., Alexander, D. M., et al. 2014, *ApJ*, 782, 9

Hildebrand, R. H. 1983, *QJRAS*, 24, 267

Hoffman, M. D. & Gelman, A. 2014, *J. Machine Learning Res.*, 15, 351

Högbom, J. A. 1974, *A&AS*, 15, 417

Holland, W. S., Bintley, D., Chapin, E. L., et al. 2013, *MNRAS*, 430, 2513

Holwerda, B. W., Kelvin, L., Baldry, I., et al. 2019, *AJ*, 158, 103

Hood, C. E., Kannappan, S. J., Stark, D. V., et al. 2018, *ApJ*, 857, 144

Hopkins, A. M., Miller, C. J., Nichol, R. C., et al. 2003, *ApJ*, 599, 971

Hubble, E. P. 1926, *ApJ*, 64, 321

Hughes, D. H., Robson, E. I., Dunlop, J. S., & Gear, W. K. 1993, *MNRAS*, 263, 607

Jaffe, W., Ford, H. C., Ferrarese, L., van den Bosch, F., & O'Connell, R. W. 1993, *Nature*, 364, 213

Karim, A., Swinbank, A. M., Hodge, J. A., et al. 2013, *MNRAS*, 432, 2

Kassin, S. A., Weiner, B. J., Faber, S. M., et al. 2007, *ApJL*, 660, L35

Kauffmann, G., Heckman, T. M., Tremonti, C., et al. 2003, *MNRAS*, 346, 1055

Kaviraj, S., Ting, Y.-S., Bureau, M., et al. 2012, *MNRAS*, 423, 49

Keating, L. C., Richings, A. J., Murray, N., et al. 2020, *MNRAS*, 499, 837

Kelly, B. C., Shetty, R., Stutz, A. M., et al. 2012, *ApJ*, 752, 55

Kelvin, L. S., Bremer, M. N., Phillipps, S., et al. 2018, *MNRAS*, 477, 4116

Kelvin, L. S., Driver, S. P., Robotham, A. S. G., et al. 2014, *MNRAS*, 439, 1245

Kelvin, L. S., Driver, S. P., Robotham, A. S. G., et al. 2012, *MNRAS*, 421, 1007

Kewley, L. J., Dopita, M. A., Sutherland, R. S., Heisler, C. A., & Trevena, J. 2001, *ApJ*, 556, 121

Kewley, L. J. & Ellison, S. L. 2008, *ApJ*, 681, 1183

Kewley, L. J., Groves, B., Kauffmann, G., & Heckman, T. 2006, *MNRAS*, 372, 961

Kirk, J. M., Gear, W. K., Fritz, J., et al. 2015, *ApJ*, 798, 58

Kormendy, J. & Bender, R. 2012, *ApJS*, 198, 2

Kormendy, J. & Kennicutt, Robert C., J. 2004, *ARA&A*, 42, 603

Kron, R. G., Bonoli, F., Federici, L., Zitelli, V., & Vigotti, M. 1983, *A&A*, 127, 29

Labbé, I., Huang, J., Franx, M., et al. 2005, *ApJL*, 624, L81

Lamperti, I., Saintonge, A., De Looze, I., et al. 2019, *MNRAS*, 489, 4389

Lanz, L., Stepanoff, S., Hickox, R. C., et al. 2022, *ApJ*, 935, 29

Lewandowski, D., Kurowicka, D., & Joe, H. 2009, *Multivariate Anal.*, 100, 1989

Lewis, I. J., Cannon, R. D., Taylor, K., et al. 2002, *MNRAS*, 333, 279

Liddle, A. R. 2007, *MNRAS*, 377, L74

Lintott, C., Schawinski, K., Bamford, S., et al. 2011, *MNRAS*, 410, 166

Lintott, C. J., Schawinski, K., Slosar, A., et al. 2008, *MNRAS*, 389, 1179

Lisenfeld, U., Espada, D., Verdes-Montenegro, L., et al. 2011, *A&A*, 534, A102

Liske, J., Baldry, I. K., Driver, S. P., et al. 2015, *MNRAS*, 452, 2087

MacArthur, L. A., Courteau, S., & Holtzman, J. A. 2003, *ApJ*, 582, 689

Macchetto, F., Pastoriza, M., Caon, N., et al. 1996, *A&AS*, 120, 463

Maddox, S. J. & Dunne, L. 2020, *MNRAS*, 493, 2363

Mahajan, S., Drinkwater, M. J., Driver, S., et al. 2018, *MNRAS*, 475, 788

Mainzer, A. K., Eisenhardt, P., Wright, E. L., et al. 2005, in Society of Photo-Optical Instrumentation Engineers (SPIE) Conference Series, Vol. 5899, UV/Optical/IR Space Telescopes: Innovative Technologies and Concepts II, ed. H. A. MacEwen, 262–273

Man, A. & Belli, S. 2018, *Nature Astron.*, 2, 695

Mancini, C., Daddi, E., Juneau, S., et al. 2019, *MNRAS*, 489, 1265

Marigo, P. & Girardi, L. 2007, *A&A*, 469, 239

Marino, R. A., Rosales-Ortega, F. F., Sánchez, S. F., et al. 2013, *A&A*, 559, A114

Martig, M., Bournaud, F., Teyssier, R., & Dekel, A. 2009, *ApJ*, 707, 250

Martin, D. C., Fanson, J., Schiminovich, D., et al. 2005, *ApJL*, 619, L1

Martin, D. C., Wyder, T. K., Schiminovich, D., et al. 2007, *ApJS*, 173, 342

Martin, G., Kaviraj, S., Devriendt, J. E. G., Dubois, Y., & Pichon, C. 2018, *MNRAS*, 480, 2266

Martinsson, T. P. K., Sarzi, M., Knapen, J. H., et al. 2018, *A&A*, 612, A66

Massey, P., Puls, J., Pauldrach, A. W. A., et al. 2005, *ApJ*, 627, 477

Masters, K. L., Mosleh, M., Romer, A. K., et al. 2010, *MNRAS*, 405, 783

Mateos, S., Alonso-Herrero, A., Carrera, F. J., et al. 2012, *MNRAS*, 426, 3271

Medling, A. M., Cortese, L., Croom, S. M., et al. 2018, *MNRAS*, 475, 5194

Misgeld, I. & Hilker, M. 2011, *MNRAS*, 414, 3699

Mitzkus, M., Cappellari, M., & Walcher, C. J. 2017, *MNRAS*, 464, 4789

Moffett, A. J., Ingarfield, S. A., Driver, S. P., et al. 2016, *MNRAS*, 457, 1308

Naslim, N., Kemper, F., Madden, S. C., et al. 2015, *MNRAS*, 446, 2490

Natale, G., Popescu, C. C., Rushton, M., et al. 2022, *MNRAS*, 509, 2339

Nayyeri, H., Keele, M., Cooray, A., et al. 2016, *ApJ*, 823, 17

Negrello, M., Amber, S., Amvrosiadis, A., et al. 2017, *MNRAS*, 465, 3558

Negrello, M., Hopwood, R., De Zotti, G., et al. 2010, *Science*, 330, 800

Nelder, J. A. & Mead, R. 1965, The Computer Journal, 7, 308

Nersesian, A., Xilouris, E. M., Bianchi, S., et al. 2019, *A&A*, 624, A80

Noeske, K. G., Weiner, B. J., Faber, S. M., et al. 2007, *ApJL*, 660, L43

Oke, J. B. & Gunn, J. E. 1983, *ApJ*, 266, 713

PACS Team. 2019, The PACS Handbook, HERSCHEL-HSC-DOC-2101, version 4.0.1, https://www.cosmos.esa.int/web/herschel/legacy-documentation-pacs, accessed 22/3/22

Peng, Y., Maiolino, R., & Cochrane, R. 2015, *Nature*, 521, 192

Peng, Y.-j., Lilly, S. J., Kovač, K., et al. 2010, *ApJ*, 721, 193

Peng, Y.-j., Lilly, S. J., Renzini, A., & Carollo, M. 2012, *ApJ*, 757, 4

Pettini, M. & Pagel, B. E. J. 2004, *MNRAS*, 348, L59

Phillipps, S., Bremer, M. N., Hopkins, A. M., et al. 2019, *MNRAS*, 485, 5559

Pilbratt, G. L., Riedinger, J. R., Passvogel, T., et al. 2010, *A&A*, 518, L1

Poglitsch, A., Waelkens, C., Geis, N., et al. 2010, *A&A*, 518, L2

Popescu, C. C. & Tuffs, R. J. 2003, *A&A*, 410, L21

Porter-Temple, R., Holwerda, B. W., Hopkins, A. M., et al. 2022, *MNRAS*, 515, 3875

Rémy-Ruyer, A., Madden, S. C., Galliano, F., et al. 2014, *A&A*, 563, A31

Robotham, A. S. G., Driver, S. P., Davies, L. J. M., et al. 2014, *MNRAS*, 444, 3986

Rodrigo, C. & Solano, E. 2020, in XIV.0 Scientific Meeting (virtual) of the Spanish Astronomical Society, 182

Roman-Duval, J., Heyer, M., Brunt, C. M., et al. 2016, *ApJ*, 818, 144

Saintonge, A., Catinella, B., Cortese, L., et al. 2016, *MNRAS*, 462, 1749

Saintonge, A., Catinella, B., Tacconi, L. J., et al. 2017, *ApJS*, 233, 22

Saintonge, A., Kauffmann, G., Kramer, C., et al. 2011, *MNRAS*, 415, 32

Saintonge, A., Wilson, C. D., Xiao, T., et al. 2018, *MNRAS*, 481, 3497

Salim, S. 2014, Serbian Astronomical Journal, 189, 1

Salim, S., Rich, R. M., Charlot, S., et al. 2007, *ApJS*, 173, 267

Salpeter, E. E. 1955, *ApJ*, 121, 161

Sansom, A. E., Glass, D. H. W., Bendo, G. J., et al. 2019, *MNRAS*, 482, 4617

Sarzi, M., Bacon, R., Cappellari, M., et al. 2007, *New Astron. Rev.*, 51, 18

Saunders, W., Bridges, T., Gillingham, P., et al. 2004, in Society of Photo-Optical Instrumentation Engineers (SPIE) Conference Series, Vol. 5492, Ground-based Instrumentation for Astronomy, ed. A. F. M. Moorwood & M. Iye, 389–400

Schawinski, K., Lintott, C., Thomas, D., et al. 2009, *MNRAS*, 396, 818

Schawinski, K., Urry, C. M., Simmons, B. D., et al. 2014, *MNRAS*, 440, 889

Schiminovich, D., Wyder, T. K., Martin, D. C., et al. 2007, *ApJS*, 173, 315

Scholz, F. & Stephens, M. 1987, *J. American Statistical Association*, 82, 918

Schwartz, G. 1978, Ann. Statist., 6, 461

Sellwood, J. A. & Wilkinson, A. 1993, Reports on Progress in Physics, 56, 173

Sérsic, J. L. 1963, Boletin de la Asociacion Argentina de Astronomia La Plata Argentina, 6, 41

Shapiro, K. L., Falcón-Barroso, J., van de Ven, G., et al. 2010, *MNRAS*, 402, 2140

Sharp, R., Allen, J. T., Fogarty, L. M. R., et al. 2015, *MNRAS*, 446, 1551

Shetty, R., Kauffmann, J., Schnee, S., & Goodman, A. A. 2009a, *ApJ*, 696, 676

Shetty, R., Kauffmann, J., Schnee, S., Goodman, A. A., & Ercolano, B. 2009b, *ApJ*, 696, 2234

Smethurst, R. J., Lintott, C. J., Bamford, S. P., et al. 2017, *MNRAS*, 469, 3670

Smethurst, R. J., Masters, K. L., Lintott, C. J., et al. 2018, *MNRAS*, 473, 2679

Smith, M. D., Bureau, M., Davis, T. A., et al. 2019, *MNRAS*, 485, 4359

Smith, M. W. L., Gomez, H. L., Eales, S. A., et al. 2012, *ApJ*, 748, 123

Solomon, P. M. & Vanden Bout, P. A. 2005, *ARA&A*, 43, 677

Sparke, L. S. & Gallagher, III, J. S. 2007, Galaxies in the Universe: An Introduction, 2nd edn. (Cambridge University Press)

Spekkens, K. & Sellwood, J. A. 2007, *ApJ*, 664, 204

Stan Development Team. 2022a, PyStan, https://pystan.readthedocs.io/en/latest/, accessed 18/12/22

Stan Development Team. 2022b, Stan Modelling Language Users Guide and Reference Manual, http://mc-stan.org, Version 2.31, accessed 18/12/22

Stasińska, G., Cid Fernandes, R., Mateus, A., Sodré, L., & Asari, N. V. 2006, *MNRAS*, 371, 972

Stasińska, G., Vale Asari, N., Cid Fernandes, R., et al. 2008, *MNRAS*, 391, L29

Steidel, C. C., Rudie, G. C., Strom, A. L., et al. 2014, *ApJ*, 795, 165

Strömberg, G. 1946, *ApJ*, 104, 12

Sutherland, W., Emerson, J., Dalton, G., et al. 2015, *A&A*, 575, A25

Tempel, E., Tuvikene, T., Kipper, R., & Libeskind, N. I. 2017, *A&A*, 602, A100

Thirlwall, J. J., Popescu, C. C., Tuffs, R. J., et al. 2020, *MNRAS*, 495, 835

Thomas, D., Maraston, C., Schawinski, K., Sarzi, M., & Silk, J. 2010, *MNRAS*, 404, 1775

Tohline, J. E., Simonson, G. F., & Caldwell, N. 1982, *ApJ*, 252, 92

Tonry, J. L., Blakeslee, J. P., Ajhar, E. A., & Dressler, A. 2000, *ApJ*, 530, 625

Toomre, A. 1964, *ApJ*, 139, 1217

Tsukui, T., Iguchi, S., Mitsuhashi, I., & Tadaki, K. 2022, arXiv e-prints, arXiv:2207.12588

Ueda, J., Iono, D., Yun, M. S., et al. 2014, *ApJS*, 214, 1

Valiante, E., Smith, M. W. L., Eales, S., et al. 2016, *MNRAS*, 462, 3146

Valtchanov, I. 2018, SPIRE Handbook v3.2, Herschel Explanatory Supplement vol. IV, https://www.cosmos.esa.int/web/herschel/legacy-documentation-spire, accessed 22/3/22

van Cittert, P. H. 1934, *Physica*, 1, 201

van de Voort, F., Davis, T. A., Kereš, D., et al. 2015, *MNRAS*, 451, 3269

van de Voort, F., Davis, T. A., Matsushita, S., et al. 2018, *MNRAS*, 476, 122

van den Bosch, R. C. E. & van de Ven, G. 2009, *MNRAS*, 398, 1117

Wall, J. V. & Jenkins, C. R. 2003, Practical Statistics for Astronomers, Cambridge Observing Handbooks for Research Astronomers (Cambridge University Press)

Wang, W., Faber, S. M., Liu, F. S., et al. 2017, *MNRAS*, 469, 4063

Wells, D. C., Greisen, E. W., & Harten, R. H. 1981, *A&AS*, 44, 363

Werle, A., Cid Fernandes, R., Vale Asari, N., et al. 2020, *MNRAS*, 497, 3251

Weston, M. E., McIntosh, D. H., Brodwin, M., et al. 2017, *MNRAS*, 464, 3882

Whitaker, K. E., Narayanan, D., Williams, C. C., et al. 2021, *ApJL*, 922, L30

White, R. L., Becker, R. H., Helfand, D. J., & Gregg, M. D. 1997, *ApJ*, 475, 479

Whittet, D. C. B. 2003, Dust in the Galactic Environment, 2nd edn. (Bristol, UK: Institute of Physics)

Wiklind, T., Combes, F., & Henkel, C. 1995, *A&A*, 297, 643

Wilson, T., Rohlfs, K., & Hüttemeister, S. 2009, Tools of Radio Astronomy, Astronomy and Astrophysics Library (Springer Berlin Heidelberg)

Wright, A. H., Robotham, A. S. G., Bourne, N., et al. 2016, *MNRAS*, 460, 765

Wright, E. L., Eisenhardt, P. R. M., Mainzer, A. K., et al. 2010, *AJ*, 140, 1868

Wuyts, S., Labbé, I., Franx, M., et al. 2007, *ApJ*, 655, 51

Wyder, T. K., Martin, D. C., Schiminovich, D., et al. 2007, *ApJS*, 173, 293

Xilouris, E. M., Georgakakis, A. E., Misiriotis, A., & Charmandaris, V. 2004, *MNRAS*, 355, 57

York, D. G., Adelman, J., Anderson, John E., J., et al. 2000, *AJ*, 120, 1579

Young, L. M., Bureau, M., Davis, T. A., et al. 2011, *MNRAS*, 414, 940

Zabel, N., Davis, T. A., Smith, M. W. L., et al. 2019, *MNRAS*, 483, 2251

Zernike, F. 1938, *Physica*, 5, 785

Appendix A

Calculating Coordinates for Equally Spaced Points on an Ellipse

In order to place equally-spaced cloudlets on an ellipse when generating models for KinMS (Chapter 2), it is necessary to calculate the individual angles for points from a reference axis for each point. Equal angles for spacing would cause the points to be more concentrated around the ends of the major axis and more spread out at the ends of the minor axis. An iterative method to provide the necessary angles for equal spacing has been coded in Python and made available[1], but the interative nature of the calculation slowed the running of the KinMS model fitting code significantly. The method uses the Python routine scipy.special.ellipeinc to calculate arc lengths for segments of a given ellipse, and adjusts the angular separation defining each segment iteratively to give equal arc lengths. The strategy employed for this study was to investigate how the angles for equal point spacing varied from equally-spaced angles, and determine an empirical means of calculating the differences so that the angles for equal point spacing can be determined without iteration.

[1] https://stackoverflow.com/questions/6972331/how-can-i-generate-a-set-of-points-evenly-distributed-along-the-perimeter-of-an-ellipse

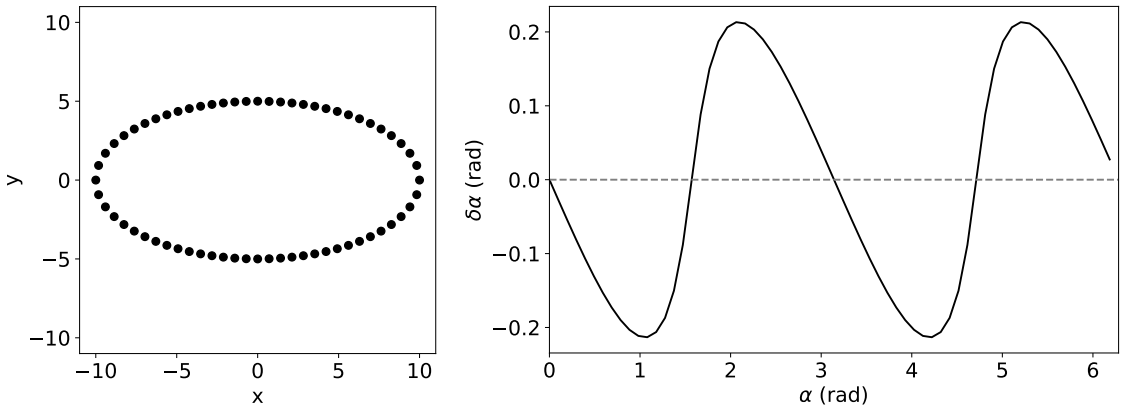

Figure A.1: Equally-spaced points on an ellipse ([x, y] coordinates) and the diffferences between the angles $\delta\alpha$ subtended by these and an equivalent number of equally-spaced angles α. Angles are measured anticlockwise from vertical.

Figure A.1 shows an array of equally-spaced points on an ellipse calculated using the iterative method, and a plot showing how the difference between an array of equal angles differs from the actual angles needed to acheve equal spacing of points. All angles are calculated clockwise from vertical in this instance. The angle differences form a tilted sinusoidal function which can be represented as follows[2]:

$$\delta\alpha = \left(\frac{c'}{t'}\right)\arctan\left(\frac{t'\sin(2\alpha)}{1 - t'\cos(2\alpha)}\right) \tag{A.1}$$

where α is the equally-spaced angle of interest, $\delta\alpha$ is the correction needed to achieve equally-spaced points, c' is the amplitude of the wave and t' is a tilting factor ranging between -1 and +1.

To create an empirical method for calculating the coordinates of equally-spaced points on an ellipse, values of c' and t' were found by curve-fitting Equation A.1 to values of $\delta\alpha$ for equally-spaced points on 12 model ellipses determined using the iterative

[2]https://math.stackexchange.com/questions/2430564/equation-of-a-tilted-sine

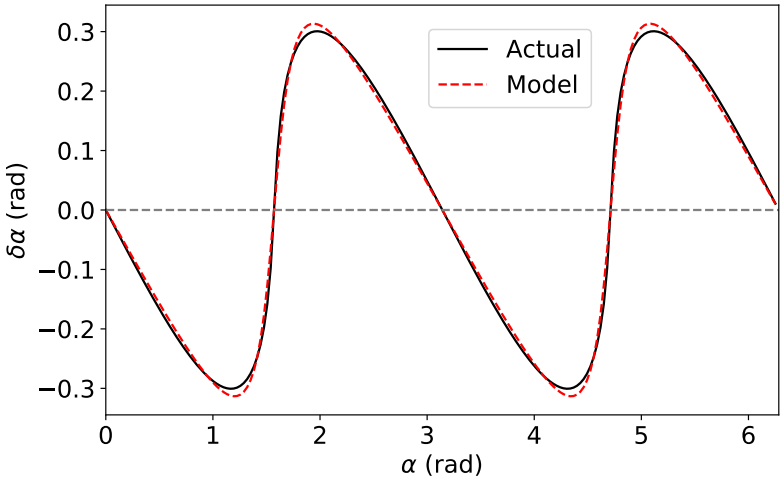

Figure A.2: Comparison of actual values of $\delta\alpha$ for an ellipse with a fitted model using Equation A.1. Axis ratio for actual ellipse is 5:1, c' = -0.2783, t' = -0.7405.

method discussed above. The model ellipses had major axis lengths of 1 and minor axis lengths ranging from 0.05 to 0.95. Figure A.2 shows an example of a derived plot of $\delta\alpha$ versus equally-spaced angles, and the fitted model from Equation A.1. The values of c' and t' obtained were then fitted to third order polynomials as a function of minor:major axis radius ratio, using SCIPY.OPTIMIZE.CURVE_FIT. Given the fitted polynomials, values of c' and t' can be estimated for an ellipse with a given axis length ratio, an array of equally-spaced angles can be set up and values of $\delta\alpha$ calculated using Equation A.1 applied to them. The coordinates of the equally-spaced points can then be calculated knowing the required angles for equally-spaced points around the ellipse. This was coded as a Python function, reproduced below. The position angle of the ellipse is also accounted for in the function, so that it can be used directly for galaxy features relevant to KINMS. The function was used to create Figure 3.6 in Chapter 2. Figure A.3 shows the equally-spaced points for an ellipse generated using the code.

```
def equal_spaced_points_on_ellipse(a, b, num, phi):

    # a = major axis radius
    # b = minor axis radius
    # num = number of points to distribute
    # phi = galaxy position angle (degrees)

    equalangles=np.linspace(0,2*np.pi,int(num))
    c = -0.02752566 - 0.42304019 * (1. - b / a) + 0.10521114 * (1. - b
                                        / a) ** 2 + 0.04202059 * (1. -
                                        b / a) ** 3
    t = -0.07020526 -1.03956471 * (1. - b / a) + 0.18692054 * (1. - b /
                                         a) ** 2 + 0.08864614 * (1. - b
                                         / a) ** 3
    adiffs = (c / t) * np.arctan(t * np.sin(equalangles * 2) / (1. - t
                                        * np.cos(equalangles * 2)))
    x = a * np.sin(equalangles + adiffs)
    y = b * np.cos(equalangles + adiffs)
    s1 = np.cos(np.radians(phi + 90.))
    s2 = np.sin(np.radians(phi + 90.))
    xout=(s1 * x) + (s2 * y)
    yout=(s2 * x) - (s1 * y)
    return xout, yout
```

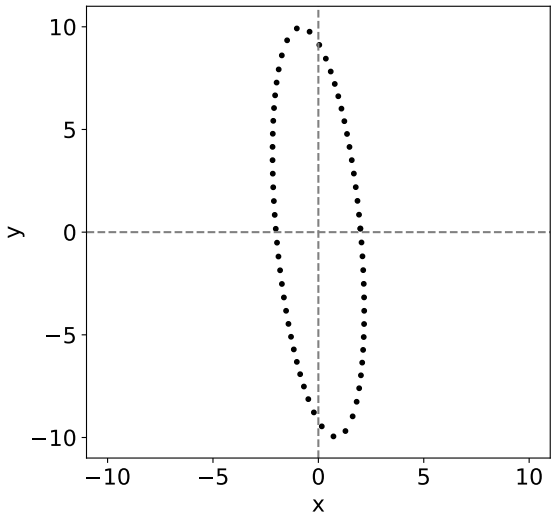

Figure A.3: Equally-spaced points generated using the PYTHON code for an ellipse with major radius = 10 units, minor radius = 2 units and position angle (anti-clockwise from vertical) of 5°.